

# Spectroscopic Investigation of Film Formation and Aggregation in Organic Solar Cell Materials

Von der Universität Bayreuth  
zur Erlangung des Grades eines  
Doktors der Naturwissenschaften (Dr. rer. nat.)  
genehmigte Abhandlung

von  
Hazem Mohammed Bakr Mohammed

aus Kairo, Ägypten

1. Gutachterin:	Prof. Dr. Anna Köhler
2. Gutachter:	Prof. Dr. Georg Herink

Tag der Einreichung:	07.12.2022
Tag des Kolloquiums:	13.04.2023



لله الحمد







# Summary

Photovoltaic technology used to convert renewable solar energy to electricity by means of solar cells is considered one of the most important technologies in today's world. This importance stems from the rapid increase in the world's electricity demands. Research in the field of solar cells went through several developments during the past decades in relation to the materials used to manufacture such devices. A big part of these developments was focused on the search for more efficient materials in terms of the solar cells power conversion efficiency and manufacturing costs. One class of such materials are organic semiconductors. The main advantage of organic semiconductors is that they can be processed from solutions. This would allow for large scale and high output manufacturing processes with low energy demands and production costs compared to conventional silicon based solar cells. However, one big challenge to overcome when developing efficient solar cells using organic materials is the disordered nature of such materials. This disordered nature –compared to the more ordered inorganic counterparts- makes it difficult to control their structural properties when solution processed into thin film solar cells. Hence, it is crucial to develop clear structure property relationships in order to have better control of the thin film properties during fabrication of organic solar cells to achieve high efficiency devices.

Within my thesis, I investigate how to better understand the physics of film formation of organic materials processed from solutions. I aim to understand the relation between the different solution processing conditions and the resulting film properties. I also try to draw a correlation between the structural properties of the resulting organic materials films and their solar cell performance.

Organic solar cells usually consist of a blend of two or more organic materials such as  $\pi$ -conjugated polymers, oligomers and fullerenes.  $\pi$ -conjugated polymers usually adopt a semi-crystalline structure consisting of disordered and more ordered polymer chains. The more ordered polymer chains often exhibit electrostatic inter-chain interactions and those chains are referred to as aggregates. The properties of these aggregates usually affect the optoelectronic properties of organic materials hence influencing organic solar cell performance. It is important then to understand how the aggregate properties change in response to different conditions during fabrication of organic solar cells. Blending results in changes in the structural properties of the constituent materials, compared to their neat state, which alters the aggregate properties of organic materials. In chapter 3, I focus on induced structural changes of PCE11 as a model  $\pi$ -conjugated donor polymer that is used to fabricate organic solar cells with > 10% efficiencies. By a

combination of temperature dependent optical spectroscopy and Raman spectroscopy, I investigate how the addition of an extra material to PCE11 affects its structural and aggregate properties. By detailed analysis of the PCE11's optical spectra both in the neat and blend states, I quantify changes appearing in the spectra in these two cases and relate them in structural changes of PCE11. I conclude that blending results in a more planarized, longer conjugated PCE11 chains with a reduced degree of inter-chain molecular coupling.

However, studying on the resulting final films of organic materials or blends does not offer a complete picture about their film formation process. To be able to study such film formation processes, insitu optical spectroscopy is an invaluable technique. In chapter 4, I try to provide a general picture on the film formation dynamics of solution processed conjugated polymers. In this chapter, I focus on the film formation of solution processed P3HT films. Although P3HT does not offer the best device performance, it has been intensively investigated for application in organic solar cells, and it is a model material with well-understood photophysical properties. By careful choice and control of the solution processing conditions and detailed analysis of the measured insitu optical spectra during P3HT film formation, I propose general guidelines to explain the different aggregation pathways that affect the final aggregate properties in the formed film. I concluded that the aggregate formation in conjugated donor polymers during their solution processing into thin films proceeds through one of two routes. The aggregate formation proceeds either via a 2-step route where aggregates form in solution before solvent evaporation or via a 1-step route where aggregates only form upon sufficient solvent evaporation at high polymer concentration. The route followed during the film formation determines the aggregate properties of the resulting final film. Aggregates formed following a 2-step route are characterized by a more planar, more ordered structure while aggregates formed following a 1-step route are characterized by a less planar, and less ordered structure.

In chapter 5, I turn my focus towards the other half of an organic blend used in organic solar cells, which is the acceptor material. In this chapter, I investigate the aggregation properties of two novel side chain polymers based on an inert polystyrene backbone and two different PDI chromophores. These two polymers, namely PPBI-alkyl and PPBI-OEG, have slightly different side chain chemical structures that affects their structural and aggregation properties in solution. Their structure offers a unique approach to control the overall polymer's aggregation properties by manipulating the conformation properties of the polymer backbone. Using steady state and time resolved optical spectroscopy; I investigate how minor changes in the side chain structure of these PDIs influence the overall polymer aggregation properties in solutions as a function of solvent properties. I show that it is possible to control the electronic interaction between the PDI chromophores by controlling

the conformation of the inert polymer backbone and the arrangement of the PDI chromophores around the backbone. The degree of solubility of the polymer's backbone controls the backbone conformation while the solvent polarity affects the arrangement of PDI chromophores around the backbone depending on the attached side chain. The interplay between the solvation and polarity may allow for tuning the aggregation of the material towards the desired properties.

Finally, in chapter 6, I try to correlate between the film formation and aggregation properties of organic materials and blends during their solution processing into films and their performance in organic solar cells. By characterizing the film formation dynamics in such blends using insitu optical spectroscopy and their solar cell performance, I aim to determine what spectral features correspond to a better solar cell performance. I then try to infer the underlying structural origins that corresponds to this better performance. This would enable one to rationally choose material systems that provide optimum morphology for enhanced solar cell performance rather than following a trial-and-error approach. I have shown that it is possible a priori to predict the viability of an organic blend to be used to fabricate efficient solar cells. By means of tracking the insitu optical spectra during film formation of different organic blends, one can gain information about the intermixing of domains between materials used in such blends. The reduction of the PL intensity over a long time after film formation indicated further formation of interfaces between the blend materials, which offers a more favorable morphology for efficient organic solar cells. This favorable morphology enhanced the charge generation efficiency of the investigated devices and resulted in better overall device efficiencies. Based on this knowledge, I was able to fabricate ternary organic solar cells with the optimum blend composition that resulted in 30% better power conversion efficiency compared to the binary solar cells.

Overall, my work shows that it is possible to extract valuable information about film formation of organic materials processed from solutions relying mainly on insitu optical spectroscopy. My work offers a general picture about the relationship between the solution processing conditions, the resulting aggregate properties and the corresponding solar cell performance. This work lays the ground towards achieving targeted solution processing of organic blend films for efficient organic solar cells.



# Zusammenfassung

Die Photovoltaik-Technologie, mit der erneuerbare Sonnenenergie mittels Solarzellen in Strom umgewandelt wird, gilt als eine der wichtigsten Technologien der heutigen Zeit. Diese Bedeutung ergibt sich aus dem raschen Anstieg des weltweiten Strombedarfs. Die Forschung auf dem Gebiet der Solarzellen hat in den letzten Jahrzehnten mehrere Entwicklungen bei dem für die Herstellung solcher Geräte verwendeten Materialien durchlaufen. Ein großer Teil dieser Entwicklungen konzentrierte sich auf die Suche nach effizienteren Materialien im Hinblick auf den Wirkungsgrad der Solarzellen und die Herstellungskosten. Eines dieser Materialklassen sind organische Halbleiter. Der Hauptvorteil organischer Halbleiter besteht darin, dass sie als Lösungen verarbeitet werden können. Dies würde Herstellungsverfahren in großem Maßstab und mit hoher Produktion Volumen bei geringem Energiebedarf und niedrigen Produktionskosten im Vergleich zu herkömmlichen Solarzellen auf Siliziumbasis ermöglichen. Eine große Herausforderung, die es bei der Entwicklung effizienter Solarzellen aus organischen Materialien zu überwinden gilt, ist jedoch die ungeordnete Natur dieser Materialien. Diese Unordnung - im Vergleich zu den geordneteren anorganischen Gegenständen - erschwert die Kontrolle ihrer strukturellen Eigenschaften bei der Verarbeitung in Dünnschicht-Solarzellen. Daher ist es von entscheidender Bedeutung, klare Struktur-Eigenschafts-Beziehungen zu entwickeln, um die Dünnschichteigenschaften bei der Herstellung von organischen Solarzellen besser kontrollieren zu können und so hocheffiziente Zellen zu erhalten.

In meiner Dissertation untersuche ich, wie man die Physik der Filmbildung von organischen Materialien, die aus Lösungen prozessiert werden, besser verstehen kann. Ich möchte die Beziehung zwischen den verschiedenen Konditionen der Lösungsverarbeitung und den resultierenden Filmeigenschaften verstehen. Außerdem versuche ich, einen Zusammenhang zwischen den strukturellen Eigenschaften der entstehenden Filme aus organischen Materialien und ihrer Solarzellenleistung herzustellen.

Organische Solarzellen bestehen in der Regel aus einer Mischung von zwei oder mehr organischen Materialien wie  $\pi$ -konjugierten Polymeren, Oligomeren und Fullerenen.  $\pi$ -konjugierte Polymere haben in der Regel eine teilkristalline Struktur, die aus ungeordneten und geordneteren Polymerketten besteht. Die stärker geordneten Polymerketten weisen häufig elektrostatische Wechselwirkungen zwischen den Ketten auf, und diese Ketten werden als Aggregate bezeichnet. Die Eigenschaften dieser Aggregate wirken sich in der Regel auf die optoelektronischen Eigenschaften der organischen Materialien aus und beeinflussen somit die Leistung organischer Solarzellen. Daher ist es wichtig zu verstehen, wie sich die Aggregateigenschaften als Reaktion auf

verschiedene Bedingungen während der Herstellung organischer Solarzellen verändern. Das Mischen führt zu Veränderungen der strukturellen Eigenschaften der einzelnen Materialien im Vergleich zu ihrem reinen Zustand, was die Aggregateigenschaften organischer Materialien verändert. In Kapitel 3 konzentriere ich mich auf die induzierten strukturellen Veränderungen von PCE11, einem  $\pi$ -konjugierten Donor polymer, das zur Herstellung von organischen Solarzellen mit einem Wirkungsgrad von über 10 % verwendet wird. Durch eine Kombination aus temperaturabhängiger optischer Spektroskopie und Raman-Spektroskopie untersuche ich, wie sich die Zugabe eines zusätzlichen Materials zu PCE11 auf seine Struktur- und Aggregateigenschaften auswirkt. Durch eine detaillierte Analyse der optischen Spektren von PCE11 sowohl im reinen als auch im gemischten Zustand quantifiziere ich die in diesen beiden Fällen auftretenden Veränderungen in den Spektren und bringe sie mit den strukturellen Veränderungen von PCE11 in Verbindung. Ich komme zu dem Schluss, dass die Vermischung zu einer stärker planarisierten, längeren konjugierten PCE11-Kette mit einem geringeren Grad an molekularer Kopplung zwischen den Ketten führt.

Die Untersuchung der resultierenden Filme aus organischen Materialien oder Mischungen bietet jedoch kein vollständiges Bild des Filmbildungsprozesses. Um solche Filmbildungsprozesse zu untersuchen, ist die optische In-situ-Spektroskopie eine beste geeignete Technik. In Kapitel 4 versuche ich, ein allgemeines Verständnis über die Filmbildungsdynamik von aus Lösung verarbeiteten konjugierten Polymeren zu vermitteln. In diesem Kapitel konzentriere ich mich auf die Filmbildung von aus Lösung prozessiert P3HT-Filmen. Obwohl P3HT nicht die bestes Effizienten bietet, wurde es intensiv für die Anwendung in organischen Solarzellen untersucht, und es ist ein Modellmaterial mit gut verstandenen photophysikalischen Eigenschaften. Durch eine sorgfältige Auswahl und Kontrolle der Verarbeitungsbedingungen für die Lösung und eine detaillierte Analyse der gemessenen optischen In-situ-Spektren während der P3HT-Filmbildung präsentiere ich ein allgemeines Verständnis zur Erklärung der verschiedenen Aggregationswege vor, die die endgültigen Aggregateigenschaften im gebildeten Film beeinflussen. Ich bin zu dem Schluss gekommen, dass die Aggregatbildung in konjugierten Donor Polymeren bei der prozessiert aus Lösung zu dünnen Filmen über einen von zwei Wegen erfolgt. Die Aggregatbildung erfolgt entweder über einen zweistufigen Weg, bei dem sich die Aggregate bereits in der Lösung bilden, bevor das Lösungsmittel verdampft, oder über einen einstufigen Weg, bei dem sich die Aggregate erst nach ausreichender Verdampfung des Lösungsmittels bei hoher Polymerkonzentration bilden. Der während der Filmbildung eingeschlagene Weg bestimmt die Aggregateigenschaften der resultierenden Filme. Aggregate, die nach einem 2-Schritt-Verfahren gebildet werden, zeichnen sich durch eine planere, stärker geordnete Struktur aus, während Aggregate, die nach einem 1-

Schritt-Verfahren gebildet werden, durch eine weniger planere und weniger geordnete Struktur gekennzeichnet sind.

In Kapitel 5 wende ich mich der anderen Hälfte eines organischen Gemischs zu, das in organischen Solarzellen verwendet wird, nämlich dem Akzeptor Material. In diesem Kapitel untersuche ich die Aggregationseigenschaften von zwei neuartigen Seitenkettenpolymeren, die auf einem inerten Polystyrol-Grundgerüst und zwei verschiedenen PDI-Chromophoren basieren. Diese beiden Polymere, PPBI-Alkyl und PPBI-OEG, haben leicht unterschiedliche chemische Seitenkettenstrukturen, was sich auf ihre Struktur- und Aggregationseigenschaften in Lösung beeinflusst. Ihre Struktur bietet einen einzigartigen Ansatz zur Steuerung der Aggregationseigenschaften des Gesamtpolymers durch Manipulation der Konformationseigenschaften des Polymerrückgrats. Mit Hilfe der stationären und zeitaufgelösten optischen Spektroskopie untersuche ich, wie geringfügige Änderungen der Seitenkettenstruktur dieser PDIs die Gesamtpolymeraggregationseigenschaften in Lösungen als Funktion der Lösungsmittleigenschaften beeinflussen. Ich zeige, dass es möglich ist, die elektronische Wechselwirkung zwischen den PDI-Chromophoren zu steuern, indem man die Konformation des inerten Polymerrückgrats und die Anordnung der PDI-Chromophore um das Rückgrat herum kontrolliert. Der Grad der Löslichkeit des Polymerrückgrats steuert die Konformation des Rückgrats, während die Polarität des Lösungsmittels die Anordnung der PDI-Chromophore um das Rückgrat in Abhängigkeit von der angehängten Seitenkette beeinflusst. Durch das Zusammenspiel von Löslichkeit und Polarität lässt sich die Aggregation des Materials auf die gewünschten Eigenschaften abstimmen.

In Kapitel 6 schließlich versuche ich, einen Zusammenhang zwischen den Filmbildungs- und Aggregationseigenschaften von organischen Materialien und Mischungen bei ihrer Verarbeitung aus Lösung zu Filmen und ihrer Performance in organischen Solarzellen herzustellen. Durch die Charakterisierung der Filmbildungsdynamik in solchen Mischungen mittels optischer Insitu-Spektroskopie und ihrer Solarzellen Effizienz möchte ich herausfinden, welche spektralen Merkmale mit einer besseren Solarzelleneffizienz einhergehen. Anschließend versuche ich, die zugrundeliegenden strukturellen Ursprünge zu ermitteln, die dieser besseren Performance entsprechen. Dies würde es ermöglichen, auf rationale Weise Materialsysteme auszuwählen, die eine optimale Morphologie für eine verbesserte Solarzelleneffizienz bieten, anstatt trial-and-error zu folgen. Ich habe gezeigt, dass es möglich ist, a priori die Eignung einer organischen Mischung für die Herstellung effizienter Solarzellen vorherzusagen. Durch die Verfolgung der optischen Insitu-Spektren während der Filmbildung verschiedener organischer Mischungen kann man Informationen über die Vermischung von Domänen zwischen den in solchen Mischungen

verwendeten Materialien gewinnen. Die Abnahme der PL-Intensität über einen langen Zeitraum nach der Filmbildung deutet auf eine weitere Bildung von Grenzflächen zwischen den Mischmaterialien hin, die eine günstigere Morphologie für effiziente organische Solarzellen bietet. Diese günstige Morphologie erhöhte die Effizienz bei der Ladungsträger Erzeugung der untersuchten Zellen und führte zu besseren Gesamtwirkungsgraden der Solarzellen. Auf der Grundlage dieser Erkenntnisse konnte ich ternäre organische Solarzellen mit der optimalen Mischungszusammensetzung herstellen, die im Vergleich zu den binären Solarzellen einen um 30 % höheren Wirkungsgrad aufweisen.

Insgesamt zeigt meine Arbeit, dass es möglich ist, Informationen über die Filmbildung von organischen Materialien zu erhalten, die aus Lösungen verarbeitet werden, indem man sich hauptsächlich auf die optische In-situ-Spektroskopie stützt. Meine Arbeit liefert eine allgemeine grundlegende Struktur der Beziehung zwischen den prozessierten Konditionen aus Lösung, den resultierenden Aggregateigenschaften und der entsprechenden Solarzelleneffizienz. Diese Arbeit legt den Grundstein für eine gezielte Lösungsprozessierung von organischen Mischschichten für effiziente organische Solarzellen.





# Table of Contents

## Chapter 1: Introduction

1.1	Motivation and thesis objective .....	1
1.2	Thesis overview .....	4
1.3	Electronic structure of organic semiconductors .....	5
1.4	Theoretical background of the experimental techniques .....	7
	i. Steady state absorption and emission .....	7
	ii. Spectral signatures of aggregates in organic materials .....	9
	iii. Franck-Condon analysis (FCA) .....	12
	iv. Time resolved photoluminescence .....	14
	v. Raman Spectroscopy .....	15
	vi. Relation between optical and Raman Spectroscopies .....	16
1.5	Fundamentals of organic solar cells .....	18
1.6	Materials for organic solar cells .....	20
	References .....	24

## Chapter 2: Methods

2.1	Introduction .....	28
2.2	Temperature dependent steady state spectroscopy .....	28
	i. Photoluminescence (PL) .....	29
	ii. Absorption .....	30
	iii. Calibration for the tungsten-halogen lamp .....	30
	iv. Exemplary data .....	31
2.3	Time-resolved photoluminescence (TRPL) .....	32
	i. Excitation .....	32
	ii. Detection .....	34
	iii. Exemplary data .....	35
2.4	In-situ optical spectroscopy .....	36
	i. Photoluminescence (PL) .....	37
	ii. Absorption .....	38
	iii. Quasi-simultaneous PL and Abs detection system .....	38

	iv. Exemplary data .....	39
2.5	Room temperature steady state optical spectroscopy .....	40
2.6	Raman spectroscopy .....	40
2.7	Device fabrication and characterization .....	41
	i. Device fabrication .....	41
	ii. Device characterization .....	41
	References .....	43

### **Chapter 3: Probing conformational changes of PffBT4T-2OD (PCE11) aggregates upon blending**

3.1	Introduction .....	44
3.2	Microstructural characterization of PCE11.....	44
3.3	Results .....	46
	i. Sample preparation .....	46
	ii. Raman Spectroscopy .....	46
	iii. Temperature dependent steady state Spectroscopy .....	48
	iv. Franck-Condon analysis (FCA) .....	51
3.4	Discussion .....	60
3.5	Conclusion & outlook .....	65
	References .....	66

### **Chapter 4: Aggregate formation dynamics in P3HT films probed by in-situ optical spectroscopy and Franck-Condon analysis**

4.1	Introduction .....	68
4.2	Theoretical background .....	69
4.3	Analysis approach .....	70
	i. Extracting the aggregate spectra .....	70
	ii. Franck-Condon analysis (FCA) .....	72
4.4	Results .....	73
	i. The solvent effect .....	73
	ii. The critical transition temperature in films.....	80
	iii. Temporal evolution of the aggregation process.....	86
	iv. Controlling the initial aggregate formation.....	93
	v. The effect of blending .....	95
4.5	Discussion .....	100

4.6	Conclusion .....	107
	References .....	109

## **Chapter 5: Polymer conformation and aggregation of PDI based side chain polymers**

5.1	Introduction .....	112
5.2	Aggregation properties of PDI polymers.....	112
	i. The uniqueness of side chain polymers .....	112
	ii. The structure of side chain PDI polymers .....	114
5.3	Results .....	115
	i. Monomer vs. Polymer .....	115
	ii. Inter- vs. Intra-molecular aggregation .....	120
	iii. Effect of Solvent choice on aggregation.....	123
5.4	Discussion .....	127
5.5	Conclusion .....	129
	References .....	131

## **Chapter 6: Film formation & aggregation of materials and blends for organic solar cells**

6.1	Introduction .....	134
6.2	Fullerene vs. PDI polymers as acceptors in solar cells .....	135
6.3	Film formation of the neat materials .....	139
6.4	Film formation of PCBM:PPBI-alkyl blends .....	144
6.5	Discussion .....	153
6.6	Outlook .....	157
6.7	Conclusion.....	158
	References .....	160

## **Chapter 7: Conclusion .....** 162

## **Acknowledgements .....** 167

## **Eidesstattliche Versicherung .....** 168



# Chapter 1: Introduction

## 1.1 Motivation and thesis objective

With the depletion of the conventional non-renewable energy sources such as oil and coal, the search for alternative and renewable energy sources became a crucial task for the future of our planet. One of such renewable energy sources is solar energy, which can be converted to other usable energy forms using different technologies. For example, solar collectors convert solar energy to thermal energy for heating and photovoltaic systems convert solar energy to electricity [1]. While all these different technologies offer a share in the supply of the world energy demands, photovoltaic technology is considered the most important and the most researched due to the rapid increase in the world's electricity demand [2].

By taking advantage of the photovoltaic effect which was first observed in 1839 by Alexandre-Edmond Becquerel, energy from the sun can be converted directly to electricity using photovoltaic modules [3]. After the photoconductivity in selenium was reported in 1873, the first practical demonstration of it was done by Charles Fritts in 1883. This demonstration was in the form of a selenium solar cell having less than 1% power conversion efficiency [4]. One of the biggest breakthroughs in the field of photovoltaics was the silicon solar cells invented by Bell labs in 1954 which had about 6% power conversion efficiency [5]. Since then, most research in the photovoltaics domain concentrated on improving the efficiency of solar cells based on silicon and other inorganic materials. First and second generation solar cells whether wafer based or thin films were mainly dependent on inorganic materials such as silicon (crystalline and amorphous) and Gallium [6]. Nevertheless, due to several drawbacks of such solar cells such as heavy weight, high energy and material requirements for manufacturing, and the long payback time, other materials were researched for use in solar cells. Third generation solar cell materials included perovskites, dyes and organic or polymer materials for fabricating the solar cell active layer (the layer where the incoming photons from the sun is converted into electrons) [7-9].

The first major demonstration of an organic solar cell was done in 1986 by Tang et al. when they made a heterojunction bilayer organic solar cell with around 1% power conversion efficiency [10]. In this solar cell, two organic materials with different electron affinities were deposited sequentially on top of each other. The charge carriers were generated mainly at the interface region between the two materials. Moving further on in time, bulk heterojunction organic solar cells were made and offered higher power conversion efficiencies compared to bilayer organic solar cells. In these

bulk heterojunction organic solar cells, the active layer consisted of a blend of two organic materials which allowed for larger interfacial area between the two organic materials and hence better charge generation [8]. These blends consist of electron-donating (donor) and electron-accepting (acceptor) organic materials such as  $\pi$ -conjugated polymers, small organic molecules, and fullerene derivatives [11-15].

While each type of solar cell material had advantages and disadvantages, organic solar cells offered many promising and unique traits. Due to the soft nature of organic materials, organic solar cells can be processed from solutions. This would allow for large area roll-to roll manufacturing processes that would lead to high output and low production costs. In addition, organic materials offer the mechanical flexibility needed for some solar cell applications such as wearables [16, 17]. Finally, organic materials can be made into transparent solar cells which again can be beneficial for some solar cell applications such as building integrated photovoltaics [16]. Nevertheless, the same soft nature that leads to the above-mentioned advantages, results in some drawbacks of organic solar cells. Opposite to inorganic materials, organic materials are disordered, i.e. they don't have a long range ordered crystalline structure. This means that structural and morphological properties of the solar cell active layers is hard to control [18]. This results in the organic solar cells lagging in power conversion efficiencies behind silicon and perovskite based solar cells [19]. Moreover, organic solar cells offer lower stability compared to silicon solar cells [20]. Based on the above characteristics of organic materials used solar cells, it became well established that the active layer morphology strongly influences the device performance. From a morphological point of view, there are three main characteristics to a good solar cell performance:

- a. The "right" domain size of the donor and the acceptor (10-20 nm)
- b. The "right" degree of order in the domains
- c. The "purity" of the donor and acceptor domains (Intermixing in domains)

Consequently, the properties of donor-acceptor blends approximated by these characteristics influence the charge separation, generation and transport in an organic solar cell, which in turn affects the overall device performance. In general, in thin films, the donor and acceptor materials exhibit electrostatic interactions (molecular coupling) leading to short range order referred to as aggregation. It has been shown that the degree and nature of this aggregation impacts the charge separation and subsequent charge transport within the active layers of organic solar cells influencing their efficiency [21]. For example, it was shown that for fullerene acceptors, the degree of molecular coupling between the fullerenes influenced the photocurrent produced in bilayer solar cells [22]. Similar results were shown when different fullerene acceptors were combined with the

same polymer donor in bulk heterojunction solar cells [11]. Since we have an idea about the desired active layer properties for a good organic solar cell, it logically follows that careful control over film formation (and the accompanied aggregate formation) during processing is crucial. This offers a better method of controlling the structure-property relationship rather than following a trial and error approach. The processing parameters that would affect the properties of the active layer include:

- a. Solvent choice and solvent additives. This choice is manifested in the solubility parameters, polarity and boiling points of the solvents used.
- b. Processing temperature.
- c. Deposition techniques (e.g. spin coating, blade coating, etc...) and the consequent deposition parameters (e.g. spin speed, blade speed & acceleration, etc...)
- d. Processing atmosphere (e.g. solvent atmosphere, air, etc...)

Unfortunately, controlling all these parameters and the interplay between them proved to be difficult. This is due to the complexity of the film formation process and the impact of these different processing parameters on the aggregate formation at different time and length scales. The route usually followed is studying the effect of these parameters in isolation, which gives an idea about how a single parameter impacts the active layer properties and subsequently the solar cell device performance. The drawback of such approach is the inability to provide a complete picture of the combined effect of all the parameters, which is critical when moving towards processing of large area organic solar cells. Finally, while recently more research focuses on the in-situ optical characterization techniques, still when it comes to tracking film formation of organic materials most reports rely on in-situ x-ray scattering techniques. While these techniques are crucial in tracking changes in thickness and crystallinity of these blends, they do not give any information about the evolution of the molecular electronic interactions (i.e. aggregation) during film formation. The objective of my thesis is to try to better understand the impact of the processing parameters as a whole on the properties of organic aggregates and the subsequent impact on the solar cell device performance. To achieve this, I mainly rely on optical spectroscopy techniques whether steady state, time resolved or in-situ applied to different organic materials and blends used to fabricate organic solar cells. This might serve as an attempt to show a clearer picture of the structure-property relationship in organic solar cells.

Based on the above-mentioned objective, the material selection plays an important role in my thesis as their properties can be impacted differently by the different processing parameters. The materials of choice within my thesis were selected as being either model materials that are well

studied in the field of organic electronics, materials that offer high solar cell device performance or materials that could have potential in being used in organic solar cells. The first section of materials in my thesis consists of P3HT and PC<sub>71</sub>BM, which are amongst the most well studied materials when it comes to the field of organic solar cells. The second section of materials in my thesis consists of the donor-acceptor (D-A) polymer PCE11 as a high performance donor polymer. The third section of materials in my thesis consists of two new acceptor polymers based on perylene diimides (PDIs). These are two side chain polymers (PPBI-alkyl and PPBI-OEG) consisting of PDI chromophores with different functional side chains attached to an inert polystyrene polymer backbone.

## 1.2 Thesis overview

### *Chapter 2*

In this chapter, I discuss the experimental techniques I used to obtain the data presented within my thesis.

### *Chapter 3*

In this chapter, I try to explore the impact of the addition of an extra material on the donor material in a blend. This impact would be manifested as changes in the molecular interaction properties of the donor material. In this part, I use PCE11, where I investigate the impact of the addition of the extra material on the PCE11 polymer conformation and aggregation properties using a combination of optical spectroscopy and Franck-Condon analysis. This is the foundation chapter as I discuss the general impact of the addition of the extra material on PCE11 aggregation without going into detail about the film formation process. Moreover, it shows a novel approach in the application of the Franck-Condon analysis to get a more detailed picture on the aggregation properties of D-A donor polymers.

I based this chapter mainly on the paper *“Conformational changes of PffBT4T-2OD (PCE11) aggregates upon blending with HDPE probed by optical spectroscopy”* which I prepared for submission together with **Konstantin Schötz, Giovanni Maria Matrone, Natalie Stingelin, Anna Köhler and Fabian Panzer.**

### *Chapter 4*

In this chapter, I try to draw a general picture on the complex relation between solution processing parameters and polymer aggregation during film formation. I focus here on the neat P3HT film formation when spin coated from solutions. I also investigate the film formation of P3HT in a blend.

In this chapter, I use insitu optical spectroscopy coupled with detailed Franck-Condon analysis to quantify the film formation process.

This chapter is based in part on the paper “A unified picture of P3HT aggregate formation during solution processing” which I prepared for submission together with **Matthew J Dyson, Stefan Wedler, Konstantin Schötz, Mihirsinh Chauhan, Paul N Stavrinou, Natalie Stingelin, Anna Köhler, and Fabian Panzer.**

## *Chapter 5*

In this chapter I investigate the conformation and aggregation properties of two side chain polymers based on an inert polystyrene backbone and PDI chromophores (PPBI-alkyl and PPBI-OEG). The idea is to study how implementing an acceptor chromophore in a side chain polymer configuration might allow over more control of their aggregation properties compared to main chain polymer or small molecule configurations. The main goal is to explore the potential of such side chain PDI polymers as acceptors in organic solar cells. In this chapter I focus on the spectroscopic characterization of these side chain polymers in solutions, while in the subsequent chapter I focus on their film formation properties and their performance in organic solar cells.

## *Chapter 6*

By this point in my work, I have had established a better understanding of the different aggregation mechanisms during film formation of organic materials whether in the neat or blend states and how these mechanisms are impacted by the processing parameters. In this chapter, I move on to a more practical approach where I try to correlate between the film formation and aggregation properties of different organic blends during their solution processing into films and the performance of those same blends in organic solar cells.

### **1.3 Electronic structure of organic semiconductors**

Organic materials in general are based on carbon and hydrogen atoms with other heteroatoms that can be found in their structure such as oxygen, nitrogen and Fluorine. Opposite to inorganic semiconductors, organic materials are inherently insulating. Organic materials can be made conducting by means of doping or through photo-generation of charge carriers through bound electron-hole pairs i.e. excitons. The semiconducting property of some organic materials then can be allowed due to the presence or alternating single and double bonds referred to as the conjugated  $\pi$ -electron system. This conjugated structure of the organic semiconductors is a result of the underlying electronic structure of the carbon atoms.

In the ground state, the carbon atom has 6 electrons distributed on the atomic orbitals as follows:  $1s^2 2s^2 2p_x^1 2p_y^1 2p_z^0$ . This means that the innermost s-orbitals are filled, and only two valence electrons in the outer p-orbitals are available for bonding. Nevertheless, when carbon is bonded with other atoms, one electron from the  $2s^2$  orbital is promoted to the empty  $2p_z$  orbital making 4 valence electrons available for bonding. The energy required to raise one of the  $2s^2$  electrons to the  $2p_z$  orbital is offset by the energy gained from the available two new extra bonds. Following this, the outer four orbitals can then mix together forming hybridized orbitals. This can happen between either all four of them, only three or only two orbitals. When the 2s orbital and the three 2p orbitals are mixed together, they form four new orbitals called the hybridized  $sp^3$  orbitals which are at  $109.5^\circ$  bond angles between each other. In another situation, only the 2s,  $2p_x$  and  $2p_y$  orbitals hybridize forming three  $sp^2$  orbitals which are at  $120^\circ$  bond angles between each other. This leaves the  $2p_z$  orbital in an orthogonal orientation to the plane containing the three hybridized  $sp^2$  orbitals. The orientation of the bonds happens following the VSEPR theory (valence shell electron pair repulsion) which describes the geometric configuration of bonds and electrons around an atom as a consequence of the repulsion forces between them [23]. Different molecules are formed depending on the different hybridized orbitals as shown in figure 1.

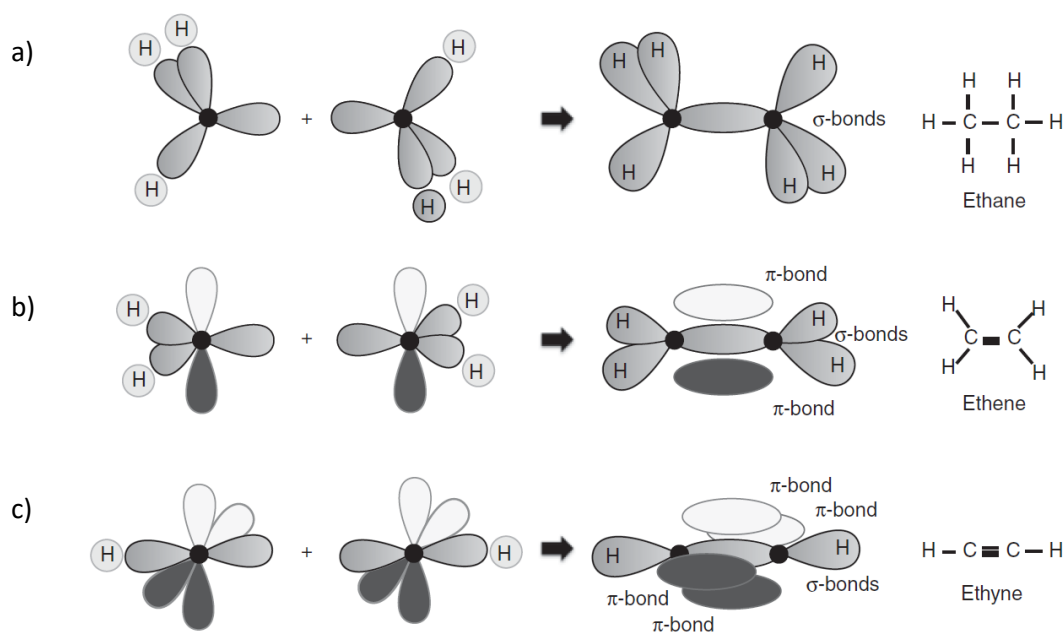


**Figure 1: Combination of different hybridized and non-hybridized orbitals to form distinct types of bonds in organic materials. a) Ethane containing 4  $\sigma$ -bonds b) Ethene containing 3  $\sigma$ -bonds and 1  $\pi$ -bond c) Ethyne containing 2  $\sigma$ -bonds and 2  $\pi$ -bonds. Reproduced from [18].**

As observed from figure 1, two types of bonds can happen in an organic material containing carbon and hydrogen. I will focus on the case of ethene (or ethylene) as it represents an example of an

organic material containing the conjugated structure that gives rise to the semiconducting properties. Firstly, each one of the three  $sp^2$  hybridized orbitals containing one electron forms three single bonds called  $\sigma$ -bonds. Two of these bonds are formed with two hydrogen atoms and the third is formed with the other carbon atom. Secondly, due to the overlap of the electron cloud between the  $p_z$  orbitals from the two carbon atoms they form two states above and below the  $\sigma$ -bond already present between these two carbon atoms. These two states are referred to as the  $\pi$ -bonding orbital or the highest occupied molecular orbital (HOMO) and the  $\pi$ -antibonding orbital or the lowest unoccupied molecular orbital (LUMO). This alternation between the single  $\sigma$ -bonds and the double  $\pi$ -bonding is what gives rise of the semiconducting properties in organic semiconductors.

As the  $\pi$ -bond is weaker than the  $\sigma$ -bond, the difference between the HOMO and LUMO orbitals are the smallest electronic transition available in organic semiconductors. As a consequence, optical excitation of organic semiconductors is possible as the difference between the HOMO and LUMO orbitals (typically 1.5 – 3 eV) coincides with visible light range (roughly 1.55 – 3.1 eV). Upon photoexcitation an electron is promoted from the HOMO to the LUMO and the molecule is in an excited state forming what is called a bound electron-hole pair or an exciton. Under certain conditions, the subsequent generated free charges from these excitons can then transport through the delocalized  $\pi$ -orbitals. This picture is analogous to inorganic semiconductors where upon excitation an electron is promoted from the valence to the conduction band through which charge transport happens. The main difference is that in the inorganic semiconductors due to their high dielectric constant (typically  $\epsilon_r > 10$ ), upon excitation the created exciton is almost instantaneously decomposed to free charge carriers. While in organic semiconductors due to their low dielectric constant (typically  $\epsilon_r = 3-4$ ), the created excitons are strongly bound together by strong electrostatic interactions [18, 24]. It is worth noting that it should not be assumed that HOMO and LUMO orbitals are equivalent to the ground and excited states. HOMO and LUMO orbitals are considered one-electron orbitals and hence, in a simple picture, the transition of an electron between these two orbitals results in the whole molecule transitioning from a ground to an excited state.

## **1.4 Theoretical background of the experimental techniques**

### **i. Steady state absorption and emission**

Although being a simple and easy to perform experimental technique, time averaged optical spectroscopy offers an important tool in understanding the organic semiconductors properties by applying various analysis techniques on the measured absorption and emission spectra. In organic

materials, on the molecular level, absorption and emission of light leads to a change in the energetic state of the molecule. By absorption of light the energy of the molecule is increased i.e. the molecule transitions from a ground state to an excited state, while the opposite occurs upon emission as the molecule loses energy. The wavefunction representing a certain molecular state can then be described by three different contributions according to the following equation:

$$\Psi_{total} = \Psi_{el} \times \Psi_{vib} \times \Psi_{spin} \quad (1)$$

Where,  $\Psi_{el}$  is the electronic wavefunction that describes the position of the electrons,  $\Psi_{vib}$  is the vibration wavefunction that describes the position of the nuclei and  $\Psi_{spin}$  is the spin wavefunction that describes the spin state of the electrons. This equation holds as long as there is no strong interaction between any of the wavefunctions. This is fulfilled following the Born-Oppenheimer approximation due to the nucleus being much heavier than the electron ( $\approx 2000$  times). Accordingly the nuclei can be considered stationary relative to the electrons motion and their respective wavefunctions can be treated separately. The probability (rate) of the transitions between two such states can be described by Fermi's golden rule:

$$\Gamma_{if} = \frac{2\pi}{\hbar} |\langle \Psi_f | V | \Psi_i \rangle|^2 \rho_f \quad (2)$$

Where,  $\Gamma_{if}$  is the transition probability (rate),  $\Psi_i$  and  $\Psi_f$  are the wavefunctions of the initial and final states and  $\rho_f$  is the final states density.  $V$  is the coupling element for interaction i.e. the parameter that couples both  $\Psi_i$  and  $\Psi_f$  leading to the transition. For absorption and emission  $V$  is the electromagnetic light waves or more specifically its electrical dipole component. The oscillating electrical dipole component of the electromagnetic waves leads to oscillations of the electrons. While the nuclei, since they are much heavier than the electrons, don't respond similarly to the electric field. The spin state of the electrons is only affected by the magnetic field component of the electromagnetic waves, but since the magnitude of such field is small it can be neglected. Consequently combining equations 1 and 2 leads to the following expression for the transition probability:

$$\Gamma_{if} = \frac{2\pi}{\hbar} |\langle \Psi_{el} | e\hat{r} | \Psi_{el} \rangle|^2 |\langle \Psi_{vib} | \Psi_{vib} \rangle|^2 |\langle \Psi_{spin} | \Psi_{spin} \rangle|^2 \rho_f \quad (3)$$

Where  $e\hat{r}$  is the operator describing the oscillating electrical dipole component of the electromagnetic light waves. Accordingly, the overall probability of a transition is mainly determined by the initial and final states electronic wavefunctions (i.e. electronic transitions/spectral intensity). Additionally, as the different nuclei oscillate inside the molecule, they couple together analogous to a system of coupled pendula. These coupled oscillations lead to

different normal vibrational modes as a function of the position of the nuclei. For each mode, distinct vibrational levels are then observed in the ground and excited electronic states and the transitions are initiated within these levels. Accordingly, the vibrational wavefunctions of the initial and final states determine the progression of the transitions (i.e. vibrational transitions/spectral shape). Figure 2 shows the combination of ground and excited electronic states with different vibrational modes and how the different transitions would be reflected on the final absorption and emission spectra.

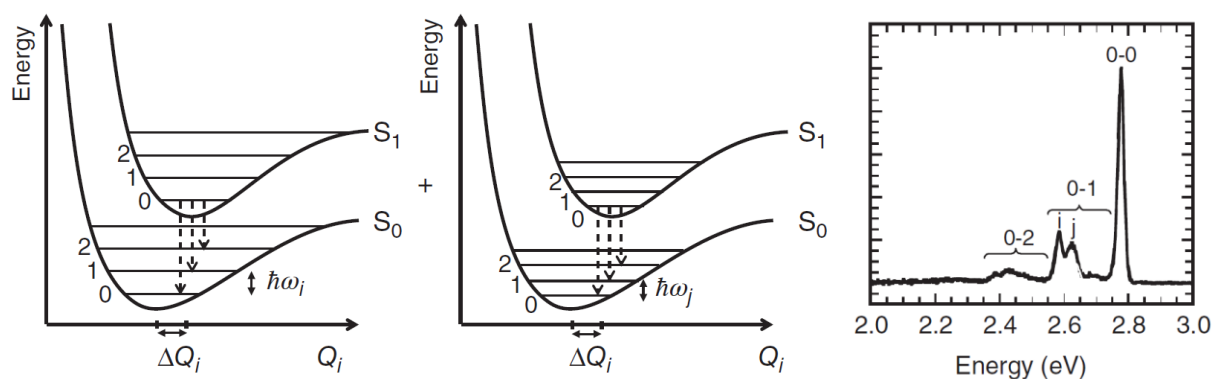


**Figure 2: Emission spectra of polyfluorene at 10K (right) and a depiction of the potential energy curves corresponding to two normal vibrational modes (left) that would give rise to the observed spectral features. Reproduced from [18].**

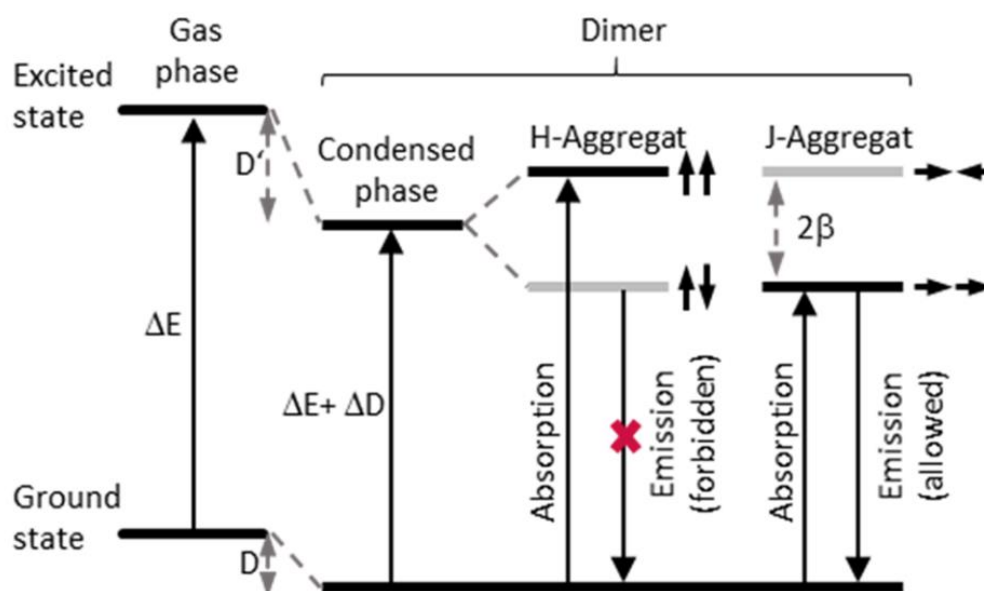
## ii. Spectral signatures of aggregates in organic materials

Up till this point, I mostly discussed organic materials in the isolated state, but organic molecules or polymers are usually present in molecular assemblies (e.g. molecules in concentrated solutions or in the solid state). This leads to the rise of molecular interactions between them which in turn alters the material's optoelectronic properties. These molecular interactions depend on how the molecules order within the molecular assemblies hence reflecting the type of arrangement of the organic molecules. In general, molecular interactions can be separated into intra- and intermolecular components. As the names imply, the intramolecular interactions arise from the properties within the same molecule or polymer chain such as the chain conformation or the effective conjugation length. While the intermolecular component arises from the interaction between the different molecules or polymers. These molecular interactions usually happen when the molecular assemblies transition from a disordered state to an ordered state. The most straightforward example would be the solution processing of organic material into thin films. For example, upon spin coating of a polymer solution, as the solvent molecules start to evaporate the polymer chains become closer to each other. At a certain point during the process when sufficient

solvent molecules evaporate, polymer chains take a certain arrangement or conformation and the molecular interactions between them manifest as changes in the optical spectra. This transition between the disordered to the ordered states and the accompanied rise in intermolecular interactions is referred to as aggregation.

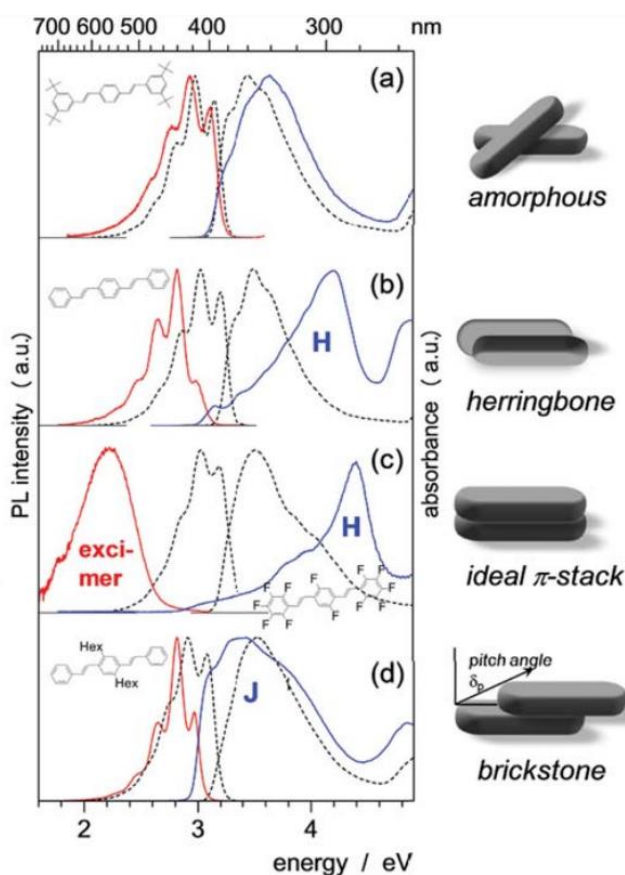
All the above means that optical spectroscopy can be used as a probe of the aggregation of organic semiconductors and the underlying intermolecular arrangements within the molecular assemblies. It is worth mentioning that the alteration of the optical spectra can arise from other factors such as the polarizability of the surrounding environment and solvation effects [18]. Kasha was the first to establish the ideas that were used to describe the relationship between the electronic molecular interactions of organic semiconductors and the accompanied changes in the optical spectra [25-27]. To understand how the photophysical properties are altered by aggregation, I discuss the simple a case of two interacting molecules (chromophores) which are also referred to as dimers.

Figure 3 shows the energy levels both of the isolated state and the dimeric states [28]. As shown in the figure in the gas phase as the molecule is isolated we have the ground and excited states separated by the energy gap  $\Delta E$ . When two molecules become closer to each other electrostatic interaction between their corresponding electron clouds arise. This results in the formation of dimer with its ground and excited states shifted to lower energies. The difference between the dimer's ground and excited states becomes  $\Delta E + \Delta D$ .  $\Delta D$  is referred to as the gas-to-crystal shift.



**Figure 3: Energy level diagram and energetic shifts upon the interaction between two isolated molecules to form a dimer. Adapted from [28].**

Moreover, depending on the mutual orientation of the molecular transition dipoles, the excited state energy splits with a separation of  $2\beta$  that is referred to as the resonance energy. The two extreme cases of such mutual dipole orientation are referred to as H and J-aggregates. H-aggregates refers to the case where the dipole moments are parallel or anti-parallel to each other. In this case, although the antiparallel configuration is lower in energy, its state is not dipole allowed, as the dipole moments sum is equal to zero. This means that absorption is allowed to the higher lying parallel excited state and the resulting spectra is blue shifted. J-aggregates refers to the case where the dipole moments are arranged face to face or face to tail. Again, because of the two possible configurations, we have a splitting to two states one of which is dipole forbidden. In the case of J-aggregates, the dipole forbidden state is the higher lying state opposite to the case of H-aggregates. This means that in the case of J-aggregates, the absorption spectra would be red shifted and emission would be allowed from the lower lying state. The aforementioned scenario assumes the ideal case, but in reality this mutual orientation is usually somewhere between those extreme cases and the dipole selection rules are not strictly followed. An example of how the molecular orientation alters the optical spectra in an organic oligomer is shown in figure 4.



**Figure 4: Relation between the optical spectra and the different molecular arrangements within a nanoparticles suspension of DSB based materials. The dashed lines show the solution spectra for comparison. Adapted from [29].**

Figure 4 shows different arrangements within different DSB based oligomers depending on the side chain substitutions and the addition of heteroatoms to the molecular backbone [29]. In the amorphous case we observe the least difference to the solution spectra. In the case of a more ordered arrangements, the deviation from the solution spectra is more significant. For example, the case of ideal  $\pi$  stacking which is often observed in several organic semiconductors shows a significant deviation from the solution spectra. In this case we observe the characteristic broad red shifted excimer emission along with the blue shifted absorption spectra. Both of these signatures are signs of H-aggregates formation [30, 31].

Developing this idea further, the relationship between aggregation and photophysical properties in the case of real systems of several interacting chromophores was established by Spano [30, 31]. This expanded Spano theory not only included the effects of electronic molecular interactions between chromophores but included the vibrational and disorder effects. In the case of conjugated polymers where the intermolecular interactions are weaker than shorter oligomers, the theory is referred to as the theory of weakly interacting H or J-aggregates [30, 31]. Following this framework, the intermolecular coupling strength could be quantified from the relative heights of the vibration peaks in absorption and from the suppression of the emission peaks [32]. As mentioned earlier, these changes can be then related to the microstructural or morphological properties of the material [33]. Within the Spano theory, the spectral signatures of H and J-aggregates within the progression of the optical spectra can be summarized in two extremes. In the case of an ideal H-aggregate, in absorption the 0-0 to 0-1 peak ratio decreases with increasing molecular interaction strength. While in emission the 0-0 peak is suppressed with decreasing disorder or at lower temperatures. In the case of J-aggregates, we have the opposite situation i.e. the absorption 0-0 to 0-1 peak ratio increases with increasing molecular interaction strength and the emission 0-0 peak is suppressed with increasing disorder or at higher temperatures [30].

### iii. Franck-Condon analysis (FCA)

Franck-Condon analysis (FCA) is a technique used to fit the measured optical spectra (absorption and photoluminescence) from which different fitting parameters can be extracted, such as the degree of disorder and molecular interaction (i.e. molecular coupling strength). These fitting parameters correlate with the underlying structure and interactions within the material that are manifested through the optical spectra. As already mentioned above upon a material's interaction with light, both electronic and vibrational transitions determine the intensity and the shape of the resulting optical spectra. The transition intensity is determined by the overlap of the vibrational wave functions of the initial and final electronic states and is referred to as the Franck-Condon

overlap integral. Squaring it gives the probability of transition between the 0<sup>th</sup> vibrational level of the ground state and the m<sup>th</sup> vibrational level of the excited state and is referred to as the Franck-Condon factor. Assuming a vibrational energy of  $\hbar\omega_m$  within one normal mode, we can describe the transition intensity  $I_{0-m}$  (Franck-Condon factor) by a Poisson distribution.  $I_{0-m}$  represents the probability of the transition from the 0<sup>th</sup> vibrational level of the ground state to the m<sup>th</sup> vibrational level of the excited state:

$$I_{0-m} = |\langle \Psi_{vib,f} | \Psi_{vib,i} \rangle|^2 = \frac{S^m}{m!} e^{-S} \quad (4)$$

Furthermore a change in the coordinates of a certain normal mode (change in mode energy) would alter the overlap integral and hence the transition intensity. So, by approximating the potential energy curves of a normal mode as a harmonic oscillator having an equilibrium coordinate  $Q$ , we can relate the change in the transition intensity to the change of the equilibrium position (i.e.  $\Delta Q$ ) by the following equation:

$$S = \frac{1}{2} k \frac{\Delta Q^2}{\hbar\omega_m} = \frac{1}{2} M\omega_m \frac{\Delta Q^2}{\hbar} \quad (5)$$

Where,  $S$  is called the Huang-Rhys parameter and  $K = M\omega^2$  represents the force constant, and  $\omega_m$  is the mode frequency.

In reality, we do not observe sharp transition lines but rather broadened ones due to disorder and environmental effects. Therefore, we need to account for this when fitting the optical spectra by using a Gaussian or Lorentzian function with a specific linewidth. In addition, we need to take into account the energy dependent refractive index of the surrounding media (e.g. solution) and the correction for the density of states (DOS). Both corrections appear in the form of the  $[n(\hbar\omega) \cdot \hbar\omega]^3$  factor for photoluminescence and  $[n(\hbar\omega) \cdot \hbar\omega]$  for absorption. Finally, we need to consider different vibrational modes rather than one, which is more often than less the situation. In this case the Franck-Condon factor can be expressed like this:

$$I_{0-m_i} = \frac{S_i^{m_i}}{m_i!} e^{-S_i} \quad (6)$$

Where,  $i$  represents the number of modes to be taken with  $m$  levels per mode.

Combining all the above, we can then arrive to a simple Franck-Condon progression that can express the overall Abs and PL spectra as follows:

$$I_{Abs}(\hbar\omega) = [n(\hbar\omega) \cdot \hbar\omega] \cdot \sum_{m_i} \prod_i I_{0-m_i} \cdot \Gamma \cdot \delta(\hbar\omega - (\hbar\omega_0 + \sum_i m_i \hbar\omega_i)) \quad (7)$$

$$I_{PL}(\hbar\omega) = [n(\hbar\omega) \cdot \hbar\omega]^3 \cdot \sum_{m_i} \prod_i I_{0-m_i} \cdot \Gamma \cdot \delta(\hbar\omega - (\hbar\omega_0 - \sum_i m_i \hbar\omega_i)) \quad (8)$$

The above equation holds true in case of no electronic interactions within the material (e.g. dilute solutions) but needs to be modified to account for the presence of interactions between molecules (e.g. aggregation). This is often the case in concentrated solutions and films of pure or blended material systems. One of these modifications in the context of the weakly coupled H-aggregates model leads to the following equation that allows to fit the PL spectra with the presence of molecular coupling (i.e. aggregation)[32]:

$$I_{PL}(\hbar\omega) = [n(\hbar\omega) \cdot \hbar\omega]^3 \left( \alpha \cdot \Gamma \cdot \delta(\hbar\omega - \hbar\omega_0) + \sum_{n_i} \prod_i \frac{S_i^{n_i}}{n_i!} e^{-S_i} \cdot \Gamma \cdot \delta(\hbar\omega - (\hbar\omega_0 - \sum_i n_i \hbar\omega_i)) \right) \quad (9)$$

Where  $\alpha$  represents a factor quantifying the intermolecular interactions taking the values  $0 < \alpha < 1$ , where 1 means negligible interaction reducing eq. 9 back to the unmodified eq.7. From the above equation we can extract different parameters namely, the disorder parameter  $\Gamma$ , the Huang-Rhys parameter  $S$ , the energy of the 0-0 transition  $\hbar\omega_0$  and molecular coupling strength parameter  $\alpha$ . These parameters are related to different material properties such as energetic disorder and aggregation properties. Ultimately, this allows us to infer information about changes in the material's microstructure as a function of different experimental conditions. Although I mostly fitted the PL spectra during my work, it is worth mentioning that a similar modification applies for fitting the Abs spectra where the coupling strength can be inferred from the ratio of the 0-0 and 0-1 transition peaks.

#### iv. Time resolved photoluminescence

In the previous sections the steady state spectra referred to the optical spectra obtained over a time scale much longer than the timescales for excitation and relaxation processes during absorption and emission. Different fast processes occurring during absorption and emission are depicted in the Jablonski energy diagram shown in figure 5 [34]. Depending on the material's structure and excitation nature different processes occur. The process of the light interaction with the material leading to absorption and emission can be broadly divided into three main steps:

- Firstly, the photons interact with the material leading to absorption where the molecule gains energy transitioning to an excited state. This process is very fast taking place within the femtosecond timescale.
- Secondly, the molecule relaxes to a lower vibrational level within the excited state. This process is non-radiative and occurs within the picosecond timescale.
- Thirdly, the molecule goes back from excited state to the ground state emitting photons in the process. This process occurs within the millisecond (phosphorescence) to the nanosecond (fluorescence) timescales.

Other processes are possible within the overall lifetime between absorption and emission as shown but I will not discuss them all here as they are outside the scope of my thesis. Accordingly time resolved photoluminescence (TRPL) refers to measuring the lifetime of the excited state during emission which can give a wealth of information about the material's structure and states on the molecular level. Additionally, the presence of different type of molecules can lead to other processes such as energy or charge transfer that would alter these lifetimes. This can also provide information about changes in molecular states as a result of interactions between the different molecules.

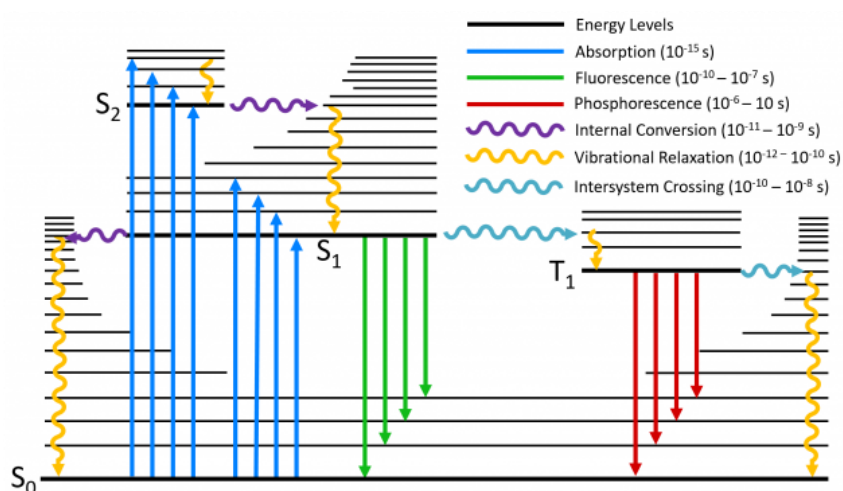


**Figure 5: Jablonski energy diagram showing the different excitation and relaxation processes during absorption and emission and their average lifetimes. Straight lines refer to radiative processes while wiggly lines refer to non-radiative ones. Adapted from [34].**

## v. Raman Spectroscopy

A process that can occur during the interaction of photons with organic molecules is scattering. If the photons do not change energy upon scattering it is referred to as Rayleigh scattering while a change in the photon energy during the process is referred to as Raman scattering. The energy lost or gained during Raman scattering is transferred to or from the vibrational modes within the molecule which leads to a change in the vibrational state of the molecule. Consequently this gives us access to a technique that we can use to measure the energies of different vibrational modes. Nevertheless, not all the vibrational modes can be accessed using Raman spectroscopy, but only those that result in a change in the molecular polarizability. Figure 6 shows the different scattering process.

Since different molecules show distinct vibrational modes, Raman measurements can be used as a probe to identify different materials. In addition Raman spectroscopy offers a technique for probing the microstructure of different organic molecules and polymers in solutions and films. This can be done by observing changes in the mode intensities and energy shifts under different experimental conditions as will be discussed in chapter 3.

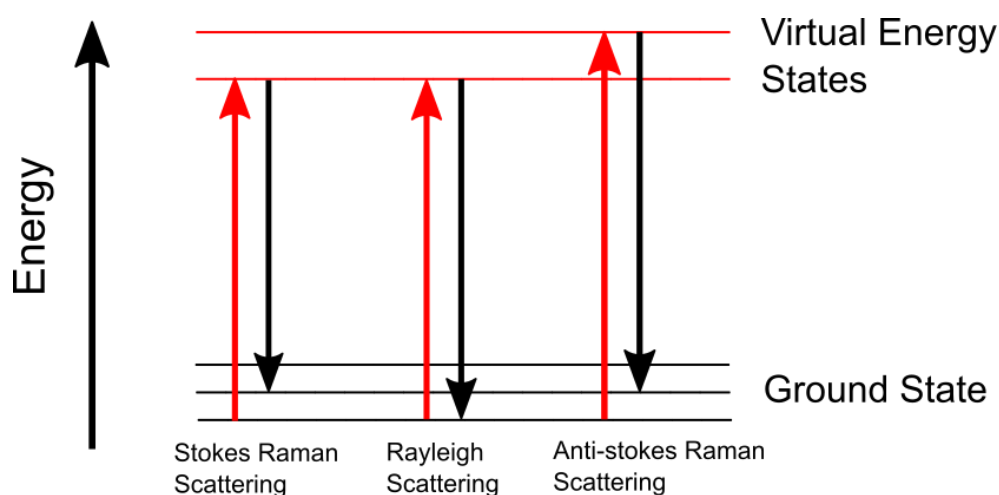


**Figure 6: Energy level diagram showing the different scattering process.**

#### vi. Relation between optical and Raman Spectroscopies

An important prerequisite for performing FCA on the optical spectra of organic materials is having an idea about which phonon modes (vibrational modes) to use. Generally, we can gain information about the different phonon modes present in a material using either Raman or FTIR spectroscopy techniques. However, the selection rules determining which modes are Raman or IR active are different. While IR active modes require a change in the dipole moment upon interaction with light, Raman active modes require a change in the polarizability ( $\alpha$ ). From a classical point of view, upon interaction of the light with an organic molecule, an electrical dipole moment is induced proportional to the oscillating electric dipole component of the electromagnetic light waves. This proportionality term is referred to as the polarizability and is a measure of how easily the molecule's electron cloud is affected by the electrical dipole component of the electromagnetic wave. However, this polarizability is not constant but changes with changes of the equilibrium coordinates of the normal phonon modes already present in the molecule.

The induced dipole moment and its relation to polarizability then can be classically expressed using the following equation [35] :

$$\mu = \alpha_0 E_0 \cos(\omega_0 t) + \frac{E_0 Q_0}{2} \left( \frac{\partial \alpha}{\partial Q} \right)_{Q=0} \{ \cos[(\omega_0 - \omega_p)t] + \cos[(\omega_0 + \omega_p)t] \} \quad (8)$$

$\mu$  is the induced dipole moment and  $E = E_0 \cos(\omega_0 t)$  is the incident electromagnetic light wave.  $Q$  is the normal mode coordinate which is considered as a simple harmonic oscillator with frequency  $\omega_p$  and amplitude  $Q_0$  indicating the equilibrium position. Finally,  $\alpha$  is the polarizability. In this equation, the first term describes Rayleigh scattering that shows no change in the photon energy upon scattering, while the second and third terms describe Raman scattering (stokes and anti-stokes). It then follows that a phonon mode will be Raman-active only in the case where a change in polarizability results from this mode i.e.  $\left( \frac{\partial \alpha}{\partial Q} \right)_{Q=0} \neq 0$ . It should be noted that this condition assumes a perfect symmetry of the polymer backbone, which is not always the case. In the case of conjugated polymers, the change in the equilibrium normal mode coordinates arises upon excitation. Hence, a difference arises between the equilibrium positions of the potential energy curves of the ground and excited states ( $\Delta Q$ ) as shown in figure 7.

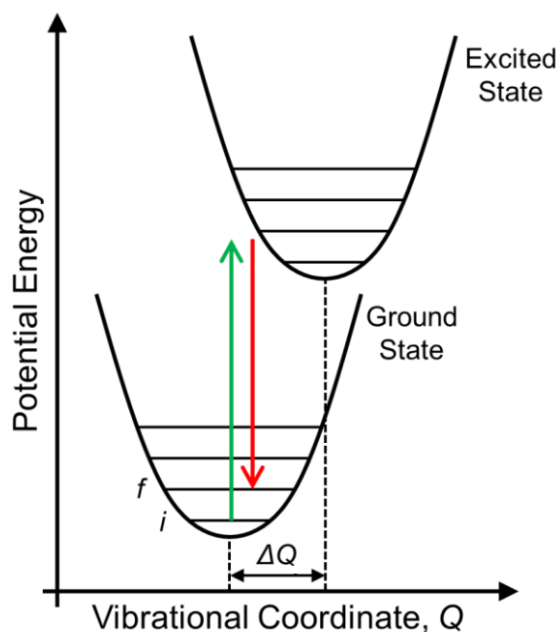


**Figure 7:** Schematic potential energy curves of the ground and excited states of an organic molecule. Reproduced from [35].

Quantum mechanically, one can then show the direct relation between the Raman phonon modes and the optical spectra. The probability of a transition from the ground state to the excited state

(and vice-versa) is determined by the square of the overlap of the wave function of the ground and the excited states (Franck-Condon factor). The magnitude of ( $\Delta Q$ ) affects both the Franck-Condon factor and the polarizability of the molecule. Hence, experimentally we would expect the modes appearing in the Raman spectra to be the ones that contribute to the vibrational progression in the optical spectra [18]. Therefore, the phonon modes extracted from Raman spectroscopy offer a logical starting point for analyzing the optical spectra using FCA.

## 1.5 Fundamentals of organic solar cells

As mentioned earlier, upon photoexcitation of organic semiconductors a strongly bound exciton is formed (binding energy around 0.3 to 0.5 eV) [18]. Due to the exciton strong binding energies, the thermal energy at room temperature is not sufficient for separating the excitons into free charge carriers. In this case, the photo-generated excitons have a high recombination probability within a very short time frame ( $< 10$  ns) [18]. To overcome this problem, in an organic solar cell the photoactive layer usually consists of a combination of two organic semiconductors having different electron affinities and sandwiched between two electrodes with different work functions. Consequently, the generated internal electric field in the active layer results in the separation of the excitons at the interface between the two materials. To facilitate this process, the organic semiconductors used in the active layer are electron-donating (donor) and electron-accepting (acceptor) materials, with the acceptor material having higher electron affinity. This means that once the exciton is separated at the interface, the generated electrons and holes move through the acceptor and donor layers to their respective electrodes [8].

Figure 8 shows the most two common organic solar cell architectures used for combining the donor and acceptor materials; the planar heterojunction commonly known as the bilayer and the bulk heterojunction (BHJ) [36].

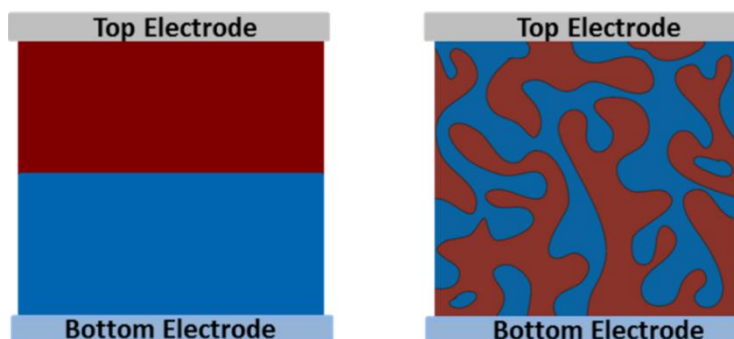


**Figure 8: Schematic diagram of the bilayer and bulk heterojunction (BHJ) active layer structures used in organic solar cells. Reproduced from [36].**

The bilayer structure is usually fabricated in a sequential manner where the acceptor layer is deposited on the cathode, then the donor layer is deposited on top and finally the anode is deposited on top. The anode is usually made from a transparent oxide material that allows for light to pass and excite the active layer. It can be deduced from the figure that bilayer architectures would not allow for high power conversion efficiencies due to two reasons. Firstly, since the exciton lifetimes is very short, if the active layer is very thick most of the excitons would recombine before reaching the interface. Secondly, if the active layers are made thin to accommodate this, the photo-generated excitons would decrease as the absorption is reduced.

These problems are mitigated in the BHJ structure where the active layer is a blend of both the donor and acceptor materials. This leads to the formation of a phase separated structure with smaller donor and acceptor phases compared to the bilayer structure. Moreover, the interfacial area between the donor and acceptor increase compared to the bilayer structure. These two characteristics lead to better exciton generation upon absorption as both the acceptor and donor contribute to light absorption. In addition to better free charge generation due to the higher probability of the exciton reaching the interface before recombining.

Figure 9 shows the journey of an exciton inside an organic solar cell from an energetic point of view [37]. This starts from the absorption of light until the generation of electricity by means of the photo-generated free charge carriers. The full process can be separated into three main steps.

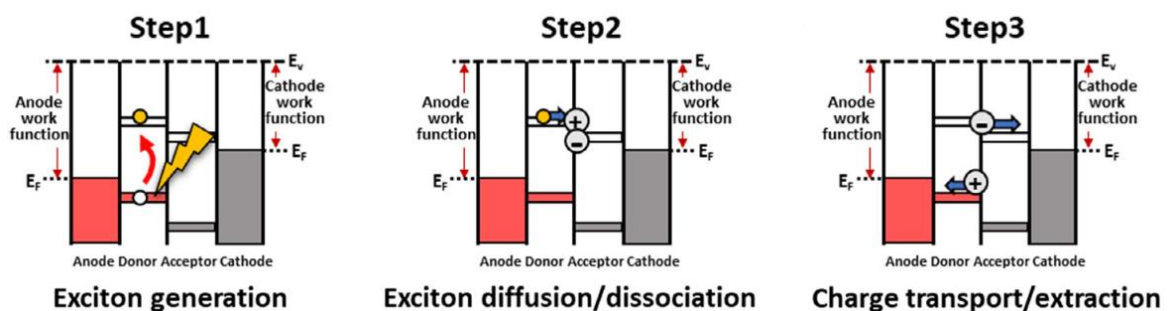


**Figure 9: Schematic energy diagram following the different processes within an organic solar cell until free charge generation. Reproduced from [37].**

In the first step, the light is absorbed by the active layer (in this example I assume it is absorbed in the donor phase) and excitons are generated. This is shown as the yellow and white circles in step 1 indicating the hole and electron respectively. In the second step, the exciton diffuses through the donor phase until it reaches a donor/acceptor interface within its lifetime. At the interface, the exciton dissociates into an electron and a hole due to the internal electric field arising from the

difference in the work function between the anode and the cathode. Due to the higher electron affinity of the acceptor, the electron transfers to the acceptor phase leaving the hole in the donor phase. In the third step, the generated free carriers transport through the donor and acceptor phases until collected at the respective electrode [8, 18]. The total power conversion efficiency of the solar cell can be thought of as a combination of the individual efficiencies of all these intermediate steps [8].

Within this journey several loss mechanisms limit the efficiency of these intermediate steps and hence the total the power conversion efficiency. Firstly, if the active layer absorption doesn't cover a sufficient range of the solar spectrum, a lot of the sunlight would not be absorbed by the active layer which decreases the efficiency of the exciton generation. Secondly, after an exciton is generated if it doesn't reach the interface within its lifetime it will recombine and re-emit the absorbed light. This occurs if there isn't enough phase intermixing which leads to a small interfacial area and larger phase separated domains. Thirdly, even if the exciton reaches the interface, recombination can still happen if the internal electric field is not sufficient to overcome the exaction's electrostatic binding energy. The recombination of excitons at the interface is referred to as geminate pair recombination (GR). The final loss mechanism can happen even after the exciton is dissociated into free charge carriers. This can be due to the free charge carrier recombining with an opposite charge carrier before reaching the electrode which is referred to as non-geminate recombination or due to the presence of traps which is referred to as trap-assisted recombination [18]. In practice, the efficiency of the solar cell can be calculated by measuring the J-V device characteristics and using the following equation:

$$PCE = \frac{J_{sc} \times V_{oc} \times FF}{P_{in}}$$

Where, PCE refers to the power conversion efficiency,  $J_{sc}$  is the short circuit current i.e. the current density without applied external voltage,  $V_{oc}$  is the voltage at open circuit conditions and FF is the fill factor which indicates how easy it is to extract the photo-generated carriers and  $P_{in}$  is the incident light power.

## 1.6 Materials for organic solar cells

From a material point of view, since the fabrication of the first organic solar cell employing copper phthalocyanine (CuPc) and a PDI derivative as the donor and acceptor materials [10], the field of organic photovoltaics went through several advancements. On the acceptor materials side, for a long time research focused on fullerene derivatives such PC<sub>60</sub>BM as the main electron acceptor material used in organic solar cells [11, 38]. On the donor materials side, research mainly focused

on homopolymers as the preferred donor materials with P3HT being one of the most researched [39, 40]. Nevertheless, despite great efforts the efficiency of organic solar cells following this homopolymer donors and fullerene acceptors halted around 5-6% [39]. This was in part due to the poor absorption and poor stability of fullerene derivatives besides the need of large energy offsets between the donor and acceptor energy levels for efficient exciton dissociation ( $\text{HOMO}_{\text{donor}} - \text{LUMO}_{\text{acceptor}} > 0.3 \text{ eV}$ ) [41].

A major breakthrough on the donor materials side came with the implementation of donor-acceptor copolymers (D-A polymers) that consist of weak electron donating and weak electron accepting units [42, 43]. This design philosophy of the polymer backbones using this D-A structure has been already proposed much earlier [44]. These materials were characterized by a narrow band gap and low-lying HOMO levels [45, 46]. Moreover, a sub family of D-A polymers were designed based on a fluorinated benzothiadiazole (BT) donor unit, which showed temperature dependent aggregation properties [46, 47]. This meant that the degree of aggregation of these BT-based polymers could be controlled in solution and during film processing by means of temperature [47]. This temperature dependent (TDA) aggregation properties allows for better morphological manipulation and control of the active layer to achieve higher solar cell performance. In addition, the extent of the polymer crystallinity and TDA properties could be fine-tuned by the nature of side chains and substituent heteroatoms on the polymer backbone [48-50]. This led to a wide variety of polymers with varied properties within this donor polymers family leading to solar cell efficiencies in the range of 10% with both fullerene and non-fullerene acceptors. One of such polymers was PffBT4T-2OD commonly known as PCE11 which was characterized with high crystallinity and gave 10%-11% solar cell efficiency when combined with various fullerene derivatives and not restricted only to PC<sub>60</sub>BM [38]. In addition, P3TEA with more of an amorphous character showed good performance with the SF-PDI small molecule acceptor ( $\approx 9.5\%$ ) with suppressed voltage losses [51]. Finally, PffBT4T-C9C13 which showed high solar cell performance near 12% when processed from environmentally friendly non-halogenated hydrocarbon solvents [52].

Despite all the research effort, the organic solar cell performance was pinned around 11%-12% which was mainly due to the limitations resulting from the intrinsic properties of most fullerene derivatives [41]. Hence on the acceptor materials side new alternatives were researched namely small molecule and polymer non-fullerene acceptors [53-55]. The first generation of small molecule acceptors included acceptors having the A-DD'D-A structure employing various donor cores such as indacenodithiophene (IDT) and diketopyrrolopyrrole (DPP) cores (e.g. ITIC) [53, 56]. The first generation also included dimer, trimer and tetramer small molecule acceptors based on PDIs and NDIs such as SF-PDI and di-PDI [53, 57]. With the advancements of these non-fullerene acceptors,

devices reached efficiencies up to 15% for the first time in the field of organic solar cells [54, 55]. The main drawback of such small molecule acceptors was their instability over long time frames which is why research also focused on polymer non-fullerene acceptors that offered better device stability [58]. The first generation of polymer non-fullerene acceptors was mostly based on NDIs and PDIs that improved over time to reach efficiencies up to 12% [59, 60].

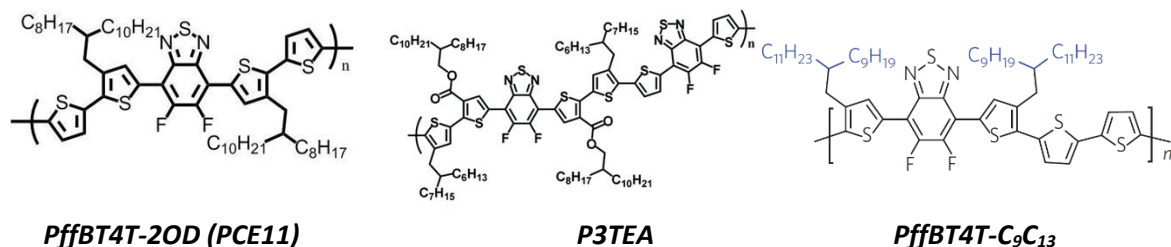


**Figure 10: The chemical structures of several TDA D-A donor polymers.**

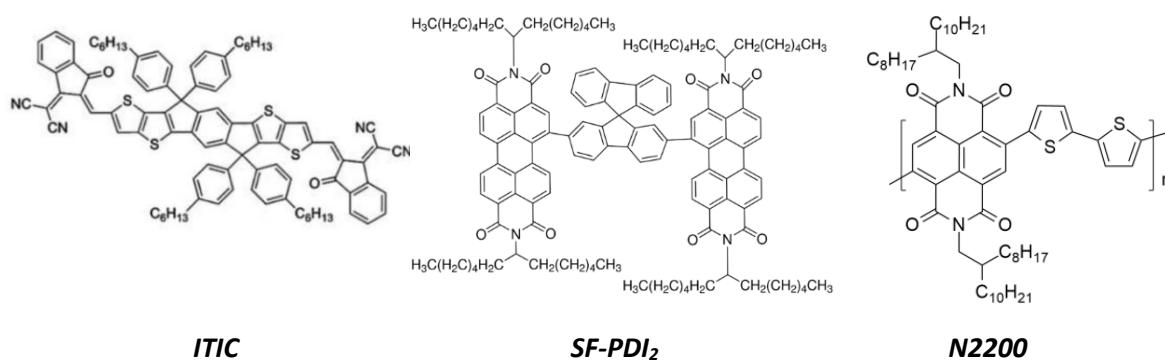


**Figure 11: The chemical structures of several first-generation small molecule and polymer non-fullerene acceptors.**

Current state of the art materials for organic solar cells mainly focus on small molecules acceptors based on the A-DA'D-A design [15]. This pushed the organic solar cell efficiency over the 15% limit of organic solar cells [61]. The highlight of these A-DA'D-A non-fullerene acceptors is the Y6 family. Y6 was the first non-fullerene acceptor that pushed the organic solar cell efficiency beyond the 15% limit in a single junction configuration [62]. Figure 12 shows the chemical structures of several small molecule acceptors within the Y6 family [15]. The Y6 molecule shows a twisted structure where the central side chains are perpendicular to the conjugated backbone plane preventing excessive aggregation. Moreover, the aggregation properties within this acceptor family could be fine-tuned by backbone, end group and side chain modifications [15]. Recently, a modified Y6 acceptor showed

unique aggregation properties where H-aggregation and J-aggregation occurred simultaneously in the BTIC-CF<sub>3</sub>- $\gamma$  single crystal [63]. Research for polymer donors matching the Y6 family in terms of energetics and morphology led to major breakthroughs in the solar cell efficiencies [14]. Most notable of these is PM6 which showed 17.8% efficiency when combined with BTP-eC9 [64] and D18 which showed 18.2% when combined with Y6 [65]. All of these advancements pave the way towards the 20% efficiency limit in single junction organic solar cells and even higher efficiencies in tandem solar cells.

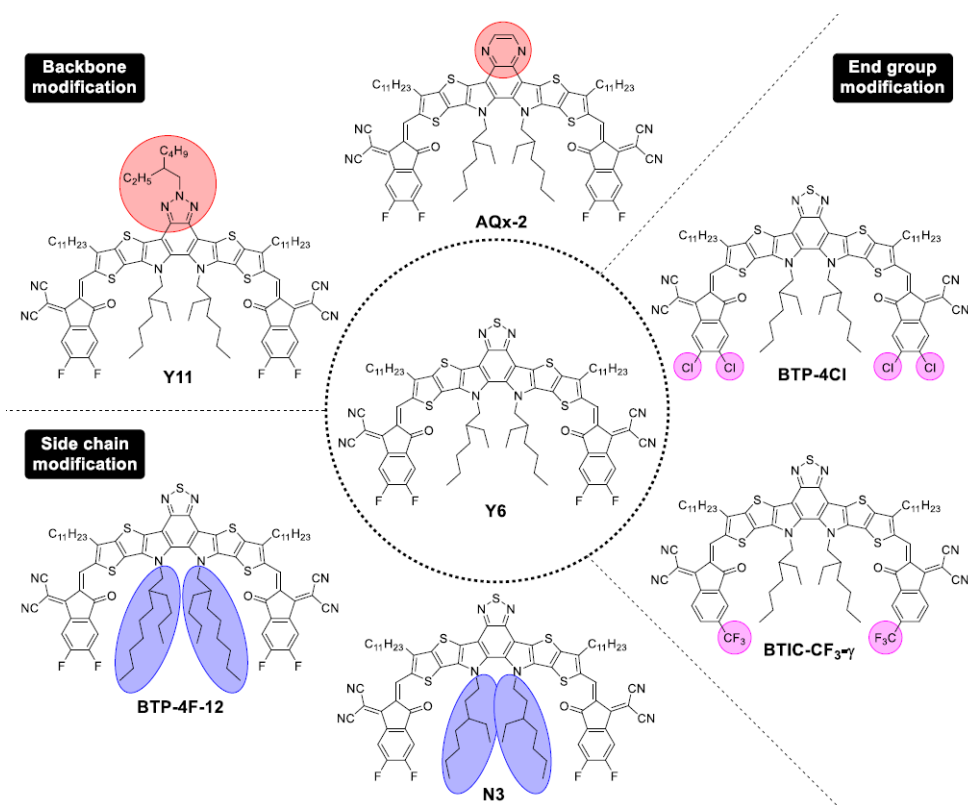


**Figure 12:** The chemical structures of several small molecule non-fullerene acceptors of the Y6 family with the A-DA'D-A design. Reproduced from [15].

## References

- [1] S.C. Bhatia, *Advanced Renewable Energy Systems*, (2014).
- [2] *Renewables 2021: Global Status Report*  
[https://www.ren21.net/wp-content/uploads/2019/05/GSR2021\\_Full\\_Report.pdf](https://www.ren21.net/wp-content/uploads/2019/05/GSR2021_Full_Report.pdf), (2021).
- [3] A.E. Becquerel, *Memoire sur les Effects d'Electriques Produits Sous l'Influence des Rayons Solaires*, *Compt. Rend. Acad. Sci.*, 9 (1839) 561-567.
- [4] W. Smith, *Effect of Light on Selenium During the Passage of An Electric Current*, *Nat Commun*, 7 (1873) 303.
- [5] D.M. Chapin, C.S. Fuller, G.L. Pearson, *A New Silicon p-n Junction Photocell for Converting Solar Radiation into Electrical Power*, *J Appl Phys*, 25 (1954) 676-677.
- [6] A. Polman, M. Knight, E.C. Garnett, B. Ehrler, W.C. Sinke, *Photovoltaic materials: Present efficiencies and future challenges*, *Science*, 352 (2016) aad4424.
- [7] A.J. Heeger, *Semiconducting polymers: the Third Generation*, *Chem Soc Rev*, 39 (2010) 2354-2371.
- [8] G. Li, R. Zhu, Y. Yang, *Polymer solar cells*, *Nat Photonics*, 6 (2012) 153-161.
- [9] M.A. Green, A. Ho-Baillie, H.J. Snaith, *The emergence of perovskite solar cells*, *Nat Photonics*, 8 (2014) 506-514.
- [10] C.W. Tang, *Two-layer organic photovoltaic cell*, *Appl. Phys. Lett.*, 48 (1986) 183.
- [11] Y.W. Zhang, A.J. Parnell, O. Blaszczyk, A.J. Musser, I.D.W. Samuel, D.G. Lidzey, G. Bernardo, *Effect of fullerene acceptor on the performance of solar cells based on PffBT4T-2OD*, *Phys Chem Chem Phys*, 20 (2018) 19023-19029.
- [12] C.H. Duan, L.M. Ding, *The new era for organic solar cells: small molecular donors*, *Sci Bull*, 65 (2020) 1597-1599.
- [13] C.H. Duan, L.M. Ding, *The new era for organic solar cells: polymer acceptors*, *Sci Bull*, 65 (2020) 1508-1510.
- [14] C.H. Duan, L.M. Ding, *The new era for organic solar cells: polymer donors*, *Sci Bull*, 65 (2020) 1422-1424.
- [15] C.H. Duan, L.M. Ding, *Highlight The new era for organic solar cells: non-fullerene small molecular acceptors*, *Sci Bull*, 65 (2020) 1231-1233.
- [16] M. Riede, D. Spoltore, K. Leo, *Organic Solar Cells-The Path to Commercial Success*, *Adv Energy Mater*, 11 (2021).
- [17] Y.W. Li, G.Y. Xu, C.H. Cui, Y.F. Li, *Flexible and Semitransparent Organic Solar Cells*, *Adv Energy Mater*, 8 (2018).
- [18] H.B. A. Köhler, *The Electronic Structure of Organic Semiconductors*, in: *Electronic Processes in Organic Semiconductors*, 2015, pp. 1-86.
- [19] A. Polman, M. Knight, E.C. Garnett, B. Ehrler, W.C. Sinke, *Photovoltaic materials: Present efficiencies and future challenges*, *Science*, 352 (2016).
- [20] W.R. Mateker, M.D. McGehee, *Progress in Understanding Degradation Mechanisms and Improving Stability in Organic Photovoltaics*, *Adv Mater*, 29 (2017).

- [21] H. Cha, S. Wheeler, S. Holliday, S.D. Dimitrov, A. Wadsworth, H.H. Lee, D. Baran, I. McCulloch, J.R. Durrant, Influence of Blend Morphology and Energetics on Charge Separation and Recombination Dynamics in Organic Solar Cells Incorporating a Nonfullerene Acceptor, *Adv Funct Mater*, 28 (2018).
- [22] F.J. Kahle, C. Saller, S. Olthof, C. Li, J. Lebert, S. Weiss, E.M. Herzig, S. Huttner, K. Meerholz, P. Strohriegel, A. Kohler, Does Electron Delocalization Influence Charge Separation at Donor-Acceptor Interfaces in Organic Photovoltaic Cells?, *J Phys Chem C*, 122 (2018) 21792-21802.
- [23] R.J. Gillespie, Electron-Densities and the Vsepr Model of Molecular-Geometry, *Can J Chem*, 70 (1992) 742-750.
- [24] X. Liu, B.M. Xie, C.H. Duan, Z.J. Wang, B.B. Fan, K. Zhang, B.J. Lin, F.J.M. Colberts, W. Ma, R.A.J. Janssen, F. Huang, Y. Cao, A high dielectric constant non-fullerene acceptor for efficient bulk-heterojunction organic solar cells, *J Mater Chem A*, 6 (2018) 395-403.
- [25] E.G. Mccrae, M. Kasha, Enhancement of Phosphorescence Ability Upon Aggregation of Dye Molecules, *J Chem Phys*, 28 (1958) 721-722.
- [26] R.M. Hochstrasser, M. Kasha, Application of the Exciton Model to Monomolecular Lamellar Systems, *Photochem Photobiol*, 3 (1964) 317-331.
- [27] M. Kasha, Energy Transfer Mechanisms and the Molecular Exciton Model for Molecular Aggregates, *Radiat Res*, 178 (2012) Av27-Av34.
- [28] F. Panzer, H. Bässler, A. Köhler, Temperature Induced Order-Disorder Transition in Solutions of Conjugated Polymers Probed by Optical Spectroscopy, *J Phys Chem Lett*, 8 (2017) 114-125.
- [29] J. Gierschner, S.Y. Park, Luminescent distyrylbenzenes: tailoring molecular structure and crystalline morphology, *J Mater Chem C*, 1 (2013) 5818-5832.
- [30] F.C. Spano, The Spectral Signatures of Frenkel Polarons in H- and J-Aggregates, *Accounts Chem Res*, 43 (2010) 429-439.
- [31] F.C. Spano, C. Silva, H- and J-Aggregate Behavior in Polymeric Semiconductors, *Annu Rev Phys Chem*, 65 (2014) 477-500.
- [32] J. Clark, C. Silva, R.H. Friend, F.C. Spano, Role of intermolecular coupling in the photophysics of disordered organic semiconductors: Aggregate emission in regioregular polythiophene, *Phys Rev Lett*, 98 (2007).
- [33] J. Clark, J.F. Chang, F.C. Spano, R.H. Friend, C. Silva, Determining exciton bandwidth and film microstructure in polythiophene films using linear absorption spectroscopy, *Appl Phys Lett*, 94 (2009).
- [34] E. Instruments, What is a Jablonski Diagram? (<https://www.edinst.com/us/blog/jablonski-diagram/>).
- [35] S. Wood, J.R. Hollis, J.S. Kim, Raman spectroscopy as an advanced structural nanoprobe for conjugated molecular semiconductors, *J Phys D Appl Phys*, 50 (2017).
- [36] H.J. Wang, C.P. Chen, R.J. Jeng, Polythiophenes Comprising Conjugated Pendants for Polymer Solar Cells: A Review, *Materials*, 7 (2014) 2411-2439.
- [37] S. Jung, Y. Cho, S.H. Kang, S.J. Yoon, C. Yang, Effect of Third Component on Efficiency and Stability in Ternary Organic Solar Cells: More than a Simple Superposition, *Sol Rrl*, 6 (2022).
- [38] Y.H. Liu, J.B. Zhao, Z.K. Li, C. Mu, W. Ma, H.W. Hu, K. Jiang, H.R. Lin, H. Ade, H. Yan, Aggregation and morphology control enables multiple cases of high-efficiency polymer solar cells, *Nat Commun*, 5 (2014).

- [39] G. Dennler, M.C. Scharber, C.J. Brabec, Polymer-Fullerene Bulk-Heterojunction Solar Cells, *Adv Mater*, 21 (2009) 1323-1338.
- [40] W.L. Ma, C.Y. Yang, X. Gong, K. Lee, A.J. Heeger, Thermally stable, efficient polymer solar cells with nanoscale control of the interpenetrating network morphology, *Adv Funct Mater*, 15 (2005) 1617-1622.
- [41] Y.F. Li, Molecular Design of Photovoltaic Materials for Polymer Solar Cells: Toward Suitable Electronic Energy Levels and Broad Absorption, *Accounts Chem Res*, 45 (2012) 723-733.
- [42] Y.Y. Liang, D.Q. Feng, Y. Wu, S.T. Tsai, G. Li, C. Ray, L.P. Yu, Highly Efficient Solar Cell Polymers Developed via Fine-Tuning of Structural and Electronic Properties, *J Am Chem Soc*, 131 (2009) 7792-7799.
- [43] H.T. Fu, Z.H. Wang, Y.M. Sun, Polymer Donors for High-Performance Non-Fullerene Organic Solar Cells, *Angew Chem Int Edit*, 58 (2019) 4442-4453.
- [44] E.E. Havinga, W. Tenhoeve, H. Wynberg, Alternate Donor-Acceptor Small-Band-Gap Semiconducting Polymers - Polysquaraines and Polycroconaines, *Synthetic Met*, 55 (1993) 299-306.
- [45] Q.T. Zhang, J.M. Tour, Alternating donor/acceptor repeat units in polythiophenes. Intramolecular charge transfer for reducing band gaps in fully substituted conjugated polymers, *J Am Chem Soc*, 120 (1998) 5355-5362.
- [46] S.C. Price, A.C. Stuart, L.Q. Yang, H.X. Zhou, W. You, Fluorine Substituted Conjugated Polymer of Medium Band Gap Yields 7% Efficiency in Polymer-Fullerene Solar Cells, *J Am Chem Soc*, 133 (2011) 4625-4631.
- [47] H.W. Hu, P.C.Y. Chow, G.Y. Zhang, T.X. Ma, J. Liu, G.F. Yang, H. Yan, Design of Donor Polymers with Strong Temperature-Dependent Aggregation Property for Efficient Organic Photovoltaics, *Accounts Chem Res*, 50 (2017) 2519-2528.
- [48] G.F. Yang, Z.K. Li, K. Jiang, J. Zhang, J.Y. Chen, G.Y. Zhang, F. Huang, W. Ma, H. Yan, Optimal extent of fluorination enabling strong temperature-dependent aggregation, favorable blend morphology and high-efficiency polymer solar cells, *Sci China Chem*, 60 (2017) 545-551.
- [49] J. Liu, L.K. Ma, F.K. Sheong, L. Zhang, H.W. Hu, J.X. Zhang, J.Q. Zhang, Z.K. Li, C. Ma, X. Han, D. Pan, H. Ade, W. Ma, H. Yan, Carboxylate substitution position influencing polymer properties and enabling non-fullerene organic solar cells with high open circuit voltage and low voltage loss, *J Mater Chem A*, 6 (2018) 16874-16881.
- [50] L. Ning, G.C. Han, Y.P. Yi, Conformational and aggregation properties of PffBT4T polymers: atomistic insight into the impact of alkyl-chain branching positions, *J Mater Chem C*, 7 (2019) 14198-14204.
- [51] J. Liu, S.S. Chen, D.P. Qian, B. Gautam, G.F. Yang, J.B. Zhao, J. Bergqvist, F.L. Zhang, W. Ma, H. Ade, O. Inganäs, K. Gundogdu, F. Gao, H. Yan, Fast charge separation in a non-fullerene organic solar cell with a small driving force, *Nat Energy*, 1 (2016).
- [52] J.B. Zhao, Y.K. Li, G.F. Yang, K. Jiang, H.R. Lin, H. Ade, W. Ma, H. Yan, Efficient organic solar cells processed from hydrocarbon solvents, *Nat Energy*, 1 (2016).
- [53] N.N. Liang, W. Jiang, J.H. Hou, Z.H. Wang, New developments in non-fullerene small molecule acceptors for polymer solar cells, *Mater Chem Front*, 1 (2017) 1291-1303.
- [54] J.Q. Zhang, H.S. Tan, X.G. Guo, A. Facchetti, H. Yan, Material insights and challenges for non-fullerene organic solar cells based on small molecular acceptors, *Nat Energy*, 3 (2018) 720-731.

- [55] A. Wadsworth, M. Moser, A. Marks, M.S. Little, N. Gasparini, C.J. Brabec, D. Baran, I. McCulloch, Critical review of the molecular design progress in non-fullerene electron acceptors towards commercially viable organic solar cells, *Chem Soc Rev*, 48 (2019) 1596-1625.
- [56] Y.Z. Lin, J.Y. Wang, Z.G. Zhang, H.T. Bai, Y.F. Li, D.B. Zhu, X.W. Zhan, An Electron Acceptor Challenging Fullerenes for Efficient Polymer Solar Cells, *Adv Mater*, 27 (2015) 1170-1174.
- [57] J.B. Zhao, Y.K. Li, H.R. Lin, Y.H. Liu, K. Jiang, C. Mu, T.X. Ma, J.Y.L. Lai, H.W. Hu, D.M. Yu, H. Yan, High-efficiency non-fullerene organic solar cells enabled by a difluorobenzothiadiazole-based donor polymer combined with a properly matched small molecule acceptor, *Energ Environ Sci*, 8 (2015) 520-525.
- [58] X. Liu, C.H. Zhang, C.H. Duan, M.M. Li, Z.C. Hu, J. Wang, F. Liu, N. Li, C.J. Brabec, R.A.J. Janssen, G.C. Bazan, F. Huang, Y. Cao, Morphology Optimization via Side Chain Engineering Enables All Polymer Solar Cells with Excellent Fill Factor and Stability, *J Am Chem Soc*, 140 (2018) 8934-8943.
- [59] L. Zhu, W.K. Zhong, C.Q. Qiu, B.S. Lyu, Z.C. Zhou, M. Zhang, J.N. Song, J.Q. Xu, J. Wang, J. Ali, W. Feng, Z.W. Shi, X.D. Gu, L. Ying, Y.M. Zhang, F. Liu, Aggregation-Induced Multilength Scaled Morphology Enabling 11.76% Efficiency in All-Polymer Solar Cells Using Printing Fabrication, *Adv Mater*, 31 (2019).
- [60] C. Lee, S. Lee, G.U. Kim, W. Lee, B.J. Kim, Recent Advances, Design Guidelines, and Prospects of All-Polymer Solar Cells, *Chem Rev*, 119 (2019) 8028-8086.
- [61] Y. Cui, H.F. Yao, L. Hong, T. Zhang, Y. Xu, K.H. Xian, B.W. Gao, J.Z. Qin, J.Q. Zhang, Z.X. Wei, J.H. Hou, Achieving Over 15% Efficiency in Organic Photovoltaic Cells via Copolymer Design, *Adv Mater*, 31 (2019).
- [62] J. Yuan, Y.Q. Zhang, L.Y. Zhou, G.C. Zhang, H.L. Yip, T.K. Lau, X.H. Lu, C. Zhu, H.J. Peng, P.A. Johnson, M. Leclerc, Y. Cao, J. Ulanski, Y.F. Li, Y.P. Zou, Single-Junction Organic Solar Cell with over 15% Efficiency Using Fused-Ring Acceptor with Electron-Deficient Core, *Joule*, 3 (2019) 1140-1151.
- [63] H.J. Lai, Q.Q. Zhao, Z.Y. Chen, H. Chen, P.J. Chao, Y.L. Zhu, Y.W. Lang, N. Zhen, D.Z. Mo, Y.Z. Zhang, F. He, Trifluoromethylation Enables a 3D Interpenetrated Low-Band-Gap Acceptor for Efficient Organic Solar Cells, *Joule*, 4 (2020) 688-700.
- [64] Y. Cui, H.F. Yao, J.Q. Zhang, K.H. Xian, T. Zhang, L. Hong, Y.M. Wang, Y. Xu, K.Q. Ma, C.B. An, C. He, Z.X. Wei, F. Gao, J.H. Hou, Single-Junction Organic Photovoltaic Cells with Approaching 18% Efficiency, *Adv Mater*, 32 (2020).
- [65] Q.S. Liu, Y.F. Jiang, K. Jin, J.Q. Qin, J.G. Xu, W.T. Li, J. Xiong, J.F. Liu, Z. Xiao, K. Sun, S.F. Yang, X.T. Zhang, L.M. Ding, 18% Efficiency organic solar cells, *Sci Bull*, 65 (2020) 272-275.

# Chapter 2: Methods

## 2.1 Introduction

All the experimental measurements presented in this thesis were performed at the *Soft Matter Optoelectronics (EPII), University of Bayreuth*, except for the Raman measurements which I performed at the *Macromolecular Chemistry II, University of Bayreuth* with the help of **Dr. Holger Schmalz**. All the experimental setups used were already available at the time of my PhD. During my PhD I was responsible for the streak camera setup and performed continuous minor adjustments for maintaining the setup efficiency and I carried out maintenance work when necessary. I prepared all the samples for measurements also at the *Soft Matter Optoelectronics (EPII), University of Bayreuth*. The blade coated neat and blended PffBT4T-2OD (PCE11) donor polymer films were prepared by **Giovanni Maria Matrone** from *Department of Materials and Centre of Plastic Electronics, Imperial College London*.

All the materials used in this thesis were commercially purchased from *Sigma-Aldrich (currently Merck)* and *1-material*, except for the pendant perylene diimide (PDI) monomers and polymers that were synthesized and provided by **Prof. Dr. Mukundan Thelakkat** and **Andreas Lang** [1] from the *Macromolecular Chemistry I, University of Bayreuth*.

## 2.2 Temperature dependent steady state spectroscopy

Steady state absorption and photoluminescence (PL) spectra were obtained using a setup built by **Fabian Panzer** and **Tobias Meier** from the *Soft Matter Optoelectronics (EPII), University of Bayreuth*. As shown in figure 1, the setup allows for automatic sequential measurements of absorption and PL spectra at different temperatures. Fixed and removable mirrors are numbered from 1-5 and the lenses from L1-L3.

The system consisting of mirrors 1-4 and lens L3 around the cryostat (shown as transparent) is implemented to account for variable intensity of the lamp used for the absorption measurements as will be explained below. The sample is placed inside a temperature controlled continuous flow helium cryostat by Oxford Instruments which allows for temperatures of 5-500 K. The sample orientation is adjusted relative to the excitation beam at a non-normal angle so that the emitted PL light is collected perpendicularly and enters the detection system.

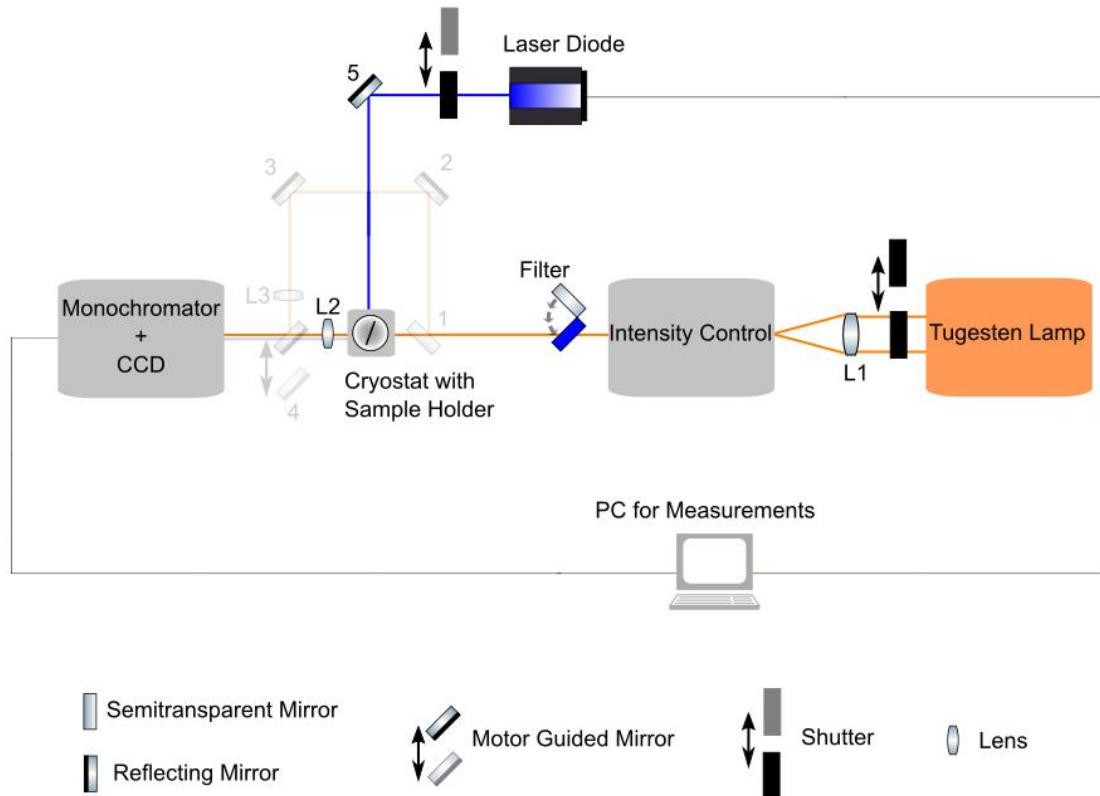


**Figure 1: Schematic of the temperature dependent steady state setup. Fixed and removable mirrors are numbered from 1-5 and the lenses from L1-L3. The orange line represents the absorption measurement light path while the blue line represents the photoluminescence measurement light path. The system consisting of mirrors 1-4 and lens L3 to account for the tungsten lamp variable intensity is shown as transparent.**

### (i) Photoluminescence (PL)

For the PL measurements, the sample is excited by a laser diode (Coherent COMPASS 405-50 CW) emitting at 405 nm (3.06 eV). The blue line indicates the excitation beam path before the sample and the emitted PL from the sample until the detection unit. The beam spot location on the sample is controlled by mirror (5). A shutter is placed in front of the laser diode to block the excitation beam during absorption measurements. After the sample is excited, the emitted PL is focused on the detection unit using lens L2. The detection system consists of a monochromator (Andor Shamrock SR-303i-B) and CCD camera (Andor iDus DU4200A-OE). To avoid the collection of the second harmonic of the laser during detection of PL emission from the sample, a filter wheel with different filters is present at the entrance of the monochromator. The resulting PL spectra are corrected for both the detection setup efficiency and the absorption intensity at the excitation wavelength.

## (ii) Absorption

For the absorption measurements, a tungsten-halogen lamp acts as a white light source. The orange line indicates the white light path before the sample and the transmitted light from the sample until the detection unit. A shutter is placed in front of the tungsten-halogen lamp to block the white light during PL measurements.

The white light goes through two main components before arriving to the sample. First, a setup consisting of entrance and exit slits coupled to a mirror system. This is used to adjust the white light intensity. Second, a filter to adjust the relative intensity of the blue to the red emission regions as the lamp is much more intense in the red region. The transmitted white light from the sample is focused using lens L3 on the same detection unit used for collecting the emitted PL. For automatic sequential measurements of PL and absorption at each temperature, a computer program controls the two shutters in front of the laser diode and the tungsten-halogen lamp.

## (iii) Calibration for the tungsten-halogen lamp

As the lamp intensity varies over time, a calibration system has been implemented to take this into consideration. This system is shown in figure 2 as normal in contrast to the other setup components shown as transparent. This calibration system consists of the semitransparent mirror (1) that splits the white light before arriving to the sample. The reflected white light -which I refer to as the calibration beam- is then guided around the cryostat by means of mirrors (2) and (3) and lens L3, then arrives to the motor guided mirror (4). This motor guided mirror can control whether the transmitted light from the sample or the calibration beam enters the detection system. The location of the guided mirror and consequently the measurement of the calibration beam and the sample transmission intensities is controlled by a computer program during measurement. The final absorption spectra is calculated using the following equation:

$$OD = -\log \left[ \frac{I_t}{I_r} \times \frac{I_{c/r}}{I_{c/t}} \right] \quad (1)$$

Where,  $I_t$  and  $I_r$  are the transmission intensities through the sample and the reference respectively.  $I_{c/t}$  and  $I_{c/r}$  are the calibration beam intensities during the sample and the reference measurements respectively. Their ratio is the correction factor for the variable lamp intensity over the duration of the measurement.

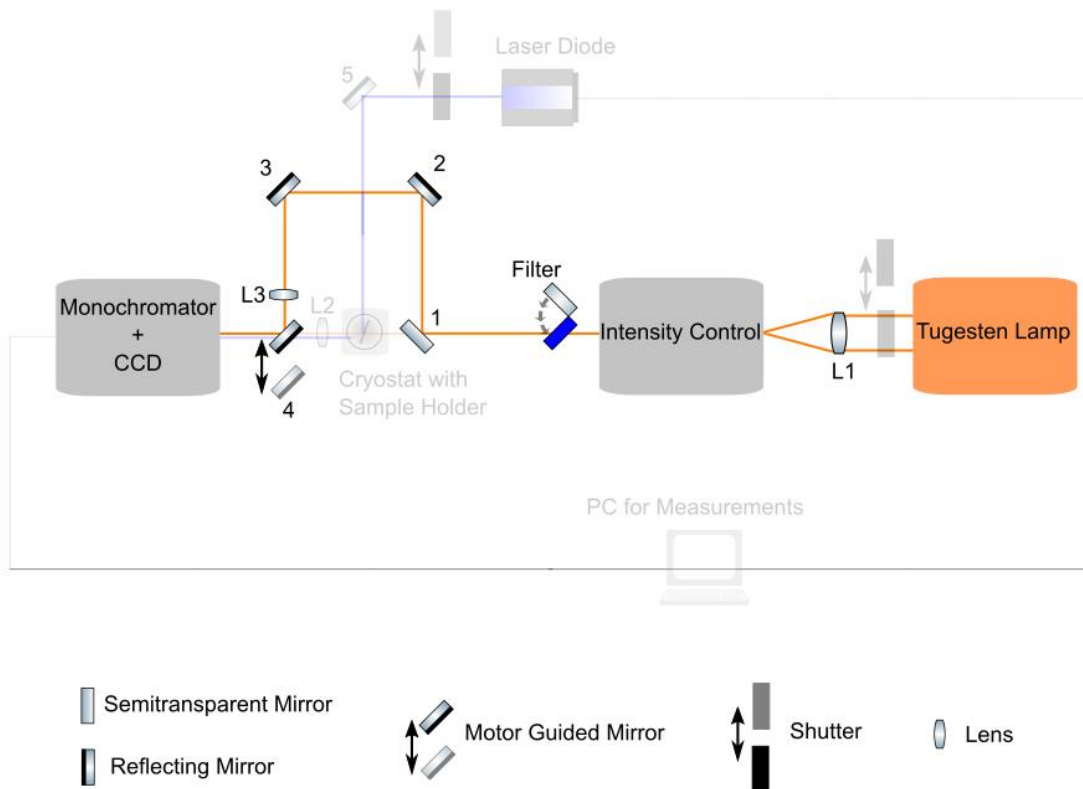


**Figure 2: Schematic of the temperature dependent steady state setup. Fixed and removable mirrors are numbered from 1-5 and the lenses from L1-L3. The orange line represents the absorption measurement light path while the blue line represents the photoluminescence measurement light path. The system consisting of mirrors 1-4 and lens L3 to account for the tungsten lamp variable intensity is shown as normal in contrast to the other setup components shown as transparent.**

#### (iv) Exemplary data

An example of the data produced by the setup is shown in figure 3. The figure shows the absorption and PL spectra for blade coated neat PCE11 films taken within the 5-300 K range with 20K steps. The presence of isobestic points can be readily observed in both spectra at around 1.65 eV for PL, 1.82 eV and 1.99 eV for absorption. The slight undulation structure present in some of the absorption spectra (e.g. between 2 eV and 2.8 eV in the green spectrum) is due to interference at the cryostat windows. This structure can be removed as needed during data processing by applying a fast Fourier transform (FFT) filter for example.

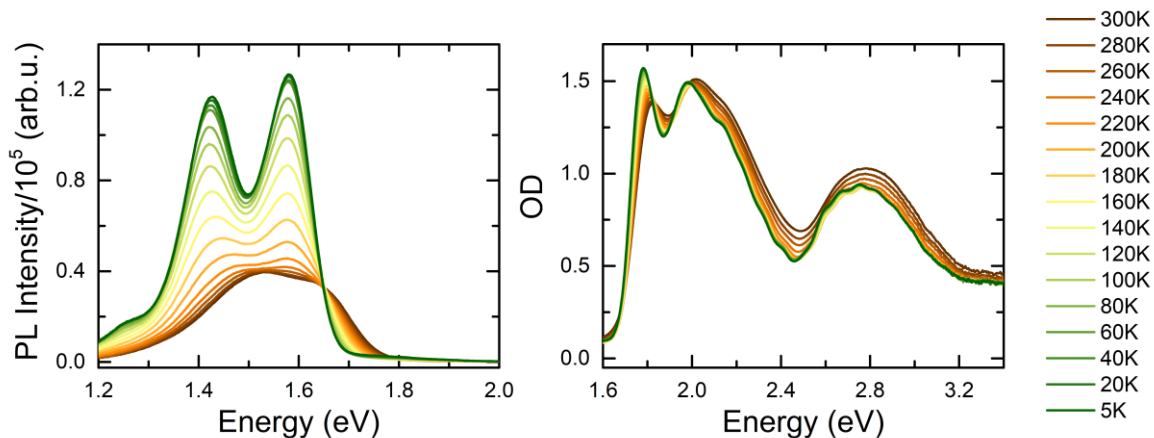


**Figure 3: Temperature dependent absorption and photoluminescence for blade coated PCE11 films from orthodichlorobenzene (oDCB) solutions at 20 mg/ml PCE11 concentration.**

### 2.3 Time-resolved photoluminescence (TRPL)

TRPL spectra were captured using a streak camera setup that is shown schematically in figure 4. Fixed and removable mirrors are numbered from 1-11 and the lenses from L1-L3. Depending on the desired excitation light properties, several optical paths can be realized as shown by the solid, dotted and dashed red lines, which will be further explained below.

#### i. Excitation

The excitation source used is a mode-locked tunable Coherent Chameleon Ultra Ti:Sapphire laser. It covers the wavelength range between 690-1020 nm with the pulses produced having  $\approx 140$  fs FWHM and an 80 MHz repetition rate corresponding to a pulse separation time of 12.5 ns. Reduction of repetition rate of the excitation pulses - if required - can be achieved by using a pulse selector. The one used here is the APE "PulseSelect" which is based on the acousto-optic effect (present in certain crystals e.g. quartz, TeO<sub>2</sub>). By applying an acoustic signal with certain frequencies, a modulation of the refractive index can be introduced through which the crystal can act as a 3D optical diffraction grating. Consequently, by adjusting the acoustic signal applied on the crystal, single laser pulses can be selected from the 80 MHz pulse train with the desired repetition rate. The possible repetition rates to be produced ranges between 4 MHz down to 1.5 Hz. The second component allowing for control over the excitation wavelength is the second harmonic generator (SHG). This allows for frequency doubling of the excitation laser by using non-linear optical interactions inside a BBO (beta-BaB<sub>2</sub>O<sub>4</sub>) crystal. This allows for an extension of the excitation wavelength to cover the 345-510 nm range.

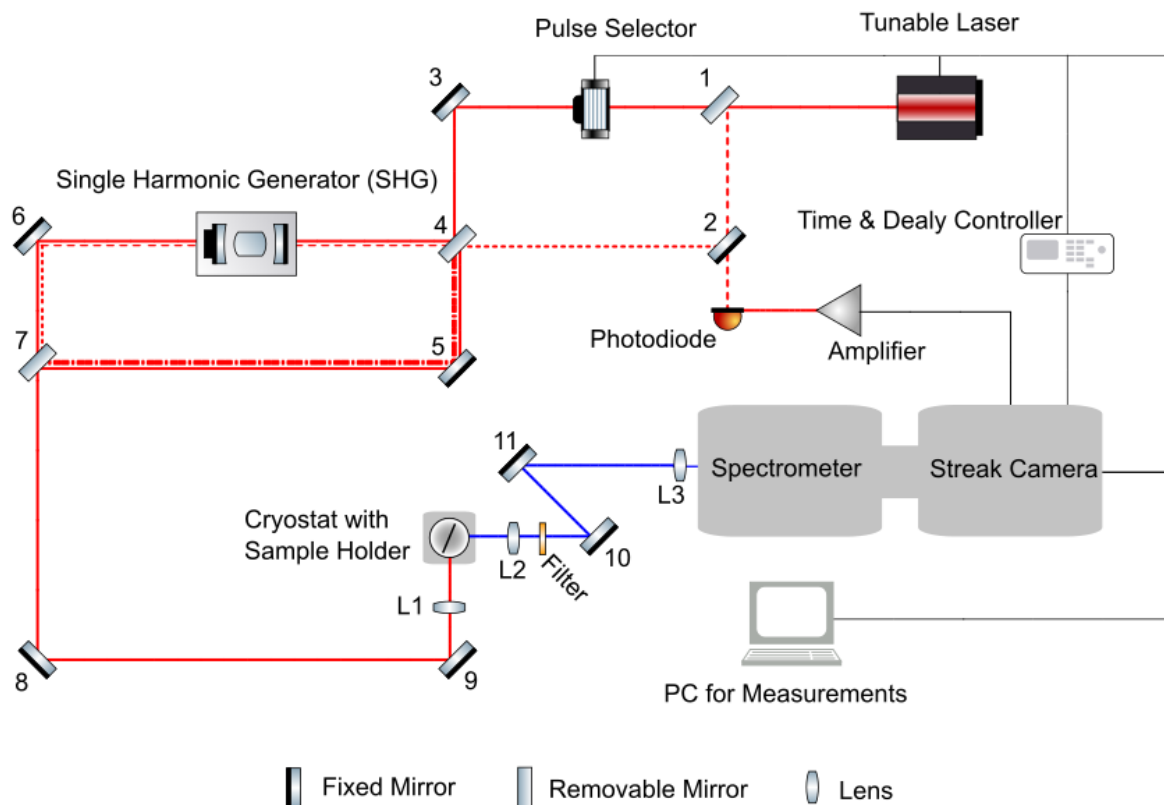


**Figure 4: Schematic of the streak camera setup used for time resolved PL measurements. Fixed and removable mirrors are numbered from 1-11 and the lenses from L1-L3. The solid red line represents the laser excitation as produced by the tunable laser, the dotted and dashed red lines represent different paths of the laser beam after passing through different optical components, and the blue line represents the emitted light from the sample.**

Depending on the desired excitation properties, four optical paths can be realized by removing or inserting the removable mirrors 1, 4 and 7 as follows:

- For measurements using the original pulse repetition rate of 80 MHz, mirror 1 is inserted so that the beam bypasses the pulse selector. After this mirrors 4 and 7 can be both either inserted or removed to either bypass or go through the SHG depending. This is decided depending on the desired excitation wavelength, whether it is needed to be between 690-1020 nm (mirrors inserted) or between 345-510 nm (mirrors removed).
- For measurements using a reduced repetition rate mirror 1 is then removed so that the beam passes through the pulse selector. After this, again mirrors 4 and 7 can be both inserted or removed depending on the desired excitation wavelength.

After adjusting for the required excitation properties, the beam is collimated onto the sample using lens L1. The sample is located inside a temperature controlled continuous flow helium cryostat by Oxford Instruments, which allows for temperatures of 5-500 K. The sample orientation is adjusted so that the emitted PL beam is collected perpendicular to the excitation beam. Finally the emitted beam is coupled to the detection unit using mirrors 10 and 11 and lenses L2 and L3 with a filter to protect the spectrometer and the streak camera against any remaining scattered laser light.

## ii. Detection

A detection unit consisting of a spectrometer (Princeton Instruments Acton SP3200) and a streak camera (Optronis SC-10) is used. After the emitted light is spectrally resolved by the spectrometer it enters the streak camera. The general operating principal of the streak camera is shown in figures 5 and 6.

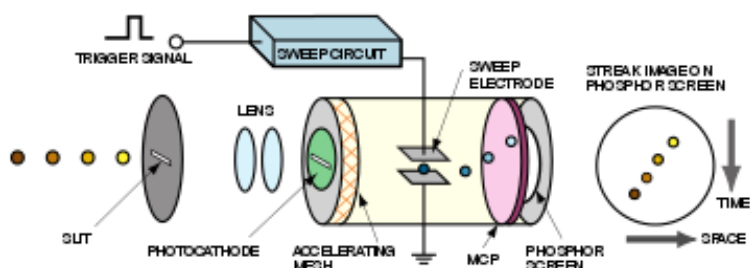


**Figure 5: The full journey of a light pulse from entering the streak camera until the generation of the final time and energy dependent data. Reproduced from [2].**

In order to better understand how the streak camera detects the time resolved PL, I consider a simple case. As shown in figure 5, we imagine four optical pulses entering the streak camera having different light intensities, wavelengths (space axis) and arriving at slightly different times. As a first step after passing through the entrance slit, these optical pulses are focused on a photocathode which converts them to electrons with an intensity proportional to their original intensity. Afterwards they are accelerated through a time varying electric field that is generated by applying a voltage on a sweep electrode. This applied voltage is synchronized with the incident light through a trigger signal. As a result the electrons are deflected at different angles depending on the time by which the corresponding optical pulses enter the camera where the yellow pulse is the first one to arrive and so on (figure 6). Then the deflected electrons are incident on a micro-channel plate (MCP) where they are intensified several orders of magnitude. Finally, they hit a phosphorescence plate through which the electrons are converted back to photons. After the phosphorescence plate, the emitted photons are captured by a CCD camera to construct the final streak image. The final image

is a 3D map where changes in the light intensity is a function of time and wavelength as shown in figure 6 and will be discussed below.

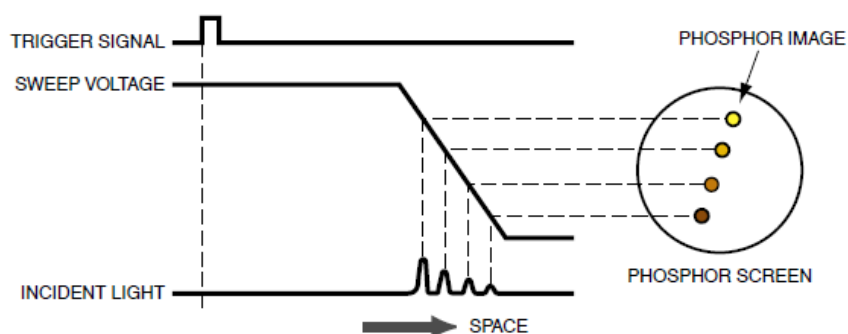


**Figure 6: Relation between the light pulse arrival time at the streak camera, the sweep voltage and the final recorded data. Reproduced from [2].**

In our setup the streak camera contains input optics, a main unit in which different sweep units can be attached, an image intensifier (MCP) and a readout unit (CCD camera). The choice of the sweep unit depends on required time frames to be measured and so one of two different sweep units can be attached to the camera:

- A fast synchroscan sweep unit (SSU11-10) with sweep speeds of 15-100 ps/mm corresponding to time bases between 300-2000 ps. This is triggered by a photodiode-amplifier system connected to the streak camera which detects a laser pulse converting it to the trigger signal. In this configuration, the single pulse selector is not used. The best measured temporal resolution using the fastest sweep speed of 15 ps/mm was  $2.17 \pm 0.01$ .
- The other unit is a slow sweep unit (TSU12-10) with sweep speeds 330 ps/mm to 5 ms/mm corresponding to time bases between 6.6 ns to 100 ms. This is triggered by the laser master clock and a time and delay controller (TDC) connected to the streak camera. The best measured temporal resolution using the fastest sweep speed of 330 ps/mm was  $90.6 \pm 0.8$  ps.

### iii. Exemplary data

The 3D data measured by the streak camera is usually visualized as a 2D intensity map with the color representing the light intensity. An example of the streak camera time TRPL data in figure 7 shows the excited state decay of a pendant perylene diimide (PDI) polymer in a chloroform (CF)

solution excited at 405 nm (3.06 eV). On this graph, the x-axis corresponds to the decay time, where 0 s corresponds to the end of the laser excitation pulse. The y-axis corresponds to the energy of the emitted light. The color map corresponds to the PL intensity (arb. u.) as a function of both time and energy.

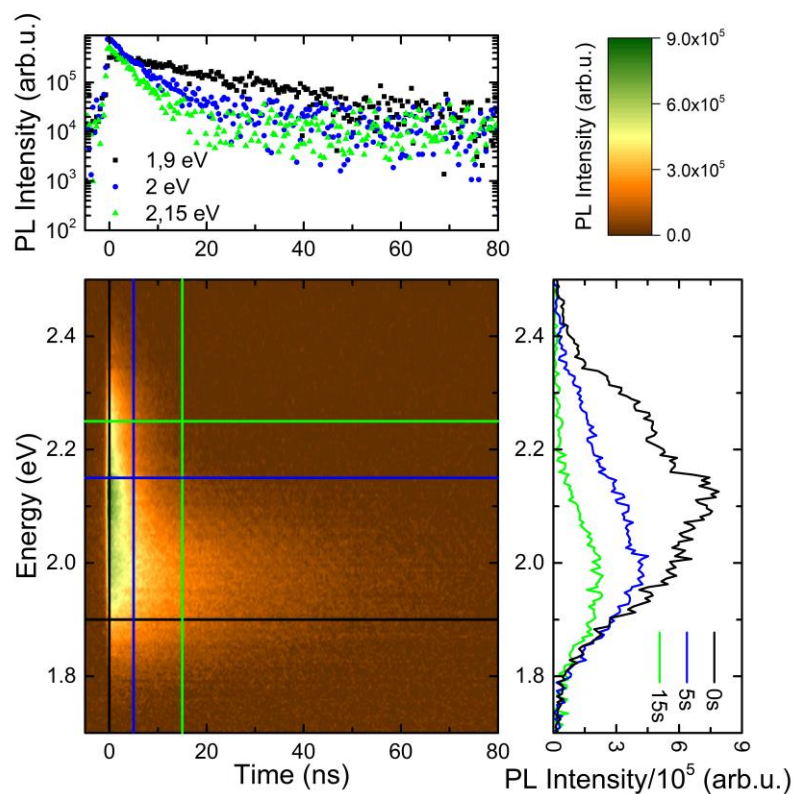


**Figure 7: Streak camera TRPL measurement showing the 2D map and line cuts for a PDI polymer in a CF solutions at 10 mg/ml polymer concentration.**

Consequently, line cuts along either axes provide us with the temporal or energetic evolution of the excited states. On one hand, vertical line cuts provide us with the evolution of the spectra as a function of time. For example, the emission between 2.2-2.4 eV decays between 0-15 s and completely disappears after 15 s. On the other hand, vertical cuts show the temporal dependence of the PL as a function of energy. It can be readily observed that the shape of the decay curves switches between mono-exponential (1.9 eV) and bi-exponential at higher energies.

## 2.4 In-situ optical spectroscopy

In-situ absorption and PL spectra were recorded quasi-simultaneously using a setup built by **Fabian Panzer** and **Michael Buchhorn** and is shown schematically in figure 8. Details of the setup were already reported elsewhere [3]. The setup allows for quasi-simultaneous detection of absorption

and PL during film formation from solutions under different processing conditions as will be discussed below.

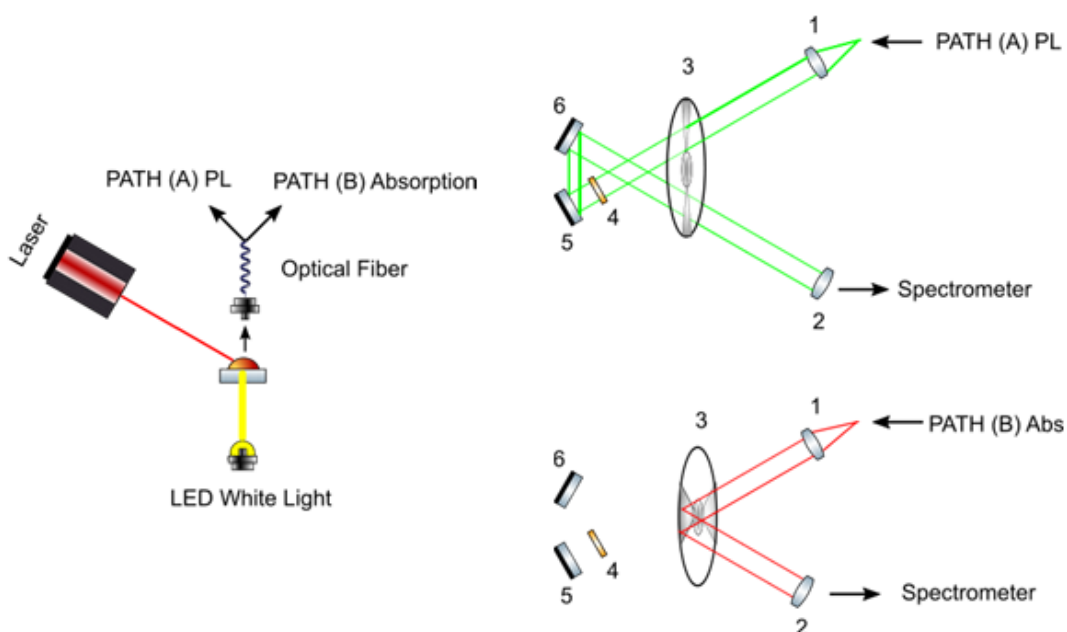


**Figure 8: Schematic drawing of the In situ optical spectroscopy setup. The green solid line represents the emission from the sample following the PL path and the red solid line represents the transmission from the sample following the absorption path.**

The sample holder consists of a temperature controlled metallic chuck by means of a Peltier element allowing a temperature range of 5-120 °C (at the time of measurement). The chuck is attached to a motor to allow for rotation of the substrate when needed. For spin coating, the rotation speed can be set up to 1000 rpm (at the time of measurement).

### (i) Photoluminescence (PL)

For PL, excitation of the sample is done by means of an interchangeable laser diode system (Thorlabs LP series) allowing excitation wavelengths between 405 - 820 nm (3.06 - 1.51 eV). The incidence angle and the spot size of the laser beam can be both adjusted according to the required excitation conditions. The emitted light from the sample is then collected by means of an optical fiber located above the sample. The exact location of the optical fiber can be adjusted in both the horizontal and vertical axes to allow for efficient coupling to the emitted light. The detection system consists of a spectrometer and CCD camera (Andor iDus DU4200A-BEX2-DD).

## (ii) Absorption

For absorption, there is a hole through the sample holder with an attached LED white light covering the spectra range between 415 – 820 nm (2.99 – 1.51 eV). The transmitted LED light through the sample is also collected using the same optical fiber. The detection system is the same as that used to detect the PL.

## (iii) Quasi-simultaneous absorption and PL detection system

The sample location above the LED light hole, the spot location and size of the laser excitation, and the optical fiber location can be finely adjusted. This fine adjustment makes it possible to capture the absorption and PL spectra from the same sample location. To be able to detect both absorption and PL quasi-simultaneously, a mechanical chopper system is implemented which includes a two slot wheel chopper with two mirror coated faces. By using this chopper system, the sample's emitted PL or transmitted white light can follow either one of two possible paths until it arrives to the detection system. For ease of visualization, the two possible paths are shown separately in figure 8 as Path (A) with a green colored solid line for PL (top) and Path (B) with a red color solid line for absorption (bottom). A microcontroller is used to adjust the orientation of the chopper wheel consequently controlling whether absorption or PL is detected. For example, for detecting PL, the LED white light is triggered off and the laser diode is triggered on while the chopper wheel is oriented so that the emitted light follows the PL path and vice versa for absorption.

For the PL spectra, the emitted light from the sample is collimated by a lens and then passes through the chopper wheel slots and then double reflected by two mirrors back through the chopper slots and finally collected by the lens towards the same detection system. Within the PL path an interchangeable filter is used depending on the excitation wavelength to block the laser beam from reaching the detection system. For the absorption spectra, the transmitted light from the sample is collimated by a lens and then is incident on the mirror coated chopper faces. A second lens then collects the reflected light from the mirrors. The collected light enters through another optical fiber to the detection system. During the time of my measurements I was able to record data at frequencies up to 12Hz corresponding to 81 ms between each two consecutive frames i.e. up to 12 individual spectra (6 Abs + 6 PL) could be recorded per second. Finally, for blade coating measurements on the same setup, I implemented a simple system using a rectangular glass substrate as the blade. This glass substrate was tilted at an angle of  $\approx 15^\circ$  relative to the sample holder where the substrate is located. To control the blade coating speed and acceleration, the

blade was attached to a linear translation Stage with a Stepper Motor (LTS 150 by Thorlabs) using optical posts.

#### iv. Exemplary data

An example of the data produced by the in-situ setup is shown in figure 9. The recorded spectra are in the form of a normalized 2D intensity map. The x-axis corresponds to the absorption energy (or emission energy in case of PL) and the y-axis corresponds to the processing time where 0 s refers to the start of film processing (e.g. start of spin coating). The color scale corresponds to the normalized light intensity as a function of both time and energy. The 2D map shows the film formation during spin coating of PffBT4T-2OD (PCE11) donor polymer from a hot solution in Orthodichlorobenzene (oDCB) at 105 °C. The substrate temperature was maintained at 80 °C for the full spin coating duration. Excitation was done using a 450 nm (2.75 eV) diode laser.

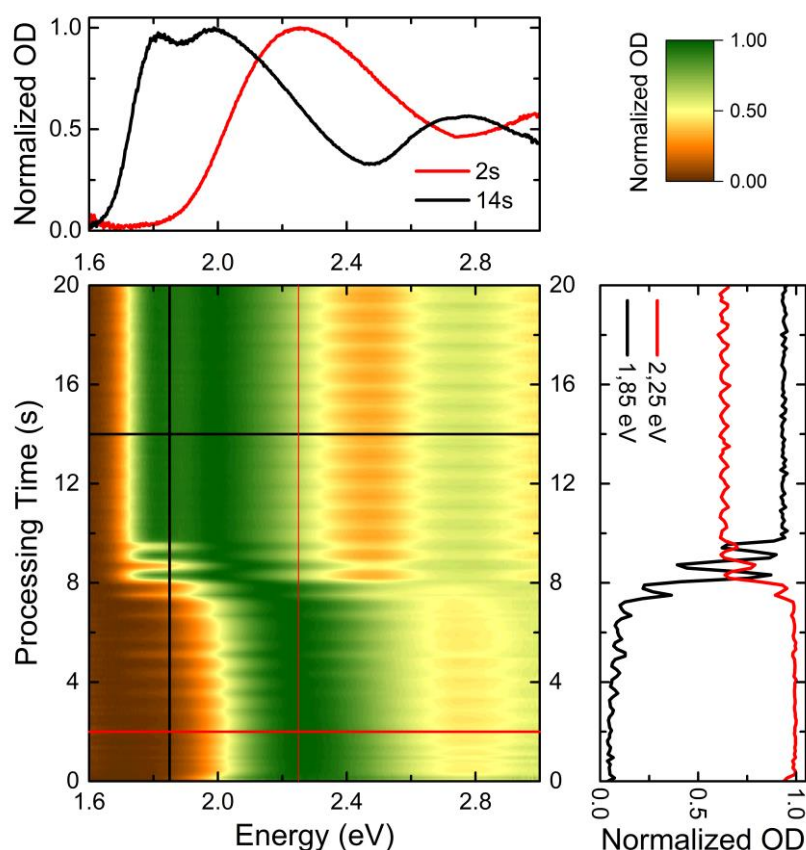


**Figure 9: Example of an in-situ absorption measurement showing the 2D map and line cuts at different energies and times during spin coating of PCE11 films from 105 °C orthodichlorobenzene (oDCB) solution at 15 mg/ml polymer concentration on an 80 °C substrate.**

Line cuts along either axes provides us with the temporal or energetic evolution of absorption or PL during the film formation process. Horizontal line cuts provides us with the evolution of the spectra as a function of time. We observe the transition from non-aggregated spectra (2 s) corresponding to the featureless peak at 2.38 eV to the aggregated spectra (14 s) featuring the 0-0 and 0-1 absorption peaks at 1.7eV and 1.9 eV respectively. Vertical cuts shows the evolution of the absorption intensity at specific energies as a function of the processing time. The transition time (the time at which the polymer chains transition from the non-aggregated to the aggregated state) can be readily observed with the rise of the peak intensity at 1.85eV and the concomitant decrease of the peak intensity at 2.25 eV.

The undulation effect appearing in the 2D intensity maps as a function of time is mainly due to motor vibrations of the sample holder during spin coating. Other reasons include the inhomogeneity of the film thickness, variations in the chopper frequency or slight variations in the alignment of the mirrors reflecting the light beam on the absorption path. This undulation effect can be smoothed out during data processing when needed by averaging over the appropriate time window or by Fourier filtering

## **2.5 Room temperature steady state optical spectroscopy**

For the room temperature steady PL measurements, I used a commercial spectrofluorometer (Jasco FP-8600) with the excitation source consisting of a Xenon lamp and a monochromator allowing for the excitation energy range 200 – 850 nm (6.2 – 1.46 eV).

For the room temperature steady state absorption measurements, I used a commercial UV-Vis-NIR spectrophotometer (Agilent Cary 5000). The setup uses a double beam configuration where a sample and the appropriate reference transmittance are measured simultaneously. This means that the final absorption spectrum is measured without need of post measurement correction.

## **2.6 Raman spectroscopy**

I did the Raman measurements on a commercial combined Raman-Imaging/Scanning Force Microscope System (WITEC ALPHA 300 RA+) at the *Macromolecular Chemistry II, University of Bayreuth*. All the measurements were done at room temperature with either a 532 nm (2.33 eV) or a 732 nm (1.69 eV) laser excitation source at different excitation intensities. The raw data was always corrected for the fluorescence background using a B-spline function.

## 2.7 Device fabrication and characterization

### i. Device fabrication

Throughout my thesis I only used a conventional configuration for fabricating the organic solar cells (OSCs). This configuration consisted of *anode/hole transport layer (HTL)/photoactive layer/electron transport layer (ETL)/cathode*. I used this configuration to fabricate the solar cells in either bulk heterojunction (BHJ) or bilayer architectures. The bottom part of the devices consisted of a PEDOT:PSS or MoO<sub>3</sub> as the HTL on top of an ITO covered glass substrate as the anode. First, the ITO coated glass substrates were cleaned in a sequence of soap, deionized water, acetone and finally isopropanol in an ultrasonic water bath. The substrates were then dried and treated with oxygen plasma for 2 minutes to remove any organic impurities and increase the ITO's work function. Directly afterwards the cleaned substrates were transported to a glove box under an inert gas atmosphere to coat the hole transport layer on top. Either a 10 nm MoO<sub>3</sub> layer was evaporated under high vacuum in an evaporation chamber inside the glove box or a 40-50 nm PEDOT:PSS layer was spin coated also inside the glove box. Afterwards, the photoactive layer was spin coated on top of the HTL. In case of a bilayer architecture, the donor layer was spin coated first then the acceptor layer was spin coated on top using orthogonal solvents. Regardless of the material combination used for the bilayer device, the thickness of the donor layer was kept around 60 nm while that of the acceptor layer was kept around 20 nm. Finally, the top part of the device was evaporated under high vacuum on top of the active layer. The top layer consisted of sequentially evaporated 20 nm Calcium (Ca) layer as the ETL and 100 nm Aluminum (Al) layer as the cathode.

Other than OSCs, electron only devices were fabricated to calculate the electron mobility of the different acceptors using space charge limited current (SCLC) technique. For this measurement, the photoactive layer consisted only of a spin coated acceptor layer with different thicknesses. The SCLC device architecture was similar to that of the OSCs except for replacing the bottom ETL layer with a 100 nm Al layer to block hole injection to the acceptor layer.

### ii. Device characterization

Current-voltage properties (J-V curves) of the fabricated OSCs were measured using a Keithly SMU238 source meter. The illumination source used was a standard one sun (100 mw/cm<sup>2</sup>, AM 1.5) light source. This light source was provided by a Newport sun simulator (model no. ss-150 w, fully reflective, AAA). The J-V curves of the fabricated SCLC devices were measured under dark conditions using also a Keithly SMU238 source meter. To extract the electron mobility, the measured J-V curves were fitted by the Mott-Gurney equation [4]:

$$J = \mu \frac{9}{8} \times \varepsilon_r \times \varepsilon_0 \times \frac{V^2}{d^3} \quad (2)$$

Where,  $J$  is the current density,  $\varepsilon_r$  is the acceptor's material permittivity,  $\varepsilon_0$  is the vacuum permittivity,  $V$  is the applied voltage,  $d$  is the acceptor layer thickness and  $\mu$  is the calculated SCLC electron mobility. To measure the J-V curves of both the OSCs and the SCLC devices, the devices were transported from the glove box to the measurement setup in a vacuum sample holder and was kept under vacuum during the whole measurement.

## References

- [1] A.S. Lang, M. Thelakkat, Modular synthesis of poly(perylene bisimides) using click chemistry: a comparative study, *Polym Chem-Uk*, 2 (2011) 2213-2221.
- [2] Hamamatsu, Guide to streak cameras, (2008).
- [3] M. Buchhorn, S. Wedler, F. Panzer, Setup to Study the in Situ Evolution of Both Photoluminescence and Absorption during the Processing of Organic or Hybrid Semiconductors, *J Phys Chem A*, 122 (2018) 9115-9122.
- [4] N.F. Mott, R.W. Gurney, *Electronic processes in ionic crystals*, (1940).

# Chapter 3: Probing conformational changes of PffBT4T-2OD (PCE11) aggregates upon blending

## 3.1 Introduction

I based this chapter mainly on the manuscript *“Conformational changes of PffBT4T-2OD (PCE11) aggregates upon blending with HDPE probed by optical spectroscopy”* which is prepared for submission together with **Konstantin Schötz, Giovanni Maria Matrone, Natalie Stingelin, Anna Köhler, and Fabian Panzer**. In this paper, we explore the effect of blending on the conformational changes of the PCE11 polymer chains in its aggregate phases in thin films. As a first approach, we explore this by a combination of resonant Raman and steady state optical spectroscopy measurements. Following this, we quantify the conformational changes upon blending by applying a Franck-Condon analysis (FCA) on the measured temperature dependent optical spectra. Finally, we are able to confirm the validity of the FCA results by a new approach that allows us to test the reliability of the results. We show that blending results in a more planarized, longer conjugated PCE11 chains with a reduced degree of interchain molecular coupling.

I start first by discussing the current literature regarding PCE11 in terms of its microstructural characterization and the importance of quantifying its aggregation properties. Then I show and discuss the experimental result. On the experimental side, I performed all the Raman spectroscopy measurements. I did the temperature dependent steady state optical spectroscopy measurements on the PCE11/HDPE blend film. Regarding the analysis, I performed FCA on the blend PCE11/HDPE PL measurements. I finally combined the extracted parameters from FCA of the neat PCE11 and blend PCE11/HDPE films with a new approach to validate the reliability of the results.

## 3.2 Microstructural characterization of PCE11

Microstructural properties of PCE11 have been extensively investigated using different scattering techniques (e.g. GIWAXS, SAXS, NAXS, etc...). Using such techniques, conclusions can be given about chain conformation changes in terms of its relation to the substrate (face-on, edge-on) or in terms of change in degree of crystallinity and molecular ordering. These microstructural properties have been investigated in terms of processing conditions [1] or acceptor addition [2]. The acceptor used was mainly PCBM [2] though there are also some reports including NFAs [3]. In general, most reports have shown that that the PCE11 film morphology in terms of phase separation and polymer

domain purity is insensitive to the type of fullerene used while it has an effect on the molecular packing and crystallinity of PCE11 [1, 2, 4].

It has been shown that for the PCE11, spin coating above and below the critical transition temperature  $T_c$  (the temperature at which chains transition from a non-aggregated to an aggregated state), we arrive at a film with roughly the same fraction of PCE11 polymer aggregates. However, these aggregates differ with respect to their interchain coupling, conjugation lengths and disorder leading to different film morphologies [5]. The importance of identifying the properties of the aggregate domains is related to its effect on the processes occurring in optoelectronic devices based on conjugated polymers such as organic photovoltaics (OPVs). The photoactive layers in such OPVs are usually a blend of electron donating (donor) and electron accepting (acceptor) organic materials forming what is called a bulk heterojunction (BHJ). In a thin film, these BHJs usually adopt semi-crystalline morphologies containing domains of both non-aggregated (amorphous) and more aggregated polymer chains. Changes in the nature of these domains affects the efficiency limiting processes of OPVs such as charge generation and transport [6, 7].

Contrary to the scattering techniques, which focus on long range order characterization, optical spectroscopy allows one to investigate short range order properties i.e. aggregate properties [8]. These aggregate properties can be extracted by applying different analysis approaches to the measured data such as FCA. However, while optical spectroscopy in general offers a valuable tool to extract this information in single component films, the situation is more complex in a PCE11 BHJ (and D-A polymers in general) for two reasons. Firstly, FCA of conjugated homopolymers such as P3HT can be carried out easily due to their well-structured optical spectra, allowing for reliable results [9, 10]. In contrast, PCE11 (and most state of the art D-A polymers) usually shows significantly less structured optical spectra, which makes it more complex to ensure reliable results from the FCA [4, 5]. Secondly, in a BHJ, the presence of two or more interacting materials leads to the rise of unwanted effects. For example, the formation of charge transfer states at the donor-acceptor interface leads to quenching of the PL of the individual compounds, thus hindering the analysis of the spectra. In addition, the presence of these several components can lead to them affecting the conformations of one another. For example, using scattering techniques, it has been shown that the presence of PCBM as an acceptor led to a change in the PCE11 conformation in the film [2]. Therefore, detailed investigations using optical spectroscopy on PC11 are limited. This includes the effect of blending on its conformation, its microstructure, and the affected aggregated domain properties.

To overcome the change in the optical spectra due to blending effects as mentioned above, we mimic the blend state by mixing PCE11 with the optically inert, insulating high-density polyethylene (HDPE). This PCE11:HDPE blend combination helps in avoiding quenching and charge transfer effects and relating changes in the optical spectra only to the microstructural changes as a function of blending. To address the issue of reliability of FCA on the rather unstructured optical aggregate spectra, we consider PL and absorption spectra measured at different temperatures in the range 5 – 300K. We then analyze the measured spectra using an approach that I will describe in detail in the FCA section. This approach provided a more reliable FCA for identifying the changes of the PCE11 aggregate properties upon blending with HDPE. The results suggest a more planarized chain conformation accompanied by less inter chain coupling and more order within the PCE11 aggregated domains as a function of blending.

### 3.3 Results

#### i. Sample preparation

Neat PCE11 and blend PCE11/HDPE thin films were deposited by *Giovanni Maria Matrone* from the *Imperial college in London* using a home built wire bar coater. The PCE11 used had  $M_n = 83000$  g/mol and PDI = 2.14. He prepared the active-layer solutions at 20 mg/ml in Orthodichlorobenzene (oDCB). Due to the polymers high molecular weight and the required high solution concentrations, solution preparation and deposition were done at high temperature and the prepared solutions were stirred for 30 minutes at 110 °C to make sure that the polymer is well dissolved and the solution is homogenous. Then, the films were directly deposited from the hot solutions on preheated heated glass substrates (100 °C) with a coating speed of 2 cm/s. The final thicknesses were 50 nm and 190 nm for neat PCE11 and blend PCE11:HDPE (50%:50%) films respectively.

#### ii. Raman Spectroscopy

I performed the Raman measurements using a commercial combined Raman-Imaging / Scanning Force Microscope System (WITEC ALPHA 300 RA+) at the *Macromolecular Chemistry II, University of Bayreuth* with the help of *Dr. Holger Schmalz*. I did all the measurements at room temperature with a 532 nm laser excitation (2.33 eV excitation energy) and 0.2 mW excitation intensity. The fluorescence background was removed using a B-spline function.

Figure 1 shows the chemical structure for PCE11 and HDPE along with the normalized Raman spectra for the neat PCE11 (black) and the blend PCE11/HDPE (red) films. Both films show the same peaks at  $430\text{ cm}^{-1}$ ,  $853\text{ cm}^{-1}$ ,  $1330\text{ cm}^{-1}$ ,  $1442\text{ cm}^{-1}$ ,  $1533\text{ cm}^{-1}$  and a collection of lower intensity peaks in the range  $1000\text{ cm}^{-1}$  -  $1200\text{ cm}^{-1}$ . I observed no shifts in the peak energies as a function of

blending. However, blending leads to a change of the relative peak intensities. Compared to the neat PCE11, the blend PCE11/HDPE film shows an increase in the relative intensities of the peaks at  $430\text{ cm}^{-1}$ ,  $853\text{ cm}^{-1}$  and  $1330\text{ cm}^{-1}$  with a concomitant decrease of the relative intensity of the peak at  $1533\text{ cm}^{-1}$ . The change in the relative intensities of the high-energy peaks is shown in more detail in the inset of figure 1.b, where the difference between the neat and the blend films is more apparent. The magnitude of this change is similar, as the peak at  $\approx 1330\text{ cm}^{-1}$  rises from 0.71 to 0.75, while the one at  $\approx 1533\text{ cm}^{-1}$  decreases from 0.62 to 0.58.

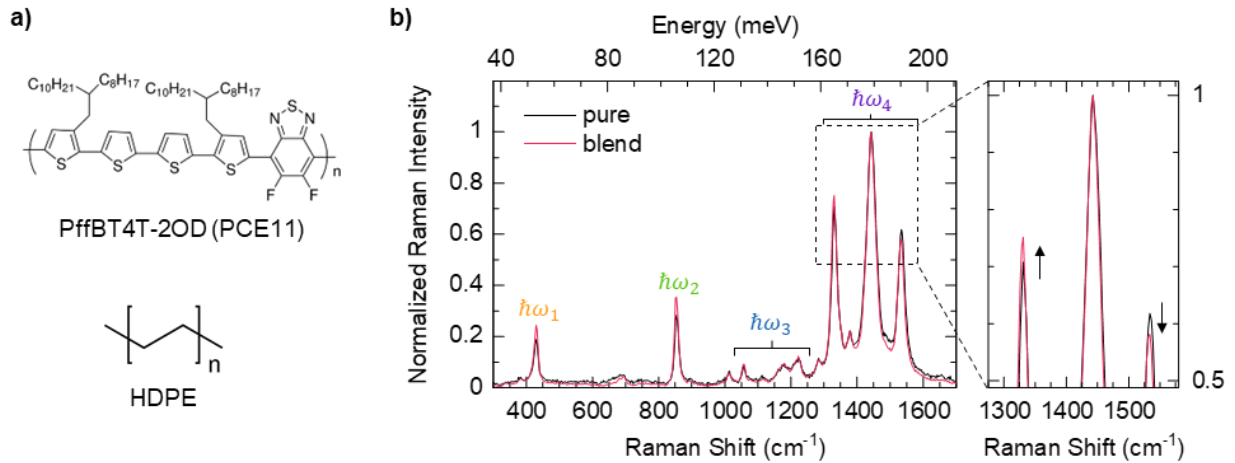


**Figure 1:** (a) Chemical structure of PffBT4T-2OD (PCE11) and high-density polyethylene (HDPE). (b) Normalized Raman spectra of the neat PCE11 film (black line) and the PCE11/HDPE blend (red line), excited at 2.33 eV. The inset shows a zoom-in of the three dominant Raman peaks of both samples.

For the purposes of the FCA - as will be discussed later - the different peaks were grouped into several effective modes. As shown in figure 1.b, the peaks at  $430\text{ cm}^{-1}$ ,  $853\text{ cm}^{-1}$  were treated individually as the two FCA modes  $\hbar\omega_1$  and  $\hbar\omega_2$  respectively. The collection of peaks in the range  $1000\text{ cm}^{-1}$  -  $1200\text{ cm}^{-1}$  were considered as one effective mode  $\hbar\omega_3$ . Finally, the three high-energy peaks were considered as one effective mode  $\hbar\omega_4$ . By comparing the energies of the different peaks to literature values [11-14], I was able to assign the observed peaks to the different phonon modes. The summary of this assignment is shown in table 1. For each peak, I show the Raman shift (peak energy) of the main peaks, the corresponding phonon mode (vibrational mode), its location on the polymer backbone and the corresponding FCA mode used in fitting the optical spectra.

To investigate the effect of the HDPE Raman spectrum on the observed changes in PCE11/HDPE relative peak intensities, I compared to the Raman spectrum of HDPE from literature. Figure 2 shows the Raman spectrum of HDPE [11]. The Raman peak assignment for the HDPE spectrum is also summarized in table 1. The most intense peaks appear at  $1132\text{ cm}^{-1}$ ,  $1067\text{ cm}^{-1}$ ,  $1299\text{ cm}^{-1}$  and  $1445\text{ cm}^{-1}$ .

**Table 1: Assignment of the peaks in the Raman spectra of PCE11 to the equivalent phonon modes and the characteristic phonon modes of HDPE [11-13]**

Material	Raman shift (cm <sup>-1</sup> )	Phonon Mode	Location	FCA Mode
PCE11	1533 (0.190 meV)	C–C aromatic stretch [12, 13]	BTD Unit	$\hbar\omega_4$
	1442 (0.179 meV)	C=C symmetric stretch [12, 13]	Thiophene Unit	$\hbar\omega_4$
	1330 (0.165 meV)	C=N stretch & C=N-S deformation [13]	BTD Unit	$\hbar\omega_4$
	1220 (0.151 meV)	C–C inter-ring stretch [12, 13]	Thiophene Unit	$\hbar\omega_3$
	1058 (0.131 meV)	C–H bending [12, 13]	Thiophene Unit	$\hbar\omega_3$
	853 (0.106 meV)	C–H out of plane bend [13]	BTD Unit	$\hbar\omega_2$
	430 (0.053 meV)	Ring deformation modes [12, 13]		$\hbar\omega_1$
HDPE	1445 & 1421	CH <sub>2</sub> bending [11]		
	1299	CH <sub>2</sub> twisting [11]		
	1132 & 1067	C–C stretching [11]		

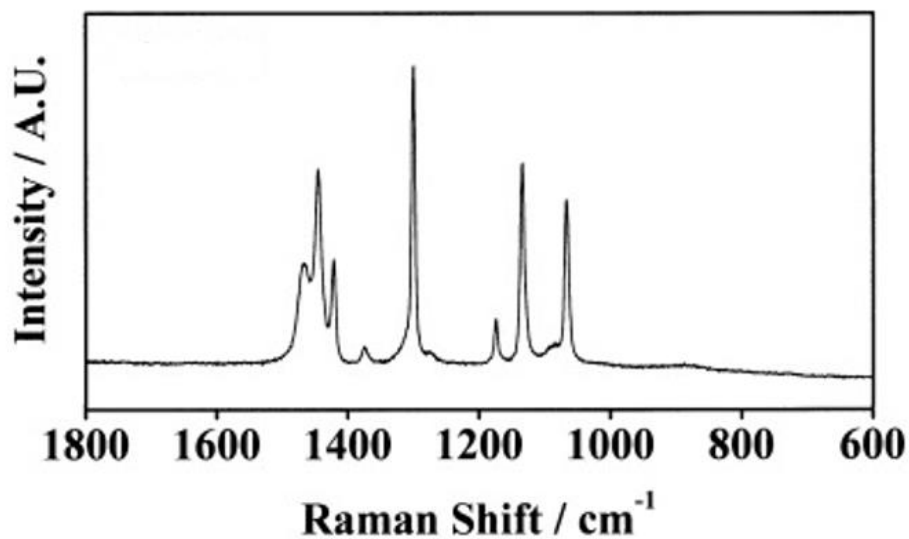


**Figure 2: Characteristic Raman spectrum of HDPE. Reproduced from [11]**

### iii. Temperature dependent steady state Spectroscopy

Konstantin Schötz and I measured the steady state optical spectra for both films. Figures 3 & 4 show the normalized PL and absorption spectra of both neat PCE11 and blend PCE11/HDPE films as a function of temperature between 5k and 300K respectively.

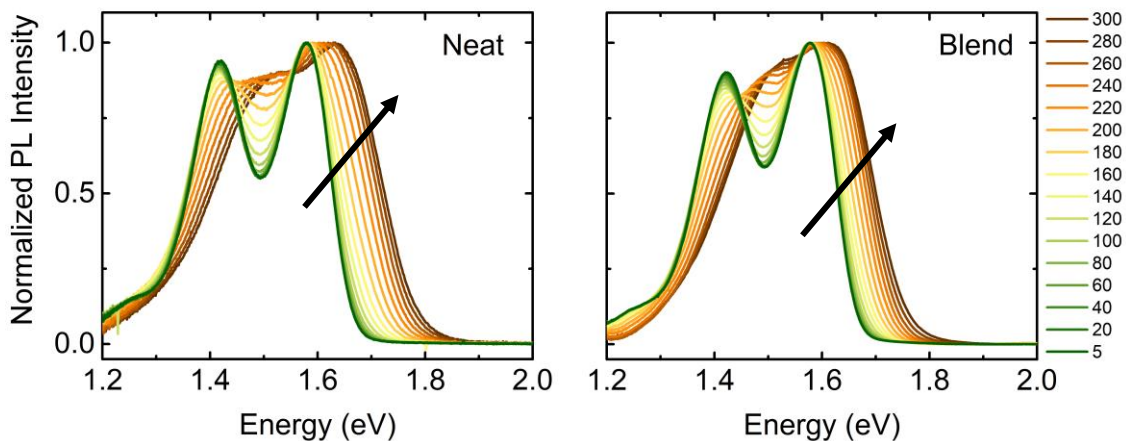


**Figure 3:** PL spectra of neat (left) PCE11 and blend PCE11/HDPE (right) films measured between 5 K & 300 K and normalized to unity at the 0-0 peak. The black arrow indicates the direction of increasing temperature.

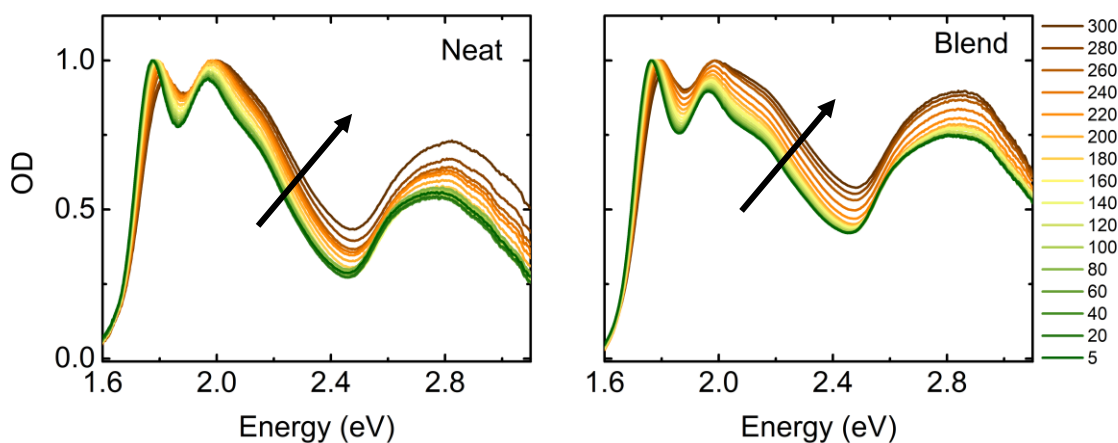


**Figure 4:** Normalized Abs spectra of neat PCE11 (left) and blend PCE11/HDPE (right) films measured between 5 K & 300 K. The black arrow indicates the direction of increasing temperature.

The absorption and PL spectra are mirror images of each other. Both spectra show the characteristic PCE11 0-0 and 0-1  $S_1 \rightarrow S_0$  transitions [4, 5]. In general, both films show a broadening of the spectra and a shift of the 0-0 and 0-1 transition peaks to higher energies as the temperature increases. For PL, at 5K, the spectra for both film are structured and well defined. They consist of the two main 0-0 and 0-1 transitions peaks located at 1.6 eV and 1.4 eV respectively [4, 5]. As the temperature is increased, the peak at 1.4 eV decreases in intensity relative to the peak at 1.6 eV accompanied by the shift of both peaks to higher energies. At 300K, we can still resolve the two peaks but accurately determining the exact position requires further analysis as the spectra become very broad. Concerning the absorption spectra, at 5K, the spectra for both films look similar insofar that the

two main 0-0 and 0-1 transition peaks are located at 1.7 eV and 1.97 eV respectively [4]. The peak at 1.7 eV has a higher intensity than the one at 1.97 eV. As we increase the temperature, we observe a reduction of the intensity of peak 1.7 eV relative to peak 1.97 eV, also accompanied by a shift of both peaks to higher energies. Finally, at 300 K, the peak at 1.97 eV has a higher intensity.

For ease of comparison between the neat and the blend films, I focus on the spectra of both films side by side at specific temperatures for both PL and Abs. This allows for a clearer description of how the spectra evolves as a function of temperature and the different trends as a function of blending. Figure 5 shows the normalized Abs and PL spectra of both films at 5K, 100K, 200K and 280K. The bottom panel in figure 5.a shows the PL spectra at 5 K for both the neat (black line) and the blend (red line) films. At this temperature, both spectra look similar for both films. As already mentioned, the 0-0 and 0-1 transition peaks ( $E_{0-0}$  and  $E_{0-1}$ ) are located at 1.6 eV and 1.4 eV respectively with no difference between the neat and the blend films. Compared to that of the blend film, the neat film shows a higher relative intensity of  $E_{0-1}$  (0.94 vs 0.89). As the temperature increases, we observe a broadening of the spectra and a shift of  $E_{0-0}$  to higher energies for both films.

Moving to the second panel showing the spectra at 100 K, the neat and blend film spectra still look similar albeit with a more reduction in the relative intensity of  $E_{0-1}$  in the blend film compared to the neat one (0.93 vs. 0.86). As shown in the 3<sup>rd</sup> panel at 200 K, this trend persists at higher temperatures accompanied by a broadening of both spectra. Because of the increase of the linewidth, the spectra appear more featureless for both films. Notably, the neat film spectrum appears broader than that of the blend film. Although at 200K the neat film spectra appears broader, in the 4<sup>th</sup> panel at 280 K, the onset of both spectra at the high-energy side gives the appearance of a similar the linewidths of both spectra (similar slope). However, the spectrum of the neat film extends over a larger energy range. Unfortunately, we cannot accurately identify the spectral positions of the 0-0 and the 0-1 peaks due to this increased linewidth. Hence, it is not straightforward to distinguish if the reason of this extended spectrum in the neat film is due to a larger linewidth than the blend film or due to an increased separation between the 0-0 and the 0-1 peaks. However, at this temperature  $E_{0-0}$  of the blend film is located at a lower energy (red shifted) than that of the neat film by  $\approx 16$  meV.

The absorption spectra of both films are shown in figure 5.b. At 5 K, for both films, as already mentioned, the 0-0 and 0-1 transition peaks ( $E_{0-0}$  and  $E_{0-1}$ ) are located around 1.7 eV and 1.97 eV respectively. Opposite to the corresponding PL spectrum at 5K,  $E_{0-0}$  of the blend film is shifted to lower energies (red shifted) compared to that of the neat film. The relative intensity of the 0-1 peak

is higher for the neat film (0.94) than the blend film (0.90). At higher temperatures, these differences persist, as both spectra broaden and shift to higher energies, albeit this spectral shift and broadening being not as pronounced as for the PL spectra.

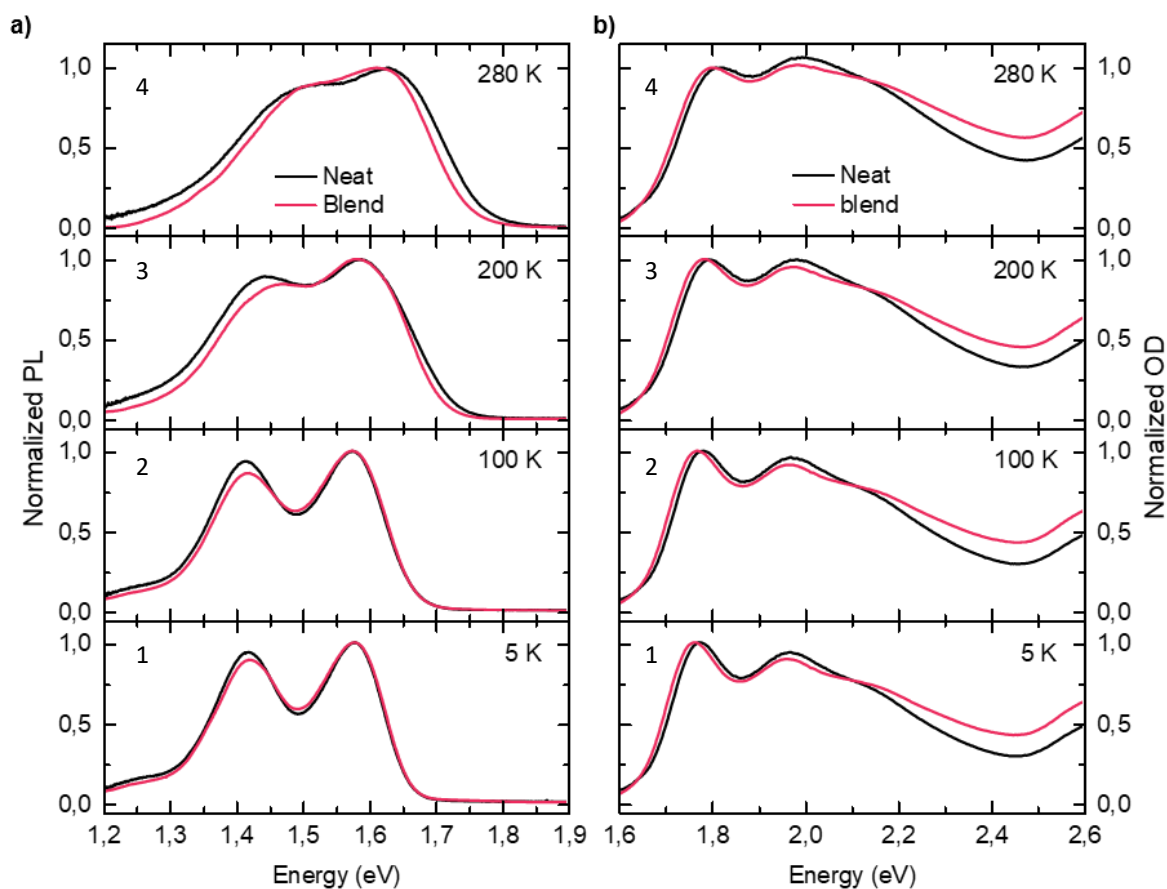


**Figure 5: Normalized PL (a) and absorption (b) spectra of the neat (black) and the blend (red) films at selected temperatures from figures 4 and 5.**

#### iv. Franck-Condon analysis (FCA)

The main difference between the absorption and PL spectra of PCE11 is due to the nature of the states that both probe. The PCE11 absorption spectrum typically contains contributions from both, non-aggregated and the aggregated chromophores. Figure 6 shows a measured absorption spectrum of spin coated neat PCE11 film showing the contribution of both the non-aggregate and aggregate phases which is in agreement with literature [4, 5]. This means that the absorption intensity around 2.4 eV observed in figures 5 & 6 can be attributed to absorption from the PCE11 non-aggregated chains.

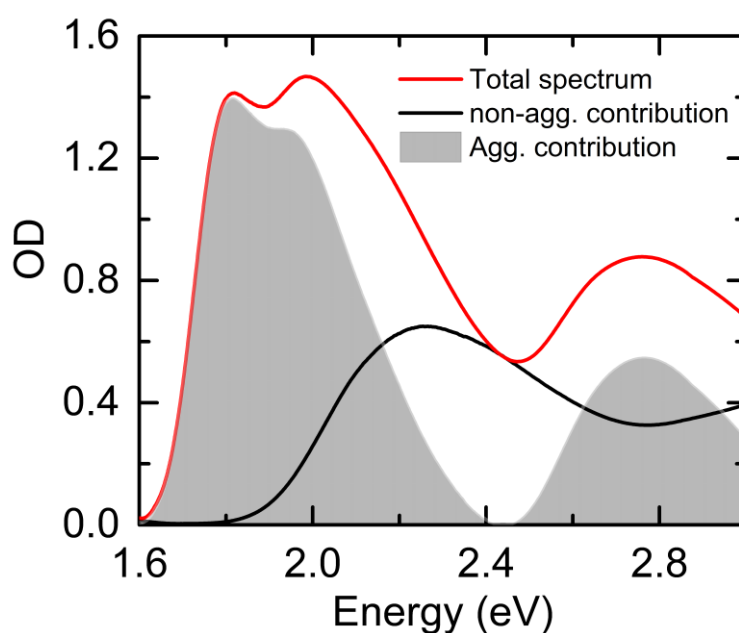


**Figure 6: Absorption spectrum of PCE11 film (red) showing both aggregated and non-aggregated phase contribution. The non-aggregated contribution shown in black is the measured PCE11 solution spectrum at high temperature (80°C) above the critical transition temperature (48°C) of PCE11. The grey area is the difference between the total spectrum and the non-aggregated spectrum and indicates the aggregate contribution to the absorption spectrum**

On the contrary, a feature from non-aggregated chains is not present in the PCE11 PL spectra, which can be simply explained by the fast and efficient energy transfer from the non-aggregated to the aggregated chromophores in a film. Therefore, contributions from aggregated chromophores dominate the emission spectra of PCE11. In general, it is well established that contributions from aggregated chromophores dominate the emission spectra of most semi-crystalline conjugated polymers [10, 14, 15].

Since I am mainly concerned by identifying changes on the aggregate properties of PCE11 as a function of blending, I focus on FCA. By fitting the measured optical spectra, it is possible to extract various material parameters such as the energetic disorder and molecular coupling strength which can be related to the PCE11 polymer chains conformation and aggregate properties. We thus focus on applying FCA on the PL spectra since no spectral deconvolution of non-aggregated and aggregated contributions is necessary which would be the case in absorption. Such deconvolution procedures can introduce artifacts and errors to the original measured spectra. Hence, the extracted parameters from FCA for PL will offer more reliable results than a similar analysis on the absorption spectra. To do this I fit the PL within the context of the weakly coupled H-aggregates

model using eq. 9 shown in chapter 1. Within the weakly coupled H-aggregates model, a factor  $\alpha$  is added to represent the strength of intermolecular interactions. It takes the values  $0 < \alpha < 1$ , where 0 means negligible interaction and 1 means maximum interaction. In homopolymers such as P3HT, usually it is possible to fit the spectra using FCA accurately using only one effective mode (usually the C–C stretching mode); applying the same approach to PCE11 is not possible (will be discussed later in figure 8). Hence, fitting the spectra of PCE11 using several modes extracted from the Raman measurements seems a reasonable approach. As mentioned earlier, the different peaks appearing in the Raman spectra of PCE11 were grouped into four effective modes. This choice was motivated by the integrated peak intensities as shown in figure 7.

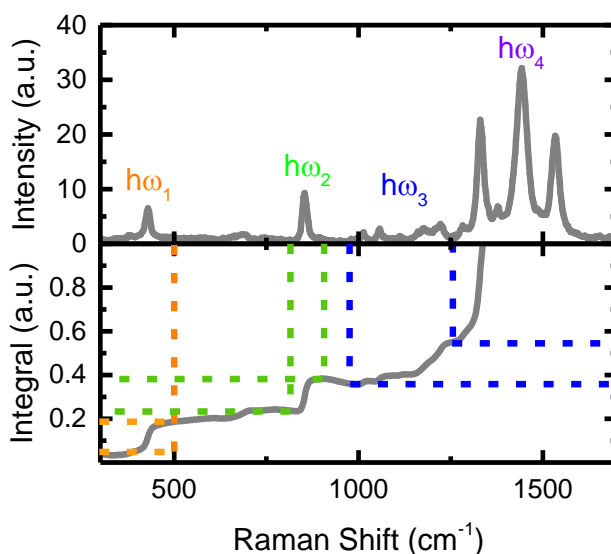


**Figure 7: Integrated Raman peak intensities calculated from the Raman spectra of the neat PCE11 film shown in figure 1a (Courtesy of Konstantin Schötz)**

The peaks at  $430 \text{ cm}^{-1}$ ,  $853 \text{ cm}^{-1}$  show similar integrated intensities and so we consider them as two separate FCA modes  $\hbar\omega_1$  (59 meV) and  $\hbar\omega_2$  (106 meV) respectively. In addition, the collection of peaks in the range  $1000 \text{ cm}^{-1} - 1200 \text{ cm}^{-1}$  show similar integrated intensity to  $\hbar\omega_1$  and  $\hbar\omega_2$  and so we considered them as one effective mode  $\hbar\omega_3$  at 135 meV which is the mean value of this range. Finally, due to their energetic proximity and comparable intensities we treated the three high-energy peaks at  $1330 \text{ cm}^{-1}$ ,  $1442 \text{ cm}^{-1}$  and  $1533 \text{ cm}^{-1}$  as one effective mode  $\hbar\omega_4$ . The starting value for this mode was an intensity-weighted average of the energies of these three high-energy. However, to account for the change in their relative intensities, the energetic position for this mode was allowed to shift as a function of temperature and blending.

However, applying FCA using several normal modes leads to another difficulty. As the PCE11 spectra is much broader and less structured than that of homopolymers, fitting the spectra using several effective modes has a high degree of freedom in the choice of the fitting parameter. In other words, by using the same four modes but interchanging all the various fitting parameter values during different fitting attempts, we are able to arrive to fits with sufficient quality. The varied parameters included the energetic position of the 0-0 peak ( $E_{0-0}$ ), the disorder parameter ( $\sigma_{PL}$ ), the molecular interaction parameter ( $\alpha$ ), the energetic position of the  $\hbar\omega_4$  mode, and the Huang-Rhys parameters for the 4 modes used in fitting the spectra.

Figure 8 shows two fitting attempts for the PL spectra of the blend film at 140 K. It can be readily seen that the fitting quality is nearly identical, although two different sets of all the parameters were used. This difference can be seen visibly by the different ratios of the peak intensity corresponding to the modes  $\hbar\omega_1 - \hbar\omega_4$ . The same variations arise for all the other fitting parameters albeit with different magnitudes. Table 2 shows the values of all the fitting parameters for the two fitting attempts that corresponds to the spectra shown on figure 9.

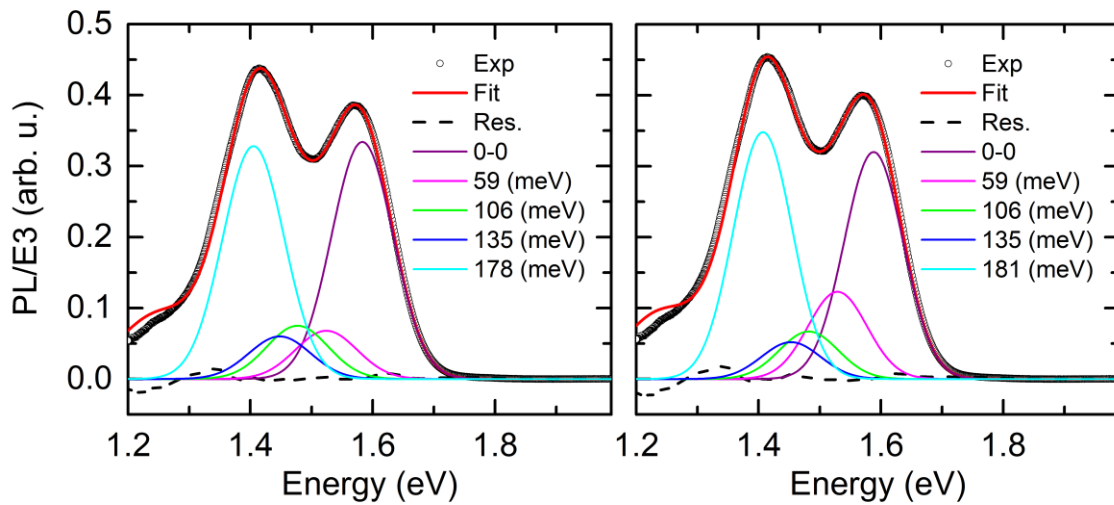


**Figure 8: Normalized PL spectra of Neat and Blend films measured between 5 K & 300 K. The hollow black circles show the measured data while the solid red line indicate the fitted spectra. The dashed black line shows the difference between the measured and fitted spectra. The other solid lines indicate the 0-0 peak (purple) and the different Raman modes used in fitting the PL spectra denoted by  $\hbar\omega_1 = 59$  meV (magenta),  $\hbar\omega_2 = 106$  meV (green),  $\hbar\omega_3 = 135$  meV (blue) and  $\hbar\omega_4$  taking the values of 178 meV & 181 meV for the two fitting attempts.**

Consequently, the following approach was adopted to our fitting procedure. Rather than fitting the spectra once, I performed several independent fitting attempts (five attempts) per temperature for both the neat and the blend films. I did the fitting of the blend film PL while *Konstantin Schötz* did

the fitting of the neat film PL. I then analyzed the fitting results as an average value of the five fitting attempt plus an error factor. This error factor reflects the range between the minimum and maximum parameter values within all the fitting attempts. Using this approach, I quantified the temperature dependence of the individual fitting parameters as well as the degree of their uncertainty (reliability).

**Table 2:** All the fitting parameters corresponding to two fitting attempts of the PCE11/HDPE film spectra at 140K. Fit 1 and Fit 2 correspond to the left and the right spectra in figure 9 respectively.

	$E_{0-0}$ (eV)	$\sigma$ (meV)	$\alpha$	$\hbar\omega_4$ (meV)	$S_1$	$S_2$	$S_3$	$S_4$
Fit 1	1.58	50.3	0.34	178	0.07	0.08	0.06	0.33
Fit 2	1.59	48.1	0.32	181	0.12	0.07	0.05	0.35

Figures 9 and 10 show representative Franck-Condon fits of the PL spectra of the blend PCE11 films at all the investigated temperatures. Figure 11 shows the different extracted parameters from FCA as a function of temperature for both the neat and the blend films. The black circles and red squares represent the mean value of the five fitting attempts for both the neat and the blend films respectively. The shaded areas around the dots represent the range between the minimum and maximum parameter values of the five fitting attempts. Moving forward, this is referred to as the error range.

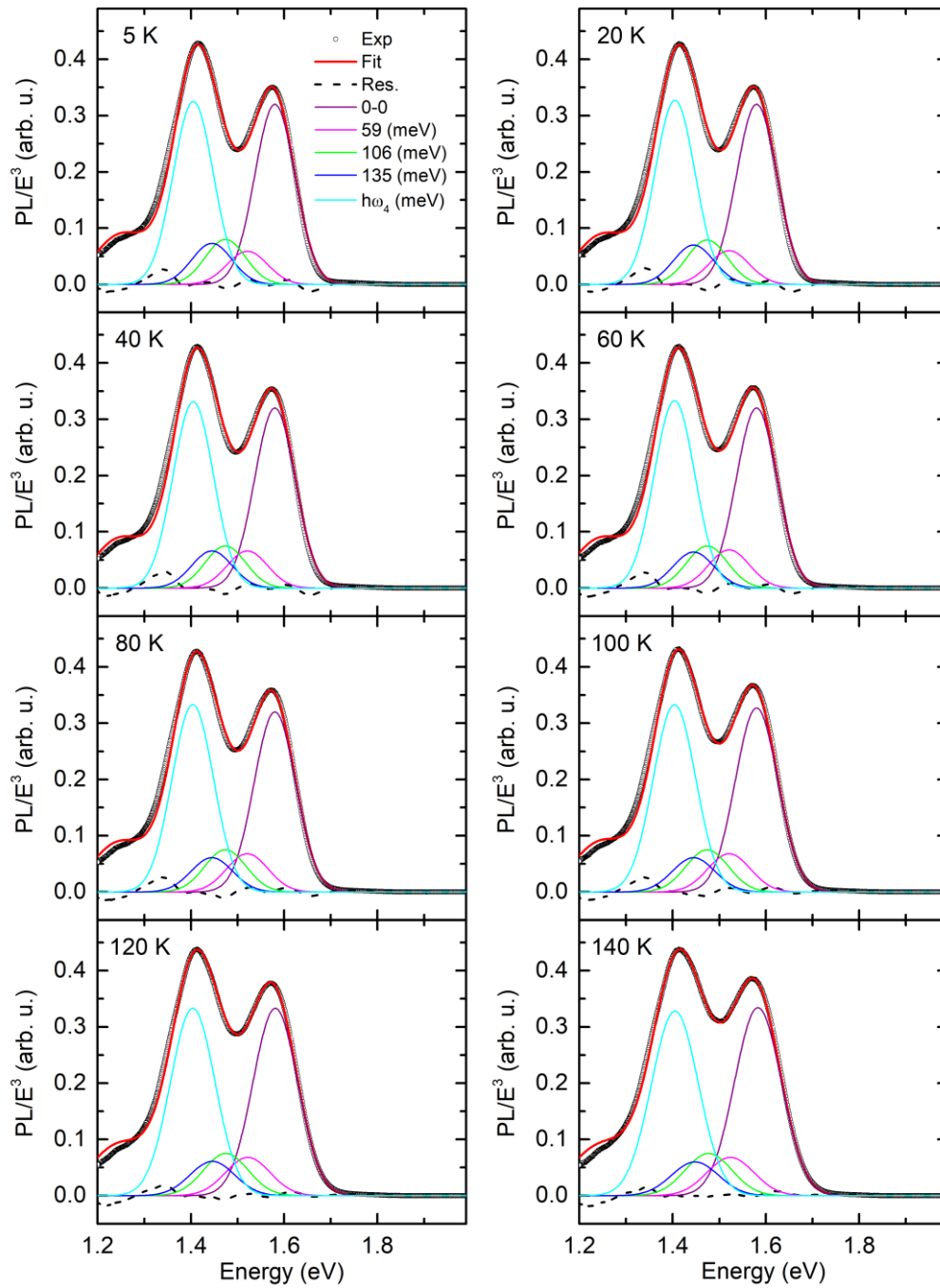


**Figure 9: Normalized PL spectra of the blend films measured between 5 K & 140 K. The hollow black circles show the measured data while the solid red line indicate the fitted spectra. The dashed black line shows the difference between the measured and fitted spectra. The other solid lines indicate the 0-0 peak (purple) and the different Raman modes used in fitting the PL spectra denoted by  $\hbar\omega_1 = 59$  meV (magenta),  $\hbar\omega_2 = 106$  meV (green),  $\hbar\omega_3 = 135$  meV (blue) and  $\hbar\omega_4$  (light blue) which is allowed to vary depending on temperature.**

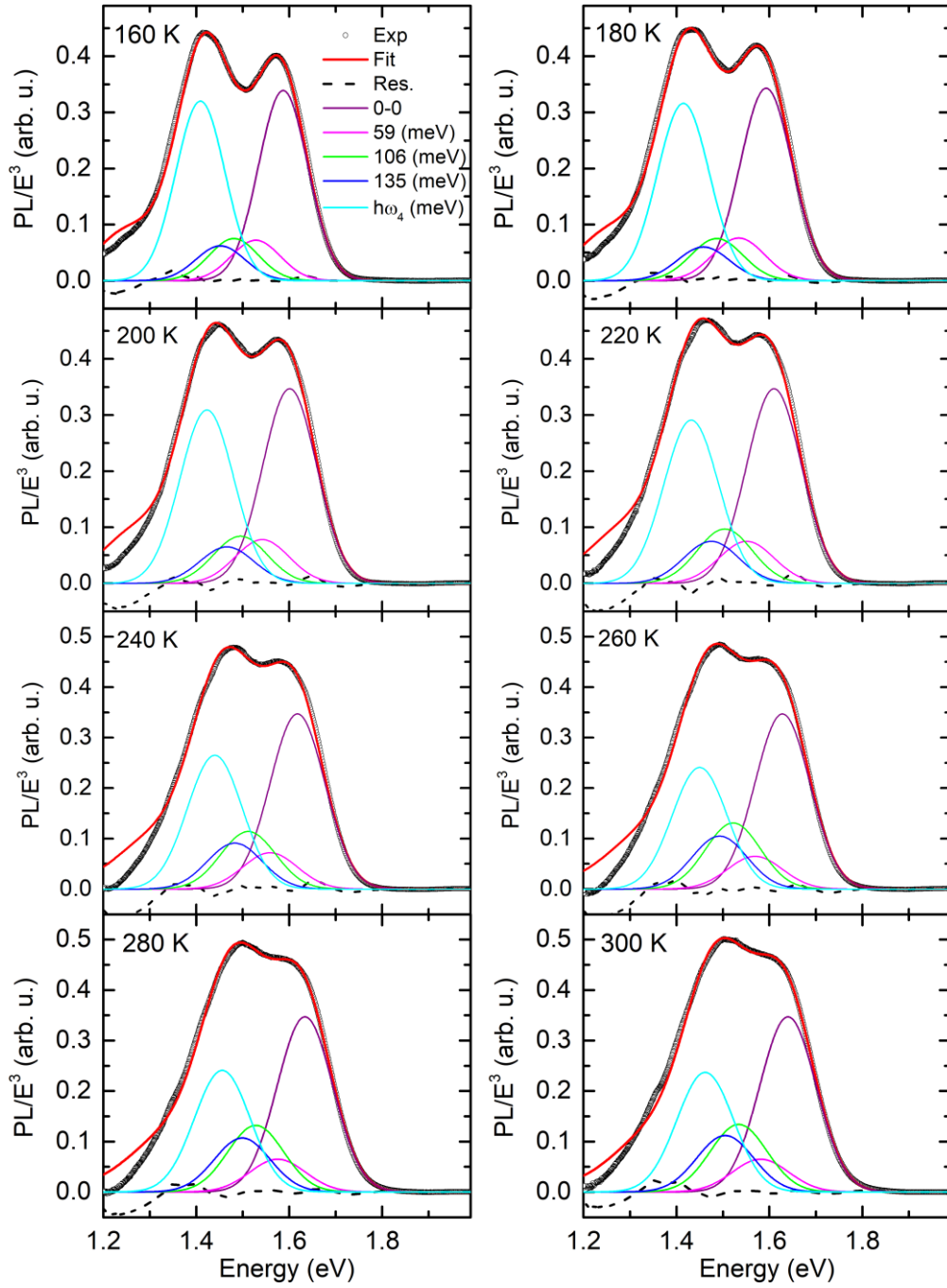


**Figure 10: Normalized PL spectra of the blend films measured between 160 K & 300 K. The hollow black circles show the measured data while the solid red line indicate the fitted spectra. The dashed black line shows the difference between the measured and fitted spectra. The other solid lines indicate the 0-0 peak (purple) and the different Raman modes used in fitting the PL spectra denoted by  $\hbar\omega_1 = 59$  meV (magenta),  $\hbar\omega_2 = 106$  meV (green),  $\hbar\omega_3 = 135$  meV (blue) and  $\hbar\omega_4$  (light blue) which is allowed to vary depending on temperature.**

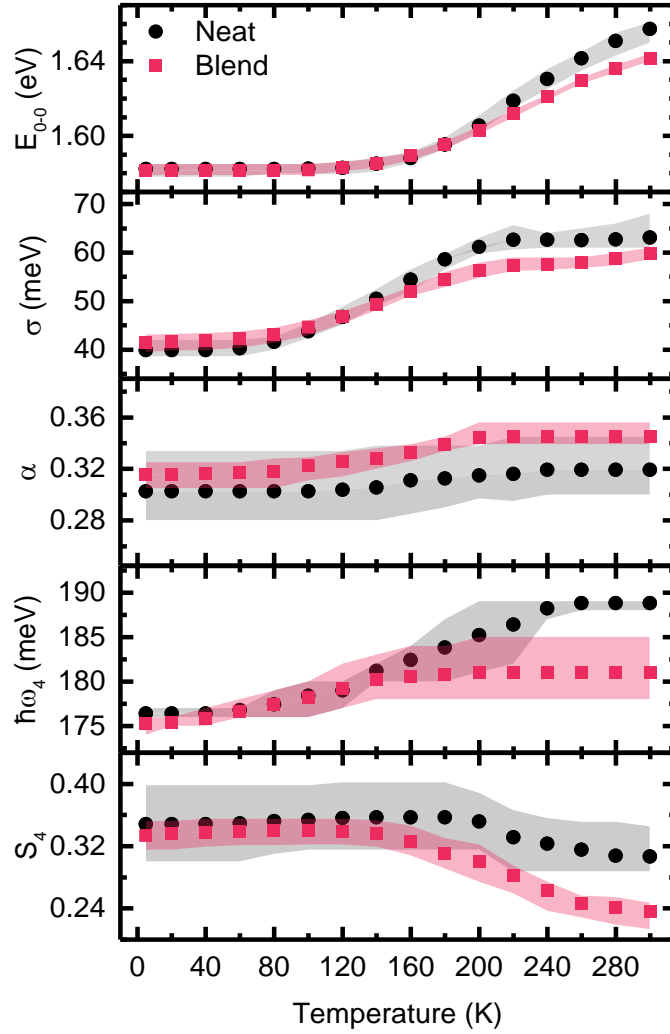


**Figure 11: Average value of FCA parameters extracted for the neat (black circles) and blend (red squares) films over the temperature range 5 K – 300 K. The black (neat film) and red (blend film) shaded areas represent the range between minimum and maximum values of 5 fitting attempts per temperature**

The upper two panels of figure 11 show the change in  $E_{0-0/PL}$  and  $\sigma_{PL}$  as a function of temperature. At 5K,  $E_{0-0/PL}$  is identical for both films ( $\approx 1.58$  eV) and stays constant until around 100 K. For higher temperatures,  $E_{0-0/PL}$  increases. This increase is more pronounced for the neat film, so that at room temperature,  $E_{0-0}$  of the neat film is higher by  $\approx 16$  meV compared to that of the blend film. Similar to  $E_{0-0/PL}$ , at 5 K,  $\sigma_{PL}$  is identical for both films ( $\approx 40$  meV) and stays constant until around 60 K. Between 60 K and 140 K  $\sigma_{PL}$  for both films increase with a similar magnitude. Above 140 K, the magnitude of this increase becomes different and the values for both films starts to deviate. At room temperature (300K),  $\sigma_{PL}$  of the neat film ( $\approx 63$  meV) is higher than  $\sigma_{PL}$  of the blend film ( $\approx 59$  meV). In general, for both  $\sigma_{PL}$  and  $E_{0-0/PL}$ , a small error range is observed. That makes the observed differences in values of  $\sigma_{PL}$  and  $E_{0-0/PL}$  between the neat and blend films significant within our

approach albeit seeming small. Consequently, small changes upon blending can be resolved reliably.

The third panel of figure 11 shows  $\alpha$  as a function of temperature. As mentioned earlier and in Chapter 2,  $\alpha$  is a measure of the intermolecular coupling strength between different polymer chains. At low temperatures,  $\alpha$  is slightly higher for the blend with 0.32 compared to the neat film with 0.30. With increasing temperature,  $\alpha$  increases slightly for both films, reaching 0.34 for the blend film and 0.32 for the neat film. However, the error range of  $\alpha$  overlap throughout the whole temperature range, so that this difference is not significant within our approach.

The mode associated with  $\hbar\omega_4$  shows the most significant changes in the Raman spectra as a function of blending and it dominates over all the other modes in terms of intensity (Figure 1b). Consequently, we concentrate on its temperature dependence. The bottom two panels of figure 11 show the energy ( $\hbar\omega_4$ ) and the Huang-Rhys parameter ( $S_4$ ) of this mode. At low temperatures,  $\hbar\omega_4$  is similar for both films with 176 meV and increases with temperature. Similar to  $E_{0-0}$  and  $\sigma$ , this increase is more pronounced for the neat film. While  $\hbar\omega_4$  of the blend film flattens around 140 K with a value of 181 meV, it increases further for the neat film to  $\approx 189$  meV at room temperature. It is worth noting that despite the wide error ranges of  $\hbar\omega_4$  for both films, they do not overlap.  $S_4$  is nearly constant with approx. 0.35 for both films up to  $\approx 140$  K. Above 140 K,  $S_4$  starts to decrease for both films. Opposite to the changes in  $\hbar\omega_4$ , this decrease is more pronounced for the blend film, leading to a lower  $S_4$ . At 300 K, for the blend film,  $S_4 \approx 0.24$  is much lower than that of the neat film with  $S_4 \approx 0.31$ . Again, the error ranges of  $S_4$  do not overlap at higher temperatures. Therefore, the observed differences in values of  $\hbar\omega_4$  and  $S_4$  between the neat and blend films are significant within our approach.

Since absorption and PL probes different parts of the material's DOS, comparing the fitting parameters extracted from applying FCA on both would offer more insights. Moreover, as the error ranges of  $\sigma_{\text{PL}}$  and  $E_{0-0/\text{PL}}$  are small compared to the other parameters; we focus on their absorption counterparts ( $\sigma_{\text{ABS}}$  and  $E_{0-0/\text{ABS}}$ ) extracted from one fitting attempt. Figure 12 shows  $\sigma_{\text{ABS}}$  and  $E_{0-0/\text{ABS}}$  of the absorption spectra as a function of temperature.  $\sigma_{\text{ABS}}$  is nearly identical for both films throughout the whole temperature range. It increases continuously from 52 meV at 5 K to 64 meV at RT.  $E_{0-0/\text{ABS}}$  shows a similar temperature trend as  $\sigma_{\text{ABS}}$ , starting at 1.76 eV at 5 K and increasing to 1.78 eV at room temperature for the case of the blend film.  $E_{0-0/\text{ABS}}$  of the neat film is consistently  $\approx 12$  meV higher. This agrees with our observations from the temperature dependent absorption spectra.

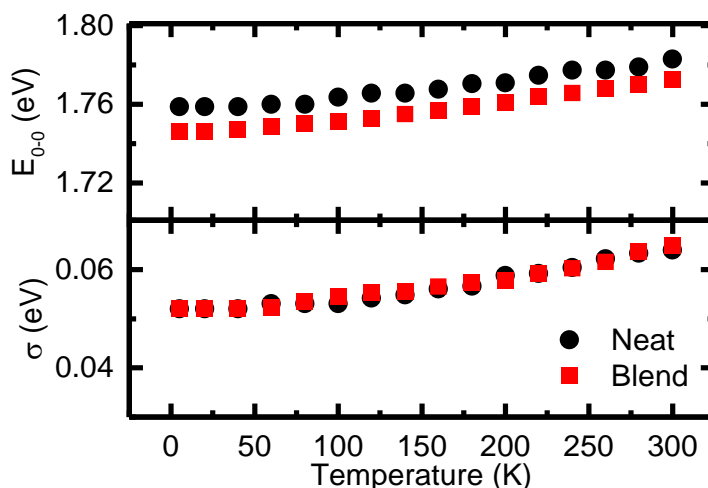


**Figure 12:**  $\sigma_{ABS}$  and  $E_{0-0/ABS}$  extracted from FCA of the neat (black circles) and the blend (red squares) films over the temperature range 5 K – 300 K.

Summarizing the effect of blending on the mean values of  $E_{0-0}$  and  $\sigma$  for both neat and blend films extracted from fitting the absorption and PL spectra, we observe different behaviors.  $E_{0-0/ABS}$  (neat) is  $\approx 12$  meV higher than  $E_{0-0/ABS}$  (blend) over the whole temperature range while for PL, at 5K,  $E_{0-0/PL}$  (neat)  $\approx E_{0-0/PL}$  (blend). They deviate at higher temperatures so that at 300K,  $E_{0-0/PL}$  (neat) is  $\approx 16$  meV higher than  $E_{0-0/PL}$  (blend). At 5k,  $\sigma_{PL}$  (both neat and blend)  $< \sigma_{ABS}$  (both neat and blend) by  $\approx 10$  meV (42 meV vs 52 meV) while at 300k,  $\sigma_{PL}$  (neat)  $\approx \sigma_{ABS}$  (neat and blend)  $> \sigma_{PL}$  (blend) (64 meV vs 59 meV).

### 3.3 Discussion

Raman spectroscopy as a probe for studying microstructure of conjugated polymers has been already established as a powerful technique. Changes of molecular order was related to the shift of the Raman peak positions and to change in their relative intensities or FWHM. In P3HT, the increase in intensity of the C-C intra-ring stretching mode ( $1380\text{ cm}^{-1}$ ) relative to the C=C symmetric stretching mode ( $1440\text{ cm}^{-1}$ ) was a sign of increased chain planarity. This was due to the relation of these phonon modes to the  $\pi$ -electron delocalization, where this change indicated an increased  $\pi$ -electrons density on C-C (increased CT from C=C). Consequently, the ordered P3HT phase was identified by longer conjugation length with a more planar chain conformation compared to the disordered phase [16-19]. Similar approaches were taken to analyze the Raman spectra of donor-acceptor polymers. In the F8BT polymer consisting of an F8 acceptor unit and BT (Benzothiadiazole) donor unit, the two main Raman phonon modes were assigned to the F8 ring-stretching mode ( $1608\text{ cm}^{-1}$ ) and the C-C stretching mode ( $1357\text{ cm}^{-1}$ ) on the BT unit. Several studies showed that

the decrease of  $I_{1357}/I_{1608}$ , indicated a decrease in the torsion angle between F8 and BT units, i.e. the polymer backbones adopt a more planar conformation. This was explained based on a weaker electronic coupling between the BT and F8 units along the conjugated backbone in a more twisted conformation (lower intra-chain coupling) [19-22]. These studies, based on both experiments and calculations as shown in figure 13, showed that the tendency of the polymer chains to planarize under different conditions is characterized by a reduction in the intensity of the Raman peaks originating from donor unit phonon modes relative to those originating from the acceptor unit.

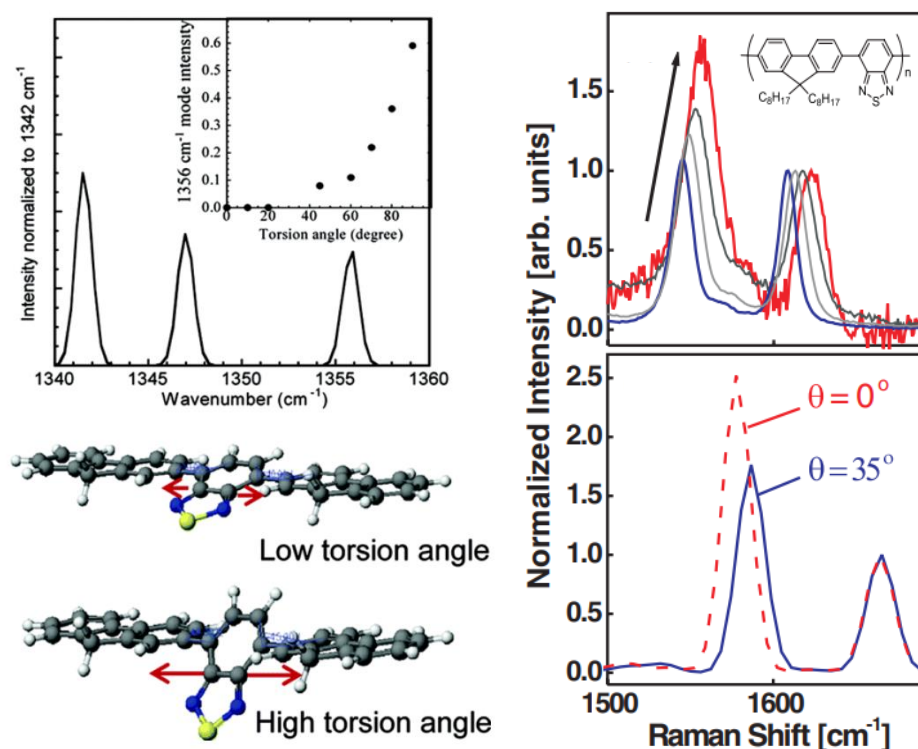


**Figure 13:** Calculated Raman spectra of F8BT as a function of the torsional angle between the F8 donor and BT acceptor units along the polymer's backbone (left). Reproduced from [20]. Measured Raman spectra (top right) as a function of increasing pressure as indicated by the black arrow. Reproduced from [21]. Calculated Raman spectra for an F8-BT-F8 unit at two different torsional angles (0 °C & 35 °C) (bottom right). Reproduced from [21].

The above results concur with our measured Raman spectra on neat and blend PCE11 (having a similar structure and the same acceptor unit as F8BT). It can then be concluded that blending of PCE11 leads to a reduction in the torsion angle between the adjacent donor and acceptor units along the polymer backbone and hence the formation of aggregates with more planarized and longer conjugated chains in the final film. Nevertheless, the role of HDPE in the changes observed in the PCE11/HDPE blend Raman spectra should be also ruled-out to confirm that these changes

are indeed a result of conformational changes of the PCE11 polymer chains. Figure 14 shows a staggered plot of the PCE11 neat Raman spectrum and the HDPE Raman spectrum from literature. On one hand, no peak shifts is observed in the PCE11/HDPE blend film spectrum within the regions of the intense HDPE Raman peaks. This is indicated by both the blue and yellow regions in figure 14. If an impact of HDPE was present we would have observed some shifts in the peak positions in the PCE11/HDPE blend film Raman spectrum within these regions. On the other hand, some changes in the relative peak intensities in the PCE11/HDPE blend film compared to the PCE11 neat film are observed in regions beyond the Raman spectrum of neat HDPE (green region). While in regions with significant Raman intensity of HDPE (yellow region) no changes in the relative peak intensities in the PCE11/HDPE blend film are observed.

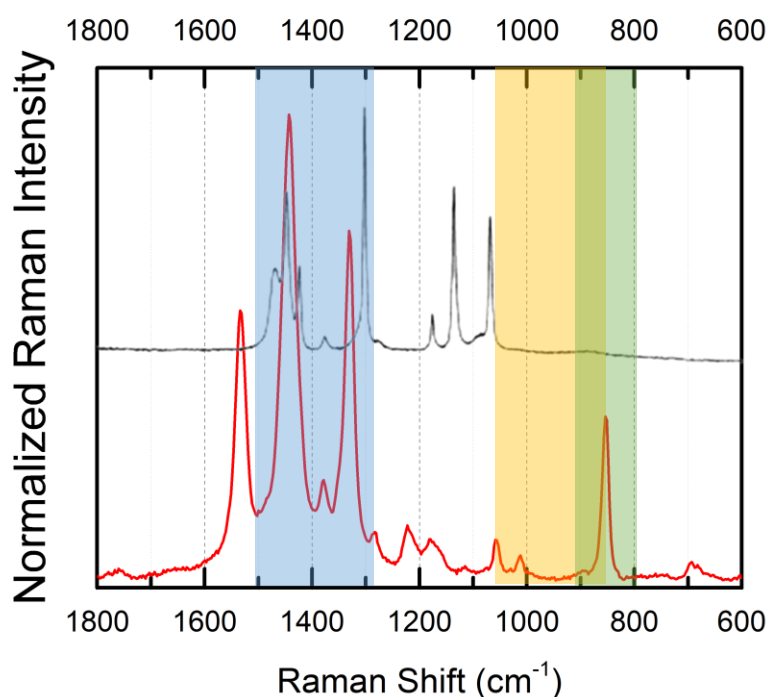


**Figure 14:** Staggered plot of the measured neat PCE11 Raman spectrum (red) and the HDPE Raman spectrum (black) from literature [11].

Combining all the above observation, I concluded that the contribution of the HDPE modes in the Raman spectrum of the blend is negligible, and the observed change in the relative intensities upon blending is indeed due to structural changes of the PCE11 polymer chains. This is to be expected, due to the large Raman cross section of conjugated polymers compared to non-conjugated polymers. The large Raman cross section of conjugated polymers stems from the coupling of the phonon modes to the  $\pi$ - $\pi^*$  electronic excitations as already explained in chapter 2 [23, 24].

This conclusion is further strengthened by the observed changes in the absorption and PL spectra. It is well established that planarization of the polymer chains (increased conjugation) is reflected in the absorption spectra by a red shift of the 0-0 transition peak and a reduction in the intensity of the 0-1 transition peak relative to the 0-0 transition peak (i.e. reduction of  $I_{0-0}/I_{0-1}$ ) [25]. We observe those two behaviors in the measured absorption spectra over the whole temperature range.

Having this conclusion in mind, we then proceed further by analyzing the dependence of the parameters extracted from FCA on both temperature and blending. This would offer more insights about the changes in the molecular coupling strength and disorder in the final film aggregates. In steady state PL, the emission comes from those states at the bottom of the Gaussian DOS after relaxation. On contrary, absorption takes place to any chromophore within the DOS. Because of this, we observe a difference between the 0-0 transition of PL and absorption. Analyzing this in the frame of spectral diffusion [26], allows us to investigate the effect of blending on the temperature behavior on the transfer of the excited states within the DOS. This can then be related for example to energetic disorder and conjugation length. At high temperatures (compared to the width of the Gaussian DOS), i.e.  $\sigma/KT \leq 3$ , emission happens after relaxation of the excited states to the quasi-equilibrium energy  $\Delta\varepsilon = -\sigma^2/KT$ . Consequently, emission happens from states with a lifetime near the intrinsic lifetime i.e. emitting from the quasi-equilibrium energy states [26]. Upon lowering the temperature, we would observe a red shift of the PL spectrum until it becomes constant at temperatures where the excited states need more time to arrive at this quasi-equilibrium level than the intrinsic lifetime itself [26].

From figure 11, we observed this behavior with the red shift of  $E_{0-0}$  for both the neat and blend films between 300 K and 140 K. Below 140K the position becomes constant and identical for both films. This can be confirmed quantitatively by plotting  $\Delta\varepsilon/\sigma$  as a function of  $K_B T/\sigma$  and comparing with the expected behavior from the spectral diffusion model [26, 27]. This is shown in figure 15 where  $\sigma_{PL}$  is used and  $\Delta\varepsilon$  is taken as the difference between  $E_{0-0/PL}$  and  $E_{0-0/ABS}$ . For  $K_B T/\sigma > 0.25$  the behavior of both the neat and blend films is in accordance with the expectation from the spectral diffusion model. While for  $K_B T/\sigma < 0.25$  we observe the flattening of the curve as expected since the excitations decay before reaching the equilibrium value [26].

Thus, I can conclude that the temperature-dependent changes of  $E_{0-0/PL}$  and  $\sigma_{PL}$  that we observe for both the neat and blend films are due to spectral diffusion of the excited states within the DOS. In addition, while the blend has less energetically disordered aggregated domains as observed by the lower  $\sigma_{PL}$  of the blend film at higher temperatures, the whole DOS (as probed by absorption) is not

affected by blending as  $\sigma_{\text{ABS}}$  is identical for both the neat and blend films over the whole temperature range.

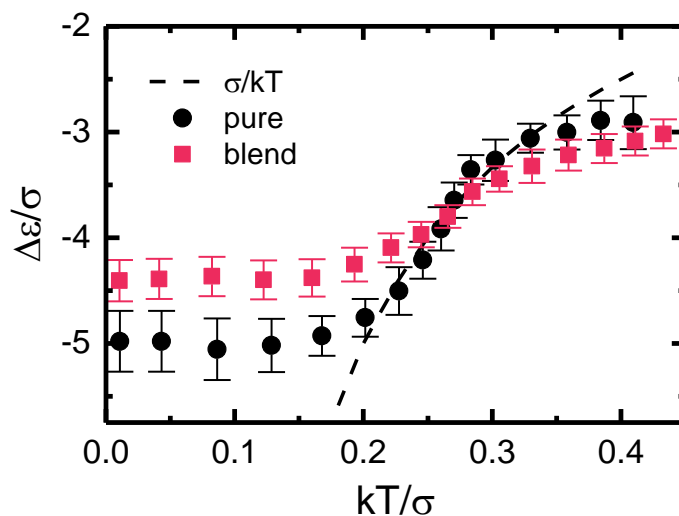


**Figure 15:**  $\Delta\varepsilon/\sigma$  vs.  $K_B T/\sigma$  for neat PCE11 (black circles) and blend PCE11/HDPE (red squares) films with the expected curve from the spectral diffusion model (black dashed lines).

Having established this, one can move further with investigating the blending effect on the other parameters. Following the weakly interacting H-aggregate model,  $\alpha$  as a measure of the 0-0 peak suppression in PL is a reflection of changes in either disorder or molecular coupling strength. An increased  $\alpha$  indicates a reduced molecular coupling strength between different polymer chains (reduced inter-chain coupling)[25]. Upon blending of PCE11, we observe higher  $\alpha$  value along with a reduction of  $\sigma_{\text{PL}}$  (blend) over the temperature ranges above 140 K. From this, we can conclude that when blending, the observed suppression of the 0-0 peak in PL is a result of reduced interchain coupling of the PCE11 chains. This reduced inter-chain coupling upon blending hints towards a more delocalized  $\pi$  electron cloud over the conjugated polymer planes. This is consistent with the above conclusion that blending leads to a more planarized PCE11 chains.

Finally, analyzing the characteristics of the  $\hbar\omega_4$ , we readily observe the consistency between its values and the observed changes from the Raman spectra. The reduction of  $\hbar\omega_4$  of the blend film compared to the neat film reflects the relative change in intensity of the three high-energy peaks of this mode upon blending. In addition, this shift of  $\hbar\omega_4$  for the neat film to higher values at higher temperature explains the apparent broadness of the neat film PL compared to that of the blend. This more apparent broadness is mainly due to an increased separation between 0-0 and 0-1 transition peaks of the PL rather than the difference in the disorder between the two films. This is

confirmed by observing the PL spectra of both neat and blend films at 200 K (figure 6.a). Despite having similar disorder values, the neat film PL spectrum appears broader than the blend counterpart does. Furthermore, it has been shown that the Huang-Rhys parameter is inversely proportional to the number of monomers along the conjugated chain, where lower Huang-Rhys parameter indicates higher conjugation and vice-versa [28]. For PCE11, we observe a reduction in  $S_4$  for the blend film. This indicates higher conjugation and hence further confirms the more planarized PCE11 chains in the aggregates of the blend film.

### 3.5 Conclusion & Outlook

In conclusion, I investigated the effect of blending on the conformational changes within the aggregate domains of the donor-acceptor type polymer PCE11 in collaboration with **Konstantin Schötz**. Analyzing the temperature-dependent optical spectra in terms of the spectral diffusion model, we found that the behavior of  $E_{0-0}$  and  $\sigma_{PL}$  agrees with the model in both the neat and blend films. In contrast, the effect of the blending was reflected in the changes of the optical spectra and the extracted FCA parameters between neat and blend PCE11 film. These changes suggested that blending results in a more planarized, longer conjugated PCE11 chains with a reduced degree of interchain molecular coupling. This is an agreement with the observed differences of the Raman spectra of the neat and the blend film. The changes in the relative intensities ratio of the donor specific and the acceptor specific phonon modes were reflected in the PL spectra by a reduced energy of the effective mode  $\hbar\omega_4$  containing both contributions.

Thus, this work shows experimentally how changes in the Raman mode characteristics of conjugated polymers are closely related to changes appearing in the optical spectra. Taking this idea a step further, temperature dependent Raman spectrum can be compared to the temperature dependent optical spectra to explore if this correspondence is consistent at a wide temperature range. In addition, this work shows the importance of the detailed Frank Condon analyses by which one can extract detailed information about the microstructural changes of donor-acceptor-type conjugated polymers in different environments.

## References

- [1] W. Ma, G.F. Yang, K. Jiang, J.H. Carpenter, Y. Wu, X.Y. Meng, T. McAfee, J.B. Zhao, C.H. Zhu, C. Wang, H. Ade, H. Yan, Influence of Processing Parameters and Molecular Weight on the Morphology and Properties of High-Performance PffBT4T-2OD:PC71BM Organic Solar Cells, *Adv Energy Mater*, 5 (2015).
- [2] Y.W. Zhang, A.J. Parnell, O. Blaszczyk, A.J. Musser, I.D.W. Samuel, D.G. Lidzey, G. Bernardo, Effect of fullerene acceptor on the performance of solar cells based on PffBT4T-2OD, *Phys Chem Chem Phys*, 20 (2018) 19023-19029.
- [3] H. Cha, S. Wheeler, S. Holliday, S.D. Dimitrov, A. Wadsworth, H.H. Lee, D. Baran, I. McCulloch, J.R. Durrant, Influence of Blend Morphology and Energetics on Charge Separation and Recombination Dynamics in Organic Solar Cells Incorporating a Nonfullerene Acceptor, *Adv Funct Mater*, 28 (2018).
- [4] Y.H. Liu, J.B. Zhao, Z.K. Li, C. Mu, W. Ma, H.W. Hu, K. Jiang, H.R. Lin, H. Ade, H. Yan, Aggregation and morphology control enables multiple cases of high-efficiency polymer solar cells, *Nat Commun*, 5 (2014).
- [5] M. Reichenberger, D. Kroh, G.M.M. Matrone, K. Schotz, S. Proller, O. Filonik, M.E. Thordardottir, E.M. Herzig, H. Bässler, N. Stingelin, A. Köhler, Controlling aggregate formation in conjugated polymers by spin-coating below the critical temperature of the disorder-order transition, *J Polym Sci Pol Phys*, 56 (2018) 532-542.
- [6] C. Schwarz, S. Tscheuschner, J. Frisch, S. Winkler, N. Koch, H. Bässler, A. Köhler, Role of the effective mass and interfacial dipoles on exciton dissociation in organic donor-acceptor solar cells, *Phys Rev B*, 87 (2013).
- [7] Y. Tamai, Delocalization boosts charge separation in organic solar cells, *Polym J*, 52 (2020) 691-700.
- [8] A. Salleo, R.J. Kline, D.M. DeLongchamp, M.L. Chabinyc, Microstructural Characterization and Charge Transport in Thin Films of Conjugated Polymers, *Adv Mater*, 22 (2010) 3812-3838.
- [9] F. Panzer, M. Sommer, H. Bässler, M. Thelakkat, A. Köhler, Spectroscopic Signature of Two Distinct H-Aggregate Species in Poly(3-hexylthiophene), *Macromolecules*, 48 (2015) 1543-1553.
- [10] A.L.T. Khan, P. Sreearunothai, L.M. Herz, M.J. Banach, A. Köhler, Morphology-dependent energy transfer within polyfluorene thin films, *Phys Rev B*, 69 (2004).
- [11] H. Sato, M. Shimoyama, T. Kamiya, T. Amari, S. Sasic, T. Ninomiya, H.W. Siesler, Y. Ozaki, Raman spectra of high-density, low-density, and linear low-density polyethylene pellets and prediction of their physical properties by multivariate data analysis, *J Appl Polym Sci*, 86 (2002) 443-448.
- [12] K. Kotwica, E. Kurach, G. Louarn, A.S. Kostyuchenko, A.S. Fisyuk, M. Zagorska, A. Pron, Alternating copolymers of thiadiazole and quaterthiophenes - Synthesis, electrochemical and spectroelectrochemical characterization, *Electrochim Acta*, 111 (2013) 491-498.
- [13] M. Gora, W. Krzywiec, J. Mieczkowski, E.C.R. Maia, G. Louarn, M. Zagorska, A. Pron, Alternating copolymers of diketopyrrolopyrrole or benzothiadiazole and alkoxy-substituted oligothiophenes: spectroscopic, electrochemical and spectroelectrochemical investigations, *Electrochim Acta*, 144 (2014) 211-220.
- [14] T. Unger, F. Panzer, C. Consani, F. Koch, T. Brixner, H. Bässler, A. Köhler, Ultrafast Energy Transfer between Disordered and Highly Planarized Chains of Poly[2-methoxy-5-(2-ethylhexyloxy)-1,4-phenylenevinylene] (MEH-PPV), *Acs Macro Lett*, 4 (2015) 412-416.

- [15] F. Panzer, H. Bässler, A. Köhler, Temperature Induced Order-Disorder Transition in Solutions of Conjugated Polymers Probed by Optical Spectroscopy, *J Phys Chem Lett*, 8 (2017) 114-125.
- [16] Y.Q. Gao, J.K. Grey, Resonance Chemical Imaging of Polythiophene/Fullerene Photovoltaic Thin Films: Mapping Morphology-Dependent Aggregated and Unaggregated C=C Species, *J Am Chem Soc*, 131 (2009) 9654-9662.
- [17] W.C. Tsoi, D.T. James, J.S. Kim, P.G. Nicholson, C.E. Murphy, D.D.C. Bradley, J. Nelson, J.S. Kim, The Nature of In-Plane Skeleton Raman Modes of P3HT and Their Correlation to the Degree of Molecular Order in P3HT:PCBM Blend Thin Films, *J Am Chem Soc*, 133 (2011) 9834-9843.
- [18] J.K. Grey, Resonance Raman Spectroscopy and Imaging of Franck-Condon Vibrational Activity and Morphology in Conjugated Polymers for Solar Cells, *Accounts Chem Res*, 52 (2019) 2221-2231.
- [19] J.J. Yun, J. Peet, N.S. Cho, G.C. Bazan, S.J. Lee, M. Moskovits, Insight into the Raman shifts and optical absorption changes upon annealing polymer/fullerene solar cells, *Appl Phys Lett*, 92 (2008).
- [20] C.L. Donley, J. Zaumseil, J.W. Andreasen, M.M. Nielsen, H. Sirringhaus, R.H. Friend, J.S. Kim, Effects of packing structure on the optoelectronic and charge transport properties in poly(9,9-di-n-octylfluorene-alt-benzothiadiazole), *J Am Chem Soc*, 127 (2005) 12890-12899.
- [21] J.P. Schmidtke, J.S. Kim, J. Gierschner, C. Silva, R.H. Friend, Optical spectroscopy of a polyfluorene copolymer at high pressure: Intra- and intermolecular interactions, *Phys Rev Lett*, 99 (2007).
- [22] J.M. Winfield, C.L. Donley, R.H. Friend, J.S. Kim, Probing thin-film morphology of conjugated polymers by Raman spectroscopy, *J Appl Phys*, 107 (2010).
- [23] J.S. Kim, P.K.H. Ho, C.E. Murphy, N. Baynes, R.H. Friend, Nature of non-emissive black spots in polymer light-emitting diodes by in-situ micro-Raman spectroscopy, *Adv Mater*, 14 (2002) 206-+.
- [24] S. Wood, J.R. Hollis, J.S. Kim, Raman spectroscopy as an advanced structural nanoprobe for conjugated molecular semiconductors, *J Phys D Appl Phys*, 50 (2017).
- [25] F.C. Spano, The Spectral Signatures of Frenkel Polarons in H- and J-Aggregates, *Accounts Chem Res*, 43 (2010) 429-439.
- [26] H.B. A. Köhler, The Electronic Structure of Organic Semiconductors, in: *Electronic Processes in Organic Semiconductors*, 2015, pp. 1-86.
- [27] S.T. Hoffmann, S. Athanasopoulos, D. Beljonne, H. Bässler, A. Köhler, How do Triplets and Charges Move in Disordered Organic Semiconductors? A Monte Carlo Study Comprising the Equilibrium and Nonequilibrium Regime, *J Phys Chem C*, 116 (2012) 16371-16383.
- [28] W. Barford, M. Marcus, Theory of optical transitions in conjugated polymers. I. Ideal systems, *J Chem Phys*, 141 (2014).

# Chapter 4: Aggregate formation dynamics in P3HT films probed by in-situ optical spectroscopy and Franck-Condon analysis

## 4.1 Introduction

This chapter is based in part on the manuscript “*A unified picture of P3HT aggregate formation during solution processing*” which is prepared for submission together with **Matthew J Dyson, Stefan Wedler, Konstantin Schötz, Mihirsinh Chauhan, Paul N Stavrinou, Natalie Stingelin, Anna Köhler, and Fabian Panzer**. The paper aims to provide a general picture of the aggregate formation dynamics in solution processed conjugated polymer films by exploring the underlying combined kinetic and thermodynamic effects during film formation. This was done by careful choice and control of the solution processing conditions including the polymer solubility, the deposition temperature and the solvent evaporation rate. By detailed analysis of the measured in-situ optical spectra during the film formation, a general picture is proposed to explain the different aggregation pathways that impact the final aggregate properties in the formed film.

Experimentally, quasi-simultaneous in-situ photoluminescence and absorption spectra were acquired during blade coating and spin coating of neat P3HT and blend P3HT:PEO films at different temperatures. These in-situ spectra were measured for solutions using various solvents that have different P3HT solubility. The in-situ spectra were analyzed in the framework of the Franck-Condon analysis (FCA) to quantify the evolution of the aggregate properties during the transition from the initial solution phase via solidification to the final film. The final fraction of aggregates formed, their energetic disorder and the balance between inter and intra-chain coupling in the aggregates were extracted and then used to construct a general picture of the aggregate formation pathways under the different processing conditions. I performed all the in-situ blade and spin coating of neat P3HT and blend P3HT:PEO measurements. Some of the blend P3HT:PEO were done in collaboration with *Matthew J Dyson*. The temperature dependent spectroscopic measurements in solutions and the insitu measurements in a controlled solvent atmosphere were performed by *Konstantin Schötz* and *Stefan Wedler* respectively. I analyzed the insitu spectra following a Franck-Condon analysis (FCA) approach using a python code developed by *Matthew J Dyson* and *Stefan Wedler*.

I start first by discussing the theoretical background regarding the relation between processing conditions and aggregation of conjugated polymers. Then I highlight the analysis approach of fitting

and analyzing the spectra using FCA to extract the relevant parameters. Finally, I show and discuss the experimental results.

## 4.2 Theoretical background

As already discussed in the previous chapter, in thin films conjugated polymers usually adopt a semi-crystalline morphology consisting of domains where the polymer chains are fully disordered (amorphous) and domains that contain aligned and interacting polymer chains that we refer to as aggregates [1]. Within these aggregates the polymer chains exhibit electrostatic inter- and intra-chain interactions [1-3]. As a result, the aggregates affect various photophysical processes that impact the device performance when conjugated polymers are employed in thin film optoelectronic devices [4-7]. The properties of these aggregates (e.g. interaction strength, disorder, etc...) are a priori determined by the underlying film deposition conditions [8-13].

Typically, the conjugated polymer films are made by solution processing using various deposition techniques such as blade coating and spin coating [14, 15]. Unfortunately, there is no detailed picture of the general relation between the various solution processing conditions and the final aggregate properties. This relation is usually investigated by exploring the effect of specific conditions in isolation such as the impact of spin rate, temperature, and solubility following a trial and error approach [9-11]. In addition, these experiments mostly focus on the final film properties without detailed investigation of the changes happening during film formation by solidification from solution as a function of the different processing conditions.

In a conjugated polymer solution, the degree of solubility of the polymer in the solvent (i.e. the solvent quality) at a specific concentration affects the chain-chain and chain-solvent interactions within this solution. In a good solvent the polymer chains usually adopt a more extended conformation due to the preferential interaction between the polymer and the solvent molecules rather than the polymer chains with itself or with other polymer chains. On the contrary, in a bad solvent, the polymer chains would adopt a less extended conformation with the preferential interaction of the polymer chains with themselves. Consequently, in a bad solvent in addition to other factors, polymer aggregates might form even in solution [16, 17]. Moreover, for the same solvent, the degree of solubility of a conjugated polymer can be varied (i.e. manipulating the solvent quality) by changing the solution temperature. In general, decreasing the temperature leads to a reduced degree of solubility of the polymer (i.e. reducing the solvent quality) which in turn leads to a higher probability of the chain aggregating within the solution. At a certain temperature, depending on both the solvent and polymer, we observe a transition from a disaggregated to an aggregated polymer phase within the solution. This temperature is referred to as the critical

transition temperature ( $T_c$ ) [2, 17]. Hence, temperature dependent optical spectroscopy measurements allow one to measure  $T_c$  by tracking changes in the measured spectra over a wide temperature range.

From a film processing point of view, the relation between a solution's critical transition temperature ( $T_c$ ) and the processing temperature were shown to affect the aggregate properties in several solution processed conjugated polymer films. When spin coating various conjugated polymers at temperatures above and below  $T_c$ , the aggregates formed in the final film were found to vary in terms of their inter-chain coupling, conjugation lengths and disorder [18]. In addition, the solvent properties also impact the aggregate formation dynamics during solution processing of conjugated polymer films. It has been shown that, solvent pairs with the same solubility parameters but different boiling points ( $B_p$ ) affected the fraction of the aggregated domains in spin coated thin films of several conjugated polymers [19]. Therefore, the solvent properties in combination with the temperature under which film deposition from solution is done are the main factors influencing the aggregate formation. Experimentally, these choices translate into the relation between the critical transition temperature ( $T_c$ ), the deposition temperature which I controlled here by fixing the substrate temperature ( $T_s$ ) and the solvent's boiling point ( $B_p$ ). A unified picture of the combined effect of these deposition parameters is still lacking in literature. Hence, in this chapter I try to provide a more general picture of the combined effect of these parameters on the aggregate formation in solution processed conjugated polymer films.

### 4.3 Analysis approach

#### i. Extracting the aggregate spectra

As already highlighted in chapter 3, when analyzing conjugated polymer films one is often mostly concerned with the aggregate properties as they have the largest impact on the device performance. However, the optical spectra of conjugated polymers usually include contributions from both non-aggregated (amorphous) and aggregated polymer chains [17, 18]. Thus, disentangling these two contributions is an important preliminary step to focus solely on the aggregates for further analysis.

Figure 1 shows an example of the P3HT photoluminescence and absorption spectra including both the amorphous and aggregates contributions. The pale orange regions in the optical spectra correspond to the emission and absorption of the phases with non-aggregated polymer chains. The pale blue regions correspond to the emission and absorption of the phases with the aggregated polymer chains. We readily observe the energetic separation between both contributions, where

the part of the spectra pertaining to aggregates is red shifted relative to the amorphous part. This is a result of the  $\pi$ - $\pi$  ordering and planarization of the aggregated polymer chains as depicted schematically in the middle of figure 1 [1, 20, 21].

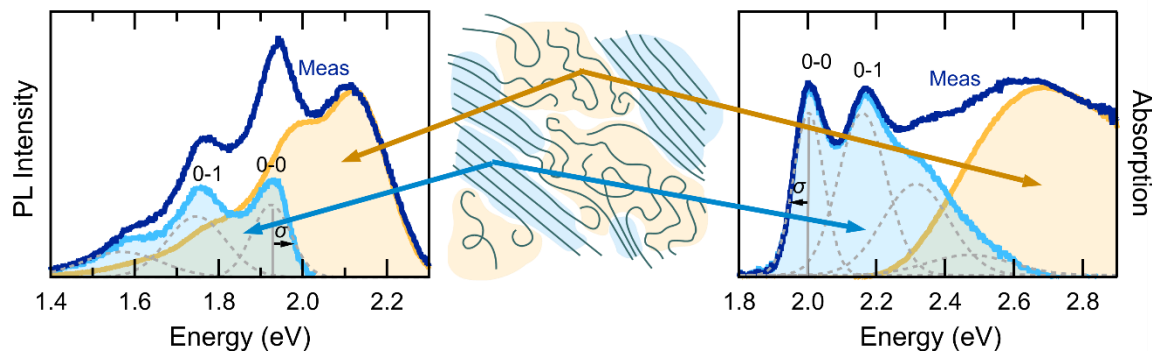


**Figure 1: Photoluminescence and absorption spectra of P3HT (blue line) during blade coating from CF solutions at  $T_s = 5^\circ\text{C}$  showing the aggregate phase contribution (pale blue spectra) and the amorphous phase contribution (pale orange spectra). An exemplary fit of the aggregates spectra (dashed grey lines) is shown, from which one can extract the 0-0/0-1 peak ratio and the disorder parameter  $\sigma$**

Practically, the procedure of separating those two contributions can be explained by referring to figure 1. The first requirement would be obtaining a spectrum where the polymer chains are completely non-aggregated (pale orange spectra in figure 1). Such spectrum can be obtained from solution measurements at a temperature much higher than the critical transition temperature to ensure complete polymer disaggregation. Following this, with the assumption that PL or absorption at the high energy end are mostly originating from the non-aggregated polymer chains, the spectrum corresponding to these non-aggregated polymer chains is normalized to match the high energy tail of the overall spectrum and then subtracted from it.

The resulting spectra from this procedure can then be attributed to the aggregates (pale blue spectra in figure 1) where the vibronic progression of these spectra becomes visible. The 0-0 and 0-1 transition peaks of the  $S_0$ - $S_1$  electronic transition of the P3HT aggregates can then be clearly distinguished and further analyzed [22-24]. These aggregate spectra are then analyzed using FCA to extract quantitative information about the aggregate properties which then can be related to the underlying electronic structure [23]. In the context of our work, the two important parameters are the disorder parameter ( $\sigma$ ) extracted from the peak widths and the 0-0/0-1 peak ratio extracted from the peak heights. These two parameters can be related to the microstructure of the aggregate phases in terms of the degree of disorder ( $\sigma$ ) and the competition between the inter-chain and

intra-chain coupling strength between the polymer chains within these phases (0-0/0-1 peak ratio) [24].

## ii. Franck-Condon analysis (FCA)

Similar to what I did in the previous chapter, I also fitted the PL spectra of the aggregates using eq. 9 introduced in chapter 1. Within the framework of the weakly coupled H-aggregates model this equation allows one to fit the PL spectra with the presence of molecular coupling [23]. Nevertheless, several modifications and approximations are made in the application of FCA on the aggregated PL spectra here due to the properties of the P3HT system.

Firstly, only one effective vibrational mode is considered for fitting the spectra, which I initially took at  $\approx 0.175$  eV. I slightly changed this mode energy between different datasets to achieve the best fitting quality. This was chosen as it mainly corresponds to the C=C symmetric stretch mode of P3HT at  $\approx 1450$   $\text{cm}^{-1}$  ( $\approx 0.18$  eV) which has been already shown to be the mode that dominates the coupling to the electronic transition in P3HT and is commonly used when fitting its optical spectra [22, 23, 25]. Secondly, an additional broadening term ( $\Delta\sigma$ ) is included as shown in eq.1 (also included when fitting the absorption spectra of the aggregates as shown in eq.2). This extra term was added to account the overlap of different vibronic modes with near energies when considering a high number of them for fitting ( $m = 4$  is considered here) [26]. This overlap leads to an extra broadening that reduces the fitting quality and affects the reliability of the fitting results [27-29]. Finally, a fixed Huang-Rhys parameter of 1 and a constant refractive index within the fitted energetic range is considered [22, 28, 30]. The Huang-Rhys parameter is typically extracted by fitting the dilute PL spectra of P3HT where only intra-chain coupling prevails and usually yields a value around 1 which I considered for fitting [23, 30]. A constant refractive index is considered as I fitted the PL spectra over a narrow range between 1.5 eV to 2 eV where it has been shown that no significant variation of the solvents refractive indices occur [31]. Consequently, one arrives at a more simplified version of FCA, yet with the appropriate modifications to provide reliable fits for the P3HT system:

$$PL(E) \propto E^3 \left[ \alpha \exp\left(\frac{(E - E_0)^2}{2\sigma^2}\right) + \sum_{m=1}^{m=3} \frac{S_{\text{eff}}^m}{m!} \text{Exp}\left(-\frac{(E - (E_0 - mE_{\text{vib}}))^2}{2(\sigma + m \cdot \Delta\sigma)^2}\right) \right] \quad (1)$$

Where  $E$  is the energy,  $E_0$  is the position of the peak corresponding to the (0-0)  $S_1$ - $S_0$  electronic transition,  $S_{\text{eff}} = 1$  is the Huang-Rhys parameter,  $\alpha$  is the factor accounting for the electronic molecular coupling between the polymer chains,  $m$  is the peak number taken as 4,  $\sigma$  is the peak width and  $\Delta\sigma$  is the additional broadening.

Regarding absorption, the aggregate spectra is simply fit by a series of Gaussian peaks with a fixed separation in-between as shown in eq.2, while also including the additional broadening term ( $\Delta\sigma$ ) as discussed for PL. This was considered as an imperfect normalization and subtraction of the non-aggregate spectra in addition to any scattering losses would introduce deviations to the resulting aggregate spectra [5]. This might make it harder to reliably fit the aggregate absorption spectra using the tradition FCA approach introduced in chapter 1 and used here for fitting the PL spectra (eq. 1). It is then sufficient within the context here using eq. 2 to be able to reliably extract the required parameters, namely the disorder and the 0-0/0-1 peak ratio.

$$Abs(E) = E \sum_{m=0}^{m=3} A_m \exp\left(-\frac{(E - (E_0 + mE_{vib}))^2}{2(\sigma + m \cdot \Delta\sigma)^2}\right) \quad (2)$$

## 4.4 Results

### i. The solvent effect

In this section, as a first step I investigate the combined effect of the critical transition temperature ( $T_c$ ) and the solvent's boiling point ( $B_p$ ) on the final aggregates. This is done by film deposition from P3HT solutions using three solvents having different boiling points and different degrees of solubility for P3HT. These solvents are Chlorobenzene (CB), Chloroform (CF) and Tetrahydrofuran (THF). The critical transition temperature is typically determined by tracking the changes in the temperature dependent optical spectra of the solutions measured over a wide temperature range. In my case, I extracted the critical transition temperatures of P3HT for CF and THF from the absorption measurements of the solutions which were done and provided by *Konstantin Schötz*. For CB, the critical transition temperature was taken to be approximately 5°C as already reported in literature [18]. This was confirmed by measurements done by *Matthew J Dyson*.

Figure 2 shows the absorption spectra of P3HT solutions over the temperature range between 2°C - 27°C for CF and 22°C - 47°C for THF both at 10 mg/ml P3HT concentration. The absorption spectra were taken at 5°C steps for both solutions. Due to the high polymer concentration the detector saturates at higher energies and the spectra is distorted. It is readily apparent that the aggregates present in solution increase with decreasing the solution temperature. The CF absorption spectra at high temperatures show a broad structure less absorption spectra with absorption onset around 2.2 eV. At lower temperatures the spectra are more structured with the absorption onset red shifted to around 1.9 eV which can be attributed to the aggregate absorption. The THF absorption spectra shows the same two distinct spectral shapes as a function temperature. The transition

between the two spectral shapes happens between 7°C and 12°C for CF and between 37°C and 42°C for THF.

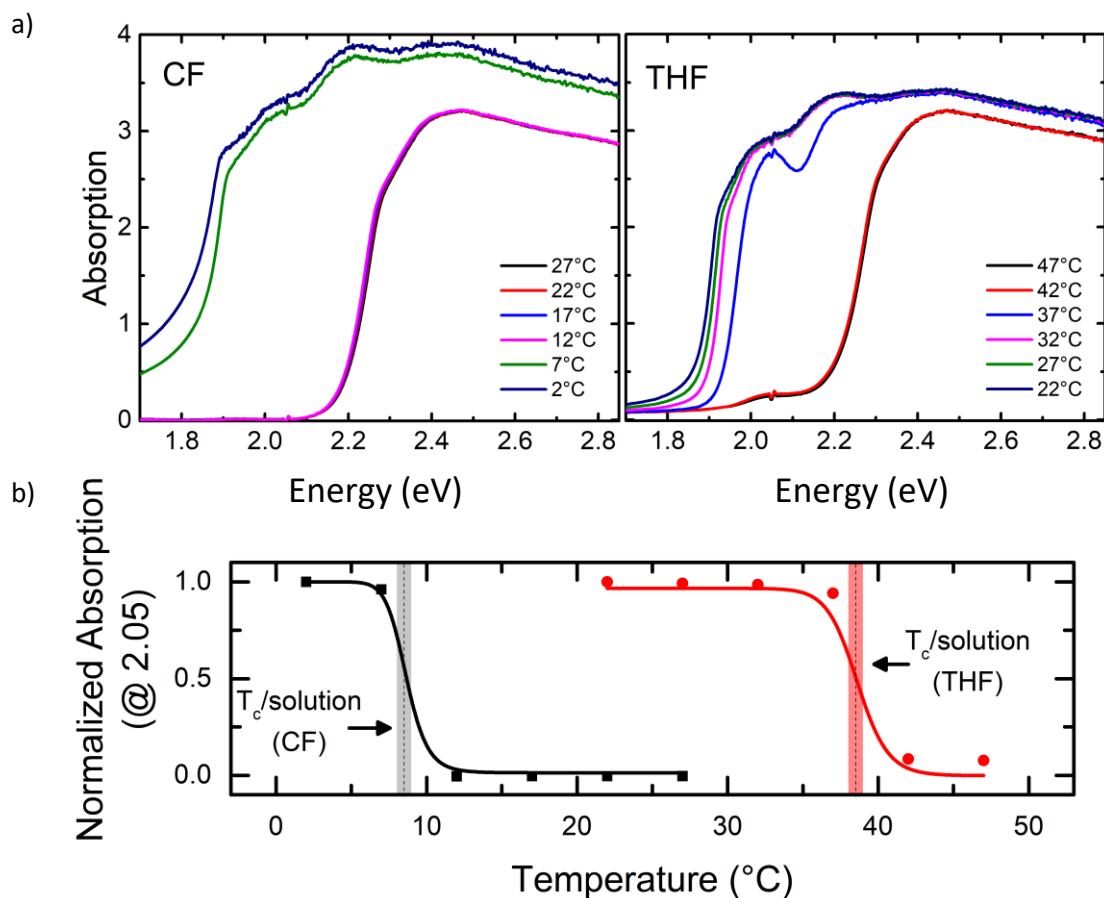


**Figure 2: a) Absorption spectra of P3HT in CF (left) and THF (right) solutions at different temperatures taken at 5°C step. Due to the high polymer concentration, the detector saturates at higher energies and the spectra are distorted. b) Temperature dependence of the solution absorption at 2.05eV normalized to the maximum value. This was taken from the solution spectra at the different temperatures shown in a), and corresponds to the absorption of the P3HT aggregates when they are formed in solution.**

To determine this disorder to order transition which corresponds to the critical transition temperature, one usually calculates the fraction of aggregates present in the solutions at the different temperatures and determines  $T_c$  as the inflection point as the fraction of aggregates change from near 0% (corresponding to the non-aggregated polymer chains) to near 100% (corresponding to the aggregated polymer chains). Nevertheless, as the spectra are distorted due to the detector saturation such procedure might yield inaccurate results about the fraction of aggregates. Alternatively, I extracted the absorption intensity at 2.05 eV, which corresponds to the 0-0 transition of the aggregates. This also provides an indication about the extent of aggregation as

we cool booth CF and THF solutions from high temperatures and will be sufficient to determine the  $T_c$ . This temperature dependence of the extent of aggregation in solutions is shown in the lower panel of figure 2 and it shows a sigmoidal trend from which the critical transition temperature of P3HT in the solutions ( $T_{c/solution}$ ) can be estimated. The estimated  $T_c$  from the inflection points were  $9.0 \pm 2.5$  °C for CF and  $39.0 \pm 2.5$  °C for THF. It is worth noting that the error margin was fixed at 2.5 °C, which is half the measurement step of 5 °C. Attempting to fit the data as a best mathematical fit produces very small errors that would be considered physically incorrect. The solvent properties are then shown in table 1 [32, 33] along with the solubility parameters of P3HT in each solvent [34].

**Table 1: The properties of CB, CF and THF.  $T_c$  refers to the critical transition temperature of P3HT in the respective solvent.  $\delta_t$  corresponds to the total Hildebrand solubility parameter.  $\delta_d$ ,  $\delta_p$ , and  $\delta_h$  correspond to the dispersion, polar and hydrogen bonding contributions of the three component Hansen solubility parameters.  $B_p$  corresponds to the solvent's boiling point and  $T_c$  corresponds to the critical**

Solvent	$\delta_t$ (MPa <sup>1/2</sup> )	$\delta_d$ (MPa <sup>1/2</sup> )	$\delta_p$ (MPa <sup>1/2</sup> )	$\delta_h$ (MPa <sup>1/2</sup> )	$B_p$ (°C)	$T_c$ (°C)
CB	19.6	19	4.3	3.2	132	5
CF	19	17.8	3.1	5.7	61	10 <sup>b</sup>
THF	19.4	16.8	5.7	8.0	66	40 <sup>b</sup>
P3HT	19.1 <sup>a</sup>	18.6	2.9	3.2	-	-

<sup>a</sup> I calculated this value from the reported Hansen solubility parameters using equation 3

<sup>b</sup> The extracted  $T_c$  for CF and THF were rounded to the nearest whole number for ease of comparison

From the table, it becomes apparent that the solvents choice was rationalized by having solvent pairs with the nearly similar boiling points but different solubility for P3HT, which is the case for THF and CF. In addition to CB, which has a much higher boiling point than THF and CF while having good solubility for P3HT. The second column of table 1 contains the Hildebrand solubility parameters for the three solvents alongside with that for P3HT. Based on the simple like dissolves like concept one could assume that the three solvents are equally good solvents for P3HT as evident by the similar Hildebrand solubility parameters. Nevertheless, the total solubility parameter does not give the full details about individual contributions to the overall solubility value. Hence, I included the Hansen solubility parameters that divide the total solubility into its individual components. Columns 3, 4 and 5 show the three component Hansen solubility parameters which divides overall solubility parameter into three components corresponding to the dispersion ( $\delta_d$ ),

polar ( $\delta_p$ ) and hydrogen bonding ( $\delta_h$ ) contributions. A total Hansen solubility parameter (which should correspond to the Hildebrand solubility parameter) can be calculated from these three components based on the following equation [35, 36]:

$$\delta_t^2 = \delta_d^2 + \delta_p^2 + \delta_h^2 \quad (3)$$

Following the Hansen solubility three component system, the solvent quality of the three solvents can be compared quantitatively using the so called Hansen sphere which is beyond the scope of my thesis [36]. In my case here, I used the critical transition temperature values in combination with the Hansen solubility parameters to compare the quality of the three solvents. As mentioned earlier, the critical transition temperature ( $T_c$ ) can be related to the solvent quality. The lower the critical transition temperature ( $T_c$ ) the better the solvent dissolves the solute (i.e., P3HT), in other words one has to decrease the temperature further to reduce the solvent's quality to reach the disorder to order transition. The last column in Table 1 shows the critical transition temperatures ( $T_c$ ) of P3HT in CB, CF and THF. It can be clear from table 1 that CB has the best solubility for P3HT evidenced by its low  $T_c$  and very similar values of the Hansen solubility parameters followed by CF and finally THF, which can be considered as the worst solvent for P3HT relative to CB and CF.

After having an initial idea about the solvent properties, I move on to investigate how these properties would affect the P3HT aggregates formation in films deposited from the different solutions. Regarding film deposition, the technique of choice was mainly blade coating which offer more reproducibility of the experimental results. As mentioned earlier, the deposition temperature is controlled here by fixing the substrate temperature during the measurement duration; hence, I refer to the deposition temperature as the substrate temperature ( $T_s$ ). To normalize the effect of  $T_s$  and to be able to compare between the three solvents as a function of their critical transition temperatures and boiling points, I blade coated the films at fixed substrate temperatures relative to the respective solvent's  $T_c$ . Figure 3 shows the overall absorption spectra (black lines) of the final films of P3HT blade coated. The figure shows the P3HT films blade coated from from the CB, CF and THF solutions either 5°C below or above the solvent's critical transition temperature. The absorption spectra of the amorphous phase are shown as the shaded red area and was taken as the first absorption spectrum when starting film deposition while the absorption spectra of the aggregates is shown as the shaded blue area and was extracted following the analysis approach presented in section 4.3.i.

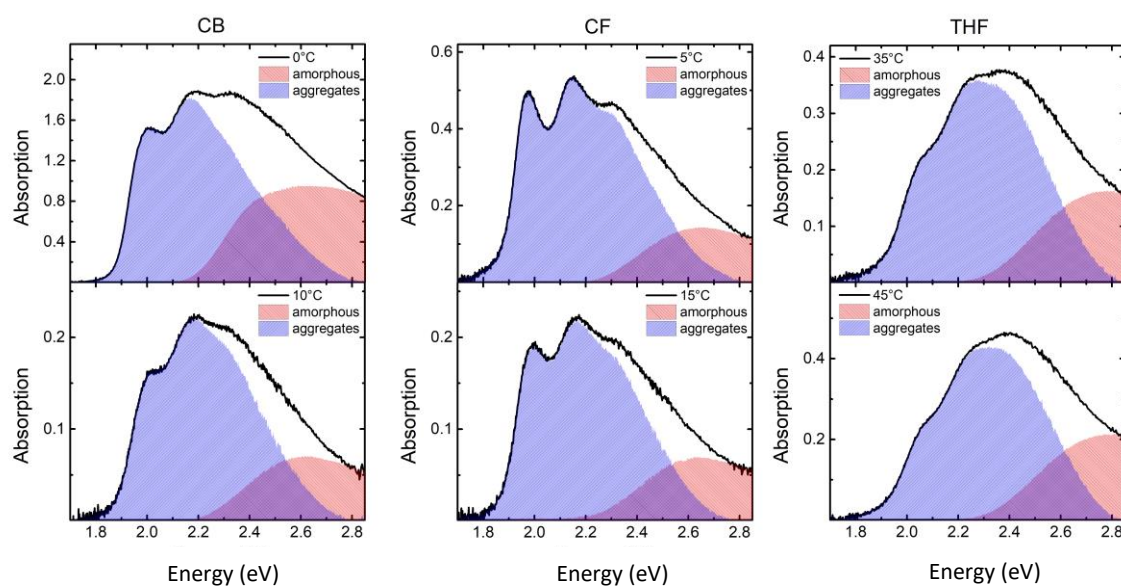


**Figure 3: Overall absorption spectra (black lines) of the films blade coated with a substrate temperature ( $T_s$ ) either 5°C below (top row) or 5°C above (bottom row) the critical transition temperature ( $T_c$ ) for CB ( $T_s = 0^\circ\text{C}$  and  $10^\circ\text{C}$ ), CF ( $T_s = 5^\circ\text{C}$  and  $15^\circ\text{C}$ ) and THF ( $T_s = 35^\circ\text{C}$  and  $45^\circ\text{C}$ ). The amorphous spectrum for each film is shown as the red area, which is taken as the first absorption spectrum when starting film deposition. The blue area shows the P3HT aggregates absorption extracted by subtracting the amorphous spectrum from the overall absorption spectrum**

From figure 3, it is clear that the solvent choice influences the shape of the overall absorption spectra and consequently the aggregate spectra (the shape of the amorphous spectra should be the same regardless of the solvent used as it corresponds to the non-aggregated P3HT polymer chains). The most notable difference between the absorption spectra of the films deposited from the three solvents is the ratio between the 0-0 and the 0-1 absorption peaks centered around 2.05 eV and 2.2 eV respectively [30]. This ratio has been shown to reflect changes in the polymer chain conjugation lengths and intermolecular interaction strength depending on solvent choice, molecular weights and the synthesis method of P3HT [30]. While the presence of the solvent dependence of the peak ratios is not affected by the substrate temperature, its magnitude clearly depends on whether  $T_s$  is above or below  $T_c$ . This should be clearer when we focus on comparing the aggregate spectra for the same solvent.

Figure 4 shows the normalized aggregate spectra for the two films deposited from each solvent below and above  $T_c$ . One can readily observe that the films deposited from THF below and above  $T_c$  show minimal differences in the final aggregate spectra. The film blade coated below  $T_c$  is slightly red shifted with a slightly higher shoulder around 2.05eV corresponding to the 0-0 transition compared to the one blade coated above  $T_c$ . On the contrary, the films deposited from CB below

and above  $T_c$  show differences that are more significant. We observe an increase in the 0-0 transition peak intensity located at 2 eV and the disappearance of the high energy shoulder observed in the aggregate spectrum of the film deposited above  $T_c$ . The films deposited from CF show similar differences with a magnitude that can be considered an intermediate between those observed in CB and THF.

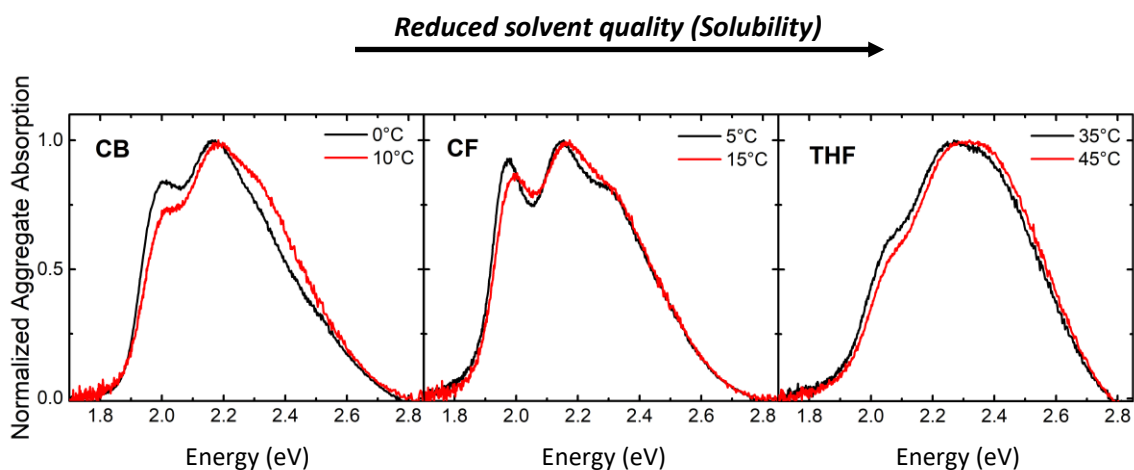


**Figure 4:** Normalized final absorption aggregate spectra of the films blade coated with a substrate temperature ( $T_s$ ) either 5°C below (black lines) or 5°C above (red lines) the transition critical temperature ( $T_c$ ) for: CB ( $T_s = 0^\circ\text{C}$  and  $10^\circ\text{C}$ ), CF ( $T_s = 5^\circ\text{C}$  and  $15^\circ\text{C}$ ) and THF ( $T_s = 35^\circ\text{C}$  and  $45^\circ\text{C}$ ).

To get a more in-depth information about the solvent and solubility effects on the properties of the formed aggregates in the film in terms of the disorder and the intermolecular interactions, I fitted the aggregate absorption spectra using FCA eq. 2 introduced in section 4.3(ii). Figure 5 shows the fits of the extracted aggregate spectra for the same films shown in figure 4. Table 2 shows the disorder ( $\sigma$ ) and the 0-0/0-1 peak ratio from the fits shown in figure 5. The fitting result confirms the qualitative observations from figure 4.

As observed in table 2, films deposited from CB solutions show the largest percent decrease in the 0-0/0-1 peak ratio (15%) compared to films deposited from CF (7%) and THF (5%) when blade coating at a temperature above  $T_c$ . These observed changes showing a dependence on both the solvent and the substrate temperature hints towards a combined effect of both variables rather than a general effect of the film deposition above or below the used solvent's  $T_c$ . In other words, the observed trend in the effect of blade coating below or above the solvent's  $T_c$  is correlated with the difference between the  $T_c$  measured in solution (which reflects the degree of P3HT solubility) and the solvent's boiling point. This difference then affects the solvent's evaporation rate and consequently the aggregate formation dynamics.

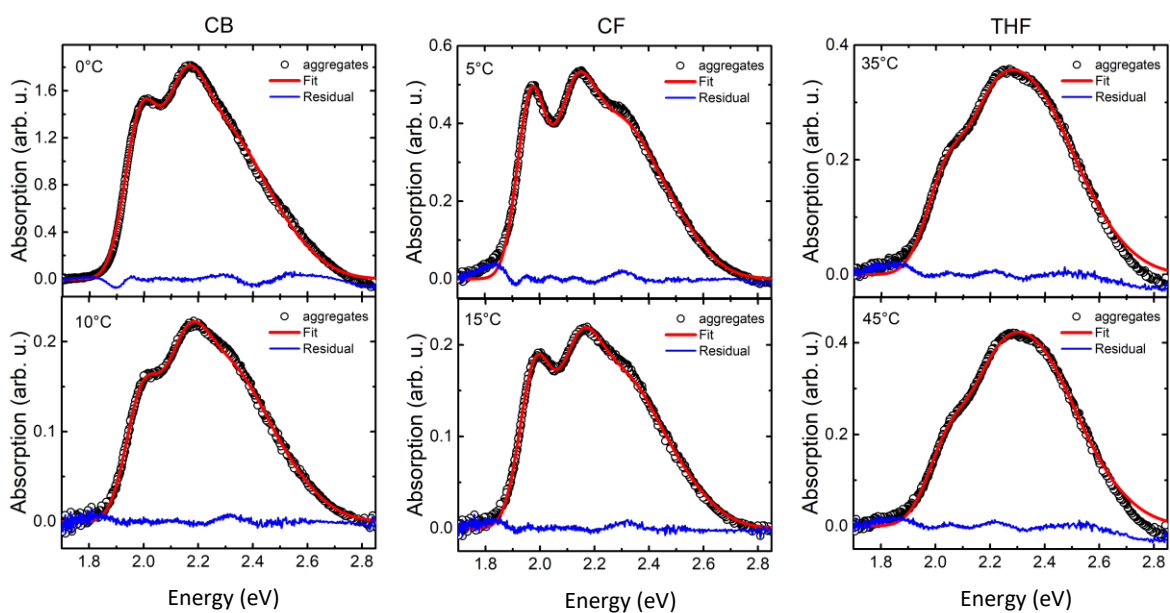


**Figure 5:** Aggregate absorption spectra (hollow circles) of the films blade coated with a substrate temperature ( $T_s$ ) either 5°C below (top row) or 5°C above (bottom row) the transition critical temperature ( $T_c$ ) for CB ( $T_s = 0^\circ\text{C}$  and  $10^\circ\text{C}$ ), CF ( $T_s = 5^\circ\text{C}$  and  $15^\circ\text{C}$ ) and THF ( $T_s = 35^\circ\text{C}$  and  $45^\circ\text{C}$ ). The solid red lines represent the fits for each film using eq.2 and the solid blue lines represent the difference between the data and the fits.

**Table 2:** The fitting parameters of the film deposited from CB, CF and THF solutions at temperatures below and above the  $T_c$  of P3HT in the respective solvent. %change of the 0-0/0-1 peak ratio refers to the change in its values when depositing films at substrate temperatures higher than  $T_c$  compared to its values when depositing films at substrate temperatures below  $T_c$ .

Solvent	$T_s$ ( $^\circ\text{C}$ )	$\sigma$ (meV)	0-0/0-1	% change in 0-0/0-1	$T_c$ ( $^\circ\text{C}$ )
CB	0	58.8	0.66		5
CB	10	59.6	0.56	-15%	5
CF	5	51	0.76		10
CF	15	56.3	0.71	-7%	10
THF	35	71.9	0.56		40
THF	45	74.5	0.53	-5%	40

For CB, where the biggest changes are observed, blade coating of the film was done at temperatures much lower than its boiling point. Thus, in this case the solvent's evaporation is extremely slow which might give the aggregates very long times to form (assuming they form in solution at  $T_s < T_c$  and before sufficient solvent evaporation). This leads to aggregates with higher 0-0/0-1 peak ratio when the films are deposited at temperatures lower than  $T_s$ , which corresponds to longer conjugated polymer chains with decreased intermolecular interactions opposite to the aggregates form when the films are deposited at temperatures higher than  $T_s$ . Hence, in the case of CB the solubility of P3HT might be the limiting factor for the final properties of the aggregates formed in the film. For THF, the situation is the opposite. We observe less significant changes whether the blade coating was performed above or below  $T_c$ . THF's boiling point is 66°C and so irrespective of whether blade coating is performed below  $T_c$  ( $T_s = 35^\circ\text{C}$ ) or above  $T_c$  ( $T_s = 45^\circ\text{C}$ ) the aggregates might not have time to form in solution due to the fast solvent evaporation rate. This leads to aggregates with near 0-0/0-1 peak ratio whether deposited at temperatures lower or higher than  $T_s$ . Hence, in the case of THF the solvent's evaporation rate is the limiting factor for determining the properties of the aggregates present in the final film. For CF, the difference between processing temperature and boiling point is intermediate between the cases of CB and THF (CF has a boiling point of 61°C while the films are blade coated at  $T_s = 5^\circ\text{C}$  and  $T_s = 15^\circ\text{C}$ ). It then logically follows that CF offers an intermediate situation where both the solvent's evaporation rate and solubility contribute to the properties of the aggregates in the films.

Opposite to the solvent dependence of the 0-0/0-1 peak ratios, the disorder parameters ( $\sigma$ ) does not show a similar trend. Nevertheless, the results are consistent with the above conclusions. For THF,  $\sigma$  is around 40% higher than that of CB. This higher  $\sigma$  in THF can be rationalized by the faster solvent evaporation, which does not allow enough time for the polymer chains to order prior to solidification. For CF,  $\sigma$  is a little lower than that of CB although the boiling point of CF is much lower than that of CB, which should lead to a faster evaporation rate. This might hint that in the case of CF because the blade coating temperatures is further away from its boiling point compared to THF; other factors influence the disorder within the formed aggregates. This will be discussed later in more details when investigating the aggregate formation dynamics in the different solvents under different conditions.

## ii. The critical transition temperature in films

As the next step, I move forward to investigate the effect of  $T_s$  relative to  $T_c$  for films over a wider temperature range. I focus on comparing CF and THF as they have similar boiling points but different solubility of P3HT. In addition, CF and THF offer the experimental accessibility to a wider

range of deposition temperatures below  $T_c$  compared to CB. As mentioned, when discussing the solvent's properties, the critical transition temperature of P3HT in the CB, CF and THF solutions were extracted from absorption measurements over a wider temperature range. Similar to the solutions, I measured the absorption of P3HT films made from CF and THF solutions (at the same 10 mg/ml concentration) at a wide temperature range. To determine the critical transition temperature using the film absorption spectra, I fitted the film spectra for each temperature following eq. 2 to extract the 0-0/0-1 peak ratio and the disorder as will be discussed later. Figure 6 shows the the overall absorption spectra with its aggregate and amorphous contributions along with the fits of the aggregate spectra for the P3HT films deposited from a CF solution at substrate temperatures between 5°C and 30°C at 5°C temperature steps. Figure 7 shows the the overall absorption spectra with its aggregate and amorphous contributions along with the fits of the aggregate spectra for the P3HT films deposited from a THF solution at substrate temperatures between 5°C and 30°C at 5°C temperature steps. For the films deposited from the CF solution, similar to the solution measurements, the onset of the absorption spectra shifts to higher energies and the 0-0/0-1 peak ratio decreases as the temperature increases. The trend is similar in the films deposited from the THF solution.

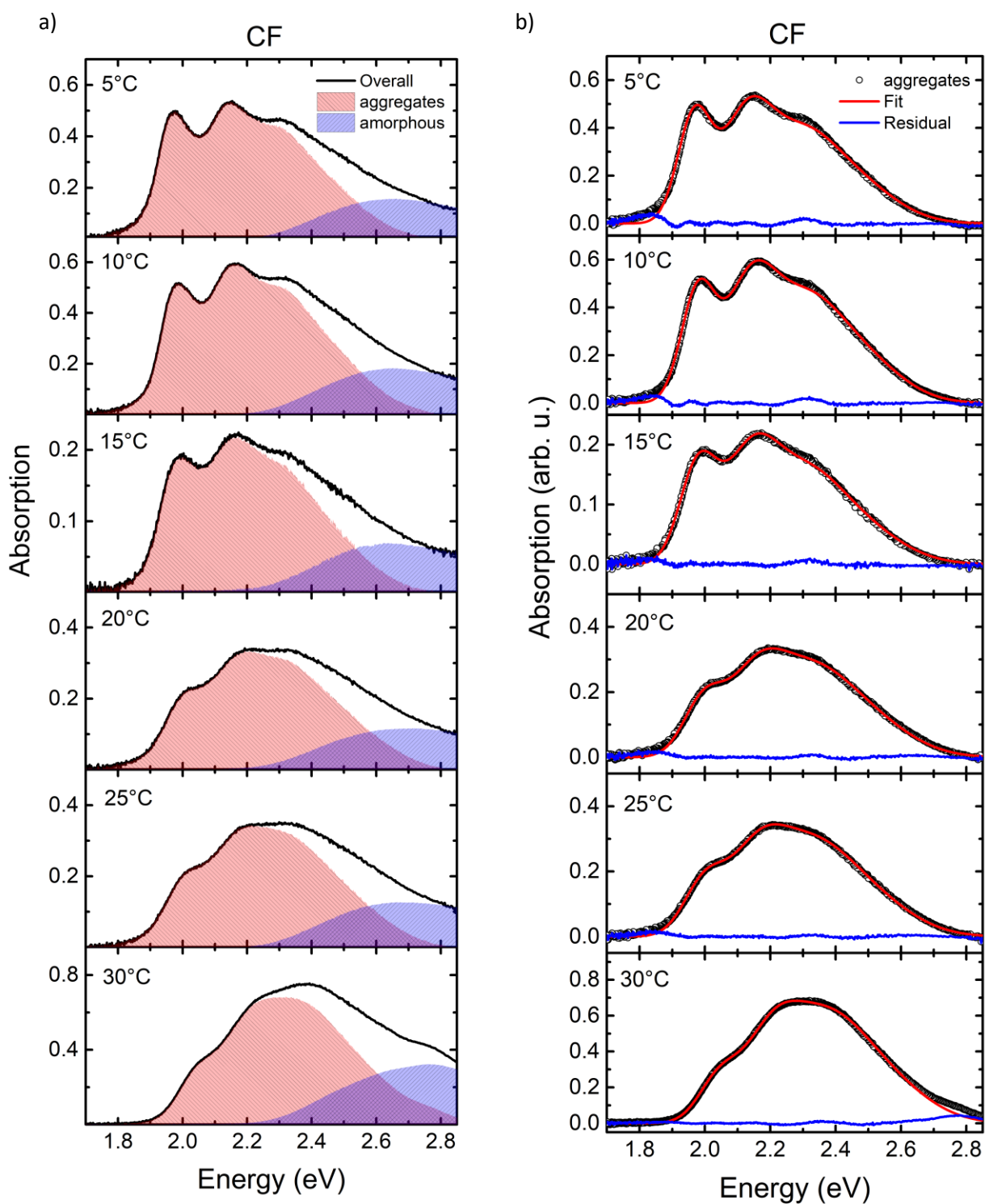


**Figure 6:** a) The Total absorption spectra showing the aggregate absorption contribution (red area) and the amorphous contribution (blue area) of P3HT films deposited from a CF solution at different temperatures taken at 5°C steps. b) Aggregate absorption spectra (hollow circles) corresponding to the red area from a). The solid red lines represent the fits for each film using eq.2 and the solid blue lines represent the difference between the data and the fits.

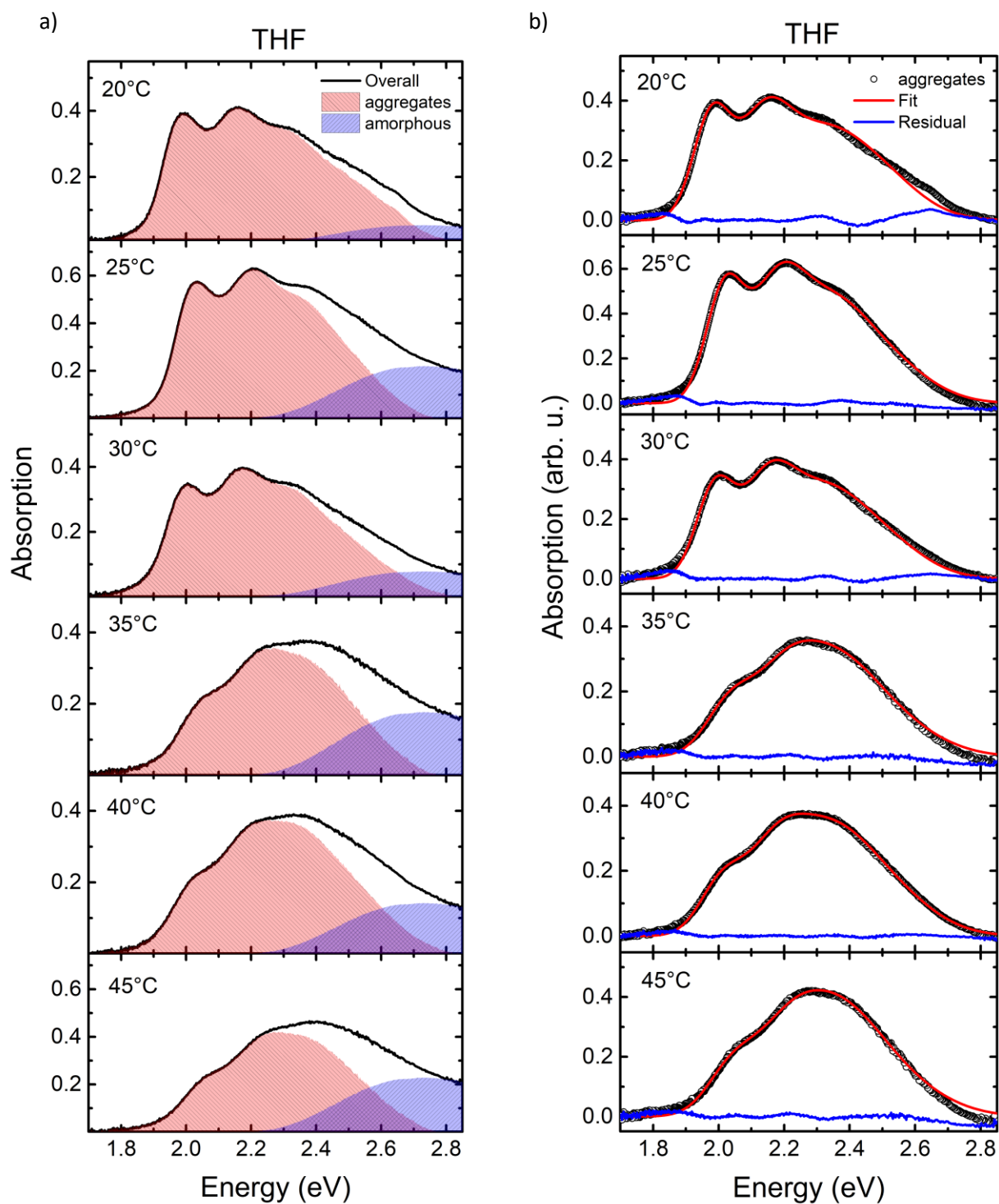


**Figure 7:** a) Total absorption spectra showing the aggregate absorption contribution (red area) and the amorphous contribution (blue area) of P3HT films deposited from a THF solution at different temperatures taken at 5°C steps. b) Aggregate absorption spectra (hollow circles) corresponding to the red area from a). The solid red lines represent the fits for each film using eq.2 and the solid blue lines represent the difference between the data and the fits.

Figure 8 shows the temperature dependant  $\sigma$  and 0-0/0-1 values extracted from fitting the absorption aggregate spectra of the films blade coated from THF and CF solutions shown in figures 6 and 7.

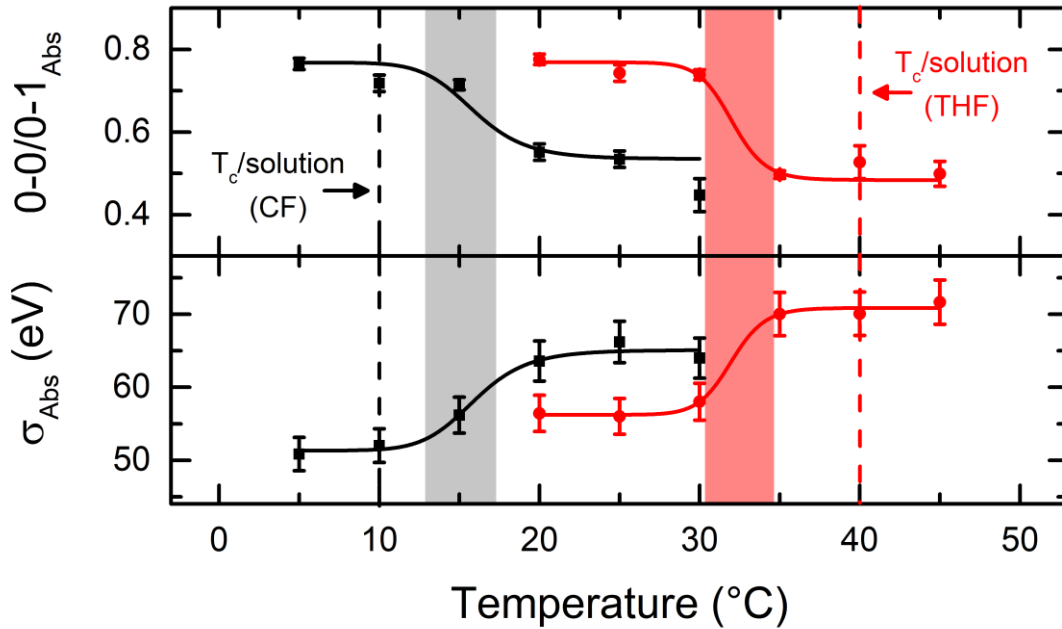


**Figure 8: Temperature dependence of the 0-0/0-1 peak ratios (top panel) and of the  $\sigma$  values (bottom panel) extracted by fitting the aggregate absorption spectra using eq. 2 for films blade coated from CF (black squares) and THF (red circles) solutions of P3HT. The temperature refers to the substrate temperature ( $T_s$ ). The black and red lines represent the sigmoidal behavior of the data points to emphasize the transition trend. The black and red shaded areas are a visual representation of the transition width. The dashed black and red lines correspond to the  $T_c$  of CF and THF respectively estimated from the absorption measurements as shown in figure 2.**

In the case of blade coated films, there is a clear deposition temperature dependence of both  $\sigma$  and the 0-0/0-1 peak ratio. We observe a decrease in 0-0/0-1<sub>Abs</sub> as the substrate temperature ( $T_s$ ) increases (0.76 vs. 0.45 for CF and 0.78 vs. 0.5 for THF). On the contrary, we observe an increase in the disorder ( $\sigma_{Abs}$ ) as the substrate temperature ( $T_s$ ) increases (51 meV vs. 64 meV for CF and 56 meV vs. 72 meV for THF). This temperature dependence shows a sigmoidal trend (similar to the case of solutions shown in figure 2) that can be used to estimate a transition temperature that corresponds to a change in the character of the formed aggregates in the P3HT films. I refer to this temperature as  $T_{ch}$  ('ch' refers to the change in aggregate characteristics). It is worth noting that while  $T_c$  and  $T_{ch}$  correspond to a change in the state of the aggregates they are fundamentally different. Since aggregates are always present in the film with varying degrees regardless of the deposition temperature,  $T_{ch}$  only refers to the deposition temperature at which the properties of

the formed aggregates change. Oppositely, in the case of solutions, the critical transition temperature in solution ( $T_{c/solution}$ ) refers to the temperature at which aggregates start to form in solution. Following the above,  $T_{ch}$  can be estimated for films deposited from both CF and THF solutions as the inflection point on the  $\sigma$  and 0-0/0-1 sigmoidal curves. I estimated  $T_{ch}$  (taken as the inflection point for either the  $\sigma$  or the 0-0/0-1 sigmoids) to be  $15.5 \pm 2.5$  °C for CF and  $32 \pm 2.5$  °C for THF. Similar to the case of extracting  $T_c$  for the solutions, the error margin was fixed at 2.5 °C, which is half the measurement step of 5 °C.

Two main differences between the temperature dependence of the solution and film measurements can be observed from figure 8, namely the steepness of the transition and the estimated transition temperature values. For the normalized absorption of the 0-0 peak which corresponds to the aggregates in solution, at temperatures lower than  $T_{c/solution}$  (2°C and 7°C for CF, 22°C, 27°C, 32°C and 37°C for THF) the aggregate absorption is at its maximum value. On the contrary, at temperatures higher than  $T_{c/solution}$  (12°C 17°C, 22°C and 27°C for CF, 42°C and 47°C for THF) the aggregate absorption is at its minimum value. The change between these two extremes is characterized by an abrupt transition as I schematically depicted by the narrow black and red shaded areas around  $T_{s/solution}$ . In a similar manner, the values of  $\sigma_{Abs}$  (middle panel) and 0-0/0-1 $_{Abs}$  (bottom panel) extracted from the aggregate spectra are confined between two extreme cases. We can consider these as two states of the final aggregate properties or characteristics. At  $T_s$  significantly higher than  $T_{ch}$  we observe aggregates with higher  $\sigma_{Abs}$  and lower 0-0/0-1 $_{Abs}$  (e.g., 25°C for CF and 40°C for THF), While at  $T_s$  significantly lower than  $T_{ch}$  we observe aggregates with lower  $\sigma_{Abs}$  and higher 0-0/0-1 $_{Abs}$  (e.g. 5°C for CF and 20°C for THF). Within these temperature ranges, further increasing or decreasing the temperature has an insignificant effect on the values of  $\sigma_{Abs}$  and 0-0/0-1 $_{Abs}$  and hence we would consider the aggregates arising from deposition at these substrate temperatures to have a similar character. The change between these two aggregate states is characterized by a somewhat smooth transition as I depicted schematically by the wide black and red shaded areas around  $T_{ch}$  (compared to those present in the case of solutions). Hence, at the region  $T_s \approx T_c$ , we would expect that control over the deposition parameters could be beneficial in fine-tuning the values of  $\sigma_{Abs}$  and 0-0/0-1 $_{Abs}$  as will be discussed later.

The major difference between the solution and film measurements appears in the discrepancy between  $T_{c/solution}$  and  $T_{ch/film}$ . For both CF and THF,  $T_{c/solution}$  and  $T_{ch/film}$  differ by an equal magnitude of more than 5°C, but in opposite directions. For CF (the better solvent),  $T_{c/solution}$  is lower than  $T_{ch/film}$ , while for THF (the worse solvent)  $T_{c/solution}$  is higher than  $T_{ch/film}$ . It would make sense that this difference is related to the solvent quality (solubility) as the solvents' boiling points are quite similar (61°C vs 66°C). This discrepancy means that if one considers  $T_c$  extracted from solution

measurements as the pivot point for determining the processing temperature of the films where the properties of the aggregates formed in the final film is determined by processing the films at temperatures either above or below this  $T_c$  would fail. An example of this is the case for the film blade coated from the THF solution at a 35°C substrate temperature. In this case if one only considers  $T_{c/solution}$  ( $\approx 40^\circ\text{C}$ ) we would expect the films deposited at temperatures below 40°C (e.g.,  $T_s = 35^\circ\text{C}$  and  $T_s = 30^\circ\text{C}$ ) would have aggregates formed with more or less the same properties. This is not the case as  $T_s = 35^\circ\text{C}$  is below  $T_{c/solution}$  but it is rather above  $T_{ch/film}$ , hence we obtain a final film characterized by aggregates with lower 0-0/0-1 and higher disorder similar to the films blade coated at  $T_s = 45^\circ\text{C}$  and not the films blade coated at  $T_s = 30^\circ\text{C}$ .

Thus, in conclusion, a more accurate determination of the deposition temperature that one would consider would depend on the  $T_{ch}$  values extracted from film measurements. This is important as it directly influences the properties of the aggregates formed in the final film. So, by considering  $T_{ch/film}$  rather than  $T_{c/solution}$ , one can conclude that in the case of film deposition at  $T_s > T_{ch/film}$  the aggregates formed are characterized by higher disorder and lower 0-0/0-1 while for the case of blade coating at  $T_s < T_{ch/film}$  the aggregates formed show the opposite properties.

### iii. Temporal evolution of the aggregation process

In the next sections, I investigate the aggregate formation dynamics during the deposition process under different conditions. I first focus on the temporal evolution of the P3HT aggregate formation dynamics for films blade coated from CF solutions at three temperature points covering a wide range of deposition temperatures. These temperature points are  $T_s = 5^\circ\text{C}$  and  $T_s = 25^\circ\text{C}$  corresponding to the two limiting cases at  $T_s$  sufficiently lower and higher than  $T_{ch/film}$  and at  $T_s = 15^\circ\text{C}$  corresponding to an intermediate case where  $T_s \approx T_{ch/film}$ . The important question here is under which conditions during the blade coating process aggregates form and how these conditions impact their final properties. This understanding then would allow us to manipulate the aggregate formation dynamics beyond the simple route of solvent choice and film deposition below or above  $T_c$ .

Figure 9.a top panel shows the photoluminescence and absorption 2D maps of the aggregate evolution during blade coating of a P3HT film from a CF solution at  $T_s = 5^\circ\text{C}$ . The second panel shows the normalized intensity of aggregate emission and absorption, which is an indication of the fraction of aggregates formed during the whole process. The bottom two panels show the corresponding values of  $\sigma$  and 0-0/0-1 extracted from fitting the individual spectra of photoluminescence and absorption for both films during the whole process. Figure 9.b shows selected absorption and emission spectra at different times during blade coating. Both the total spectra and the aggregate

spectra are shown. The aggregate spectra were extracted following the same procedure introduced earlier.

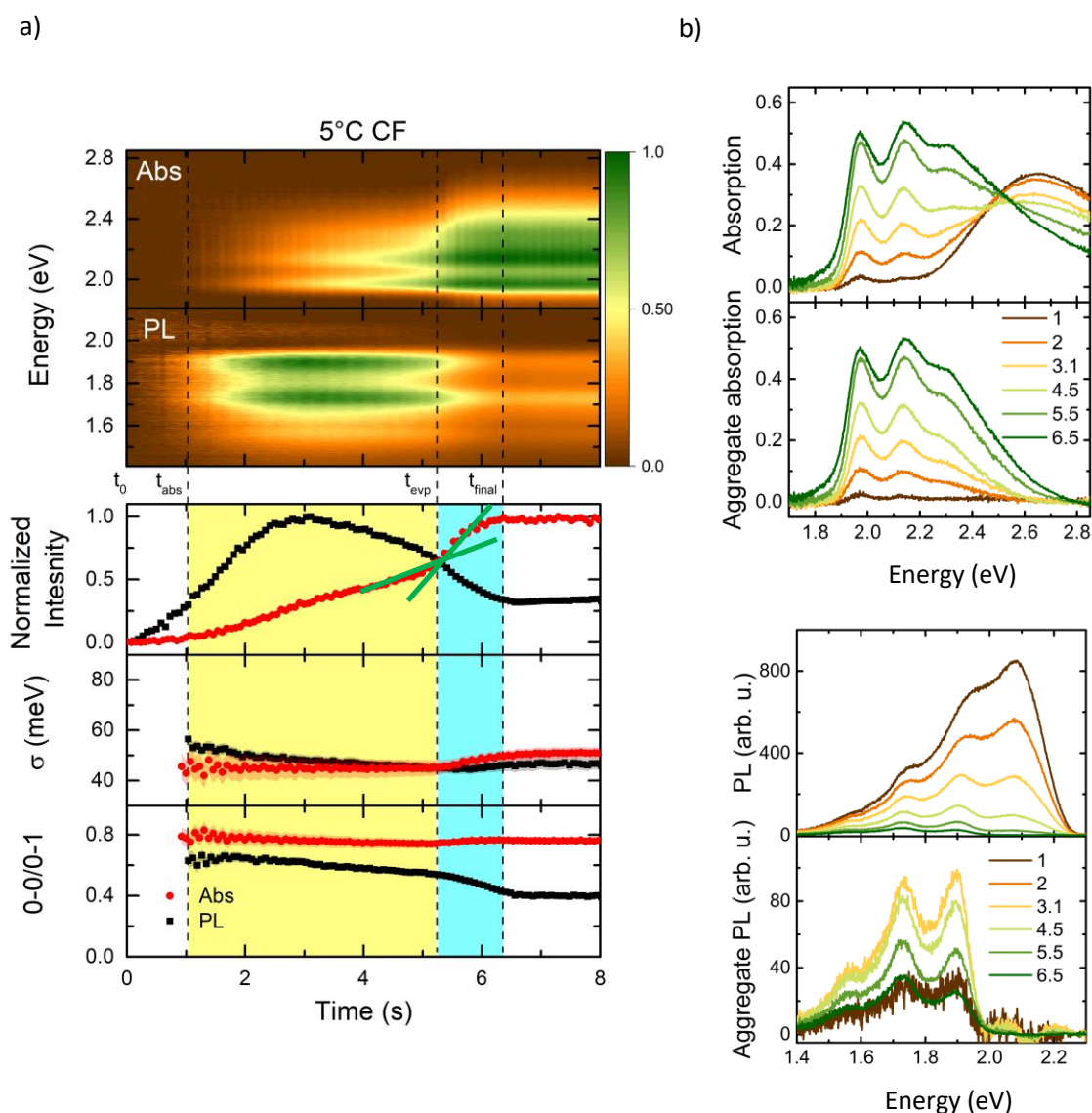


**Figure 9: Photoluminescence and absorption spectra of the P3HT aggregates during blade coating of films from CF solutions at  $T_s = 5$  °C. a) The Top panels show the 2D heat maps of photoluminescence and absorption. The bottom panels show the normalized photoluminescence (black squares) and absorption (red circles) intensities, the  $\sigma$  values and the 0-0/0-1 peak ratio extracted from fitting the photoluminescence and the absorption spectra using FCA. The red and black shadowed regions around the data points represent the error. The green lines drawn over the normalized absorption intensity is a schematic representation of the slope at different times during blade coating. b) Selected spectra at different times during blade coating showing the total and aggregate-only photoluminescence and absorption.**

I specified four different time steps that allow us to quantify, track and compare the aggregate formation dynamics while blade coating at the different temperatures. Firstly,  $t_0 = 0$  s is the starting

time defined by the appearance of the first spectra after the blade has already passed over the solution. Secondly,  $t_{abs}$  is the time at which aggregate absorption starts to occur as evident by the appearance of the absorption peaks in the lower energy band below 2.2 eV. This is quantitatively determined as the time at which absorption intensity exceeds  $\approx 2-3\%$  (calculated as integrated area of the aggregate only absorption spectra). Thirdly,  $t_{evp}$  is the time at which the solvent is evaporated to the extent allowing the solid film formation. This is determined at the time where we have a noticeable change in the emission or absorption intensity as marked by a change in the slopes of their normalized integrated intensity. The two green lines shown in the figure represent the slopes of the normalized absorption intensity at different times. The intersection of these two lines roughly coincides with  $t_{evp}$ . This is also then noticeable in the trends for  $\sigma$  and 0-0/0-1 where we have a sudden change in the trend steepness or direction. Finally,  $t_{final}$ , which is the time after which no further changes are observed in the spectra. This is reflected as stable values for  $\sigma$  and 0-0/0-1.

From the normalized intensity, we firstly observe emission from the aggregates directly after  $t = 0$  s with no apparent absorption until  $t_{abs}$ . We then observe a gradual increase of the aggregate absorption intensity over an extended time range between around  $t_{abs} \approx 1.0$  s until  $t_{evp} \approx 5.1$  s (yellow region). During this time, the emission intensity reaches a maximum at  $t \approx 3.0$  s with a subsequent decrease until  $t_{final}$ . Between  $t_{evp} \approx 5.1$  s and  $t_{final} \approx 6.4$  s we observe a faster rate of increase of the absorption intensity with a further decrease of the emission intensity (blue region) after which no further changes are observed. Concomitantly,  $\sigma_{PL}$  and 0-0/0-1<sub>PL</sub> both start at high values and decrease within the time between  $t_{abs}$  and  $t_{evp}$  ( $\sigma_{PL}$  from 55 meV to 45 meV, 0-0/0-1<sub>PL</sub> from 0.65 to 0.55). After  $t_{evp}$ ,  $\sigma_{PL}$  slightly increases, (to 47 meV at  $t_{final}$ ) while 0-0/0-1<sub>PL</sub> continues to further decrease to reach a value of 0.4 at  $t_{final}$ . The changes in their absorption counterparts is much smaller.  $\sigma_{Abs}$  stays constant until  $t_{evp}$  where it then increases slightly until reaching its final value (45 meV to 51 meV). 0-0/0-1<sub>Abs</sub> shows a similar behavior where it slightly decreases until  $t_{evp}$  and then increases back to near its original starting value of 0.76 at  $t_{final}$ .

I then move to the next temperature point at  $T_s = 15^\circ\text{C}$ . From figure 8 it was already observed that the values of  $\sigma$  and 0-0/0-1 peak ratio for the blade coated film at  $15^\circ\text{C}$  ( $\approx T_{c/film}$ ) are very similar to the values for the films blade coated at  $T_s$  lower than  $T_{c/film}$  ( $5^\circ\text{C}$  and  $10^\circ\text{C}$ ). Figure 10.a shows the in-situ aggregate absorption and emission 2D maps along with the temporal evolution of the aggregate intensity,  $\sigma$  and 0-0/0-1 peak ratio for a P3HT film blade coated at  $T_s = 15^\circ\text{C}$  in a similar arrangement to figure 9.a. In addition, similar to figure 9b, figure 10.b shows selected total and aggregate only absorption and emission spectra at different times during blade coating.

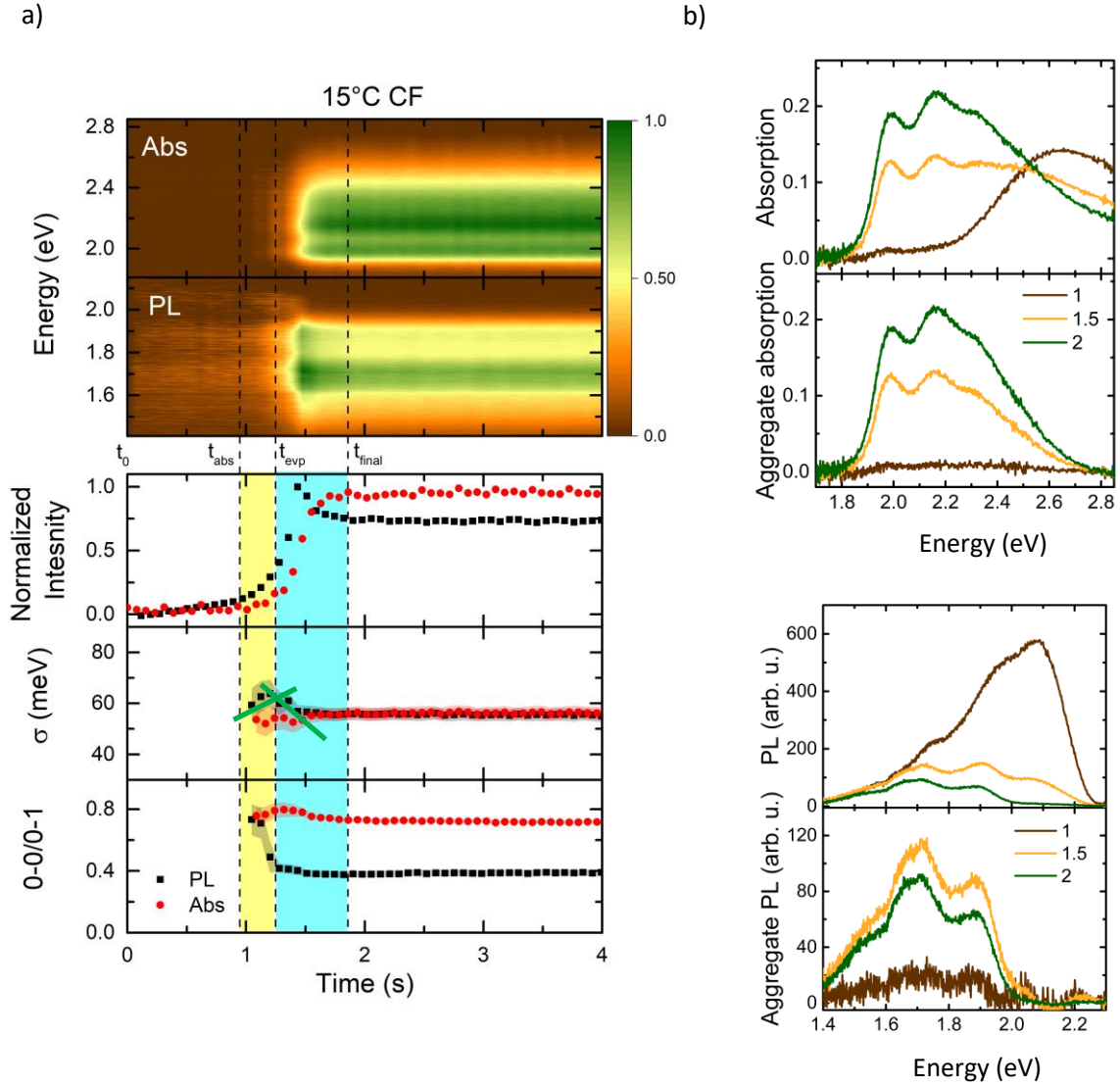


**Figure 10: Photoluminescence and absorption spectra of the P3HT aggregates during blade coating of films from CF solutions at  $T_s = 15$  °C. a) The Top panels show the 2D heat maps of photoluminescence and absorption. The bottom panels show the normalized photoluminescence (black squares) and absorption (red circles) intensities, the  $\sigma$  values and the 0-0/0-1 peak ratio extracted from fitting the photoluminescence and the absorption spectra using FCA. The red and black shadowed regions around the data points represent the error. The green lines drawn over the  $\sigma$  values is a schematic representation of the slope at different times during blade coating. b) Selected spectra at different times during blade coating showing the total and aggregate-only photoluminescence and absorption.**

Indeed, in figure 10.a we observe that aggregates form within the solution phase between  $t_{abs} \approx 0.95$ s and  $t_{evp} \approx 1.25$ s (yellow shaded area) with  $\sigma_{Abs} \approx 55$  meV and  $0-0/0-1_{Abs} \approx 0.75$ . This solution phase is followed by the solvent evaporation phase (blue shaded area) where  $\sigma_{Abs}$   $0-0/0-1_{Abs}$  does not vary much until reaching their final values at  $t_{final} \approx 1.8$  s. It is worth noting that although the time allowed for aggregates to form before  $t_{evp}$  which is very short (less than 0.5 s) in the film blade coated at 15°C, the final values of  $\sigma$  and 0-0/0-1 are nearly similar to that for the aggregates present

in the film blade coated at 5°C (Figure 9.a). This is quite surprising given that the time allowed for aggregates to form during this phase in the latter case is about 7 times longer ( $\approx 3.5$  s). This raises the question about the impact of the time allowed for aggregates to form in solution prior to solidification for determining the final aggregate properties.

Despite this difference between the aggregate formation dynamics at 5°C and 15°C, the aggregate properties at both temperatures are similar. The aggregates present in the film blade coated at 5°C and 15°C are characterized by similar disorder within their error ranges ( $\sigma_{\text{Abs}}$  at 5°C  $\approx \sigma_{\text{Abs}}$  at 15°C in the range of 55 meV) and similar chain planarity within their error ranges (0-0/0-1<sub>Abs</sub> at 5°C  $\approx$  0-0/0-1<sub>Abs</sub> at 15°C in the range of 0.75). To get a clearer picture about the impact of the time allowed for aggregates to form in the period between  $t_{\text{abs}}$  and  $t_{\text{evp}}$ , I move forward to investigate the aggregate formation dynamic at a temperature above  $T_{\text{ch/film}}$ .

Figure 11.a shows the in-situ aggregate absorption and emission 2D maps along with the temporal evolution of the aggregate intensity,  $\sigma$  and 0-0/0-1 peak ratio for a P3HT film blade coated from a CF solution at  $T_s = 25^\circ\text{C}$  in a similar arrangement to the previous two figure. Figure 11.b shows selected total and aggregate only absorption and emission spectra at different times during blade coating. Opposite to the films blade coated at 5°C and 15°C, the film blade coated at 25°C show a different behavior, with more abrupt changes during the film formation process. Although at higher temperatures the solvent is expected to evaporate faster, absorption from the P3HT aggregates appear later at around  $t_{\text{abs}} \approx 1.5$  s (vs.  $t_{\text{abs}} \approx 1$  s for 5°C and 15°C). It is important to point out that the noticeable PL signal appearing around 2 eV after a short time from  $t_0$  and before  $t_{\text{abs}}$  is not real emission from the solvent layer. This is an artifact due to normalizing the amorphous contribution to the high-energy end of the total spectra and subtracting it to extract the aggregate emission as explained at the beginning of this chapter.

It can be then observed that opposite to the films blade coated at 5°C and 15°C, the PL and absorption intensity of the aggregates increase abruptly quasi-simultaneously where both reach maximum values within less than 0.5s (which corresponds to about four subsequent frames recorded with the CCD camera). Consequently, at 25°C, I considered  $t_{\text{abs}}$  and  $t_{\text{evp}}$  to be the same and that aggregation occurs at the same time as the significant solvent evaporation with no significant aggregation forming prior to that time. After  $t_{\text{final}} \approx 1.9$  s, we observe no further changes in the spectra. The evolution of  $\sigma$  and 0-0/0-1 for both PL and absorption almost follow the same trend as the second phase of the aggregate evolution for the film blade coated from 5°C and 15°C (compare only the blue region in both cases). Despite considering  $t_{\text{abs}}$  and  $t_{\text{evp}}$  to coincide in the case of  $T_s = 15^\circ\text{C}$ , if one examines closely the first couple of frames at  $t_{\text{abs}}$  (1.5 s and 1.6 s) a change of slope is

observed for the normalized absorption intensity indicated by the two green lines. This could mean that a region between  $t_{\text{abs}}$  and  $t_{\text{evp}}$  (the yellow region discussed for the other temperatures) might be present during film formation but is not resolved within our setup resolution. Nevertheless, assuming that this is true, it does not influence the final aggregate properties in the formed film reflected by the final values of  $\sigma$  and 0-0/0-1.

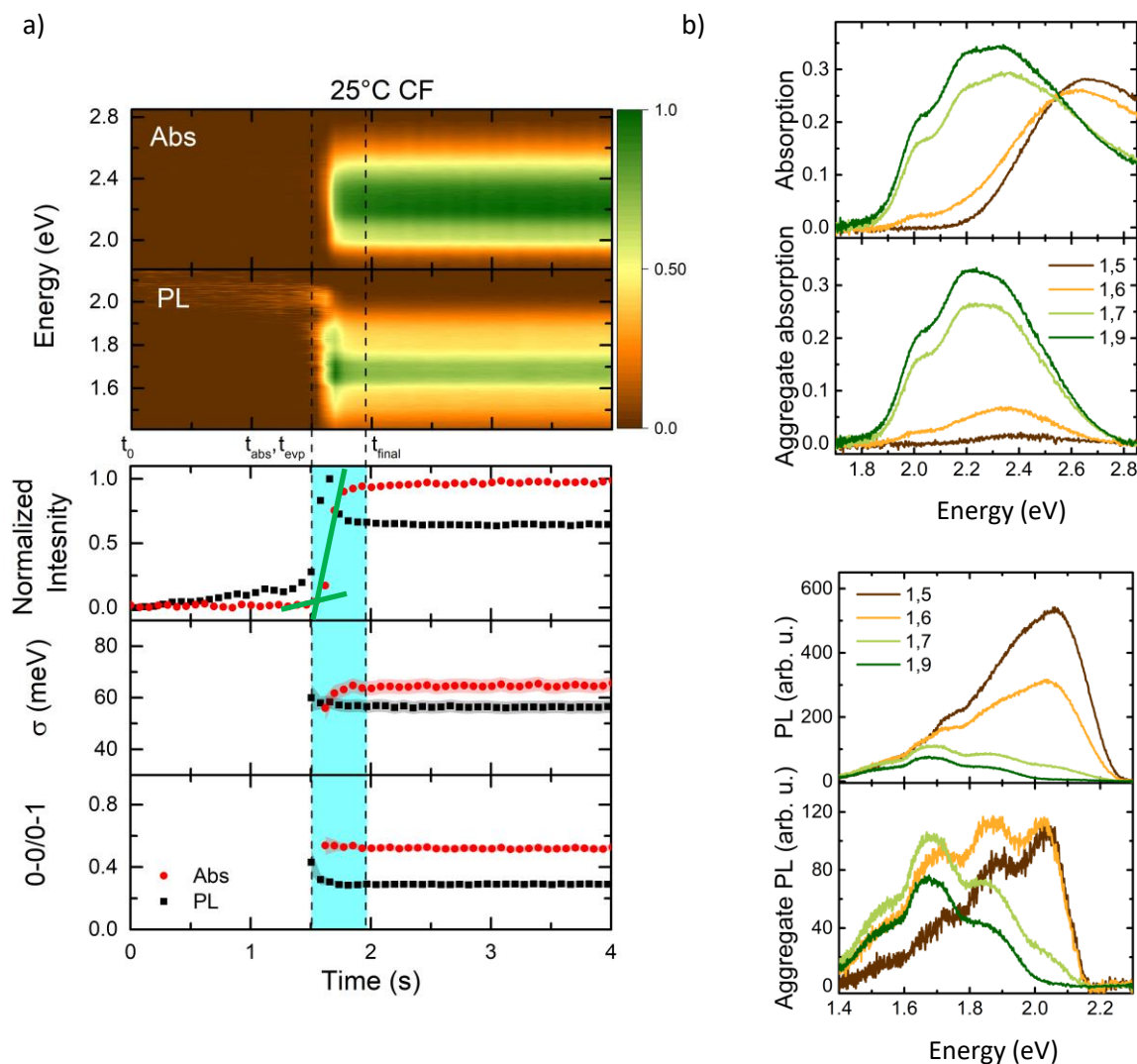


**Figure 11: Photoluminescence and absorption spectra of the P3HT aggregates during blade coating of films from CF solutions at  $T_s = 25$  °C. a) The Top panels show the 2D heat maps of photoluminescence and absorption. The bottom panels show the normalized photoluminescence (black squares) and absorption (red circles) intensities, the  $\sigma$  values and the 0-0/0-1 peak ratio extracted from fitting the photoluminescence and the absorption spectra using FCA. The red and black shadowed regions around the data points represent the error. The green lines drawn over the normalized absorption intensity is a schematic representation of the slope at different times during blade coating. b) Selected spectra at different times during blade coating showing the total and aggregate-only photoluminescence and absorption**

In general, the final films blade coated at 5°C and 15°C show lower  $\sigma$  and higher 0-0/0-1 peak ratios compared to that blade coated at 25°C. By observing the differences of the aggregate formation dynamics at these three temperatures, I conclude that aggregate formation during film deposition follows one of two paths. The aggregate formation following these paths can be considered as either a 2-step or a quasi-1-step process. On one hand, at 5°C and 15°C we observe the occurrence of a 2-step aggregate formation process. We have at the beginning what we can call a pre-aggregation phase where aggregates start to form gradually in solution. During this phase as the solvent evaporates, the polymer concentration increases within the solution accompanied by the formation of aggregates. During this initial phase, the polymer chains have the time to planarize and order without mobility restrictions. The 2<sup>nd</sup> step starts when a critical polymer concentration is reached upon significant solvent evaporation where the solid film starts to form. Within this phase the aggregates properties evolve under more mobility restricted conditions for the polymer chains. On the other hand, at 25°C we observe a quasi-1-step process where aggregate formation is not apparent in the solution and only occurs directly at a critical polymer concentration upon significant solvent evaporation with a fast formation process. In this case, one could consider that the aggregates form under more restricted conditions for the polymer chains in terms of their mobility and planarization. This is reflected in the final aggregates' properties characterized by more disorder and lower molecular coupling.

From the above conclusion, I would like to point out to two important considerations to look out for when investigating the time allowed for aggregates to form in solution:

- 1- The change between the two aggregate formation pathways (2-step vs 1-step) should not be thought of with an abrupt separation. In other words, as the deposition temperature increases and becomes in the vicinity of  $T_{ch}$ , the window allowed for aggregates to form in solution is reduced. This reduction reaches a point where its presence has no significant effect on the properties of the formed aggregates and the aggregate formation follows a 1-step pathway. This means that a careful choice of the deposition temperature would allow us to fine-tune the time span of this window and target the desired aggregate properties.
- 2- While fine-tuning of the window allowed for aggregates to form in solution is possible to change between a 2-step and 1-step aggregation pathway, it does not have to span a long period within the film deposition process.
- 3- In theory, the minimum width of this window that would allow for aggregate formation following a 2-step process can be determined. Nevertheless, this needs a setup with low

temporal resolution and examining several deposition temperatures with a narrow range in the vicinity of  $T_{ch}$ .

Having had a generalized picture regarding the aggregate formation pathways, it is interesting to investigate the possibility of redirecting the aggregate formation between the 1-step and the 2-step process by varying certain processing conditions to obtain the desired aggregate properties in the final film.

#### iv. Controlling the initial aggregate formation

The easiest approach that would allow for redirecting the aggregate formation between the 1-step and the 2-step process would be to manipulate the solvent's evaporation. By controlling the solvent's evaporation, one would assume that having a slower solvent evaporation would allow more time for aggregates to form in solution prior to the solid film formation and vice versa. Reducing the solvent evaporation was done via blade coating a P3HT film from a THF solution under THF rich atmosphere which in theory should allow aggregates to start forming in solution even at  $T_s > T_{ch/film}$ .

Figure 12 shows the in-situ aggregate absorption and emission 2D maps along with the temporal evolution of the aggregate intensity, disorder parameter  $\sigma$  and 0-0/0-1 peak ratio for two P3HT films blade coated at 35°C under normal conditions (12.a) and under a THF rich atmosphere (12.b). The difference between the two cases can be readily observed from the time windows within the shaded blue and yellow areas. The film blade coated under normal conditions at  $T_s = 35^\circ\text{C}$  shows a similar behavior as already discussed for the film blade coated from CF solution at 25°C (figure 9.b). The aggregate formation in this case happens upon sufficient solvent evaporation with no signs of aggregate formation in solution. Within a short time window between  $t_{start} \approx t_{solid} \approx 0.35$  s and  $t_{final} \approx 0.85$  s the whole aggregation process is completed. We hardly observe any variation of the  $\sigma$  values over the whole process while we observe a slight reduction of the 0-0/0-1 ratio between  $t_{start}/t_{solid}$  and  $t_{final}$  (from 0.67 to 0.43 for 0-0/0-1<sub>Abs</sub> and from 0.4 to 0.34 for 0-0/0-1<sub>PL</sub>). Moving on to the film blade coated under saturated solvent atmosphere, we readily observe two main differences. Firstly,  $t_{start}$  shifts to much later times after starting the process ( $\approx 1.9$  s) which indicates the reduced evaporation rate of THF. Secondly, we observe the appearance of aggregate emission prior to aggregate absorption and a two-step variation of the evolution of the  $\sigma$  and the 0-0/0-1 values similar to the case of blade coating from CF solutions at  $T_s = 5^\circ\text{C}$ . This indicates that some aggregates form in solution prior to solvent evaporation within a very small time window ( $t_{start} \approx 1.9$  s to  $t_{solid} \approx 2.3$  s) similar to the case of blade coating from a CF solution at

15°C (fig 10.a). Within this time window ( $\approx 0.4$  s) indicated by the yellow region, we observe a reduction in  $\sigma_{PL}$  accompanied by an increase in 0-0/0-1<sub>PL</sub>.

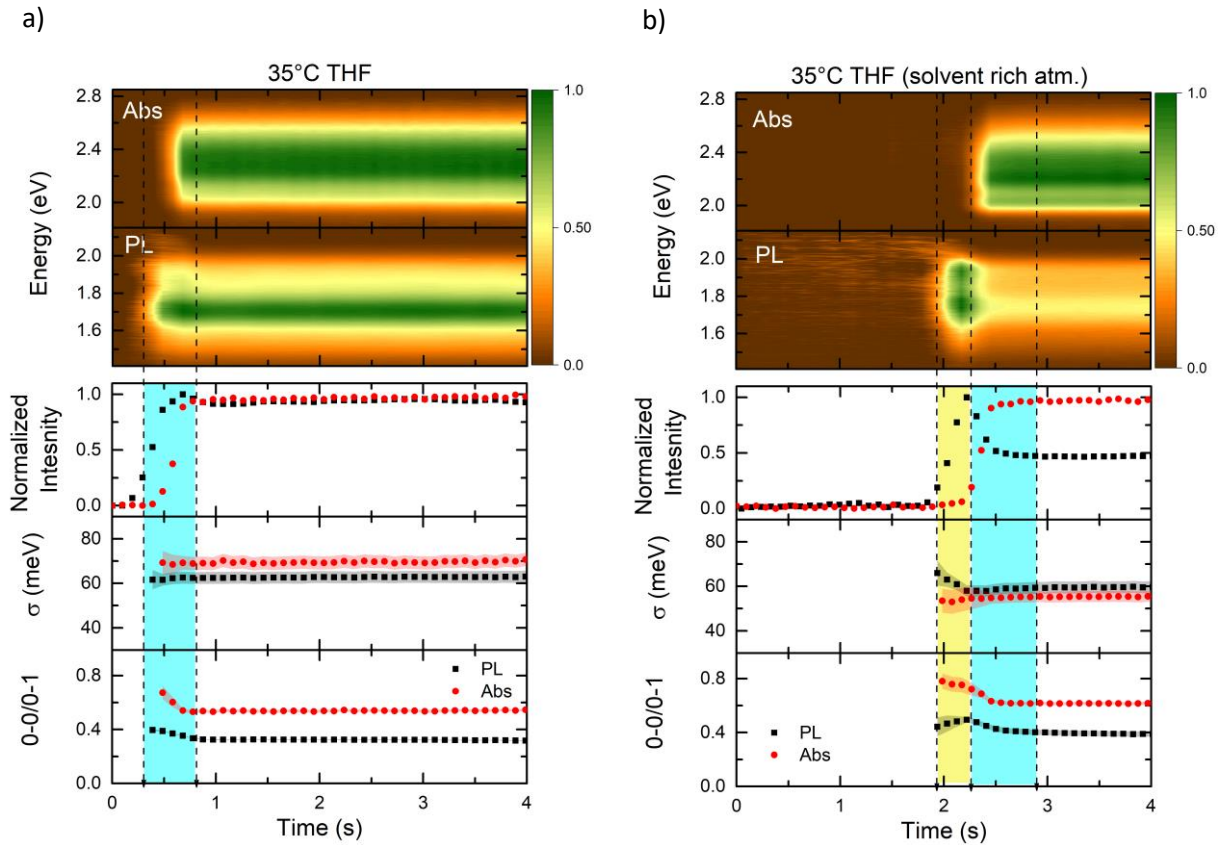


**Figure 12: Photoluminescence and absorption spectra of the P3HT aggregates during blade coating of the films from THF solutions at  $T_s = 35$  °C under a) normal atmospheric conditions and b) THF rich atmosphere. The top panels show the 2D heat maps of photoluminescence and absorption. The bottom panels show the normalized photoluminescence (black squares) and absorption (red circles) intensities, the disorder parameter  $\sigma$  and the 0-0/0-1 peak ratio extracted from fitting the photoluminescence and absorption spectra using FCA. The red and black shadowed regions around the data points represent the error ranges of the parameter values.**

Both of these trends might indicate the presence of chain planarization and ordering within the solution prior to solvent evaporation. Conversely, we observe no significant change in  $\sigma_{Abs}$  while 0-0/0-1<sub>Abs</sub> decrease slightly (0.78 to 0.75), yet within the error range. Following this step and upon the appearance of the aggregate absorption, the evolution of  $\sigma$  and 0-0/0-1 extracted from both photoluminescence and absorption follow closely the same trend observed within the same time window of the film blade coated under normal conditions. This further confirms that the behavior between  $t_{start} \approx 1.9$  s and  $t_{solid} \approx 2.3$  s for the film blade coated under saturated THF atmosphere is

indeed due to the formation of aggregates in solution. This was a result of delaying the onset of THF evaporation by reducing its evaporation rate. By comparing the final  $\sigma$  and the 0-0/0-1 values from both films, we observe the reduction of  $\sigma_{\text{Abs}}$  (70 meV to 56 meV) and the increase of 0-0/0-1 peak ratio (0.54 to 0.62) as a function of blade coating under a reduced solvent evaporation. The same is observed for  $\sigma_{\text{PL}}$  (63 meV to 59 meV) and 0-0/0-1<sub>PL</sub> (0.31 to 0.39).

From all the above, one can conclude that the film blade coated in a solvent rich atmosphere (while all the other conditions are kept constant) produced aggregates characterized by reduced disorder and more planar chains compared to the film blade coated without manipulating the solvent's evaporation. Blade coating in a solvent rich atmosphere would result in a reduced solvent evaporation. This reduced evaporation would give time for aggregates to start forming in the solution within a very short time window before sufficient solvent evaporation. This result confirms that it is possible to switch between the possible aggregation pathways by fine-tuning of the solvent evaporation. This would allow one to target the desired aggregate properties as needed.

#### v. The effect of blending

As already shown, it is apparent that controlling the aggregate formation- although it is a complex process- is possible by careful choice of the different deposition parameters. From an application point of view, most devices employ conjugated polymers in their photoactive layer in combination with other materials. This photoactive layer in a solar cell is comprised of a blend of two or more components including conjugated polymers, small molecules or even fullerenes. In this respect, it is important to understand how the addition of an extra material influences the aggregate formation dynamics of the conjugated polymer and their final properties in the blend. Based on this understanding, the ultimate goal is then to target the optimum blend morphology that would provide the best device performance.

I have already concluded in chapter 3 that the addition of an extra material to PCE11 leads to more ordered aggregates. Nevertheless, the underlying reasons were not investigated due to the complex fitting process of PCE11. This makes it hard to analyze PCE11 film formation using a similar approach to the one taken to analyze the aggregate formation in P3HT. So, the aim of this part is it to analyze the temporal evolution of P3HT:PEO blend films as a model system to try to understand the effect of PEO on the aggregate formation as compared to neat P3HT. In this respect, it also will be interesting to see in what way blending can be considered as a processing parameter in the general aggregation picture that is developed in the framework of this work. Similar to HDPE used with PCE11 in chapter 3, PEO is a non-photoactive polymer, so it offers the same benefits of no electronic interaction with P3HT and thus no alteration to the optical spectra of P3HT aggregates is

expected. As a first step to separate the blending effect from the other processing conditions, I investigate the effect of blending on the the critical transition temperature ( $T_c$ ) of P3HT estimated from the fitted film aggregate spectra. For ease of comparison, I focus on films blade coated from neat P3HT and P3HT:PEO from CF solutions. Figure 13 shows the the overall absorption spectra of P3HT:PEO films deposited from a CF solution at substrate temperatures between 10°C and 30°C at 5°C temperature steps. In addition, the corresponding aggregate and amorphous contributions along with the fits of the aggregate spectra are shown.

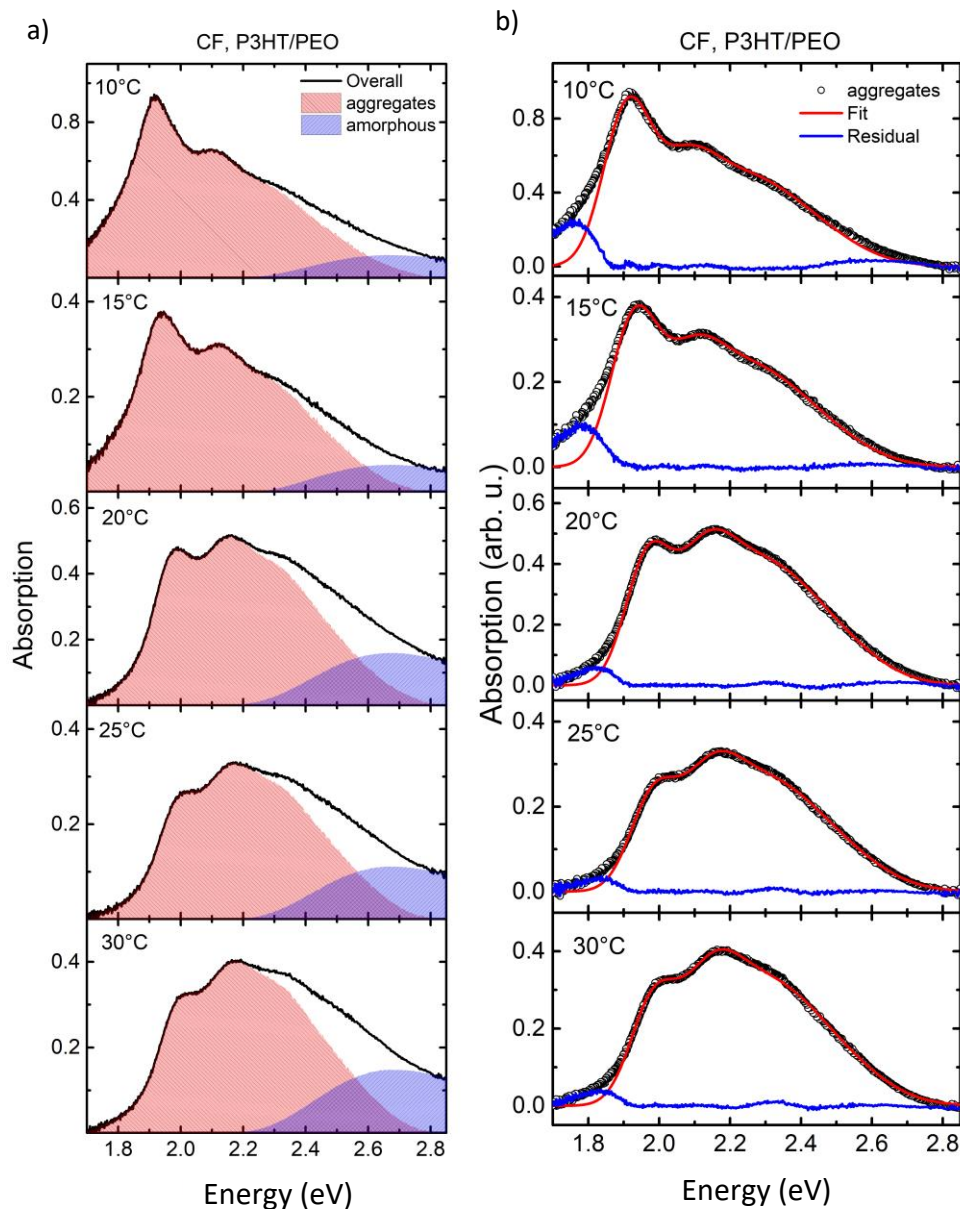


**Figure 13:** a) The Total absorption spectra showing the aggregate absorption contribution (red area) and the amorphous contribution (blue area) of P3HT:PEO films deposited from a CF solution at different temperatures taken at 5°C steps. b) Aggregate absorption spectra (hollow circles) corresponding to the red area from a). The solid red lines represent the fits for each film using eq.2 and the solid blue lines represent the difference between the data and the fits.

Similar to the neat P3HT films deposited from the CF solution (figure 6), the onset of the absorption spectra shifts to higher energies and the 0-0/0-1 peak ratio decreases as the temperature increases. Nevertheless, the spectra of the P3HT:PEO films blade coated at 5°C and 10°C show clear differences to the neat P3HT films blade coated at the same temperatures (figure 6). Firstly, a signal below 1.8 eV is observed in the absorption spectra of P3HT:PEO films along with a peculiar line shape that could be attributed to scattering. Secondly, the 0-0 peak intensity is notably higher for the P3HT:PEO films compared to the neat P3HT blade coated films. The temperature dependent  $\sigma$  and 0-0/0-1 are then extracted from the fits to estimate  $T_c$  in the case of P3HT:PEO.

Figure 14 shows the temperature dependent aggregate absorption spectra of the final P3HT:PEO films along with the temperature dependent  $\sigma$  and 0-0/0-1 extracted by fitting these spectra (black squares). For comparison the  $\sigma$  and 0-0/0-1 for the neat P3HT film is shown (red squares). For the P3HT:PEO films, the 0-0 transition peak ( $E_{0-0}$ ) shows a significant shift ( $\approx 80$  meV) towards higher energies as the films are blade coated at higher  $T_s$  ( $E_{0-0}$  (10°C)  $\approx 1.92$  eV vs.  $E_{0-0}$  (30°C)  $\approx 2$  eV). The extracted  $\sigma$  and 0-0/0-1 values show similar a trend for both the neat and blend film where no significant change in  $T_c$  is observed albeit a significant difference in the absolute extracted values.

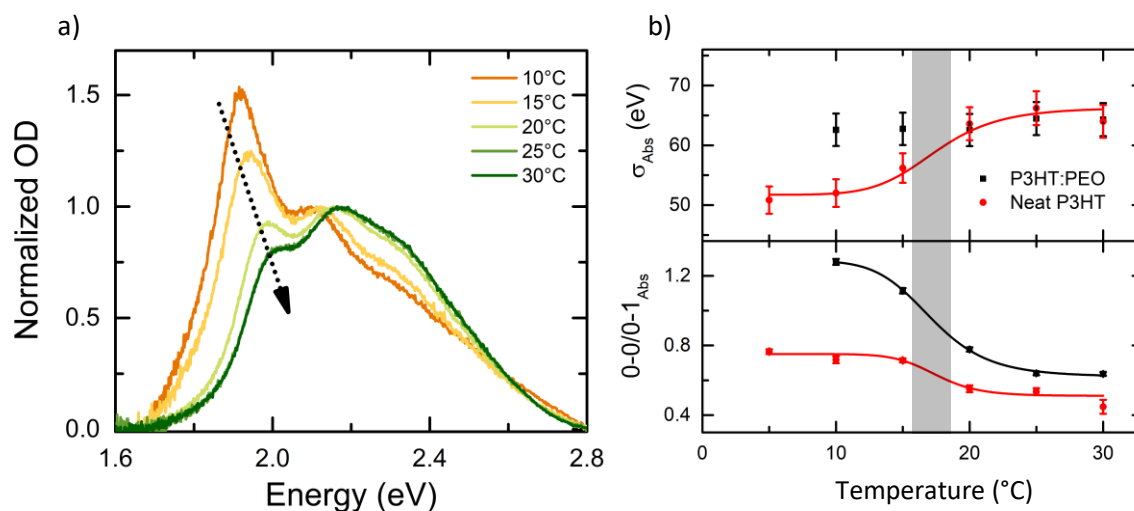


**Figure 14: a) Final film aggregate spectra of P3HT:PEO films blade coated from CF solutions at different temperatures, b) Extracted  $\sigma_{Abs}$  (top panel) and 0-0/0-1 $_{Abs}$  (bottom panel) from the final aggregate film spectra of blend P3HT:PEO (black squares) and neat P3HT (red circles) with the sigmoidal fits shown as the red and black lines. The black area shows the region of  $T_c$  for the P3HT:PEO film.**

For P3HT:PEO, I estimated  $T_{ch/film}$  from the inflection point along the sigmoidal curve of 0-0/0-1 $_{Abs}$  following a similar approach shown in figure 14. The estimated value is  $17.1 \pm 1.5$  °C compared to  $15.5 \pm 2.5$  °C for the neat P3HT films. Concerning the 0-0/0-1 peak ratio in the absorption spectra, its absolute value for the blended films is much higher than that of the neat film over the whole temperature range. This means that for P3HT:PEO blends regardless of blade coating below or

above  $T_c$ , we end up with aggregates having an enhanced 0-0/0-1 ratio compared to the aggregates formed in the neat P3HT films. The difference is more noticeable at  $T_s < T_c$  where we observe  $\approx 80\%$  increase in the 0-0/0-1 ratio for blend films blade coated at the same  $T_s$  as the neat P3HT reference film (0.71 vs. 1.28 at  $10^\circ\text{C}$ ). This difference is much smaller when blade coating the blends above  $T_c$  albeit these values are near the values of the 0-0/0-1 peak ratio for the neat films blade coated below  $T_c$  (0.71 at  $10^\circ\text{C}$  (neat) vs. 0.65 at  $25^\circ\text{C}$  (blend)). It is important to note that the 0-0/0-1 values higher than 1 for the blend films blade coated at  $10^\circ\text{C}$  and  $15^\circ\text{C}$  might be indicative of a J-like orientation [37]. On the contrary, the  $\sigma$  values of the blend show no significant variation over the whole temperature range (62 meV at  $10^\circ\text{C}$  vs. 64 meV at  $30^\circ\text{C}$ ). Similar to the 0-0/0-1 peak ratio, the difference between  $\sigma_{\text{neat}}$  and  $\sigma_{\text{blend}}$  is more apparent when blade coating at  $T_s < T_c$  ( $\sigma_{\text{neat}} = 52$  meV vs.  $\sigma_{\text{blend}} \approx 62$  meV at  $10^\circ\text{C}$ ). This difference diminishes as films are blade coated at higher  $T_s$  until  $\sigma_{\text{neat}} \approx \sigma_{\text{blend}}$  at  $30^\circ\text{C}$ . This result shows that for P3HT:PEO blends, blade coating below or above  $T_c$  does not have a big impact on the disorder within the aggregates opposite to the case of P3HT neat films.

For a better understanding of the underlying reason for this behavior, I compare the temporal evolution of the aggregates when blade coating neat P3HT and blend P3HT:PEO from CF solutions. Figure 15 shows the in-situ aggregate absorption and emission 2D maps along with the temporal evolution of the integrated aggregate intensity,  $\sigma$  and 0-0/0-1 peak ratio for neat and blend films. The data corresponding to the neat film blade coated at  $25^\circ\text{C}$  has been already discussed previously (figure 11.a). Therefore, I focus on the different behavior observed for the blend P3HT:PEO film.

The first observed difference is the shift of  $t_{\text{abs}}$  of the blend film compared to the neat film to a later time (3.4 s vs. 1.5 s). This is an indicator of a reduced solvent evaporation rate as a consequence of blending P3HT with PEO. Secondly, we observe the appearance of aggregate emission at much earlier times than aggregate absorption and for a longer time compared to the neat film. The aggregate emission reaches  $\approx 65\%$  of its maximum value within  $\approx 2$  s before aggregate absorption appears compared to  $\approx 25\%$  within  $\approx 1$  s for the neat film.

One can further observe that between  $t_{\text{evp}}$  and  $t_{\text{final}}$  the evolution of both  $\sigma_{\text{PL}}$  and 0-0/0-1<sub>PL</sub> follow the same behavior observed during the same time window in the neat P3HT film at  $25^\circ\text{C}$ . For both the neat and blend films both  $\sigma_{\text{PL}}$  and 0-0/0-1<sub>PL</sub> decrease slightly after  $t_{\text{evp}}$  within a very short time span ( $\approx 0.2\text{s}$ ) within which they reach their final value. After  $t_{\text{evp}}$  we start to observe a sharp rise in aggregate absorption indicating the aggregate formation upon solvent evaporation.  $\sigma_{\text{Abs}}$  for both the neat and blend film show a similar behavior, with the exception that for the neat film  $\sigma_{\text{Abs}}$  increases slightly between  $t_{\text{abs}}/t_{\text{evp}}$  and  $t_{\text{final}}$ . Nevertheless, we end up with the same  $\sigma_{\text{Abs}}$  for both

the neat and the blend films. Opposite to  $\sigma_{Abs}$ ,  $0-0/0-1_{Abs}$  shows a different behavior in the blend film compared to the neat film. Whereas  $0-0/0-1_{Abs}$  in the neat film is almost constant over the whole process,  $0-0/0-1_{Abs}$  for the blend film decreases after  $t_{abs}/t_{evp}$  until around 4 s and then increases slightly until  $t_{final}$  (0.74 to 0.61 to 0.64). This difference is apparent in the final values where  $0-0/0-1_{Abs}$  for the P3HT: PEO is considerably higher than the value for neat P3HT (0.64 vs 0.51). Finally, we observe that the time window between  $t_{evp}$  and  $t_{final}$  for the blend film is much longer than that of the neat film (2.5 s vs. 0.5 s) which might be a consequence of slower solvent evaporation. All these observations indicate that the aggregate formation in both the neat and blend films blade coated at 25°C follow a 1-step pathway, yet the  $0-0/0-1$  peak ratio of aggregates in the final film show a significant difference.

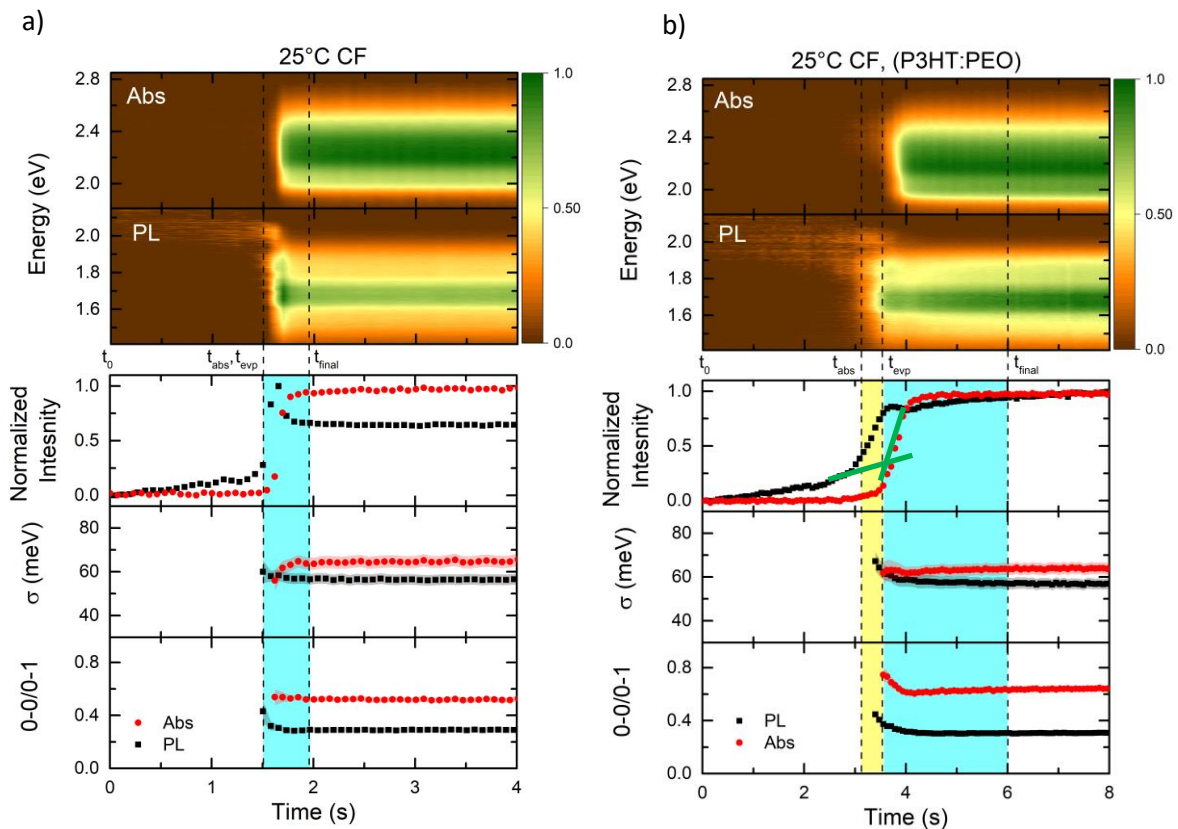


**Figure 15: Photoluminescence and absorption spectra of the P3HT aggregates during blade coating of films at  $T_s = 25^\circ\text{C}$  from a) neat P3HT CF solutions and b) blend P3HT:PEO CF solutions. The Top panels show the 2D heat maps of photoluminescence and absorption. The bottom panels show the normalized photoluminescence (black squares) and absorption (red circles) intensities, the  $\sigma$  and the  $0-0/0-1$  peak ratio extracted from fitting the photoluminescence and absorption spectra using FCA. The red and black shadowed regions around the data points represent the error.**

## 4.5 Discussion

Understanding the pathways through which aggregates form during solution processing of conjugated polymer films is a crucial step towards better control of film microstructure, which is reflected in the performance of organic optoelectronic devices. This understanding would allow us to manipulate the film processing conditions to reach the desired aggregate properties for a specific application in a systematic manner. As evident by the results shown in this chapter, the aggregate formation during deposition of conjugated polymer films is a complex process with several interacting factors determining the outcome.

It has been already established that an important factor determining the type of aggregates present in the final film is the deposition temperature relative to the solution's  $T_c$ . For PCE11, having  $T_{c/solution} \approx 48^\circ\text{C}$ , spin coating at  $T_s$  sufficiently lower ( $\approx 22^\circ\text{C}$ ) than  $T_c$  results in aggregates characterized by higher 0-0/0-1 peak ratio compared to those present in the film spin coated at  $T_s$  sufficiently higher than  $T_c$  ( $\approx 70^\circ\text{C}$ )[18]. Based on the weakly interacting H-aggregates model, this was interpreted as an increased intra-chain coupling relative to the inter-chain counterpart [5]. The underlying mechanism was attributed to the formation of aggregate nucleation sites in the solution prior to solvent evaporation in the case of  $T_s < T_c$ . However, the reasons why these aggregates adopt a more planar conformation evidenced by the higher 0-0 absorption peak ratio was not investigated. I confirmed that the above results are also true for P3HT in the extreme cases where  $T_s$  is sufficiently higher or lower than  $T_c$ . Nevertheless, this does not take into account other parameters that would affect the aggregate properties when depositing films at temperatures  $T_s \approx T_c$ .

As a first step, I have shown that  $T_c$  extracted from solution measurements is not always an accurate representation of the actual  $T_c$  that should be considered when choosing the film deposition temperature. As shown for P3HT in CF (the better solvent),  $T_{c/solution}$  was lower than  $T_{ch/film}$  while the opposite was the case for THF (the worse solvent). This can be clear from figure 16 below showing the  $T_c$  estimated for solutions and  $T_{ch}$  estimated for films as already presented separately in figures 2b and 7. It is important in this context to recall the difference between  $T_c$  and  $T_{ch}$ . While both refer a change in the state of the aggregates, the critical transition temperature in solution ( $T_{c/solution}$ ) refers to the temperature at which aggregates start to form in solution and  $T_{ch}$  only refers to the deposition temperature at which a change in the character of aggregates occurs. A possible reason for this discrepancy between  $T_{c/solution}$  and  $T_{ch/film}$  might be the concentration dependence of  $T_c$ , which has been already shown in literature for P3HT in other solvents [38]. In our case, an example of this is shown experimentally in figure 17.

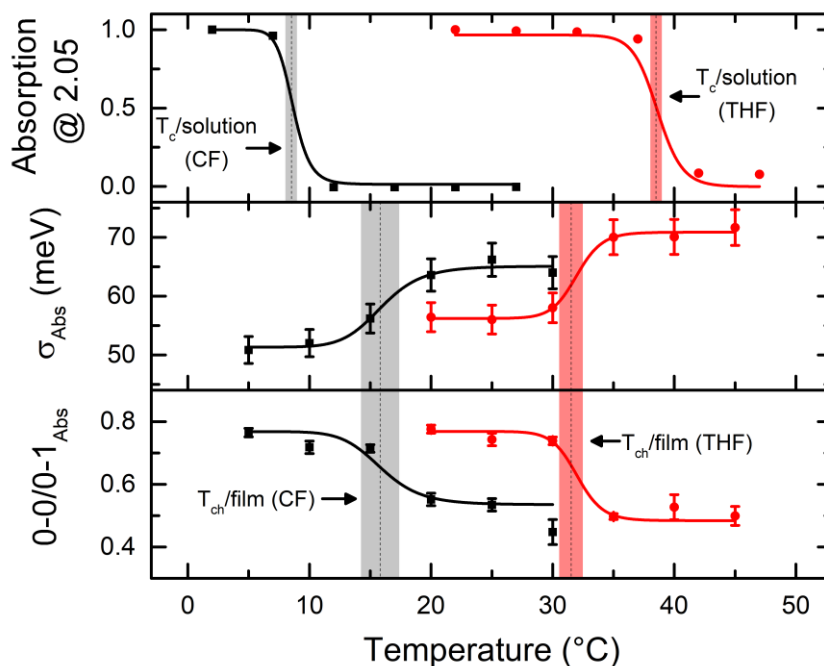


**Figure 16: Comparison of  $T_{c/solution}$  estimated from the temperature dependent solution measurements of P3HT in both CF and THF and  $T_{ch/film}$  estimated from the temperature dependence of the 0-0/0-1 peak ratios (middle panel) and of the  $\sigma$  values (bottom panel).**

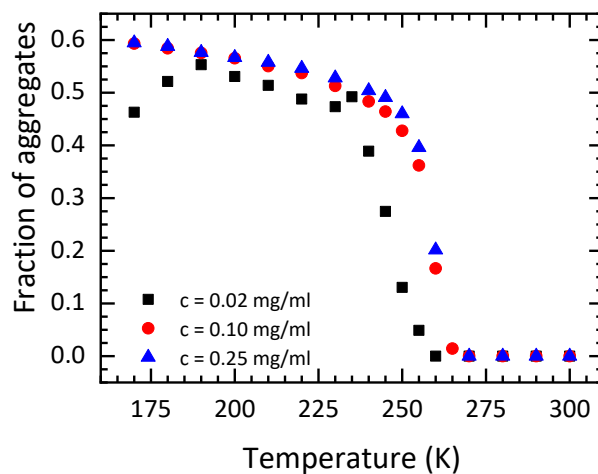


**Figure 17: Fraction of aggregates (FOA) of P3HT in THF solution at different concentrations (Courtesy of Matthew J. Dyson)**

Figure 17 shows the fraction of aggregates as a function of polymer concentration of P3HT in THF solution. It is evident by the shift of the onset of aggregation that  $T_c$  increases with the polymer concentration in solution. While in the case of solutions, the polymer concentration is assumed to be constant over the whole process of aggregation, this is not a valid assumption in case of film

deposition from solution due to the occurring solidification and the associated solvent evaporation. In the latter case, during blade coating as the solvent evaporates the polymer concentration increases up to a point where the disorder-order transition happens at a higher temperature compared to the case of the solution i.e.,  $T_{c/film} > T_{c/solution}$ . However, the above conclusion only explains the case of CF where  $T_{c/film} > T_{c/solution}$  but not the opposite case of THF. To explain this, it is necessary to discuss the other difference between the two solvents which is their solubility of P3HT i.e. the solvent quality. As mentioned in the introduction, the difference between a good and bad solvent determines the balance between the polymer-polymer and polymer-solvent interactions. In a good solvent polymer chains will be disaggregated with a more extended conformation [16, 17]. As a result, as the solvent starts to evaporate the interaction between polymer chains is minimal until a critical point during solvent evaporation process where the polymer concentration increases and the polymer chains are close enough to each other to form aggregates. Hence, for the case of CF, we can conclude that at  $T_s \approx T_{ch/film}$  aggregates can form already at a higher temperature than the  $T_{c/solution}$  that was determined at a lower concentration due to the increase of polymer concentration during formation with no opposing force to hinder the process.

On the contrary, in a poor solvent, even in a dilute solution the polymer-polymer interactions are preferential to the polymer-solvent interactions. This behavior leads to a more tightly coiled chain conformation [16, 17]. To account for the reduced  $T_{ch/film}$  compared to  $T_{c/solution}$ , I suggest the following scenario. The formation of aggregates requires the interaction between two coplanar segments of polymer chains[Ref.]. These coplanar parts may be short, yet they are required. This condition is easily met for a swollen-up polymer chain in a good solvent or at sufficiently high dilution. In a poor solvent, however, a dense, entangled polymer coil conformation may prevent the formation of such coplanar sections, notably at very high concentrations. As the solvent evaporates the interaction between different polymer chains is hindered due to this tightly coiled polymer conformation. This would mean that temperatures below the  $T_c$  of a dilute solution are required to enforce the collapse of the polymer coil and to enable the coplanar arrangement. Hence, for the case of THF we can conclude that at  $T_s \approx T_{ch/film}$  aggregates can form already at a lower temperature than  $T_{c/solution}$ . The observed discrepancies between  $T_{c/solution}$  and  $T_{ch/film}$  can therefore be explained by both the solvent evaporation process during film deposition and the solvent quality. From a practical point of view, this becomes a particularly crucial factor when considering deposition temperatures at  $T_s \approx T_{ch/film}$ .

It is worth noting that since CF and THF have similar boiling points but different  $T_{c/solution}$ , the deposition temperatures for THF solutions are closer to its boiling point compared to CF solutions. Hence, in reality at the same difference between  $T_s$  and  $T_c$  we expect faster solvent evaporation for

THF (the difference between  $T_c$  of P3HT in CF and CF's boiling point ( $\approx 50^\circ\text{C}$ )  $>$  the difference between  $T_c$  of P3HT in THF and THF's boiling point ( $\approx 25^\circ\text{C}$ )). This would lead to a steeper disorder-order transition in the case of THF, which we indeed observe in figure 8.

Moving forward, this allows us to understand the different pathways for aggregate formation as a function of all the solution processing conditions. As shown in figures 9, 10 and 11 the main factor determining the "nature" of aggregates formed in the final film is whether there are initial aggregates (i.e. nucleation sites) formed in solution or not. This condition divides the aggregate formation pathway into either a 2-step or a 1-step process. In case we have initial aggregation in the solution aggregate formation follows a 2-step pathway where in the first step we expect aggregates to form under reduced steric hindrance in a rich solvent medium allowing the chains to planarize prior. Then during the second step as the polymer's concentration increase and the solvent evaporates additional polymer chains follow suit resulting in more ordered and planar chains within the final aggregates. This is more pronounced in the case of a better solvent as can be observed from figure 8. For CF (the better solvent), at  $T_s$  lower than  $T_{ch/film}$  the aggregates formed in the final film show less disorder and higher 0-0/0-1 peak ratio. While for THF (the worse solvent) at  $T_s$  lower than  $T_{ch/film}$  the aggregates formed in the final film show more disorder and lower 0-0/0-1 peak ratio.

Most importantly, in the case of the 2-step aggregation pathway the time allowed for aggregates to form in solution should not be necessarily long. In other words, aggregate formation in solution does not need to happen for an extended time to reach the more ordered and more planar character of the aggregates in the final film. As shown in figure 10.a for films blade coated from CF solutions at  $15^\circ\text{C}$ , only allowing less than 0.5s for the first fraction of aggregates to form in solution provides final aggregates with similar properties to those present in the film blade coated at lower  $T_s = 5^\circ\text{C}$  (figure 9.a). Oppositely in the case is when there is no significant formation of solution aggregates prior to solvent evaporation aggregate formation follows a 1-step pathway. Within this pathway the aggregates only start to form upon sufficient solvent evaporation (i.e. at higher polymer concentration), hence forming under more steric hindrance. This does not give the time or space for the aggregates to planarize leading to the final aggregates having less ordered and less planar polymer chains within the aggregated domains. This is confirmed by the rapid increase of the aggregate absorption which we observe for P3HT blade coated from CF solutions at  $25^\circ\text{C}$  and from THF solutions at  $35^\circ\text{C}$ . It has been shown in literature that this rapid increase in aggregate absorption is a sign of aggregate formation due to the increase in polymer concentration upon sufficient solvent evaporation [39].

Finally, it can be clearly observed from figure 8 that at  $T_s$  sufficiently higher than  $T_{ch}$ , where we have a 1-step aggregate formation process, the solvent quality is still important. The aggregates formed from CF solution are more ordered and less planar than those formed from THF solution due to the better solubility of P3HT in CF due to the mechanisms discussed above. Therefore, when thinking about controlling the aggregate properties during formation of conjugated polymer films, the first step is to choose film deposition temperature according to a predetermined  $T_{ch/film}$ . At  $T_s$  much higher or much lower than  $T_{ch/film}$  the polymer solubility is the controlling factor determining which type of aggregates appear in the final film. While at deposition temperatures  $T_s \approx T_{ch/film}$ , the main issue is then to determine which aggregate properties are desired. Once this is determined, one can manipulate the different processing conditions to allow for aggregates to form following the desired route. This was shown in figures 12 for THF, whereby manipulating the solvent's evaporation the aggregation pathway was changed from a 1-step pathway to a 2-step pathway. At  $T_s$  slightly above  $T_{ch/film}$  but with a decreased solvent evaporation we enable a small time window in which aggregates are allowed to form in the solution at a lower polymer concentration before the onset of solvent evaporation (THF blade coated at  $T_s = 35^\circ\text{C}$  under THF rich atmosphere). Consequently, this leads to aggregates with reduced disorder and increased chain planarity similar to the case of blade coating below  $T_{ch/film}$ .

Apart from the solvent properties and processing temperature, I consider the effect of blending as one of the processing conditions. I observed that the addition of PEO to the P3HT solution does not significantly affect  $T_{ch/film}$  where the P3HT:PEO blend films and the neat P3HT films show similar values within their error ranges. Regarding the properties of the aggregates formed, I observed that the aggregates in the blend P3HT:PEO film shows higher 0-0/0-1 peak ratio over a wide temperature range both above and below  $T_{ch/film}$ . In addition, there is a noticeable shift in the absorption spectrum as a function of temperature as shown in figure 18. All of these observations reflect an enhanced intra-molecular coupling with better conjugated polymer chains characteristic of a more planar polymer conformation [18]. This has been attributed to a planarization of the P3HT polymer chains in solutions in case of polar solvents and generally due to the reduction of torsional disorder [18]. However, it seems that the addition of PEO stabilizes the degree of disorder within the P3HT aggregates as we hardly observe any variation in  $\sigma$  over a wide temperature range. A proposed picture to explain these trends in the in-situ evolution of the aggregate parameters should include the physical presence of PEO in combination with the solvent properties. It has been shown that in the presence of PEO, both polymers (PEO and P3HT) tend to phase separate into large domains (sub- $\mu\text{m}$  range) [40, 41]. This appears as a scattering tail in the lower energy edge of the spectrum which I observed especially when blade coating the films at  $T_s < T_c$  as shown in figure 18.a.

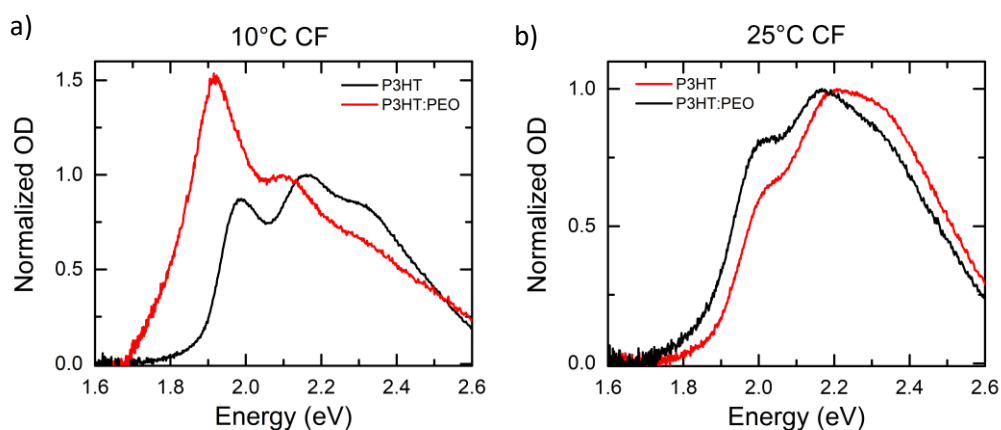


**Figure 18: Final absorption aggregate spectra of the films deposited at a) 10°C and b) 25°C from neat P3HT (red lines) and blend P3HT:PEO (black lines) CF solutions.**

It has been also shown that the extent of the intra-chain coupling strength is enhanced in aggregates of P3HT with higher molecular weights in P3HT:PEO blends [40]. This is reflected in the properties of the absorption spectra as shown in figure 19.b which shows the 0-0 peak position and the 0-0/0-1 peak ratio as a function of P3HT molecular weight in P3HT:PEO films. In this case, an increase in the 0-0/0-1 peak ratio and the red shift of the 0-0 peak position as a function of increasing molecular weight is observed. This molecular weight dependence of the 0-0 peak position and the 0-0/0-1 peak ratio is nearly identical to what I observe as a function of the deposition temperature as shown in figure 19.a. My film deposition parameters were similar to the films shown in figure 19.b. The only difference is that the films in figure 19.b were post treated by immersion in deionized water for 30 minutes after being blade coated at room temperature [40].

From figure 19.b, we observe that beyond a molecular weight of  $31.5 \text{ kg.mol}^{-1}$ , the 0-0/0-1 peak ratio exceeds 1 and intra-chain coupling takes over [40]. This is the critical molecular weight above which P3HT starts to form a two-phase semi-crystalline morphology consisting of amorphous and aggregate domains [42]. The phase transition point shown in 19.b (i.e. the point at which P3HT starts to form a two-phase semi-crystalline structure) roughly coincides with the estimated  $T_c$  for the P3HT:PEO blends ( $\approx 17 \text{ }^\circ\text{C}$ ). It is worth noting that the P3HT used in my work has a molecular weight of  $100 \text{ kg.mol}^{-1}$ . This value is much higher than the critical molecular weight where P3HT forms a semi-crystalline morphology. This means that the blade coated films presented here probably have as semi-crystalline morphology. This also means that if were no effect of the deposition temperature, I should observe values for the 0-0/0-1 peak ratio and the 0-0 peak

position over the whole temperature range similar to values within the green circles in figure 19.b ( $M_w \approx 135 \text{ kg}\cdot\text{mol}^{-1}$ ). Yet, similar values are only observed when I blade coat films at  $10^\circ\text{C}$  (the green circles in figure 19.a) and to a lesser extent at  $15^\circ\text{C}$ . The 0-0/0-1 and  $E_{0-0}$  values for the blade coated films at  $10^\circ\text{C}$  are similar to those for the films presented in figure 19.b.

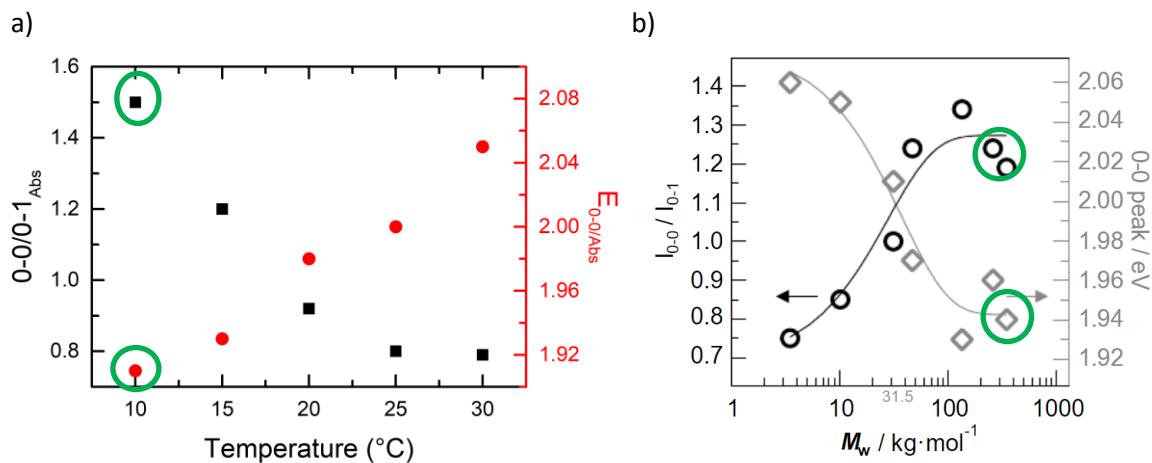


**Figure 19: a) 0-0/0-1 peak and the 0-0 peak location as a function of temperature extracted from the final absorption spectra of films blade coated from blend P3HT:PEO CF solutions, b) Same parameters from blend P3HT:PEO films as a function of the P3HT molecular weight [40]**

This means that one could control the extent of the P3HT chain coupling strength by means of either molecular weight or deposition temperature in the presence of PEO. However, the underlying reason for this variation of intra-chain coupling is different between the two cases. Increasing the molecular weight leads to the increase in the P3HT repeat units along the P3HT backbone and hence the conjugation length that enhances the degree of intra-chain coupling [40].

In our case the situation is different as the molecular weight is constant over the whole temperature range. At  $T_s$  sufficiently higher than  $T_{\text{ch}/\text{film}}$  in both neat P3HT and blend P3HT:PEO solutions, the aggregates are formed following a 1-step process. The resulting films show similar disorder which might mean that for both the neat and blend films we have a similar overall film morphology. However, the main difference as a function of the presence of PEO is that initially the polymer chains in the blend solution have a more planar conformation compared to those present in the neat P3HT. In addition, the solvent evaporation is reduced giving the aggregates more time to grow. While this apparently does not provide sufficient time for the P3HT aggregates to order, it keeps the initial more planar conformation of the P3HT chains until the film is formed. Hence, I assume that while the overall morphology for both films would consist of amorphous and aggregate regions, the aggregate regions within the blend films are more ordered with higher intra-chain coupling compared to those in the neat film.

## 4.6 Conclusion

In conclusion, I addressed the formation of conjugated polymer aggregates upon solution processing into thin films providing a general picture of their formation dynamics. This includes the interplay between different factors affecting the properties of the aggregates formed in the final film. These factors include the solvent quality, the solvent's boiling point, the film deposition temperature, the polymer's critical transition temperature in solution and the addition of an extra material. From this, I concluded that the aggregate formation in conjugated donor polymers during their solution processing into thin films proceeds through one of two routes. The aggregate formation proceeds either via a 2-step pathway where aggregates form in solution before solvent evaporation or via a 1-step pathway where aggregates only form upon sufficient solvent evaporation at high polymer concentration. The type of pathway determines the aggregate properties in the final film.

Aggregates formed following a 2-step pathway are characterized by a more planar, more ordered structure while aggregates formed following a 1-step pathway are characterized by a less planar, and less ordered structure. These properties are a result of the conditions under which the aggregates initially form. Within the 2-step pathway, the initial aggregates start to form in a solvent rich atmosphere under reduced steric hindrance allowing more time for polymer chains to order before solvent evaporation. Within the 1-step pathway, the initial aggregates form at high polymer concentration during fast solvent evaporation and under more steric hindrance. These conditions do not allow the polymer chains to order and therefore keeping their initial quenched conformation in the aggregated domains in the final film.

These pathways are determined by the relation between the film's transition temperature of the polymer for a specific solvent, the solvent's boiling point and the time available for the aggregates to form in a solvent rich atmosphere before the solvent evaporates. At deposition temperatures much higher or lower than this transition temperature, the main driver of the aggregation is the solubility of the polymer while the other parameters offer little impact on the resulting aggregates. However, at deposition temperatures in the vicinity of the transition temperature, control of the timing as a function of the solvent's evaporation becomes extremely important. Allowing a slight time window for aggregates to form in a solvent rich atmosphere leads to more ordered aggregates with a more planar conformation even at temperatures slightly higher than the film's transition temperature. From the above I can assume that the opposite is true for the case where the solvent evaporation is accelerated leading to less ordered aggregates even at deposition temperatures lower than the film's transition temperature.

Furthermore, I showed that the addition of PEO to P3HT in solution led to switching the film formation pathway from a 1-step to a 2-step process. Consequently, the final aggregates in the blend film had a more planar polymer conformation with an enhanced intra-molecular coupling compared to neat P3HT films processed under the same conditions. Yet, in both cases the overall film morphology is similar. This effect is not only due to aggregates forming in solution but also due to PEO reducing the torsional disorder within the P3HT aggregates and confining the initial more planar conformation during the solvent evaporation and film formation.

Finally, this work shows the potential of in-situ optical spectroscopy combined with in-depth spectroscopic analysis to investigate and understand microscopic processes during thin film formation. This would allow for understanding aggregate formation dynamics in conjugated polymer films during solution processing as a function of the underlying processing parameters as well as the influence of these processing parameters on the final aggregate properties. With this approach, I was able to obtain a more generalized picture of the factors influencing the aggregation process in conjugated polymer films. This knowledge is useful to ultimately manipulate and control the aggregate properties of the final films in a systematic manner depending on the desired application.

## References

- [1] R. Noriega, J. Rivnay, K. Vandewal, F.P.V. Koch, N. Stingelin, P. Smith, M.F. Toney, A. Salleo, A general relationship between disorder, aggregation and charge transport in conjugated polymers, *Nat Mater*, 12 (2013) 1038-1044.
- [2] H.B. A. Köhler, *The Electronic Structure of Organic Semiconductors*, in: *Electronic Processes in Organic Semiconductors*, 2015, pp. 1-86.
- [3] N.D. Treat, P. Westacott, N. Stingelin, *The Power of Materials Science Tools for Gaining Insights into Organic Semiconductors*, *Annu Rev Mater Res*, 45 (2015) 459-490.
- [4] C. Schwarz, S. Tscheuschner, J. Frisch, S. Winkler, N. Koch, H. Bässler, A. Köhler, Role of the effective mass and interfacial dipoles on exciton dissociation in organic donor-acceptor solar cells, *Phys Rev B*, 87 (2013).
- [5] F.C. Spano, C. Silva, H- and J-Aggregate Behavior in Polymeric Semiconductors, *Annu Rev Phys Chem*, 65 (2014) 477-500.
- [6] N.J. Hestand, F.C. Spano, Expanded Theory of H- and J-Molecular Aggregates: The Effects of Vibronic Coupling and Intermolecular Charge Transfer, *Chem Rev*, 118 (2018) 7069-7163.
- [7] Y. Tamai, Delocalization boosts charge separation in organic solar cells, *Polym J*, 52 (2020) 691-700.
- [8] B.H. Wunsch, M. Rumi, N.R. Tummala, C. Risko, D.Y. Kang, K.X. Steirer, J. Gantz, M. Said, N.R. Armstrong, J.L. Bredas, D. Bucknall, S.R. Marder, Structure-processing-property correlations in solution-processed, small-molecule, organic solar cells, *J Mater Chem C*, 1 (2013) 5250-5260.
- [9] Y.H. Liu, J.B. Zhao, Z.K. Li, C. Mu, W. Ma, H.W. Hu, K. Jiang, H.R. Lin, H. Ade, H. Yan, Aggregation and morphology control enables multiple cases of high-efficiency polymer solar cells, *Nat Commun*, 5 (2014).
- [10] W. Ma, G.F. Yang, K. Jiang, J.H. Carpenter, Y. Wu, X.Y. Meng, T. McAfee, J.B. Zhao, C.H. Zhu, C. Wang, H. Ade, H. Yan, Influence of Processing Parameters and Molecular Weight on the Morphology and Properties of High-Performance PffBT4T-2OD:PC71BM Organic Solar Cells, *Adv Energy Mater*, 5 (2015).
- [11] B.B. Fan, L. Ying, Z.F. Wang, B.T. He, X.F. Jiang, F. Huang, Y. Cao, Optimisation of processing solvent and molecular weight for the production of green-solvent-processed all-polymer solar cells with a power conversion efficiency over 9%, *Energ Environ Sci*, 10 (2017) 1243-1251.
- [12] O. Todor-Boer, I. Petrovai, R. Tarcan, A.M. Craciun, L. David, S.B. Angyus, S. Astilean, I. Botiz, Altering the optoelectronic properties of neat and blended conjugated polymer films by controlling the process of film deposition, *J Optoelectron Adv M*, 21 (2019) 367-372.
- [13] O. Todor-Boer, I. Petrovai, R. Tarcan, A. Vulpoi, L. David, S. Astilean, I. Botiz, Enhancing Photoluminescence Quenching in Donor-Acceptor PCE11:PCBMB Films through the Optimization of Film Microstructure, *Nanomaterials-Basel*, 9 (2019).
- [14] H.W. Ro, J.M. Downing, S. Engmann, A.A. Herzing, D.M. DeLongchamp, L.J. Richter, S. Mukherjee, H. Ade, M. Abdelsamie, L.K. Jagadamma, A. Amassian, Y.H. Liu, H. Yan, Morphology changes upon scaling a high-efficiency, solution-processed solar cell, *Energ Environ Sci*, 9 (2016) 2835-2846.
- [15] R. Sun, J. Guo, Q. Wu, Z.H. Zhang, W.Y. Yang, J. Guo, M.M. Shi, Y.H. Zhang, S. Kahmann, L. Ye, X.C. Jiao, M.A. Loi, Q. Shen, H. Ade, W.H. Tang, C.J. Brabec, J. Min, A multi-objective optimization-

based layer-by-layer blade-coating approach for organic solar cells: rational control of vertical stratification for high performance, *Energy Environ Sci*, 12 (2019) 3118-3132.

[16] M.S. Glaz, J.D. Biberdorf, M.T. Nguyen, J.J. Travis, B.J. Holliday, D.A. Vanden Bout, Perylene diimide functionalized polynorbornene: a macromolecular scaffold for supramolecular self-assembly, *J Mater Chem C*, 1 (2013) 8060-8065.

[17] F. Panzer, H. Bässler, A. Köhler, Temperature Induced Order-Disorder Transition in Solutions of Conjugated Polymers Probed by Optical Spectroscopy, *J Phys Chem Lett*, 8 (2017) 114-125.

[18] M. Reichenberger, D. Kroh, G.M.M. Matrone, K. Schotz, S. Proller, O. Filonik, M.E. Thordardottir, E.M. Herzig, H. Bässler, N. Stingelin, A. Köhler, Controlling aggregate formation in conjugated polymers by spin-coating below the critical temperature of the disorder-order transition, *J Polym Sci Pol Phys*, 56 (2018) 532-542.

[19] A.L.T. Khan, P. Sreearunothai, L.M. Herz, M.J. Banach, A. Köhler, Morphology-dependent energy transfer within polyfluorene thin films, *Phys Rev B*, 69 (2004).

[20] O.J. Korovyanko, R. Osterbacka, X.M. Jiang, Z.V. Vardeny, R.A.J. Janssen, Photoexcitation dynamics in regioregular and regiorandom polythiophene films, *Phys Rev B*, 64 (2001).

[21] P. Gregoire, E. Vella, M. Dyson, C.M. Bazan, R. Leonelli, N. Stingelin, P.N. Stavrinou, E.R. Bittner, C. Silva, Excitonic coupling dominates the homogeneous photoluminescence excitation linewidth in semicrystalline polymeric semiconductors, *Phys Rev B*, 95 (2017).

[22] F. Panzer, M. Sommer, H. Bassler, M. Thelakkat, A. Köhler, Spectroscopic Signature of Two Distinct H-Aggregate Species in Poly(3-hexylthiophene), *Macromolecules*, 48 (2015) 1543-1553.

[23] J. Clark, C. Silva, R.H. Friend, F.C. Spano, Role of intermolecular coupling in the photophysics of disordered organic semiconductors: Aggregate emission in regioregular polythiophene, *Phys Rev Lett*, 98 (2007).

[24] J. Clark, J.F. Chang, F.C. Spano, R.H. Friend, C. Silva, Determining exciton bandwidth and film microstructure in polythiophene films using linear absorption spectroscopy, *Appl Phys Lett*, 94 (2009).

[25] C. Botta, S. Luzzati, R. Tubino, A. Borghesi, Optical-Excitations of Poly-3-Alkylthiophene Films and Solutions, *Phys Rev B*, 46 (1992) 13008-13016.

[26] H. Yamagata, D.S. Maxwell, J. Fan, K.R. Kittilstved, A.L. Briseno, M.D. Barnes, F.C. Spano, HJ-Aggregate Behavior of Crystalline 7,8,15,16-Tetraazaterrylene: Introducing a New Design Paradigm for Organic Materials, *J Phys Chem C*, 118 (2014) 28842-28854.

[27] P.J. Brown, D.S. Thomas, A. Kohler, J.S. Wilson, J.S. Kim, C.M. Ramsdale, H. Sirringhaus, R.H. Friend, Effect of interchain interactions on the absorption and emission of poly(3-hexylthiophene), *Phys Rev B*, 67 (2003).

[28] F. Paquin, H. Yamagata, N.J. Hestand, M. Sakowicz, N. Berube, M. Cote, L.X. Reynolds, S.A. Haque, N. Stingelin, F.C. Spano, C. Silva, Two-dimensional spatial coherence of excitons in semicrystalline polymeric semiconductors: Effect of molecular weight, *Phys Rev B*, 88 (2013).

[29] L. Farouil, F. Alary, E. Bedel-Pereira, J.L. Heully, Revisiting the Vibrational and Optical Properties of P3HT: A Combined Experimental and Theoretical Study, *J Phys Chem A*, 122 (2018) 6532-6545.

[30] C. Scharsich, R.H. Lohwasser, M. Sommer, U. Asawapirom, U. Scherf, M. Thelakkat, D. Neher, A. Köhler, Control of aggregate formation in poly(3-hexylthiophene) by solvent, molecular weight, and synthetic method, *J Polym Sci Pol Phys*, 50 (2012) 442-453.

[31] A. Samoc, Dispersion of refractive properties of solvents: Chloroform, toluene, benzene, and carbon disulfide in ultraviolet, visible, and near-infrared, *J Appl Phys*, 94 (2003) 6167-6174.

- [32] M. Belmares, M. Blanco, W.A. Goddard, R.B. Ross, G. Caldwell, S.H. Chou, J. Pham, P.M. Olofson, C. Thomas, Hildebrand and Hansen solubility parameters from molecular dynamics with applications to electronic nose polymer sensors, *J Comput Chem*, 25 (2004) 1814-1826.
- [33] J. Camacho, E. Diez, I. Diaz, G. Ovejero, Hansen solubility parameter: from polyethylene and poly(vinyl acetate) homopolymers to ethylene-vinyl acetate copolymers, *Polym Int*, 66 (2017) 1013-1020.
- [34] D.T. Duong, B. Walker, J. Lin, C. Kim, J. Love, B. Purushothaman, J.E. Anthony, T.Q. Nguyen, Molecular solubility and hansen solubility parameters for the analysis of phase separation in bulk heterojunctions, *J Polym Sci Pol Phys*, 50 (2012) 1405-1413.
- [35] A.F.M. Barton, Solubility Parameters, *Chem Rev*, 75 (1975) 731-753.
- [36] J. Burke, Solubility Parameters: Theory and Application, (1984).
- [37] H. Yamagata, F.C. Spano, Interplay between intrachain and interchain interactions in semiconducting polymer assemblies: The HJ-aggregate model, *J Chem Phys*, 137 (2012).
- [38] S. Wedler, A. Bourdick, S. Athanasopoulos, S. Gekle, F. Panzer, C. McDowell, T.Q. Nguyen, G.C. Bazan, A. Köhler, What is the role of planarity and torsional freedom for aggregation in a pi-conjugated donor-acceptor model oligomer?, *J Mater Chem C*, 8 (2020) 4944-4955.
- [39] M. Abdelsamie, K. Zhao, M.R. Niazi, K.W. Chou, A. Amassian, In situ UV-visible absorption during spin-coating of organic semiconductors: a new probe for organic electronics and, *J Mater Chem C*, 2 (2014) 3373-3381.
- [40] C. Hellmann, F. Paquin, N.D. Treat, A. Bruno, L.X. Reynolds, S.A. Haque, P.N. Stavrinou, C. Silva, N. Stingelin, Controlling the Interaction of Light with Polymer Semiconductors, *Adv Mater*, 25 (2013) 4906-4911.
- [41] M.J. Dyson, E. Lariou, J. Martin, R.P. Li, H. Erothu, G. Wantz, P.D. Topham, O.J. Dautel, S.C. Hayes, P.N. Stavrinou, N. Stingelin, Managing Local Order in Conjugated Polymer Blends via Polarity Contrast, *Chem Mater*, 31 (2019) 6540-6547.
- [42] F.P.V. Koch, J. Rivnay, S. Foster, C. Muller, J.M. Downing, E. Buchaca-Domingo, P. Westacott, L.Y. Yu, M.J. Yuan, M. Baklar, Z.P. Fei, C. Luscombe, M.A. McLachlan, M. Heeney, G. Rumbles, C. Silva, A. Salleo, J. Nelson, P. Smith, N. Stingelin, The impact of molecular weight on microstructure and charge transport in semicrystalline polymer Semiconductors poly(3-hexylthiophene), a model study, *Prog Polym Sci*, 38 (2013) 1978-1989.

# Chapter 5: Polymer conformation and aggregation of PDI based side chain polymers

## 5.1 Introduction

In the last two chapters I showed how the aggregation properties in conjugated donor polymers is affected by the addition of an extra material and how these properties are impacted by the processing conditions during film formation from solution. In this chapter, I focus on exploring the aggregation properties of two side chain acceptor polymers in solution. These two polymers are based on an inert polystyrene polymer backbone and two PDI chromophores with slightly different structures. This structure offers a unique approach to control the overall polymer's aggregation properties by manipulating the conformation properties of the polymer backbone. Using steady state and time resolved optical spectroscopy, I investigate the basic characteristics of these PDIs and their aggregation in solution as a function of solvent properties (solubility parameter & solvent polarity). I also investigate how minor changes in the side chain structure influences the overall polymer aggregation properties. Both polymers have the potential to be used as polymer acceptors in organic solar cells and will be explored in the next chapter.

The pendant perylene diimide (PDI) monomers and polymers used in this chapter were synthesized and provided by **Prof. Dr. Mukundan Thelakkat** and **Andreas Lang** [1] from the *Macromolecular Chemistry I, University of Bayreuth*. I did all the experimental work and analysis presented in this chapter.

## 5.2 Aggregation properties of Pendant Perylene diimide (PDI) polymers

### (i) The uniqueness of side chain polymers

In general, the materials used as electron acceptors in blends for organic solar cells can be categorized into fullerene acceptors, non-fullerene small molecule acceptors and non-fullerene polymer acceptors [2-12]. Perylene diimide (PDI) based electron acceptors, which can take the form of small molecule or polymeric acceptors, offer a promising potential in organic solar cells due to their desirable properties. In general, PDIs are inexpensive, easy to synthesize, to functionalize, and to modify chemically and they are environmentally safe. In addition, PDIs have good absorption in the visible spectral region and good thermal stability. Moreover, PDIs have low lying LUMO levels

and high electron mobility compared to other non-fullerene acceptors. All these properties make PDIs a perfect candidate for solution processed organic solar cells [10, 11, 13-15].

Historically, PDI based small molecules were the first used acceptor in a two component organic solar cell when the first bilayer organic solar cell was reported [16]. PDI based materials as small molecule acceptors were then heavily researched as a component in solution processed organic solar cells but offered only poor performance [10, 17-19]. This was mainly due to the inability to form favorable morphologies in the blends. This was a result of the tendency of PDI small molecules to stack in a cofacial manner along the  $\pi$ -planes leading to excessive aggregation and large domain sizes [20, 21]. Such morphological profile led to inefficient charge generation as the excitons often recombine within these large PDI domains before reaching the donor-acceptor interface [21, 22]. Moreover, this excessive aggregation often leads to excimer formation which then act as energy traps [23].

To overcome these obstacles, several approaches were employed relying mainly on disrupting this cofacial stacking of PDIs. Such approaches included the synthesis of twisted PDI dimers either through imide or bay linking [18-20, 24], ring fusion of PDI monomers to form dimers or tetramers [25-27] and polymerization of PDI including different functional side chains to form various PDI polymeric acceptors [11]. It is worth noting that other than the PDI polymeric acceptors, most of the approaches employed to disrupt the excessive aggregation of PDIs led to the deterioration of their charge transport ability as charges preferably move along this  $\pi$ -stacking direction. In general, while these approaches pushed the efficiency of organic solar cells employing PDI acceptors a little bit further, PDI acceptors still significantly lagged behind fullerene and other non-fullerene small molecule acceptors concerning the achievable solar cell efficiency. The highest reported PDI-based solar cell to date is a ternary cell employing two PDI derivatives with an efficiency of 9.43% [28]. Another approach, that is not widely researched, is employing PDIs in a side chain polymer structure rather than a conjugated polymer structure [17, 29]. Although side chain polymers are not a new class of polymers, they have not been extensively investigated towards application in optoelectronic devices. From a chemical point of view, side chain polymer offers a simple route to synthesize different polymer variations based on the same inert backbone combined with different functional side chains [1]. From a structural point of view, due to the unique architecture of these polymers where the functional side chains are attached to an optically inert polymer backbone, the electronic interactions between these side chains and the subsequent overall aggregation properties are mainly controlled by this backbone conformation [29, 30].

In this chapter, I explore the factors that control the aggregation behavior of two side chain polymers based on Perylene-diimide (PDI) chromophores as the side chains in solutions. Both polymers are based on the same polymer backbone but differ in the PDI chromophore attached to it. The main question I explore here using spectroscopic characterization techniques- besides gaining information on backbone conformation- is whether the different side chains attached to the same backbone result in differences in the aggregation properties of the two polymers in solution.

## ii. The structure of side chain PDI polymers

Figure 1 shows the detailed chemical structure of the two the PDI polymers I used, PPBI-alkyl (left) and PPBI-OEG (right). The two polymers used consist of an optically inert polystyrene polymer backbone with attached PDI moieties through a  $(\text{CH}_2)_6$  linker. The PDI moieties consist of the perylene chromophore with either a hydrophilic alkyl or a hydrophobic OEG tail [1, 15].

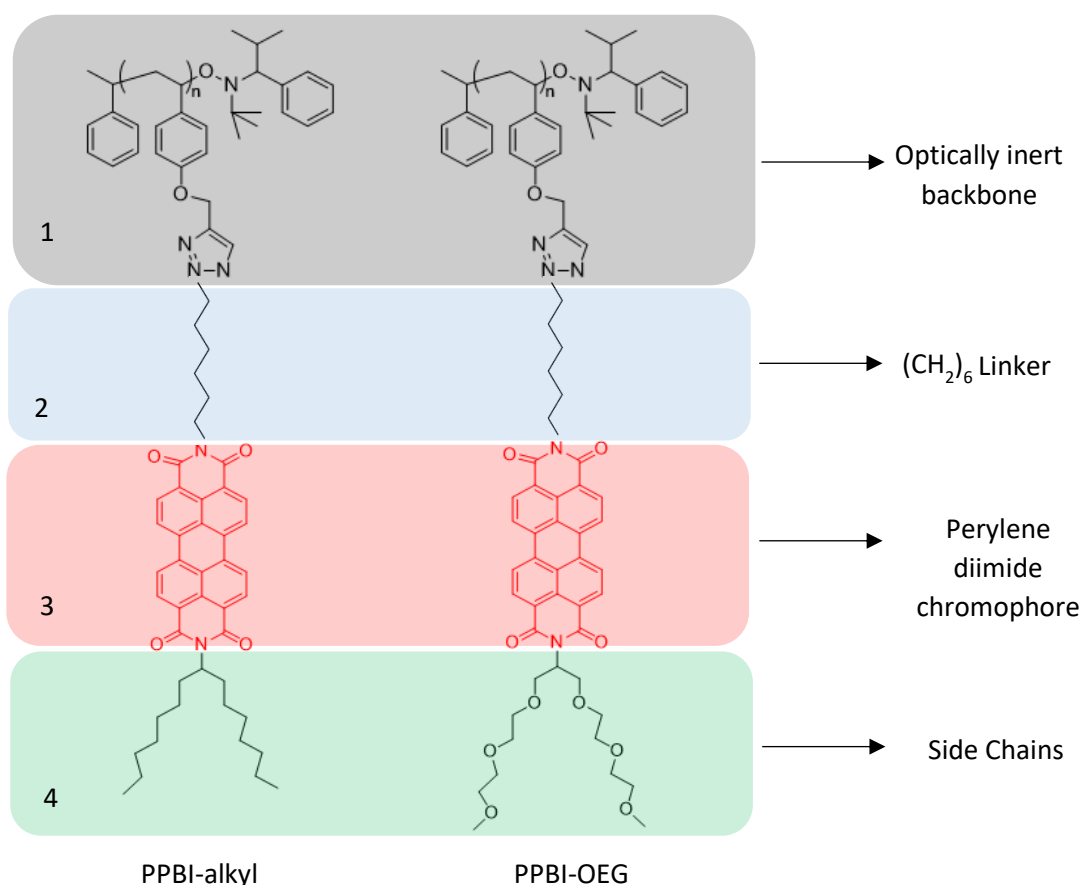


**Figure 1: Structure of the investigated side chain PDI polymers, PPBI-alkyl (left) and PPBI-OEG (right). Numbers 1-4 refer to the distinct parts of the material's structure.**

The morphological properties of these two materials have been studied in the melt where the ordering of the polymer chains has been investigated in terms of the lengths of the linker and the tails [1]. It has been shown that PPBI-alkyl tends to form a liquid crystalline structure as was shown by polarized optical microscopy [1]. This was not the case for PPBI-OEG which did not show any order indicating an amorphous morphology. These results were further confirmed by X-Ray Diffraction (XRD) and Differential Scanning Calorimetry (DSC) measurements [1]. It is worth noting that in general for other polymers and small molecules, it has been shown that OEG side chains can lead to up to 3-fold increase in a polymer's dielectric constant compared to alkyl side chains [31]. This increase in a polymer's dielectric is expected to lower the excitonic coupling and hence enhance the charge generation efficiency [32].

Apart from the already known properties stated above, the aggregation behavior of PPBI-alkyl and PPBI-OEG has not been investigated in solutions or solution processed films. Since I am more concerned about the structural and conformational properties of polymers geared towards solar cell applications, at first, I compare these two polymers in solution to investigate how the alkyl or OEG side chains impact their aggregation properties. Using steady state optical spectroscopy, I start first by comparing the PDI moieties themselves as monomers before being attached to the backbone. Then I compare both polymers in solutions using different solvents with varying solubility parameters, polarities, and boiling points.

## 5.3 Results

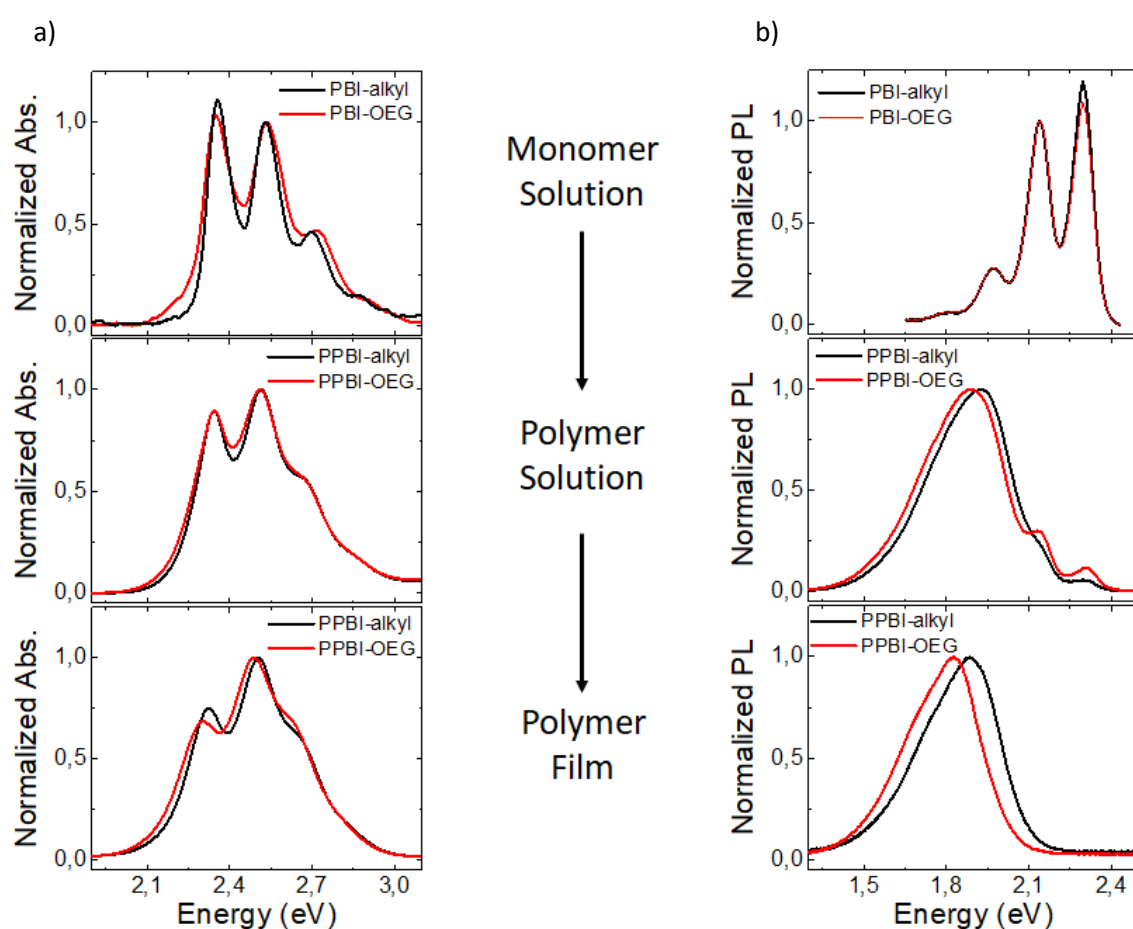
### i. Monomer vs. Polymer

Figure 2 shows the normalized photoluminescence and absorption spectra for both PBI-alkyl and PBI-OEG. The spectra of the monomer solutions where the PDI chromophores are not attached to the polystyrene backbone (part 3 in figure 1) are shown in the top panel, the spectra for the corresponding polymer solutions are shown in the middle panel, and the spectra of the spin coated polymer films are shown in the bottom panel. It is worth noting that PBI-alkyl/PBI-OEG refers to the single PDI chromophore as a monomer, while PPBI-alkyl/PPBI-OEG refers to the polymer itself consisting of the backbone and the attached PDI chromophores.

In the monomer solution, the spectra of both PDIs show the distinct 0-0, 0-1 and 0-2 vibronic peaks of the PDI monomer's absorption (2.36 eV, 2.53 eV and 2.7 eV) and emission (2.30 eV, 2.13 eV and 1.96 eV) with a spacing of  $\approx 170$ meV corresponding to the C=C stretching mode [30]. However, the 0-0/0-1 peak ratio for both monomers (1.1 in alkyl and 1.03 in OEG) are lower than the characteristic 0-0/0-1 peak ratio for the fully non-aggregated PDIs at a similar concentration which

is 1.6 [17, 33, 34]. This hints towards the presence of electronic interactions (aggregation) between the PDI monomers at these concentrations.

In the polymer solution one would expect that upon attaching the monomers to the polystyrene backbone the PDIs become closer to each other. This would lead to stronger electronic interaction between the PDI moieties even in dilute solutions. This is indeed reflected in both the photoluminescence and absorption spectra of the polymer solutions. In the absorption spectra I observe a significant reduction of 0-0 peak intensity relative to the 0-1 and 0-2 peaks and an increased absorption spectral width. In the photoluminescence spectra I observe a broad red shifted emission and a reduced contribution from the monomer's emission. These effects are further enhanced in films spin coated from the polymer solutions.



**Figure 2:** Normalized a) photoluminescence and b) absorption of PBI-alkyl and PBI-OEG as monomer solutions in CF at  $10^{-5}M$  concentration (top), polymer solutions in CF at  $10^{-5}M$  concentration (middle) and polymer films spin coated from 5g/l oDCB solutions (bottom).

If we compare the emission spectra of PPBI-alkyl and PPBI-OEG, we observe that the monomer emission intensity is slightly more enhanced in the case of PPBI-OEG. This monomer emission

disappears completely in the film spectra of both polymers implying an efficient 3-D energy transfer [34-36]. In general, for both polymer solution and polymer film the overall spectra of PPBI-OEG are slightly red shifted compared to that of PPBI-alkyl which I attribute to its higher polarity. This spectral separation is more evident in the film spectra. To confirm that the PL spectra shown in figure 2 for PBI-alkyl and PBI-OEG correspond to the monomer emission, I measured the time resolved photoluminescence of both monomer solutions at the same concentration ( $10^{-5}$  M) as shown in figure 3.a. The exciton lifetimes for both monomers at room temperature show a mono-exponential decay with a lifetime  $\approx 4.2$  ns at 2.3 eV. This is consistent with the literature values for the exciton lifetime in PDI monomers [35-37].

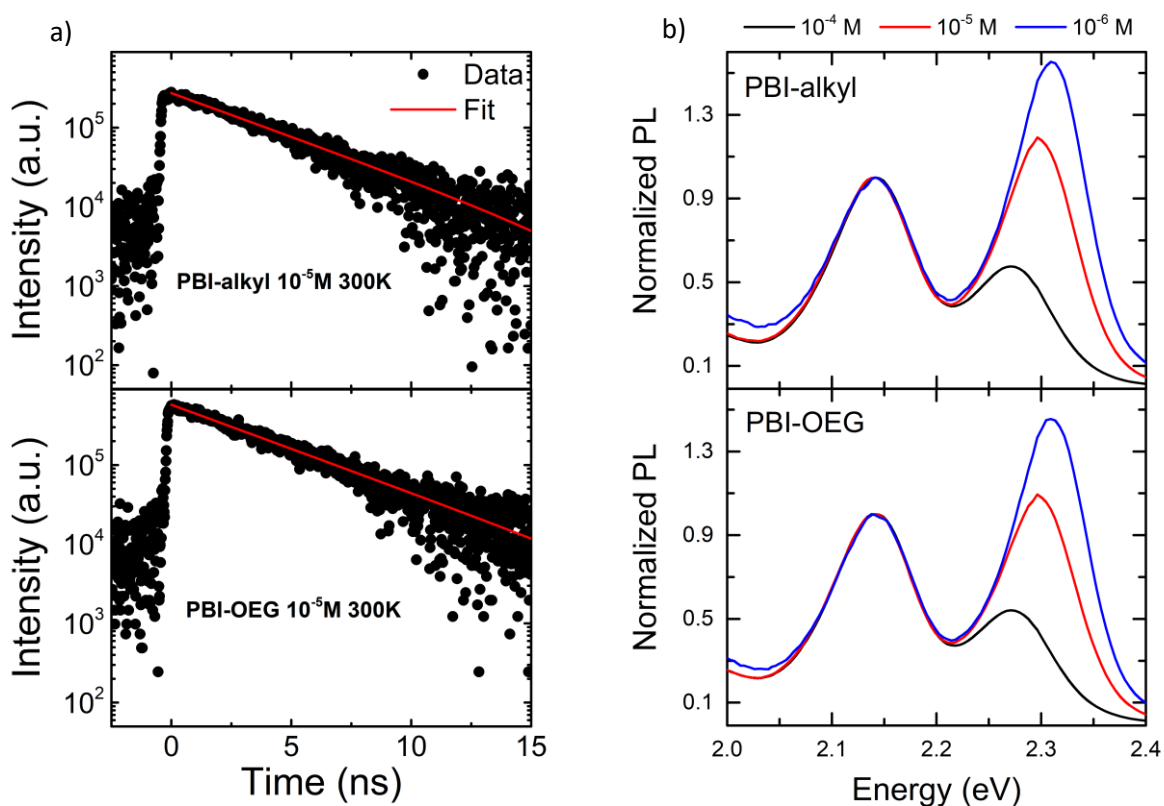


**Figure 3:** a) Time resolved photoluminescence decay curves extracted at 2.3 eV of the PBI-alkyl and PBI-OEG monomer solutions in CF at  $10^{-5}$ M concentration taken at room temperature. The red lines show a mono-exponential line fit of the data. b) Normalized photoluminescence of PBI-alkyl and PBI-OEG as monomer solutions in CF at three different concentrations,  $10^{-4}$ M (black),  $10^{-5}$ M (red) and  $10^{-6}$ M (blue).

However, to investigate the presence of electronic interactions between the PDI monomers in the monomer solutions, I measured the PL again as a function of concentration. Figure 3.b shows the spectra of both monomers over two orders of magnitude of concentration in CF solutions. Surprisingly, one can readily observe the significant reduction of the 0-0/0-1 peak ratio as a function

of the increasing monomer concentration. In the framework of the weakly-coupled H-aggregates, this would indicate a concentration dependent aggregation of the PDI monomers [33, 38]. Moving on to the polymer solution, the observed broad red shifted emission in the PL spectra cannot be attributed to the formation of ground state aggregates due to the absence of a corresponding band in absorption. This indicates that this broad red shift occurs after initial excitation which could be attributed to excimer emission [35, 36].

To unveil the origin of this peak, I measured the time resolved PL of the polymer solutions. Figure 4 shows the decay curves of excitons in the polymer solutions at different energies. These curves clearly show an energy dependent behavior in both the PPBI-alkyl and PPBI-OEG solutions. At the high energy range starting at 2.25eV, PPBI-alkyl shows a bi-exponential decay with fast and slow components while PPBI-OEG only shows a fast mono-exponential decay corresponding to one emitting species. On the contrary, at 2.15 eV, both polymers show a bi-exponential decay with fast and slow components. At 2 eV, the same behavior persists for both polymers as they show a bi-exponential decay with two emitting species. Finally, at the low energy range  $\approx 1.9$  eV, both polymers have a similar behavior as both their decay curves show a mono-exponential decay of a long-lived species. Tables 1 and 2 shows the lifetimes and amplitudes of the decay curves for both polymers measured at the different energies. This was extracted by fitting the individual decay curves by either a mono-exponential or a bi-exponential decay model.

**Table 1 Lifetimes and amplitudes corresponding to the exponential fits of the PPBI-alkyl decay curves shown in fig.4.  $t_1$  and  $A_1$  refer to the monomer while  $t_2$  and  $A_2$  refer to the excimer**

Energy (eV)	$A_1$ ( $\times 10^5$ )	$t_1$ (ns)	$A_2$ ( $\times 10^5$ )	$t_2$ (ns)
1.9	0	0	$2.1 \pm 0.05$	$22.5 \pm 1$
2	$1.3 \pm 0.2$	$4.5 \pm 0.5$	$4.3 \pm 0.1$	$22.8 \pm 0.9$
2.15	$2 \pm 0.09$	$4 \pm 0.5$	$1.5 \pm 0.05$	$23 \pm 1$
2.25	$1.1 \pm 0.06$	$4.3 \pm 0.5$	$0.2 \pm 0.06$	$24.5 \pm 1.1$

**Table 2 Lifetimes and amplitudes corresponding to the exponential fits of the PPBI-OEG decay curves shown in fig.4.  $t_1$  and  $A_1$  refer to the monomer while  $t_2$  and  $A_2$  refer to the excimer**

Energy (eV)	$A_1$ ( $\times 10^5$ )	$t_1$ (ns)	$A_2$ ( $\times 10^5$ )	$t_2$ (ns)
1.9	0	0	$3.5 \pm 0.05$	$21.4 \pm 0.8$
2	$2.3 \pm 0.04$	$4.8 \pm 0.7$	$3.8 \pm 0.04$	$22.4 \pm 1$
2.15	$6.9 \pm 0.06$	$4.2 \pm 0.1$	$0.6 \pm 0.08$	$24 \pm 1$
2.25	$5 \pm 0.04$	$4 \pm 0.7$	0	0

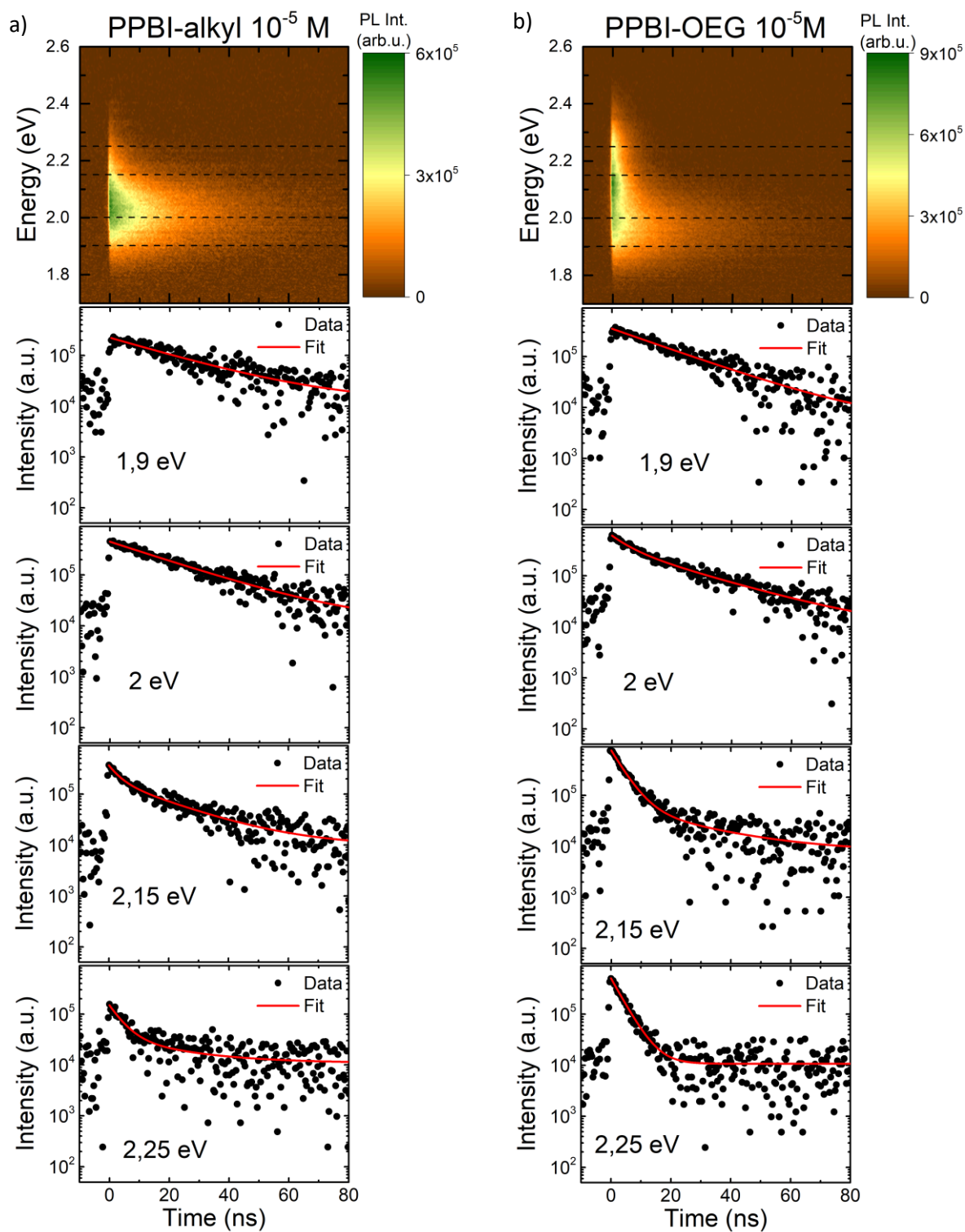


**Figure 4:** 2D maps of the time resolved photoluminescence of a) PPBI-alkyl and b) PPBI-OEG in polymer solutions in CF at  $10^{-5}M$ . The dashed lines correspond to the decay curves shown extracted from the 2D maps different wavelengths averaged over 0.1 eV. The red lines show either a mono-exponential or a bi-exponential line fit of the decay curves.

From the tables, it is apparent that in case of the bi-exponential decay curves the decay times of the short and long lives species are always in the range of  $\tau_1 \approx 4\text{-}5$  ns and  $\tau_2 \approx 21\text{-}24$  ns respectively. These values are consistent with literature values corresponding to the monomer and excimer emissions respectively [35-37]. The mono-exponential decay curves observed for PPBI-alkyl and at 1.9 eV show lifetimes of  $\tau_2 \approx 22$  ns corresponding to the excimer emission. While the mono-exponential decay curve observed for PPBI-OEG at 2.25 eV show a lifetime of  $\tau_1 \approx 4$  ns corresponding to the monomer emission. In the case of the bi-exponential decay, while the lifetimes are always within the same range for both the excimer and monomer emission, the extracted amplitudes are energy dependent. This would indicate which species dominate the emission at each energy range. At 2 eV, it is apparent from the amplitudes that the excimer species dominates the emission. On the contrary, at 2.25 eV the monomer species dominate the emission.

These results clearly confirm that the broad emission band dominating the PL spectra of both PPBI-alkyl and PPBI-OEG in polymer solutions (and subsequently the polymer films) correspond to an excimer formation. The main difference between both polymers is that the excimer emission for PPBI-alkyl is present over the whole spectral range of the PL while for PPBI-OEG the excimer emission is not present at higher energies (2.25 eV). At 2.25 eV, for PPBI-alkyl, although the monomer species dominate the emission, a small contribution from the excimers are still present as evidenced by the much smaller amplitude. For PPBI-OEG, at 2.25 eV, the monomer emission dominates the PL spectra with no contribution from the excimers. This difference might hint towards more significant excimer formation or a more efficient energy transfer in PPBI-alkyl as a result of its different side chain.

## ii. Inter- vs. Intra-molecular aggregation

After having established an initial picture about the behavior both PDIs in monomer and polymer solutions, the question remains about how this relates to the chain conformation as a whole. To answer this question, it is first important to distinguish between typical main chain conjugated polymers and side chain polymers. As discussed in chapter 4, in a conjugated polymer solution, the degree of solubility of the polymer in the solvent at a specific concentration affects the chain-chain and chain-solvent interactions within this solution which in turn affects the polymer's aggregation. In a good solvent, for a main chain polymer, aggregate formation is minimized due to the preferential interaction between the polymer and the solvent molecules. On the contrary, in a bad solvent, aggregation would occur due to the prevalence of the chain-chain interactions [30, 39]. In the case of side chain polymers the solubility of the polymer is determined by the solubility of the inert polymer backbone. This means that a good solvent for the backbone would also lead to a more

open overall chain conformation. However, this implies the PDI side chain chromophores can arrange cofacially. This would lead to higher probability of interaction between the PDI chromophores located on the same polymer backbone. On the contrary, in a bad solvent the polymer backbone would adopt a less extended or collapsed conformation where the PDI moieties have a more random orientation around the backbone and the cofacial stacking arrangement is reduced. This would then lower the probability of interaction between PDI chromophores located on the same polymer backbone resulting in less excimer formation [30]. In the latter case, one would expect a higher probability of electronic interactions between PDI chromophores located on the different less extended polymer backbones when they come in proximity in a high concentrated medium like solution processed films. Figure 5 illustrates schematically the different between conjugated and side chain polymers in both the cases of good and bad solvents.

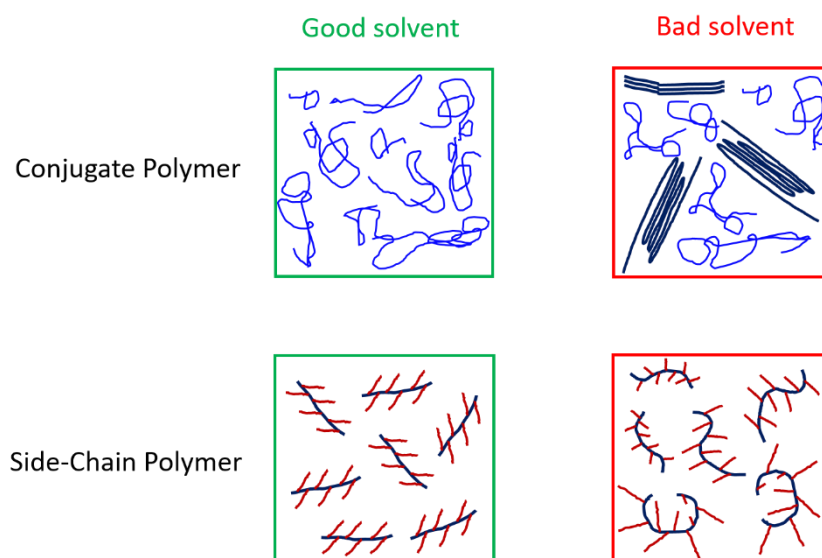


**Figure 5: 2D schematic presentation of the 3D polymer conformation in the cases of conjugated and side-chain polymers. In the case of side-chain polymers, the dark blue line represents the polymer backbone and the dark red lines present the functional chromophore attached to the polymer backbone.**

In summary, the solvent condition needed for aggregate formation in main chain polymers is opposite to that for side chain polymers. While aggregates of main chain polymers usually form in low quality solvents, aggregation of side chain polymers usually happens in high quality solvents in which the polymer backbone has good solubility [30].

To investigate the relation between chain conformation and the aggregation behavior in solution for both PPBI-alkyl and PPBI-OEG, I tracked the changes in the 0-0/0-1 peak ratios of the absorption spectra and the emission contribution from the monomers relative to the excimer emission as a

function of solution concentration. Figure 6 shows the concentration dependent absorption and photoluminescence spectra of both PPBI-alkyl and PPBI-OEG. This is measured over two orders of magnitude in solution concentration ( $10^{-5}$  M,  $10^{-6}$  M and  $10^{-7}$  M) for absorption and three orders of magnitude in solution concentration ( $10^{-5}$  M,  $10^{-6}$  M,  $10^{-7}$  M and  $10^{-8}$  M) for PL. To track the changes in the 0-0/0-1 peak ratio and the excimer to monomer emission contribution, the spectra are normalized to the 0-1 peak around 2.5 eV in absorption and the 0-1 monomer emission peak around 2.15 eV in PL.

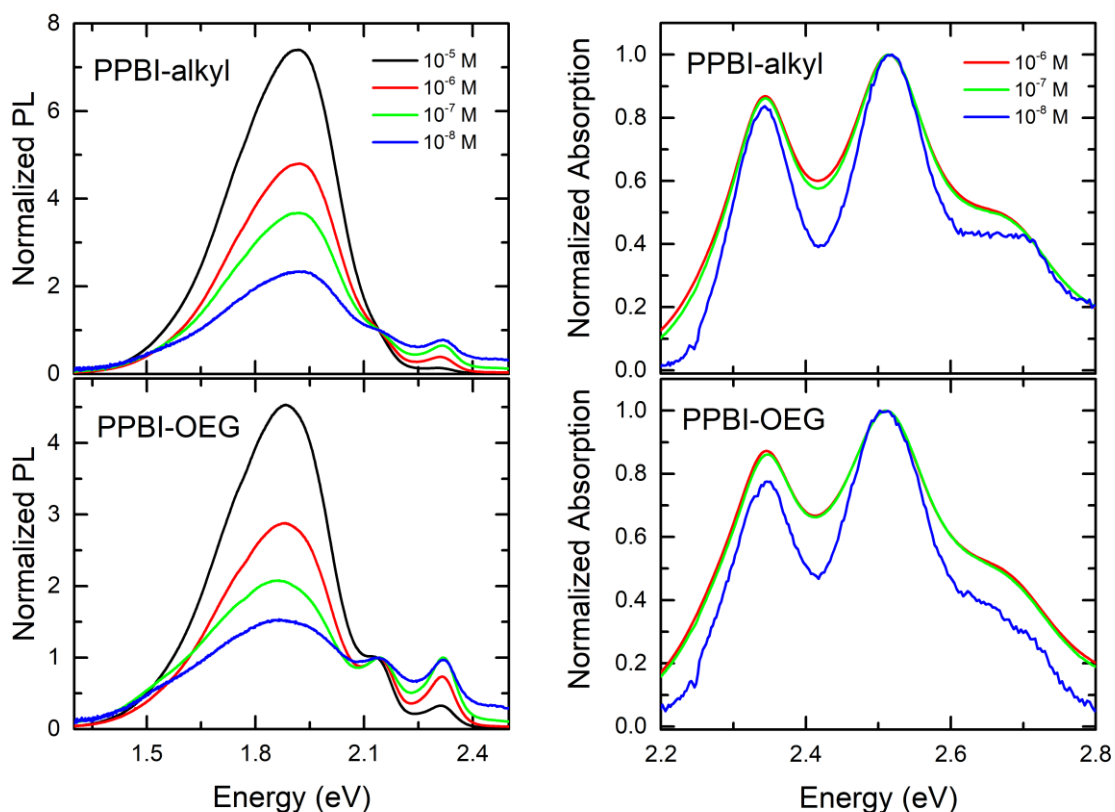


**Figure 6: Normalized photoluminescence and absorption spectra of PPBI-alkyl (top) and PPBI-OEG (bottom) as polymer solutions in CF at the four concentrations  $10^{-5}$  M (black),  $10^{-6}$  M (red),  $10^{-7}$  M (green) and  $10^{-8}$  M (blue).**

From the normalized absorption spectra of both PPBI-alkyl and PPBI-OEG, we observe a reduction of the 0-0/0-1 peak ratio compared to the monomer absorption even at lower polymer concentrations as discussed earlier (figure 2). This indicates the presence of electronic interactions between the PDI chromophores in the polymer solutions. However, no significant changes in the 0-0/0-1 peak ratios over two orders of magnitude of concentration are observed for both polymers. This means that the extent (strength) of the electronic molecular interaction between the PDIs is independent of concentration. In other words, the electronic interaction between the PDI

chromophores in a polymer solution is not affected by the presence (or non-presence) of extra polymer chains in such solution. This implies that the changes in the polymer absorption compared to the monomer absorption (e.g. 0-0/0-1 peak ratio) originate from the interaction between PDI chromophores located on the same polymer backbone. This is further confirmed by the PL spectra showing excimer emission even in very dilute solutions ( $10^{-8}$  M). If these excimers were formed between PDIs located on different polymer backbones we would expect their signature emission to disappear at such lower concentrations as the polymer chains are further apart, which is not the case here. However, the excimer emission is dependent on the solution concentration opposite to the 0-0/0-1 peak ratio in absorption. The increase of the excimer emission relative to the monomer emission at the higher concentrations can be attributed to energy transfer at these high concentrations [40].

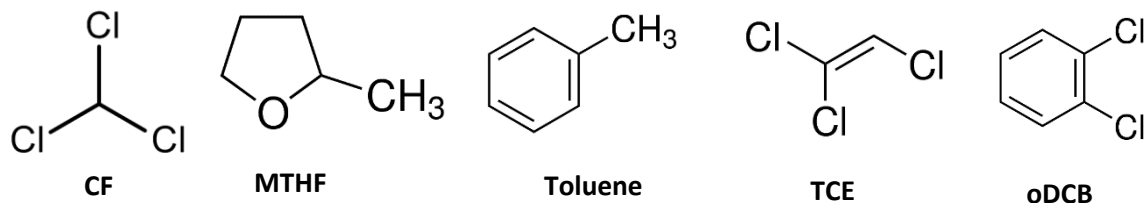
In summary, the above concentration dependent measurements imply that the difference I observe when moving from the monomer solution to the polymer solution (figure 2) is due to the electronic interaction of the PDI moieties located on the same polymer backbone. When further spin coating these solutions into films, a noticeable reduction of the 0-0/0-1 peak ratio is observed in the absorption spectra (figure 2). This implies that the further electronic interaction between the PDI moieties corresponds to the presence of additional electronic interactions which can be attributed to the interactions between PDIs located on different polymer backbones. These enhanced electronic interactions would be expected due to the high polymer concentration leading to the close proximity of the polymer chains in the film.

### iii. Effect of Solvent choice on aggregation

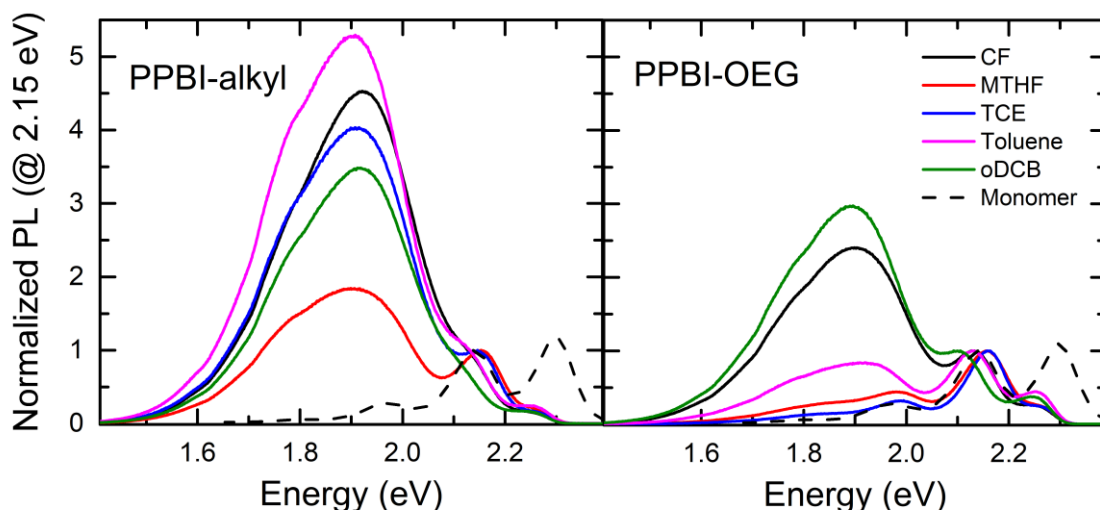
Based on the above results, control of the aggregation properties in these PDI side chain polymers would be achieved by manipulating the polymer's backbone conformation. This conformation can be manipulated by the degree of solubility or solvent quality with respect to the polymer backbone. In addition, one would expect a different impact of the solvent on both PPBI-alkyl and PPBI-OEG depending on the solvent polarity due to the different polarity of the two polymers caused by their respective side chains. To investigate this, I measured the photoluminescence spectra of the two polymers in five different solvents with varying solubility parameters, polarities and boiling points. I focus on PL as it provides direct way of comparison due to the variation between excimer and monomer emission intensities, which can give an idea about the overall chain conformation. In addition, at low concentrations PL is more sensitive than absorption.

Figure 7 shows the structure of the five solvents used: Chloroform (CF), Orthodichlorobenzene (oDCB), Toluene, Trichloroethylene (TCE), and 2-Methyltetrahydrofuran (MTHF). The relevant

solvent parameters are summarized in table 3. Figure 8 shows the normalized PL spectra for both PPBI-alkyl and PPBI-OEG in these five solvents. The monomer emission in CF is shown as the dashed black line for reference.



**Figure 7:** The structure of the solvents used in this work. By order from left to right they are: Chloroform (CF), 2-Methyltetrahydrofuran (MTHF), Toluene, Trichloroethylene (TCE), and Orthodichlorobenzene (oDCB).



**Figure 8:** Normalized photoluminescence (to the 0-1 monomer emission peak  $\approx 2.15$  eV) of PPBI-alkyl and PPBI-OEG polymers at  $10^{-5}$  M in five solvents. The dashed line corresponds to the monomer emission at  $10^{-5}$  M in CF solutions.

From figure 8, it is clear that the solvent effect is reflected in the different relative intensities of the excimer and monomer emissions. We observe a reduction of excimer emission intensity relative to the monomer emission intensity in the following order:

- For PPBI-alkyl, Toluene  $\rightarrow$  CF  $\rightarrow$  TCE  $\rightarrow$  oDCB  $\rightarrow$  MTHF
- For PPBI-OEG, oDCB  $\rightarrow$  CF  $\rightarrow$  Toluene  $\rightarrow$  MTHF  $\rightarrow$  TCE

The trend of the reduction of excimer emission intensity relative to the monomer emission intensity for PPBI-alkyl after Toluene is consistent with the Hansen solubility parameters shown in table 3. TCE and CF with very similar solubility parameters show comparable intensity of excimer emission followed by oDCB while MTHF shows the lowest excimer to monomer emission.

**Table 3 Boiling points of the different solvents and their total Hansen solubility parameters ( $\delta_t$ ) at 25°C with its dispersion ( $\delta_d$ ), polar ( $\delta_p$ ) and hydrogen bonding ( $\delta_h$ ) components [41, 42]**

Solvent	$\delta_t$ (MPa <sup>1/2</sup> )	$\delta_d$ (MPa <sup>1/2</sup> )	$\delta_p$ (MPa <sup>1/2</sup> )	$\delta_h$ (MPa <sup>1/2</sup> )	Boiling Point (°C)
<b>oDCB</b>	20.5	19.2	6.3	3.3	180
<b>CF</b>	19	17.8	3.1	5.7	61
<b>TCE</b>	19	18	3.1	5.3	87
<b>Toluene</b>	18.2	18	1.4	2	111
<b>MTHF</b>	17.7	16.8	4.8	4.6	80

Based on the simple rule of “like dissolves like” (i.e. a solvent dissolves a polymer with similar solubility parameters) and the reasoning that the excimer emission would be the most intense when the polymer backbone is the most extended, I could assume that Toluene is the best solvent for PPBI-alkyl compared to the other four solvents. On the contrary, oDCB would be considered the best solvent for PPBI-OEG compared to the other four solvents. It is important to note that a higher value of the solubility parameter doesn’t mean better solubility. What determines if a solvent has a good solvation for a certain polymer is difference between the solubility parameters of both the solvent and the polymer. This difference can be quantitatively calculated using the so called Hansen sphere as discussed in chapter 4 [43]. The smaller the difference between the solubility parameters of both the solvent and the polymer the better the solvation of this solvent for the polymer’s backbone. Based on this idea and the trend observed for the excimer emission in relation to the solvent’s solubility parameters, one could assume that the solubility parameter of PPBI-alkyl is in the range between 18.2 and 19 MPa<sup>1/2</sup>. Finally, the excimer to monomer emission trend does not show any apparent relation to the values of the polar contribution of the total solubility parameter. Figure 9 shows the same normalized PPBI-alkyl and PPBI-OEG spectra combined for each solvent to easily observe their different behavior in the same solvent

This difference in the solvent dependence of the excimer emission in PPBI-alkyl and PPBI-OEG would not be expected if only the total solubility parameter dictates how the polymers aggregates since the backbone is the same in both polymers (i.e. solvation effect). This is apparent if I compare the spectra of both PPBI-alkyl and PPBI-OEG in the same solvent. For example, in Toluene which

has the lowest polarity contribution to the overall solubility parameter, the monomer emission dominates the PPBI-OEG spectrum while the excimer emission dominates the PPBI-alkyl spectrum. This difference implies an extra role of the OEG and the alkyl side chains which is expected to affect the aggregation of the two PDI polymers depending on the side chain polarities.

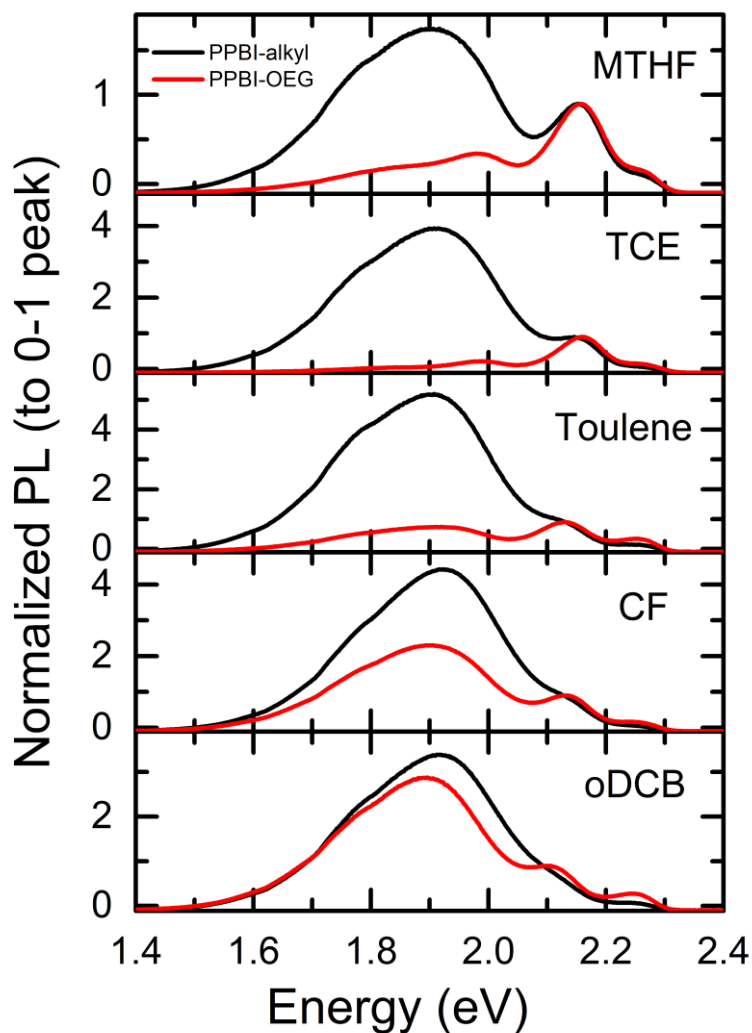


**Figure 9: Normalized photoluminescence (to the 0-1 monomer emission peak  $\approx 2.15$  eV) of PPBI-alkyl polymer and PPBI-OEG polymer at  $10^{-5}M$  in 5 solvents**

The difference observed between both polymers could have been further confirmed by repeating the above solvent dependent measurements for the monomers only. This would have allowed for isolating the OEG and the alkyl side chains effect and the backbone effect by comparing the monomer and polymer emission in the different solvents. However, due to the limited amount of monomers I had and the difficulty in synthesizing additional quantities I was not able to perform such measurement.

## 5.4 Discussion

It has been shown that due to the unique architecture of side chain polymers where the PDI moieties are attached to a polymer backbone, the aggregation properties of the PDIs are controlled by the conformation of the polymer backbone [29, 30]. It has been shown that for PDIs attached to a polynorbornene backbone the overall polymer's aggregation is controlled by the degree of the backbone solvation [30]. In a good solvent, the polynorbornene backbone adopts a more extended conformation through which the attached PDIs follow a co-facial stacking structure along the backbone leading to enhanced electronic interaction i.e. "more order" between them. On the other hand, in a bad solvent the backbone adopts a more globular conformation leading to the break of co-facial stacking of the PDI moieties as they are randomly arranged along the collapsed backbone. This would lead to lower intramolecular interaction i.e. "less order" [30] between these PDI chromophores. In a similar manner, this applies for PDIs attached to a more rigid polyisocyanopeptides backbone that has a helical structure [29]. Molecular dynamics simulations showed that depending on the linker between the backbone and the PDI side chains, three different PDI orientations can be realized in films while keeping the backbone unaffected. This side chain approach allowed for spatial control of the PDI chromophores around the stiff backbone leading to different polymer morphologies [29].

Regarding the impact of solvent polarity, it has been shown that the polarity of the side chain i.e. alkyl vs OEG, impacts the morphological and aggregation properties of PDI monomers in aqueous solution [38]. Also, it has been shown that incorporating a polar component into P3HT copolymers alters the final film morphology compared to P3HT copolymers with a non-polar component [44]. Despite all of the above studies, the combined effect of both the backbone solvation on one hand and the solvent polarity with respect to the side chain on the other hand, have not been studied simultaneously on side chain polymers. For the two polymers studied here, as discussed in figure 9, if the overall polymer aggregation is only dictated by how well the polystyrene backbone is solvated, we would expect the same solvent dependency trend of the relative intensities of the excimer and monomer emissions in both polymers. However, this is not the case here which hints towards the effect of the tail attached to the PDI side chain, i.e. whether it is alkyl or OEG. The only difference between those tails is the oxygen present in the OEG group which increases the sidechain and overall polymer polarity [32].

In the case of PPBI-alkyl with the non-polar tails, the relative intensity between the excimer and monomer emission mainly depends on the backbone conformation which is dictated by the solvent's solubility parameter. Consequently, an extended polymer backbone conformation would

lead to higher probability of interaction between the PDI moieties which I refer to here as “intramolecular coupling” in the sense that this interaction is between moieties on the same backbone. In the other extreme where the polymer backbone is less extended, the PDI moieties would adopt a more random orientation around the backbone with less cofacial stacking which lowers the probability of interaction between them and results in less excimer formation.

In the case of PPBI-OEG, I can conclude that the interplay between the solubility of the polystyrene backbone and the degree of solvent polarity (in relation to the polarity of the OEG chain) controls the overall interaction between the PDI moieties. The solubility parameter of the solvent determines the conformation of the polystyrene backbone while the solvent polarity determines the orientation of the PDI moieties around the backbone. OEG side chains are known to be more flexible compared to the alkyl side chains due to the reduced steric hindrance. This reduced steric hindrance is a result of the lower energetic barrier of rotation for the C-O bond in the OEG side chain compared to that for the C-C bond in the alkyl side chain [45, 46]. This might lead to the reduction of excimer emission appearing in the PL spectra due to the lower probability of cofacial stacking of the PDI chromophores along the same or different polymer backbones. This effect might be countered by a reduction in the  $\pi$ - $\pi$  stacking distance in case of cofacial stacking which has been shown when alkyl side chains are replaced by OEG side chains [45]. These two contrasting effects (flexibility vs. reduction in the  $\pi$ - $\pi$  stacking distance) might be further affected by the solvent polarity and its interaction with the polar OEG side chains which then determines the final overall polymer conformation.

The above reasoning is consistent with several observations from figure 9 when comparing the spectra for both PPBI-alkyl and PPBI-OEG in the same solvent. For example, in Toluene, the high excimer to monomer emission ratio is due to the expected good solubility of the polystyrene backbone in Toluene leading to the most extended conformation compared to the other solvents used. The non-polar effect of toluene is significant in the case of PPBI-OEG. In PPBI-OEG, the monomer emission dominates the PL spectra although the polymer backbone should more or less adopt the same extended conformation as in PPBI-alkyl. This means that in case of toluene the PDI moieties are randomly oriented around the polystyrene backbone breaking the cofacial stacking arrangement and hence limiting the excimer formation. The effect of solvent polarity can be also observed in the case of using oDCB. PPBI-OEG in oDCB shows the highest excimer emission compared to PPBI-OEG in the other solvents which is consistent with oDCB possessing the highest polarity as indicated by its  $\delta_p$  value while still having a good solubility for the polymer backbone compared to the other solvents. The same applies for CF which shows similar PPBI-OEG spectra to oDCB. While MTHF and CF have a comparable polarity, the behavior of PPBI-OEG in both solvents

is different. The PL spectra of PPBI-OEG in MTHF shows a significant reduction in the excimer emission and the monomer emission dominates the PL spectra opposite to the spectra of PPBI-OEG in CF. This discrepancy can be explained by the poor solubility of MTHF to the polymer backbone compared to CF.

The only deviation from the above is the case TCE. TCE and CF have nearly identical solvent properties with very similar components (table 3) which is reflected in the PL spectra of PPBI-alkyl in both of them. These two spectra of CF (black line) and TCE (blue line) from figure 8 are very similar with CF having a slightly higher excimer intensity. However, the PL spectra of PPBI-OEG in both CF (black line) and TCE (blue line) from figure 8 are very different. The spectra of PPBI-OEG in CF shows a reduced relative excimer intensity compared to PPBI-alkyl in CF. Yet the excimer emission still dominates the spectra for both polymers in CF. In TCE however, the spectra of PPBI-OEG shows an almost fully quenched excimer emission and the monomer emission with its characteristic peaks dominates the spectra. This is counterintuitive as both solvents have identical solubility indices and polarities (table 3). The only difference between both solvents are their boiling points that should not have any effect in the solutions.

It is important to note the comparisons and conclusions I show here are relative based on the solubility and polarity information of the different solvents and how they affect the PL spectra. A more exact picture of how good a specific solvent dissolves a polymer can be quantified by knowing the polymer's solubility sphere. The polymer's solubility sphere is constructed by the Hansen solubility parameter of the polymer with its three components and another parameter called the interaction Radius of polymers as mentioned previously [43]. Unfortunately, this information is not available for the polymer backbone used in this work. While the film formation dynamics are not yet discussed in detail here, it should be noted that when spin coating films from solution the resulting PL spectra are nearly identical for all the solvents and similar to what is shown for oDCB in figure 2. This is likely due to fast energy transfer between the monomers and the excimers leading to dominant excimer emission.

## 5.5 Conclusion

In this chapter, I characterized the aggregation properties of two side chain polymers based on an inert polystyrene backbone and two PDI chromophores having different side chains. I have shown that it is possible to control the electronic interaction between the PDI chromophores by controlling the polymer backbone conformation and the arrangement of the PDI chromophores around the backbone. The degree of solubility of the polymer's back bone in a certain solvent controls the backbone conformation while the solvent polarity affects the arrangement of PDI chromophores

around the backbone depending on the attached side chain. The interplay between the solvation and polarity may allow for tuning the aggregation of the material towards the desired properties.

In conclusion, I have shown the possibility of controlling the aggregation properties of side chain polymers based on PDI chromophores in solutions by varying the solvent properties. The degree of solvation controls the backbone conformation while the solvent polarity affects the orientation of PDI moieties around the backbone. The combined effect of both the solvation and polarity may allow for tuning the aggregation of the material towards the desired properties useful for device applications like organic solar cells.

## References

- [1] A.S. Lang, M. Thelakkat, Modular synthesis of poly(perylene bisimides) using click chemistry: a comparative study, *Polym Chem-Uk*, 2 (2011) 2213-2221.
- [2] H. Kang, W. Lee, J. Oh, T. Kim, C. Lee, B.J. Kim, From Fullerene-Polymer to All-Polymer Solar Cells: The Importance of Molecular Packing, Orientation, and Morphology Control, *Accounts Chem Res*, 49 (2016) 2424-2434.
- [3] N.N. Liang, W. Jiang, J.H. Hou, Z.H. Wang, New developments in non-fullerene small molecule acceptors for polymer solar cells, *Mater Chem Front*, 1 (2017) 1291-1303.
- [4] J.Y. Yuan, W.P. Guo, Y.X. Xia, M.J. Ford, F. Jin, D.Y. Liu, H.B. Zhao, O. Inganäs, G.C. Bazan, W.L. Ma, Comparing the device physics, dynamics and morphology of polymer solar cells employing conventional PCBM and non-fullerene polymer acceptor N2200, *Nano Energy*, 35 (2017) 251-262.
- [5] J.Q. Zhang, H.S. Tan, X.G. Guo, A. Facchetti, H. Yan, Material insights and challenges for non-fullerene organic solar cells based on small molecular acceptors, *Nat Energy*, 3 (2018) 720-731.
- [6] Y.W. Zhang, A.J. Parnell, O. Blaszczyk, A.J. Musser, I.D.W. Samuel, D.G. Lidzey, G. Bernardo, Effect of fullerene acceptor on the performance of solar cells based on PffBT4T-2OD, *Phys Chem Chem Phys*, 20 (2018) 19023-19029.
- [7] A. Wadsworth, M. Moser, A. Marks, M.S. Little, N. Gasparini, C.J. Brabec, D. Baran, I. McCulloch, Critical review of the molecular design progress in non-fullerene electron acceptors towards commercially viable organic solar cells, *Chem Soc Rev*, 48 (2019) 1596-1625.
- [8] C.H. Duan, L.M. Ding, The new era for organic solar cells: polymer acceptors, *Sci Bull*, 65 (2020) 1508-1510.
- [9] C.H. Duan, L.M. Ding, Highlight The new era for organic solar cells: non-fullerene small molecular acceptors, *Sci Bull*, 65 (2020) 1231-1233.
- [10] Q.F. Yan, Y. Zhou, Y.Q. Zheng, J. Pei, D.H. Zhao, Towards rational design of organic electron acceptors for photovoltaics: a study based on perylenediimide derivatives, *Chem Sci*, 4 (2013) 4389-4394.
- [11] W.T. Xiong, X.Y. Meng, T. Liu, Y.H. Cai, X.N. Xue, Z.B. Li, X.B. Sun, L.J. Huo, W. Ma, Y.M. Sun, Rational design of perylenediimide-based polymer acceptor for efficient all-polymer solar cells, *Org Electron*, 50 (2017) 376-383.
- [12] C.H. Duan, L.M. Ding, The new era for organic solar cells: small molecular donors, *Sci Bull*, 65 (2020) 1597-1599.
- [13] C. Huang, S. Barlow, S.R. Marder, Perylene-3,4,9,10-tetracarboxylic Acid Diimides: Synthesis, Physical Properties, and Use in Organic Electronics, *J Org Chem*, 76 (2011) 2386-2407.
- [14] X.W. Zhan, A. Facchetti, S. Barlow, T.J. Marks, M.A. Ratner, M.R. Wasielewski, S.R. Marder, Rylene and Related Diimides for Organic Electronics, *Adv Mater*, 23 (2011) 268-284.
- [15] A.S. Lang, M.A. Muth, C.D. Heinrich, M. Carassco-Orozco, M. Thelakkat, Pendant perylene polymers with high electron mobility, *J Polym Sci Pol Phys*, 51 (2013) 1480-1486.
- [16] C.W. Tang, Two-layer organic photovoltaic cell, *Appl. Phys. Lett.*, 48 (1986) 183.
- [17] C. Huang, W.J. Potscavage, S.P. Tiwari, S. Sutcu, S. Barlow, B. Kippelen, S.R. Marder, Polynorbornenes with pendant perylene diimides for organic electronic applications, *Polym Chem-Uk*, 3 (2012) 2996-3006.

- [18] S. Rajaram, R. Shivanna, S.K. Kandappa, K.S. Narayan, Nonplanar Perylene Diimides as Potential Alternatives to Fullerenes in Organic Solar Cells, *J Phys Chem Lett*, 3 (2012) 2405-2408.
- [19] W. Jiang, L. Ye, X.G. Li, C.Y. Xiao, F. Tan, W.C. Zhao, J.H. Hou, Z.H. Wang, Bay-linked perylene bisimides as promising non-fullerene acceptors for organic solar cells, *Chem Commun*, 50 (2014) 1024-1026.
- [20] P.E. Hartnett, A. Timalina, H.S.S.R. Matte, N.J. Zhou, X.G. Guo, W. Zhao, A. Facchetti, R.P.H. Chang, M.C. Hersam, M.R. Wasielewski, T.J. Marks, Slip-Stacked Perylenediimides as an Alternative Strategy for High Efficiency Nonfullerene Acceptors in Organic Photovoltaics, *J Am Chem Soc*, 136 (2014) 16345-16356.
- [21] Z.J. Chen, A. Lohr, C.R. Saha-Moller, F. Wurthner, Self-assembled pi-stacks of functional dyes in solution: structural and thermodynamic features, *Chem Soc Rev*, 38 (2009) 564-584.
- [22] S. Rajaram, P.B. Armstrong, B.J. Kim, J.M.J. Frechet, Effect of Addition of a Diblock Copolymer on Blend Morphology and Performance of Poly(3-hexylthiophene):Perylene Diimide Solar Cells, *Chem Mater*, 21 (2009) 1775-1777.
- [23] M. Son, K.H. Park, C.Z. Shao, F. Wurthner, D. Kim, Spectroscopic Demonstration of Exciton Dynamics and Excimer Formation in a Sterically Controlled Perylene Bisimide Dimer Aggregate, *J Phys Chem Lett*, 5 (2014) 3601-3607.
- [24] D. Sun, D. Meng, Y.H. Cai, B.B. Fan, Y. Li, W. Jiang, L.J. Huo, Y.M. Sun, Z.H. Wang, Non-Fullerene-Acceptor-Based Bulk-Heterojunction Organic Solar Cells with Efficiency over 7%, *J Am Chem Soc*, 137 (2015) 11156-11162.
- [25] Y. Zhong, M.T. Trinh, R.S. Chen, W. Wang, P.P. Khlyabich, B. Kumar, Q.Z. Xu, C.Y. Nam, M.Y. Sfeir, C. Black, M.L. Steigerwald, Y.L. Loo, S.X. Xiao, F. Ng, X.Y. Zhu, C. Nuckolls, Efficient Organic Solar Cells with Helical Perylene Diimide Electron Acceptors, *J Am Chem Soc*, 136 (2014) 15215-15221.
- [26] M. Liu, J. Yang, C.L. Lang, Y. Zhang, E.J. Zhou, Z.T. Liu, F.Y. Guo, L.C. Zhao, Fused Perylene Diimide-Based Polymeric Acceptors for Efficient All-Polymer Solar Cells, *Macromolecules*, 50 (2017) 7559-7566.
- [27] J.Q. Zhang, Y.K. Li, J.C. Huang, H.W. Hu, G.Y. Zhang, T.X. Ma, P.C.Y. Chow, H. Ade, D. Pan, H. Yan, Ring-Fusion of Perylene Diimide Acceptor Enabling Efficient Nonfullerene Organic Solar Cells with a Small Voltage Loss, *J Am Chem Soc*, 139 (2017) 16092-16095.
- [28] K.K. Weng, C. Li, P.Q. Bi, H.S. Ryu, Y.K. Guo, X.T. Hao, D.H. Zhao, W.W. Li, H.Y. Woo, Y.M. Sun, Ternary organic solar cells based on two compatible PDI-based acceptors with an enhanced power conversion efficiency, *J Mater Chem A*, 7 (2019) 3552-3557.
- [29] E. Schwartz, V. Palermo, C.E. Finlayson, Y.S. Huang, M.B.L. Otten, A. Liscio, S. Trapani, I. Gonzalez-Valls, P. Brocorens, J.J.L.M. Cornelissen, K. Peneva, K. Mullen, F.C. Spano, A. Yartsev, S. Westenhoff, R.H. Friend, D. Beljonne, R.J.M. Nolte, P. Samori, A.E. Rowan, "Helter-Skelter-Like" Perylene Polyisocyanopeptides, *Chem-Eur J*, 15 (2009) 2536-2547.
- [30] M.S. Glaz, J.D. Biberdorf, M.T. Nguyen, J.J. Travis, B.J. Holliday, D.A. Vanden Bout, Perylene diimide functionalized polynorbornene: a macromolecular scaffold for supramolecular self-assembly, *J Mater Chem C*, 1 (2013) 8060-8065.
- [31] X. Liu, B.M. Xie, C.H. Duan, Z.J. Wang, B.B. Fan, K. Zhang, B.J. Lin, F.J.M. Colberts, W. Ma, R.A.J. Janssen, F. Huang, Y. Cao, A high dielectric constant non-fullerene acceptor for efficient bulk-heterojunction organic solar cells, *J Mater Chem A*, 6 (2018) 395-403.
- [32] J. Brebels, J.V. Manca, L. Lutsen, D. Vanderzande, W. Maes, High dielectric constant conjugated materials for organic photovoltaics, *J Mater Chem A*, 5 (2017) 24037-24050.

- [33] W.E. Ford, Photochemistry of 3,4,9,10-Perylenetetracarboxylic Dianhydride Dyes - Visible Absorption and Fluorescence of the Di(Glycyl)Imide Derivative Monomer and Dimer in Basic Aqueous-Solutions, *J Photochem*, 37 (1987) 189-204.
- [34] R. Gomez, D. Veldman, R. Blanco, C. Seoane, J.L. Segura, R.A.J. Janssen, Energy and electron transfer in a poly(fluorene-alt-phenylene) bearing perylenediimides as pendant electron acceptor groups, *Macromolecules*, 40 (2007) 2760-2772.
- [35] E.E. Neuteboom, S.C.J. Meskers, E.W. Meijer, R.A.J. Janssen, Photoluminescence of self-organized perylene bisimide polymers, *Macromol Chem Phys*, 205 (2004) 217-222.
- [36] F. Spreitler, M. Sommer, M. Thelakkat, J. Köhler, Conformational dynamics of di-(perylene bisimide acrylate) and its footprints in steady-state, time-resolved, and fluorescence-correlation spectroscopy, *Phys Chem Chem Phys*, 14 (2012) 7971-7980.
- [37] W.E. Ford, P.V. Kamat, Photochemistry of 3,4,9,10-Perylenetetracarboxylic Dianhydride Dyes .3. Singlet and Triplet Excited-State Properties of the Bis(2,5-Di-Tert-Butylphenyl)Imide Derivative, *J Phys Chem-Us*, 91 (1987) 6373-6380.
- [38] J. Schill, L.G. Milroy, J.A.M. Lugger, A.P.H.J. Schenning, L. Brunsveld, Relationship between Side-Chain Polarity and the Self-Assembly Characteristics of Perylene Diimide Derivatives in Aqueous Solution, *Chemistryopen*, 6 (2017) 266-272.
- [39] F. Panzer, H. Bässler, A. Köhler, Temperature Induced Order-Disorder Transition in Solutions of Conjugated Polymers Probed by Optical Spectroscopy, *J Phys Chem Lett*, 8 (2017) 114-125.
- [40] W.R. Ware, P. Richter, Fluorescence Quenching Via Charge Transfer - Perylene-N N-Dimethylaniline System, *J Chem Phys*, 48 (1968) 1595-&.
- [41] A.F.M. Barton, *Handbook of Solubility Parameters and Other Cohesion Parameters - Barton*, *Afm*, CRC Press, 54 (1984) 153-157.
- [42] M.V. Anne-Gaëlle Sicaire, Aurore Filly, Ying Li, Antoine Bily, Farid Chemat, 2-Methyltetrahydrofuran: Main Properties, Production Processes, and Application in Extraction of Natural Products, Chemat, F., Vian, M. (eds) *Alternative Solvents for Natural Products Extraction. Green Chemistry and Sustainable Technology*. Springer, Berlin, Heidelberg, (2014) 253–268.
- [43] J. Burke, *Solubility Parameters: Theory and Application*, (1984).
- [44] M.J. Dyson, E. Lariou, J. Martin, R.P. Li, H. Erothu, G. Wantz, P.D. Topham, O.J. Dautel, S.C. Hayes, P.N. Stavrinou, N. Stingelin, Managing Local Order in Conjugated Polymer Blends via Polarity Contrast, *Chem Mater*, 31 (2019) 6540-6547.
- [45] B. Meng, H.Y. Song, X.X. Chen, Z.Y. Xie, J. Liu, L.X. Wang, Replacing Alkyl with Oligo(ethylene glycol) as Side Chains of Conjugated Polymers for Close pi-pi Stacking, *Macromolecules*, 48 (2015) 4357-4363.
- [46] B. Meng, J. Liu, L.X. Wang, Oligo(ethylene glycol) as side chains of conjugated polymers for optoelectronic applications, *Polym Chem-Uk*, 11 (2020) 1261-1270.

# Chapter 6: Film formation & aggregation of materials and blends for organic solar cells

## 6.1 Introduction

After I examined the basic characteristics of PDIs and their aggregation in solution as a function of solvent properties (solubility parameter & solvent polarity) in the previous chapter, I explore the application of these PDIs in solar cells in combination with other donor and acceptor materials. I started by comparing the performance of both PPBI-alkyl and PPBI-OEG in solar cells in both bilayer and binary BHJ architectures. Then I investigated how the mixing of fullerene and non-fullerene acceptors to form the acceptor layer in the bilayer architecture affects the resulting device performance. The underlying idea is that this combination of a fullerene and a non-fullerene polymer acceptor such as the side chain PDI polymers investigated in the previous chapter, would improve the overall solar cell performance due to the combined advantages of both acceptors. The fullerene acceptor would help in charge generation due to better mixing and diffusion within the other materials domain. Conversely, the polymer acceptor would help in creating percolation paths for better charge transport in addition to providing a more stable morphology that would lead to better device stability. The goal is to investigate how the addition of PCBM as a fullerene acceptor affects the aggregation behavior of the polymer acceptor compared to the aggregation behavior of the polymer acceptor in the neat films. By characterizing the film formation dynamics in such blends and their solar cell performance, I aim to determine what aggregation features correspond to an enhanced solar cell performance. I then try to correlate between the underlying structural origins of such enhancement to the electrical characteristics in terms of charge generation and transport. This would enable us to rationally choose material systems that provide optimum morphology for enhanced solar cell performance rather than following a trial-and-error approach.

This project was in collaboration with *Mihirsinh Chauhan* within our respective thesis work. We fabricated solar cells in different device architectures including bilayers, bilayers with a mixed acceptor layer, binary bulk heterojunctions, and ternary bulk heterojunctions. While we both worked on the optimization of the device performance, I focused on the insitu characterization and the physics of film formation, and he focused on the electrical characterization of the devices and the device physics. I performed all the insitu optical measurements and analysis while *Mihirsinh Chauhan* analyzed the field dependent and light intensity dependent measurements of the solar cells.

## 6.2 Fullerene vs. PDI polymers as acceptors in solar cells

Initially, I compared the PDI based solar cells to PCBM based solar cells, both in combination with PCE11 as the donor polymer either in bilayer or binary BHJ configurations. For the bilayers, the PCE11 donor layer was spin coated from an oDCB solution and kept at  $\approx 60$  nm thickness for all the devices. The acceptor layers were spin coated from CF as it does not dissolve PCE11, and its thickness was kept at  $\approx 20$  nm for all the devices. These thicknesses were chosen after several trials to achieve the best device performance in terms of sufficient light absorption and balanced charge mobilities. For the binary bulk heterojunction (BHJ) devices, the active layers were spin coated from oDCB solution at a 1:1 donor to acceptor weight ratio. The thickness of the binary BHJ active layers were kept at  $\approx 100$  nm for all the devices. Figure 1 shows the J-V curves of the bilayer and the binary BHJ solar cells using PCE11 as the donor and either PPBI-alkyl, PPBI-OEG or PCBM as the acceptor.

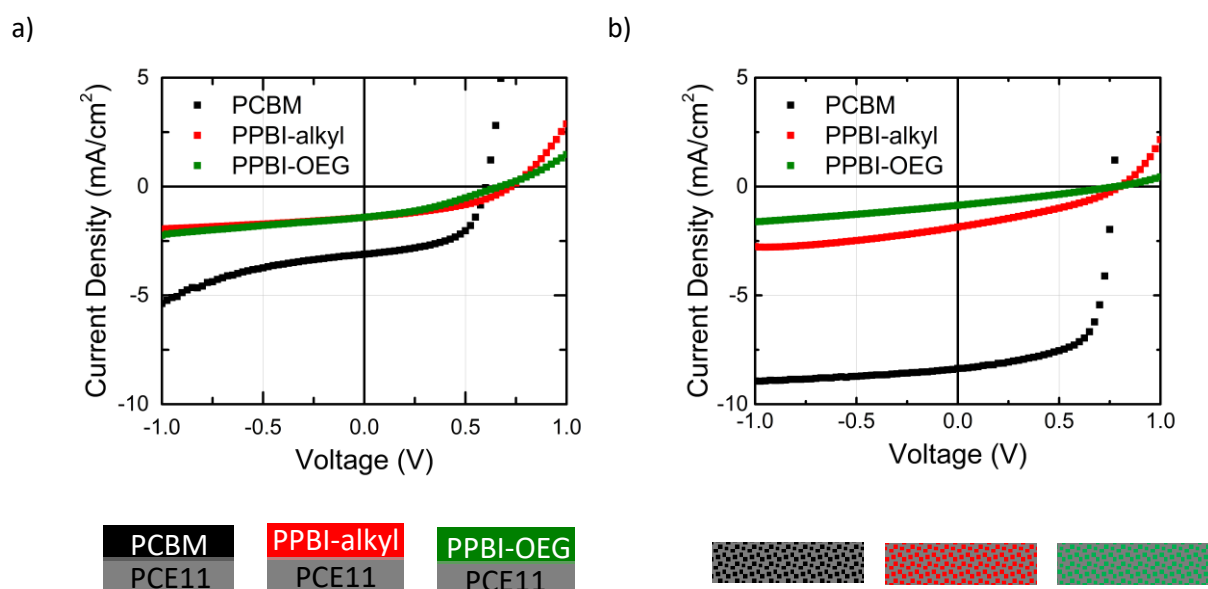


**Figure 1:** a) J-V curves of the bilayer solar cells. The donor layer for all the devices was PCE11 spin coated from oDCB solution at a 5g/l concentration with 60 nm thickness, while the top layer consisted of PCBM (black filled squares), PPBI-alkyl (red filled squares) or PPBI-OEG (green filled squares) spin coated from CF solutions at a 5g/l concentration with 20 nm thickness. Schematic of the active layer structure is shown below the J-V curves. b) J-V curves of the binary BHJ solar cells. The active layers were spin coated from an oDCB solution of PCE11:acceptor binary blends with 1:1 ratio at a 5g/l concentration. Schematic of the active layer structure is shown below the J-V curves.

From figure 1, one can clearly observe that for either bilayer or binary BHJ configuration PCBM offers a much better overall solar cell performance compared to both PDIs. It is also clearly visible that both PPBI-alkyl and PPBI-OEG offer comparable solar cell performance in both the bilayer and BHJ configurations. For the bilayer solar cells, the  $J_{sc}$  for both PDI-based devices is almost identical

with a value  $\approx 1.4 \text{ mA/cm}^2$  while  $V_{oc}$  for PPBI-alkyl is higher than that of PPBI-OEG (0.75 V vs 0.68 V). The fill factors of both PDI-based devices are much worse than that of PCBM-based ones. In addition, the J-V curve for PCBM features an increasing slope at low reverse voltages below -0.5 V compared to PDIs that show minimal current losses between -1 V and  $J_{sc}$ .

From figure 1, when comparing the performance of bilayer solar cells and the binary BHJ solar cells, we observe a significant increase in all the parameters of PCBM compared to those of PDIs. Most significantly,  $J_{sc}$  of the PCBM BHJ devices is  $\approx 2.5$  times higher than that of the PCBM bilayer device ( $3.2 \text{ mA/cm}^2$  vs.  $8.2 \text{ mA/cm}^2$ ). For PPBI-alkyl, we observe a slight increase in the  $J_{sc}$  from  $1.4 \text{ mA/cm}^2$  to  $1.9 \text{ mA/cm}^2$  along with the increase of  $V_{oc}$  from 0.75 V to 0.83 V. Despite these small improvements, the very low fill factor led to no significant difference between the overall efficiency of the BHJ device compared to the bilayer device (0.5% vs 0.42%). The situation for PPBI-OEG is even worse when combined with PCE11 in the binary BHJ solar cell.  $J_{sc}$  suffers from around 40% decrease along with the lower fill factor. Despite the increase of  $V_{oc}$  (0.68 V to 0.8 V), the overall BHJ device performance is worse than that of the bilayer device. Based on these results and having in mind that the reported electron mobility for both PDIs is comparable to that of PCBM [1], I fabricated a bilayer device where the acceptor layer consists of a mixed PCBM/PPBI-alkyl layer with different ratios. I focus on PPBI-alkyl for the solar cell fabrication throughout the rest of this chapter due to its slightly better solar cell performance. It is important to note that the energy level structure of both PCBM (HOMO = -6 eV, LUMO = -3.9 eV) [2] and PPBI-alkyl (HOMO = -6.08 eV, LUMO = -4.03 eV) [1] should allow for charge transport between both components which is an important prerequisite to ensure efficient charge generation.

Figure 2.a shows the J-V curves of the mixed bilayer solar cells along with the curves for the bilayer solar cells made with either acceptors. The thickness of the acceptor layer was kept at  $\approx 20 \text{ nm}$  for all devices. From the J-V curves, we observe a slightly enhanced solar cell performance of the mixed bilayer devices compared to the devices made with either PCBM or PPBI-alkyl alone. Most significantly, the addition of PPBI-alkyl led to an improved  $V_{oc}$  in the mixed bilayer devices at both mixing ratios. Figure 2.b shows the values of  $V_{oc}$  as a function of PPBI-alkyl and PCBM content. From the figure it is apparent that the bilayer devices consisting of a PCBM:PPBI-alkyl mixed acceptor layer produce  $V_{oc}$  values intermediate between those of the PCBM and PPBI-alkyl only devices. The device made with a PCBM:PPBI-alkyl ratio of 0.75:0.25 (25% PPBI-alkyl addition) showed the largest  $V_{oc}$  enhancement ( $\approx 50\%$ ) compared to the PCBM only bilayer device (0.46 V to 0.69 V). However, the increase of  $V_{oc}$  as a function of PPBI-alkyl content above 25% is minimal as compared to the initial increase of around 50%.

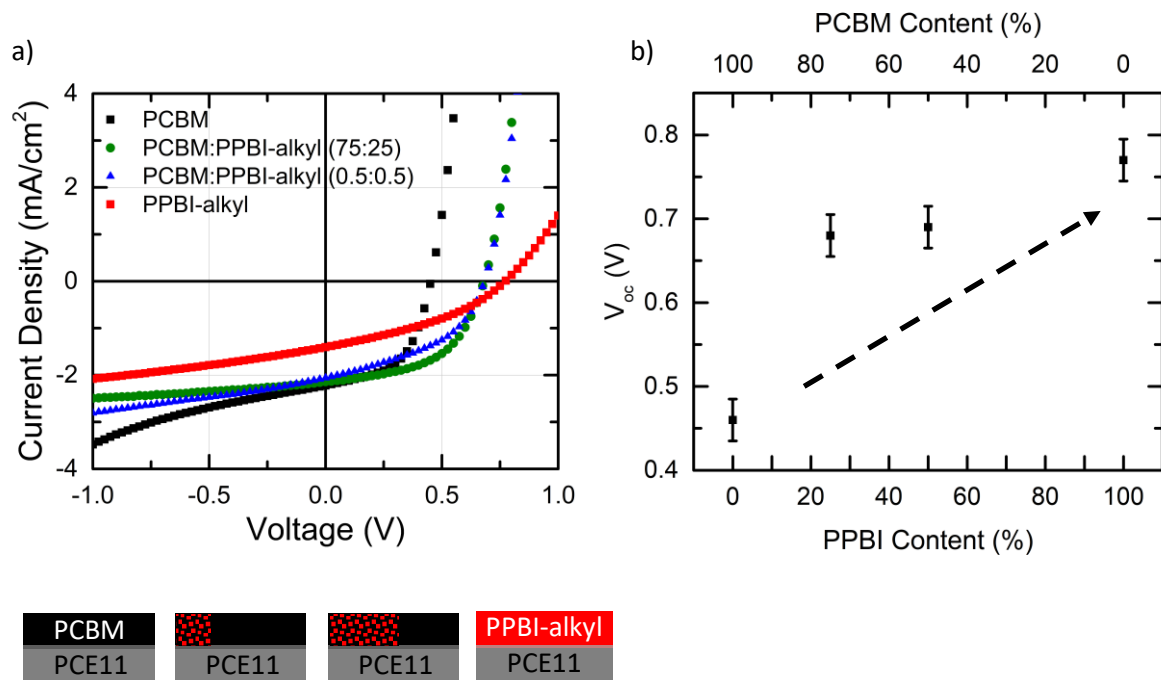


**Figure 2:** a) J-V curves of the bilayer solar cells consisting of PCE11 as the bottom donor layer while the top acceptor layer is PCBM (black filled squares), PPBI-alkyl (red filled squares) or a PCBM:PPBI-alkyl mixture with equal weight ratio of 1:1 (blue filled triangles and green filled circles). b)  $V_{oc}$  vs. PPBI-alkyl content (PCBM content) at 0% (100%), 75% (25%), 50% (50%) and 100% (0%); 100% PPBI-alkyl content indicates a PCE11/PPBI-alkyl bilayer device and 0% PPBI-alkyl content indicates a PCE11/PCBM bilayer device. The dashed black arrow shows the trend in  $V_{oc}$  as a function of PPBI-alkyl content. Schematic of the active layer structure is shown below the J-V curves where the content of the acceptor layer is shown by the ratio between the black (PCBM) and the red (PPBI-alkyl) areas.

Table 1 shows the summary of the solar cell parameters for all the PCBM:PPBI-alkyl mixing ratios. Figure 3 shows the  $V_{oc}$ ,  $J_{sc}$ , fill factor (FF) and power conversion efficiency (PCE) of the mixed bilayer devices as a function of the PPBI-alkyl content. In terms of the overall device efficiency, the best device is at the PCBM:PPBI-alkyl ratio of 0.75:0.25. Although this device doesn't have the best values for the individual parameters, it has almost double the PCE of the PPBI-alkyl only device and a 50% higher PCE compared to the PCBM only device. The main contributor to this 50% increase in PCE of the PCBM:PPBI-alkyl (0.75:0.25) device compared to the PCBM only device is the 50% increase in  $V_{oc}$ . It is finally worth noting that the current loss appearing in PCBM at high reverse voltages disappears in all the mixed acceptor layer devices. This could be attributed to a decrease in the dark current when PPBI-alkyl is added to PCBM. These results confirm the initial hypothesis that the combined advantages of both PCBM and PPBI-alkyl would lead to better solar cell performance even in bilayer solar cells.

**Table 1** Device performance of the solar cells made of a mixed PCBM:PPBI-alkyl acceptor layer at different mixing ratios

PCE11/(PC <sub>60</sub> BM:PPBI-alkyl)	J <sub>sc</sub> (mAcm <sup>-2</sup> )	V <sub>oc</sub> (V)	FF (%)	PCE (%)
1/(0:1)	1.40	0.77	37	0.40
1/ (0.50:0.50)	2.06	0.69	44	0.63
1/ (0.75:0.25)	2.14	0.68	53	0.77
1/(1:0)	2.22	0.46	53	0.54

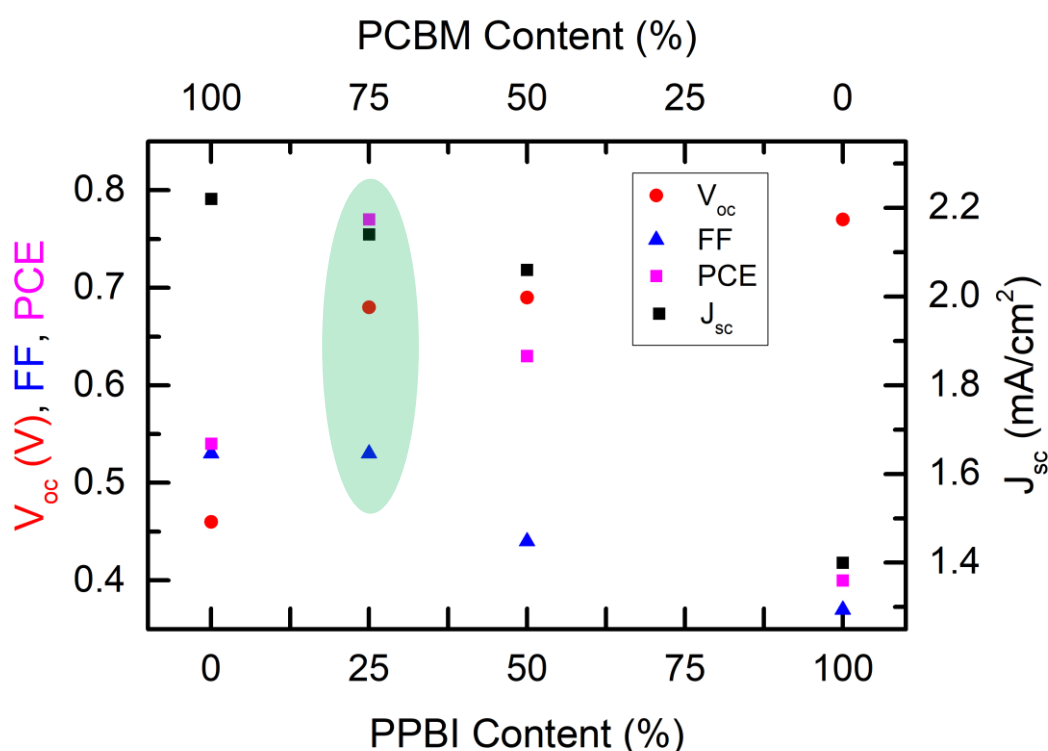


**Figure 3:**  $V_{oc}$ ,  $J_{sc}$ , FF, and PCE as a function of PPBI-alkyl content (PCBM content) at 0% (100%), 75% (25%), 50% (50%) and 100% (0%); 100% PPBI-alkyl content indicates a PCE11/PPBI-alkyl bilayer device and 0% PPBI-alkyl content indicates a PCE11/PCBM bilayer device. The light green ellipse shows the parameters of the most efficient device at PCBM:PPBI-alkyl ratio of 0.75:0.25 (25% PPBI-alkyl content)

To try to understand the morphological origin of the solar cell performance enhancement for the above devices from a structural point of view, I tracked the film formation of the different blend combinations. Examining the spectral signatures during the film formation process in a blend allows for tracking how the aggregation properties of a specific component of the blend (PPBI-alkyl) is affected by the addition of an extra material (PCBM). This allows correlating how certain aggregation properties translate into different film structural properties and hence different solar cell performance. I start first by analyzing the spectral features related to the formation of PCBM

and PPBI-alkyl neat films. When moving to the PCBM:PPBI-alkyl mixtures, I focus on the induced changes in the film formation kinetics and spectral features of PPBI-alkyl as a function of PCBM addition.

### 6.3 Film formation of the neat materials

The description of the film formation and aggregation dynamics when spin coating a material or blend from solution can be divided into three different stages during the process. These stages are shown schematically in figure 4 and I use them as a guideline to describe the film formation and aggregation dynamics for all the spin coated films in this chapter. The first stage encompasses the material's behavior in the solution state after its deposition on the substrate. The second stage encompasses the formation of a significant aggregation phase of the material as it reaches a critical concentration after solvent evaporation and the film starts to form. The third stage marks the solidification phase and the formation of the final film.

As already discussed in the context of figure 2 in chapter 5, the PPBI-alkyl polymer already shows a degree of electronic interaction between the PDI chromophores in solution as evidenced by the suppression of the 0-0 peak intensity in absorption compared to that of the 0-1 peak. This is also accompanied by excimer formation which appears as a broad red shifted peak in the PL spectra. Having this in mind, I can then describe the film formation when spin coating the neat PPBI-alkyl film from CF solutions with respect the PPBI-alkyl aggregation.

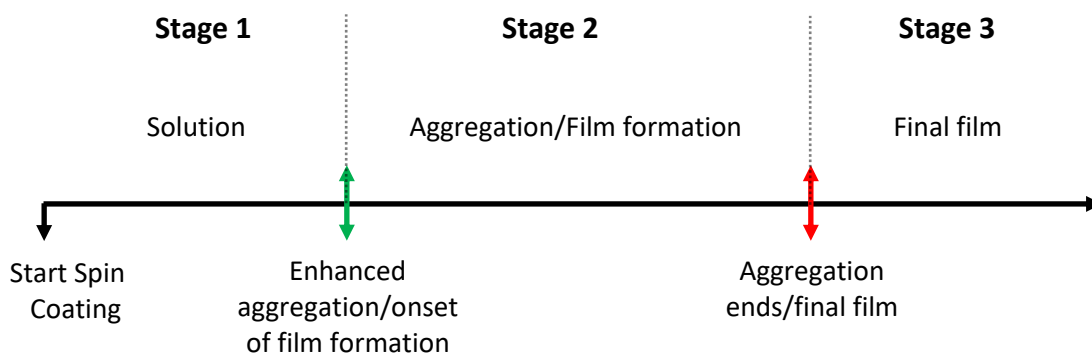
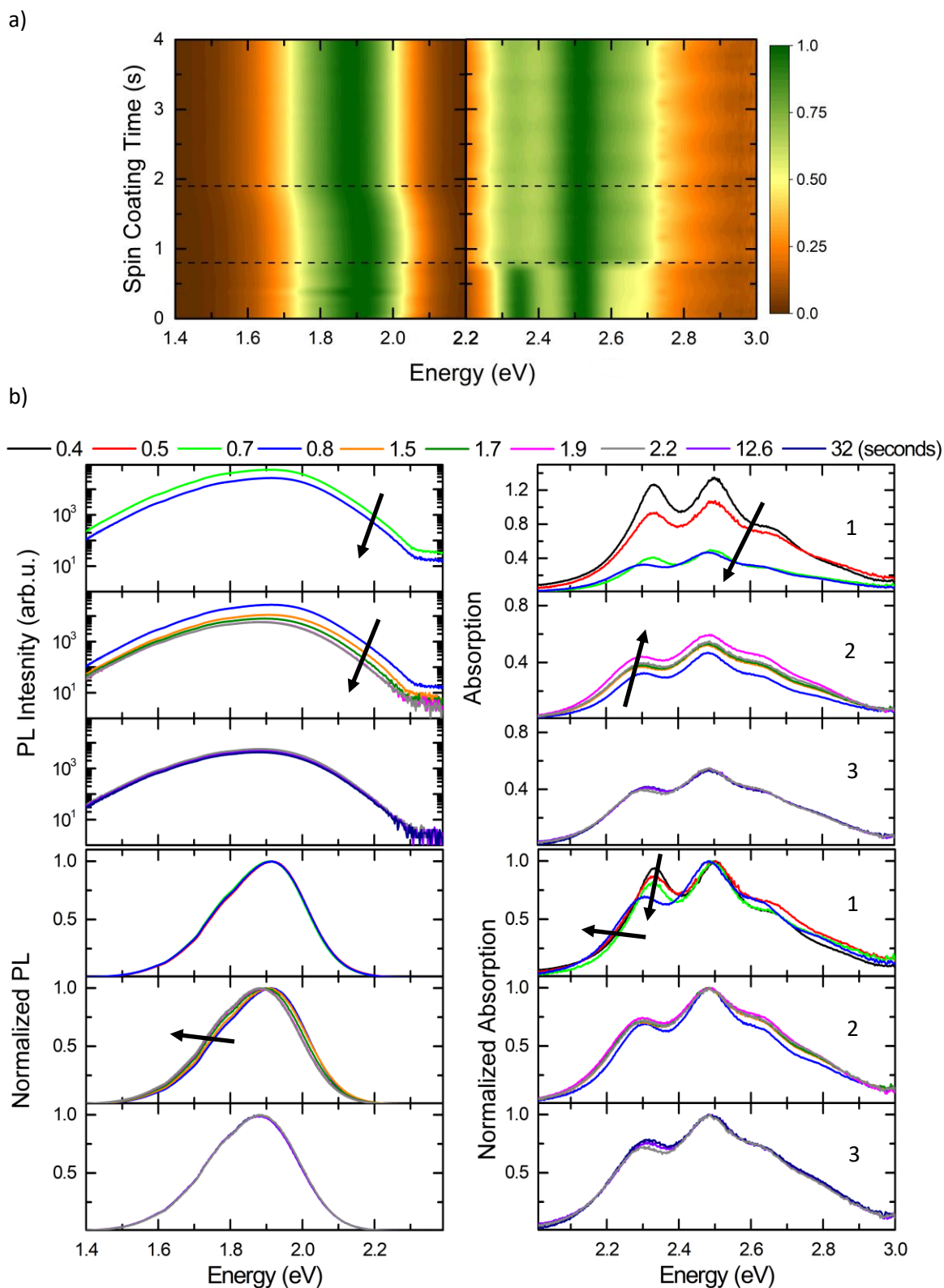


**Figure 4: Schematic figure showing the steps during the spin coating of the different films from solutions and represents a guideline to describe the film formation and aggregation dynamics in this chapter**

Figure 5 shows the normalized absorption and photoluminescence 2D intensity maps along with a selected spectra from the measured insitu photoluminescence and absorption spectra during spin coating of a PPBI-alkyl film from a CF solutions.



Following the three stages approach introduced in figure 4, the film formation of the neat PPBI-alkyl film proceeds as follow

- 1- During the first few frames after starting spin coating (0 s to 0.7 s), I observe a significant decrease in absorption intensity that I attribute to the material throw-off from the substrate due to the centrifugal forces exerted by the spin-coating process. Looking at the equivalent normalized spectra, one also observes the reduction of the 0-0/0-1 peak ratio from 0.94 at the start of spin coating to 0.82 at 0.7 s. This reduction indicates a continually increasing molecular interaction between the PDI moieties as the solvent evaporates. In the corresponding PL spectra, we observe a reduction of the emission intensity that might be attributed to the formation of non-emissive species as the PDI chromophores approach each other [3]. It is worth noting that I observe no monomer emission even in the solution stage and only excimer emission is present.
  
- 2- For both the PL and the absorption spectra we observe no spectral shifts until  $\approx 0.7$  s. Starting at  $\approx 0.8$  s both spectra show a slight red shift that marks the onset of film formation and enhanced PPBI-alkyl aggregation. Hence, I indicate  $t \approx 0.8$  s as the start of stage 2 where sufficient solvent has already evaporated and the polymer concentration has reached a critical limit where the polymer chains start to come closer to each other compared to the solution phase. For absorption, the spectral position of the 0-0 peak slightly red shifts between 0.7 s and 0.8 s and then stays almost constant. Concomitantly, the 0-0/0-1 peak ratio shows an abrupt decrease between 0.7 s and 0.8 s (0.82 to 0.7) after which it also stays almost constant. An increase in the absorption intensity is also observed after 0.8 s which I attribute to the reorientation of the PDI chromophores relative to the substrate surface. In contrast to absorption, the spectral shift of the excimer emission peak in PL continues gradually until  $\approx 1.9$  s. This is apparent from the normalized PL data where the excimer peak shift from 1.91 eV at 0.8 s to 1.88 eV at 1.9 s ( $\approx 30$  meV), after which the emission maximum stays at 1.88 eV. Within the same period (0.8 s to 1.9 s) the PL intensity gradually decreases. It is worth noting that the onset of the red shift happening in absorption is simultaneously accompanied by the onset of the excimer red shift and a 70% reduction of the PL intensity. These three signatures take place within the first two frames at the start of stage 2 (0.8 s and 0.9 s).
  
- 3- The time after which I observe no further changes in the spectra marks the end of the film formation process which is  $\approx 1.9$  s. Starting around 1.9 s, the PL intensity stays almost constant along with the PL maximum peak position. The corresponding absorption spectra

show no shift of the 0-0 peak to higher energy and the 0-0/0-1 peak ratio stays almost constant.

From the above, I can conclude that the changes in absorption and PL during film formation of the neat PPB-alkyl film go hand in hand. Although there are already electronic interactions between the PDI chromophores in the polymer solution, these interactions are significantly enhanced once the film forms which is apparent from the changes in the spectral features during spin coating. The onset of enhanced aggregation and film formation happens in less than 1 s upon starting the spin coating process and the final film is formed in less than 2 s.

Moving to PCBM, figure 6 shows the normalized absorption and photoluminescence 2D intensity maps along with as measured and normalized spectra at different times during spin coating of PCBM films from CF solution. It is worth recalling that in general, fullerene absorption in solution shows two distinct absorption peaks at  $\approx 2.6$  eV and 2.25 eV which correspond to the monomer absorption [4]. In emission, fullerene derivatives typically show two emission peak at  $\approx 1.75$  eV and 1.6 eV which correspond to the monomer emission [4, 5]. Looking at the measured PCBM spectra shown in figure 6, one can clearly see similar spectral signatures to those reported in literature.

Similar to PPBI-alkyl, the PL and absorption intensities are reduced during the first frames of spin coating (1 frame  $\approx 0.1$  s as already discussed in chapter 2), which is attributed to the removal of solution from the substrate. From the normalized absorption spectra, we observe a blue shift of the main peak from 2.7 to 2.76 between 0 and 0.5 s. Following this a newly formed peak around 2.4 eV starts to rise after 2 s accompanied by a rise in the absorption intensity at 1.8 eV. Moving further in time, while the overall absorption intensity after 0.5 s slightly changes, we observe a rise of the absorption intensity within the lower energy range (below 2.4 eV) relative to the absorption of the peak at 2.76 eV. The final absorption spectra of the dried film eventually show two main peaks having near intensities at 2.4 eV and 2.75 eV. In PL, at the beginning, emission is dominated by a peak at 1.78 eV accompanied by a shoulder around 1.6 eV. Equivalent to absorption, after 2 s, the peak at 1.78 eV red shifts by 30 meV to 1.75 eV and the shoulder around 1.6 eV forms a new peak at 1.58. These features in both PL and absorption indicate the solid state interaction and aggregation within the formed PCBM phases [6]. This indicates that the onset of PCBM film formation happened around 2 s from the start of spin coating.

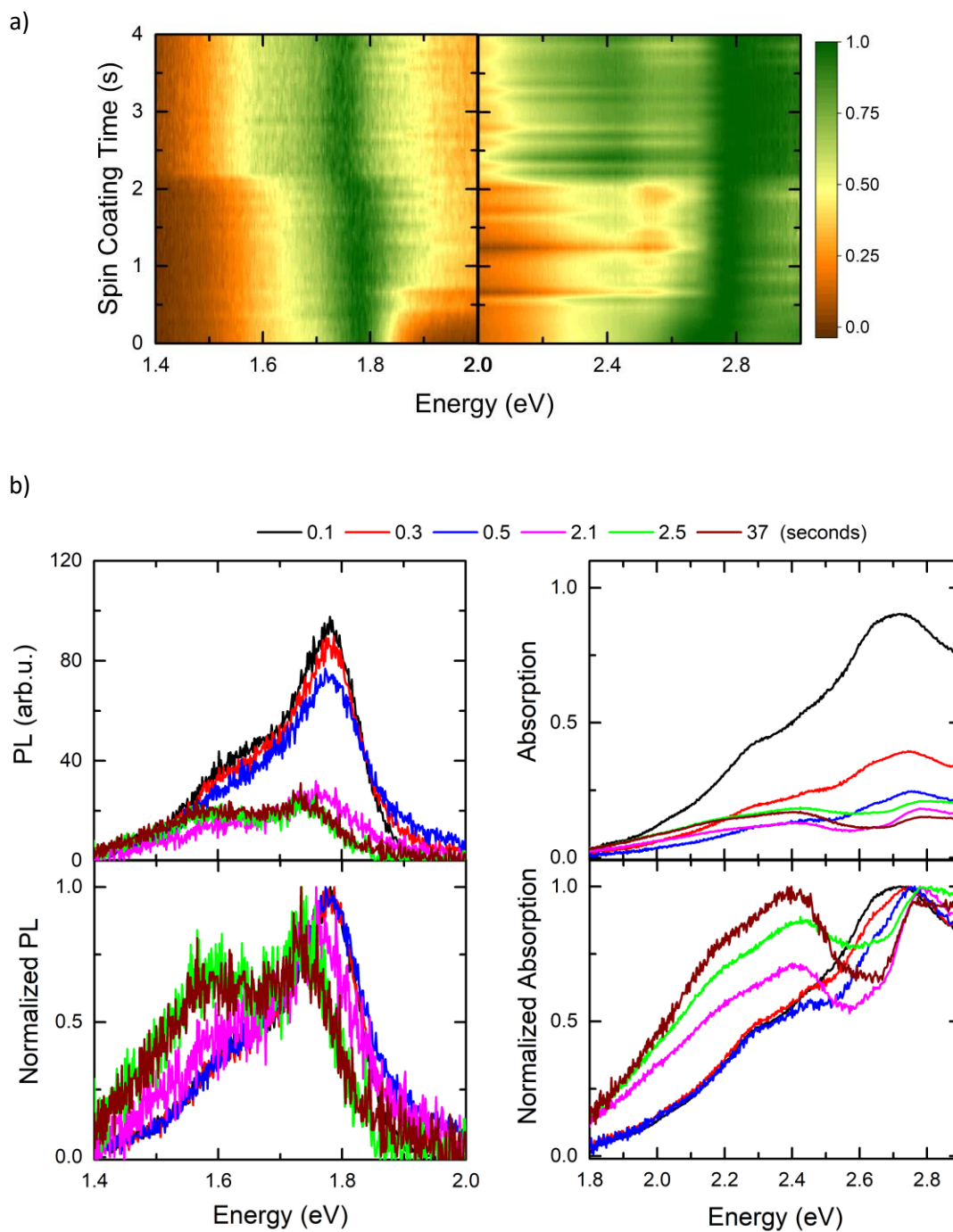


**Figure 6:** a) Normalized PL and absorption 2D intensity maps during the first 4 s after the start of spin coating of the neat PCBM film from a CF solution at 10 g/l. The dashed black lines indicate the onset and ending of the film formation highlighting the 3 stages discussed in figure 4. b) Photoluminescence (left) and absorption (right) spectra with as measured and normalized intensities during spin coating. The top 2 panels show the as measured data while the bottom 2 panels show the corresponding normalized data. PL was corrected for the absorption intensity at the excitation wavelength of 520nm.

## 6.4 Film formation of PCBM:PPBI-alkyl blends

By comparing the film formation dynamics and spectral features when spin coating mixtures of PCBM:PPBI-alkyl at different mixing ratios, I investigate how the addition of PCBM to the PPBI-alkyl affects the aggregation behavior of PPBI-alkyl. With this knowledge, I then try to relate any observed changes in the PPBI-alkyl aggregation behavior to structural changes of the acceptor layer and in turn to the variation in performance of the bilayer solar cells based on the same mixtures shown in figure 2.

Figure 7 shows the normalized photoluminescence and absorption 2D intensity maps during the first 4 s of spin coating of the mixed acceptor film from a solution of PCBM:PPBI-alkyl in CF with different weight ratios. The mixing ratios where PCBM:PPBI-alkyl 0.25:0.75, 0.5:0.5 and 0.75:0.25, where the first number always refers to the PCBM content in the solution used to make the films. Similar to the neat PPBI-alkyl, the film formation process of the mixed acceptors can be divided into three stages. The characteristic transition times between these stages are marked by the dashed black lines on the 2D normalized intensity maps while the numbers 1-3 indicate the distinct stages defined in figure 4.

Similar to the neat PPBI-alkyl, in the absorption spectra of the mixed PCBM:PPBI-alkyl, the onset of film formation and enhanced PPBI-alkyl aggregation upon reaching a critical polymer concentration is marked by the reduction of the 0-0 absorption peak intensity relative to the 0-1 absorption peak. In PL, this onset is accompanied by the fast reduction of the PPBI-alkyl emission and the appearance of a new emission peak around 1.77 eV that corresponds to the PCBM emission as will be discussed below in figures 9, 10, and 11. For the 0.75/0.25, the rise of the PCBM emission peak around 1.77 eV is not observed in the corresponding 2D map because it happens on a longer time scale as will be discussed below. It is readily observed from the position of the dashed line between phases 1 and 2 that the time of onset of film formation and enhanced PPBI-alkyl aggregation ( $t_{\text{onset}}$ ) depends on the PCBM:PPBI-alkyl mixing ratio. The onset of aggregation is shifted to later times as the PCBM content increases.

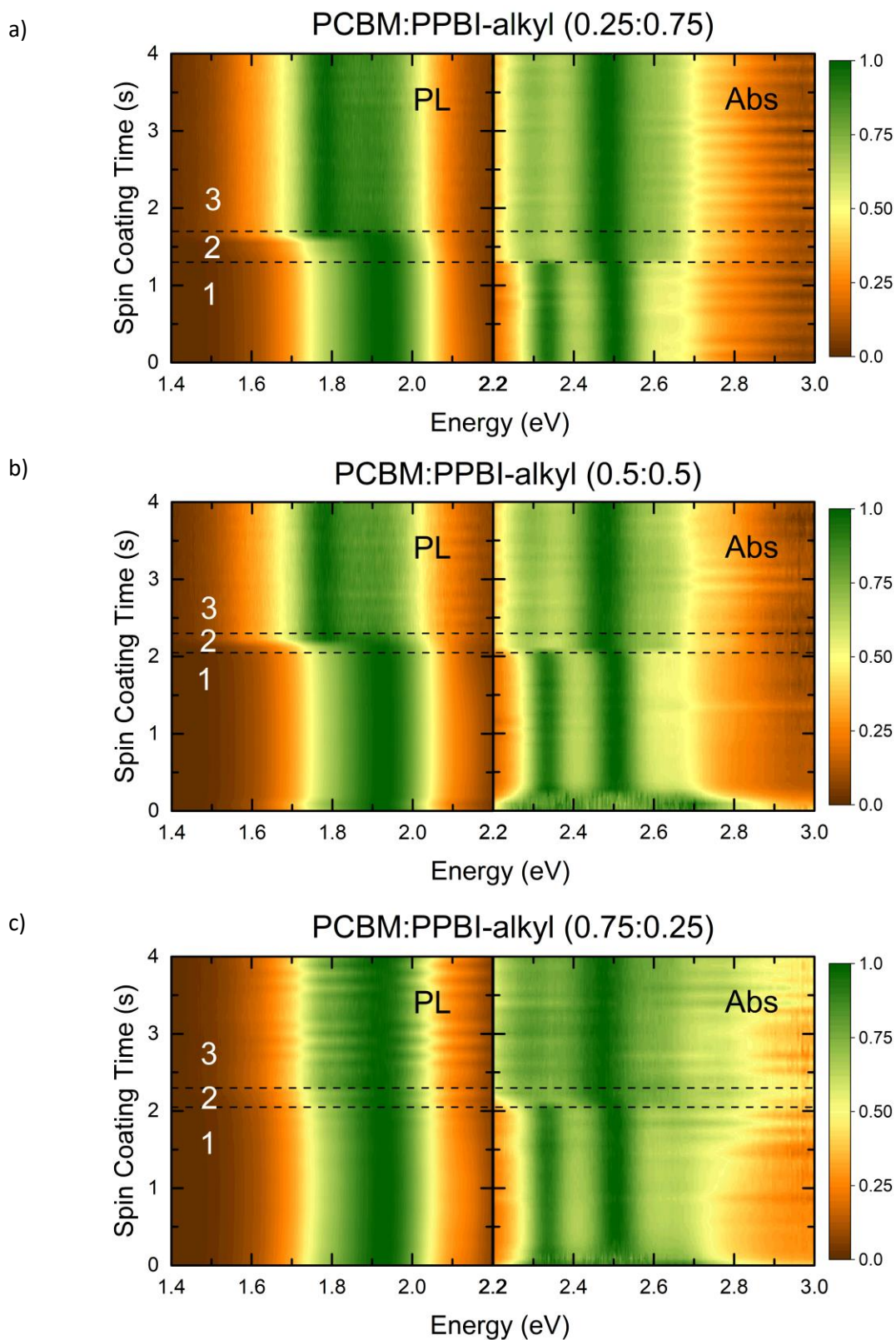


**Figure 7: Normalized Photoluminescence and absorption 2D intensity maps during the first 4 s after the start of spin coating of the PCBM/PPBI-alkyl mixture from CF solution at weight ratios of a) 0.25:0.75, b) 0.5:0.5 and c) 0.75:0.25. The dashed black lines highlight the onset and ending of the film formation stages dividing the film formation process into the 3 stages discussed in figure 3. The numbers 1, 2 and 3 refer to these stages.**

Figure 8.a) shows the evolution of the 0-0/0-1 peak ratio extracted from the absorption measurements during the first 2.5 s of spin coating for the neat PPBI-alkyl and the mixed PCBM/PPBI-alkyl at the different ratios. Figure 8.b) shows the estimated  $t_{\text{onset}}$  values which should correspond to the inflection point of the sigmoidal curves describing the evolution of 0-0/0-1 peak ratios as a function of spin coating time. Compared to the neat PPBI-alkyl film ( $t_{\text{onset}} \approx 0.8$  s), the PCBM/PPBI-alkyl (0.25/0.75) film shows a  $t_{\text{onset}} \approx 1.4$  s, and the PCBM/PPBI-alkyl films with ratios (0.5/0.5) and (0.75/0.25) shows a  $t_{\text{onset}} \approx 2$ -2.1 s.

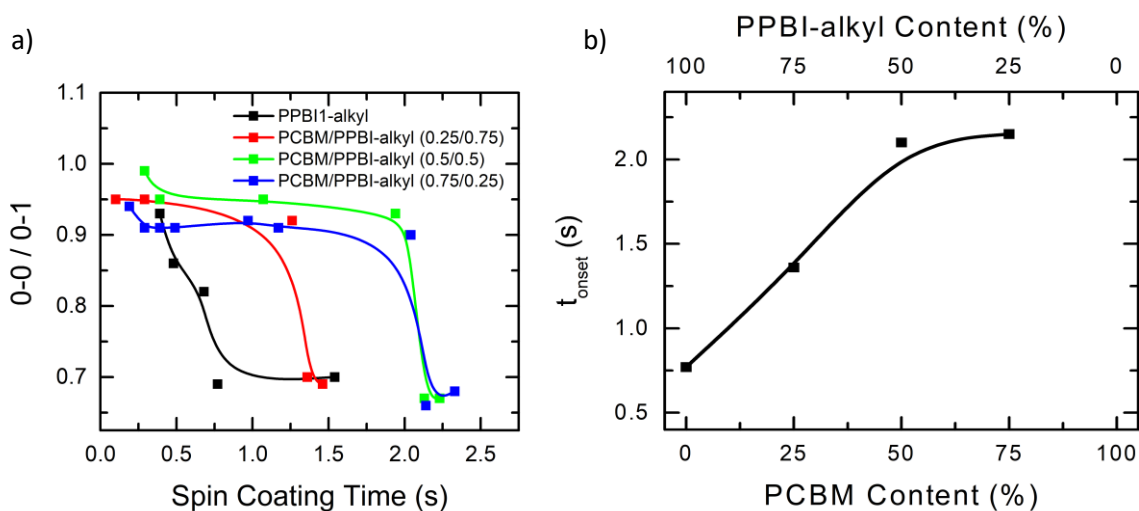


**Figure 8:** a) Extracted 0-0/0-1 peak ratios during the first 2.5 s after the start of spin coating of neat PPBI-alkyl (black) and the PCBM:PPBI-alkyl mixtures from CF solutions at PCBM:PPBI-alkyl weight ratios of 0.25:0.75 (red), 0.5:0.5 (blue), and 0.75:0.25 (green). The solid lines are a guide to show the sigmoidal behavior of the change in the 0-0/0-1 peak ratios during spin coating. b) The onset of film formation and enhanced PPBI-alkyl aggregation as a function of PCBM. These values were extracted from the 2D maps shown in figure 4 for the neat PPBI-alkyl and figure 6 for the mixed PCBM/PPBI-alkyl and correspond to the location of the black dashed lines shown in these figures.

To get more details on the evolution of the spectra during film formation, figures 9, 10 and 11 show selected spectra at different times during spin coating. These spectra cover the different film formation phases over a longer time period (over 4 s). Starting with the lowest PCBM content film, as shown in figure 9, during the first stage at the start of spin coating as the material is thrown away, we observe the reduction of the PPBI-alkyl absorption and PL intensities until  $\approx 1.3$  s. Afterwards, the second stage starts at  $t \approx 1.4$  s where the onset of enhanced PPBI-alkyl aggregation is apparent from the red shift of the 0-0 absorption peak and the reduction of the 0-0/0-1 peak ratio. In contrast to the neat PPBI-alkyl film, where the excimer peak shifts towards lower energies during this stage (shown in figure 5), no spectral shifts are present in the PL spectra of the PCBM:PPBI-alkyl (0.25:0.75) mixture. However, a slight shoulder starts to appear between 1.7 eV and 1.8 eV which corresponds to the PCBM emission (shown in figure 6). During this stage, the

overall PL intensity is further reduced. These changes only happen on a very short time scale less than 0.5 s (between 1.3 s and 1.7 s).

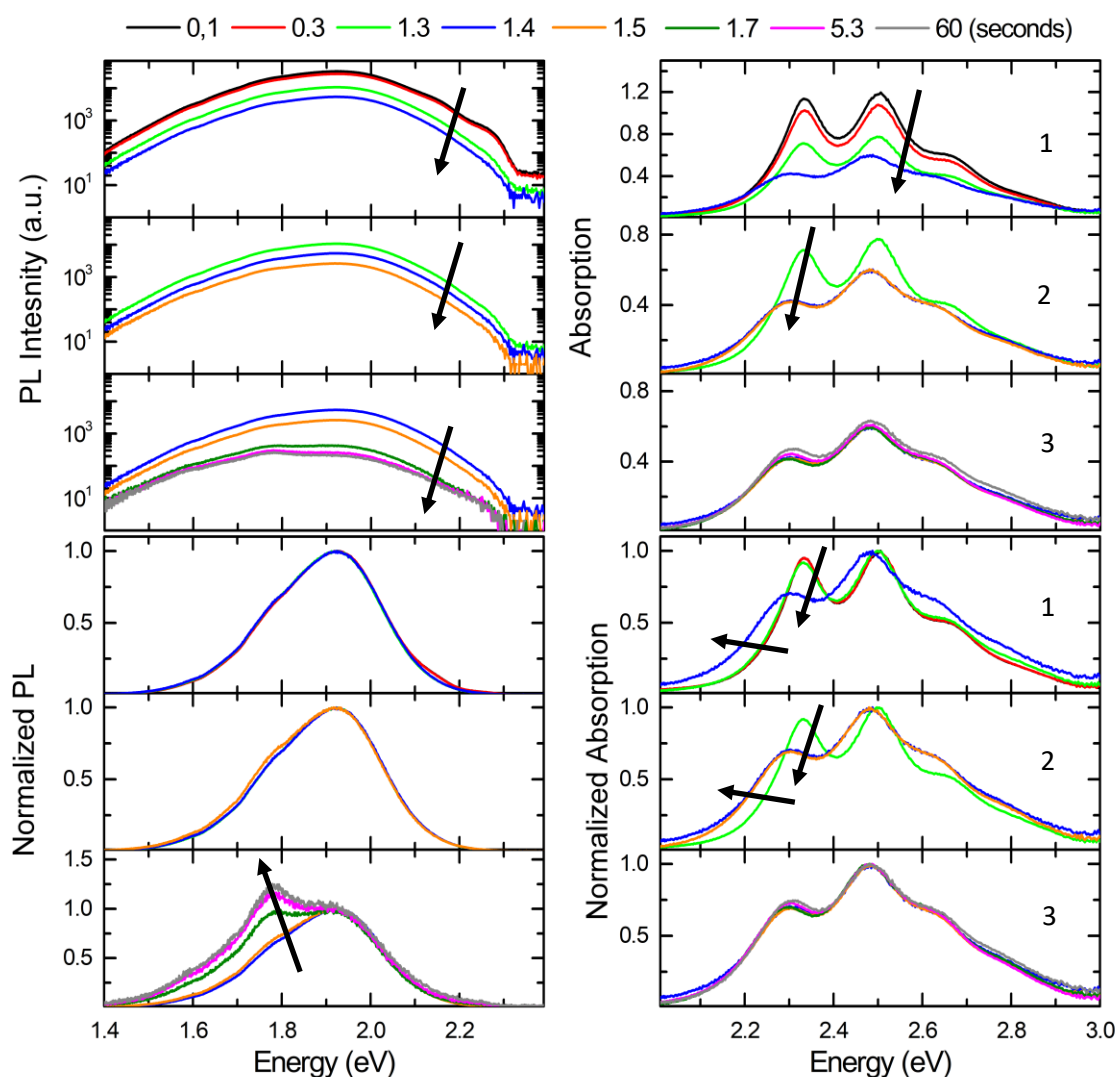


**Figure 9: Photoluminescence (left) and absorption (right) spectra during spin coating of PCBM:PPBI-alkyl (0.25:0.75) films from CF solutions at 10g/l at different times during spin coating. The top three panels show the as measured data while the bottom 3 panels show the normalized data. Photoluminescence was corrected for the absorption intensity at the excitation wavelength of 520nm.**

The third stage starts at  $\approx 1.7$  s where no significant changes are observed in the absorption spectra in terms of either the overall intensity or the 0-0/0-1 peak ratio. In contrast, during this stage the PL intensity is reduced slightly with time until  $\approx 5$  s. During this time (1.7 s and 5 s), although the PL intensity is slightly reduced, the spectral weights redistribute between PPBI-alkyl and PCBM leading to significant changes in PL as observed from the normalized PL spectra. The reduction of the PPBI-alkyl emission -as it further aggregates- leads to the enhancement of the PCBM shoulder between

1.7 eV and 1.8 eV. At the beginning of this stage ( $\approx 1.7$  s), this PCBM shoulder becomes an apparent peak and has a similar intensity to the PPBI-alkyl emission as shown in the normalized PL spectra. This relative change between both of the PPBI-alkyl and PCBM peaks continue with time (the PPBI-alkyl emission intensity decreases relative to the PCBM emission intensity), giving the appearance of a rising PCBM peak. After 5 s the PL intensity becomes constant and the PCBM peak at 1.75 eV dominates the spectra.

The insitu spectra of the second film having equal weight ratios of PCBM and PPBI-alkyl (0.5:0.5), is shown in figure 10.

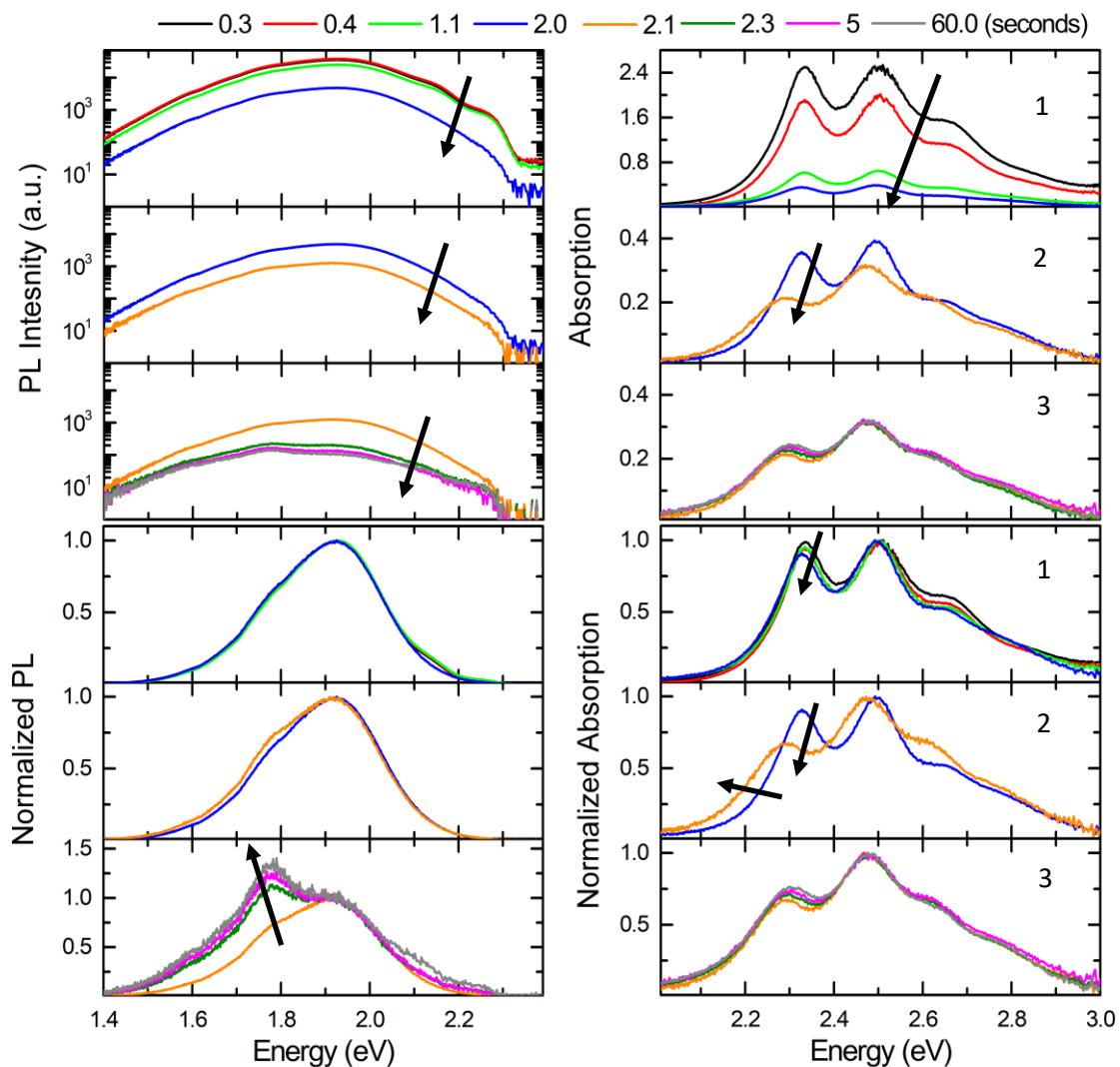


**Figure 10: Photoluminescence (left) and absorption (right) spectra during spin coating of PCBM:PPBI-alkyl (0.5:0.5) films from CF solutions at 10g/l at different times during spin coating. The top three panels show the as measured data while the bottom 3 panels show the normalized data. Photoluminescence was corrected for the absorption intensity at the excitation wavelength of 520nm.**

At this mixing ratio, the first stage lasts longer compared to the previously described film that had the lowest PCBM content (25%). PL and absorption intensity continuously decrease until  $\approx 2$  s. Then, similar to the previous film, the onset of enhanced PPBI-alkyl aggregation is apparent from the red shift of the 0-0 absorption peak and the reduction of the 0-0/0-1 peak ratio starting at 2 s. Compared to the film with the lowest PCBM content this phase lasts over a shorter time period ( $\approx 0.2$  s). Apart from this the film formation process for the PCBM:PPBI-alkyl (0.5:0.5) follows similar signatures as observed for the previous film with the lowest PCBM content. No shift of the PPBI-alkyl excimer peak is observed during the enhanced aggregation stage. The PCBM emission shoulder starts to appear at the end of the second stage (2.1 s) and dominates the spectra during the third stage (after 2.3 s) due to the reduction of the PPBI-alkyl emission intensity. Finally, this PCBM emission peak reaches its maximum intensity at  $\approx 5$  s. The time at which the PCBM emission reaches its maximum intensity coincides with the time at which the overall PL of the film becomes constant. This is almost the same for both the PCBM:PPBI-alkyl 0.25:0.75 and 0.5:0.5 films.

Finally, in the film with the highest PCBM content (75%), as shown in figure 11, the enhanced aggregation stage starts at a comparable time ( $t_{\text{onset}} \approx 2.1$  s) to the previous film with the equal PCBM and PPBI-alkyl content ( $t_{\text{onset}} \approx 2$  s). However, in contrast to the previous two films with lower PCBM content, at the onset of enhanced PPBI-alkyl aggregation the lower energy absorption edge for the 0.75:0.25 film shows a slightly different behavior. From the normalized absorption spectra starting  $\approx 2$  s we observe a rise of the absorption intensity and a change in the slope of absorption edge line shape around 2.2 eV. These changes can be related to the formation of more PCBM phases due to the high PCBM content in this mixture compared to the previous two. As shown previously in figure 6, during spin coating of PCBM, we observe a rise in the PCBM absorption between 2 eV and 2.2 eV which is similar to the changes observed here for the PCBM:PPBI-alkyl (0.75:0.25). Furthermore, in the film with the highest PCBM content we observe a very slight shift in the PPBI-alkyl excimer emission during the enhanced aggregation stage (stage 2). I estimated this shift to be less than 10 meV from the peak maxima. Although this is a very low value it still shows a difference to the previous two films with lower PCBM content where such shift was not observed.

The most significant difference between the 0.75:0.25 film and the films with lower PCBM content is the evolution of the PCBM emission peak relative to the PPBI-alkyl emission during stage 3. For the 0.75:0.25 film, as a result of the PPBI-alkyl emission intensity reduction over an extended period of time, the PCBM peak at  $\approx 1.77$  eV relatively rise for a very long-time during stage 3 and reaches its maximum value between 30 s and 40 s after the start of spin coating. This is accompanied by the slow reduction of the overall film PL. This means that these two processes (PCBM emission peak relative rise and overall PL reduction) continue for an extended time after the solid film has been

already formed. During the same time period no changes are observed in the corresponding absorption spectra. This is in contrast to the previous two films where this process is much faster ( $\approx 5$  s).

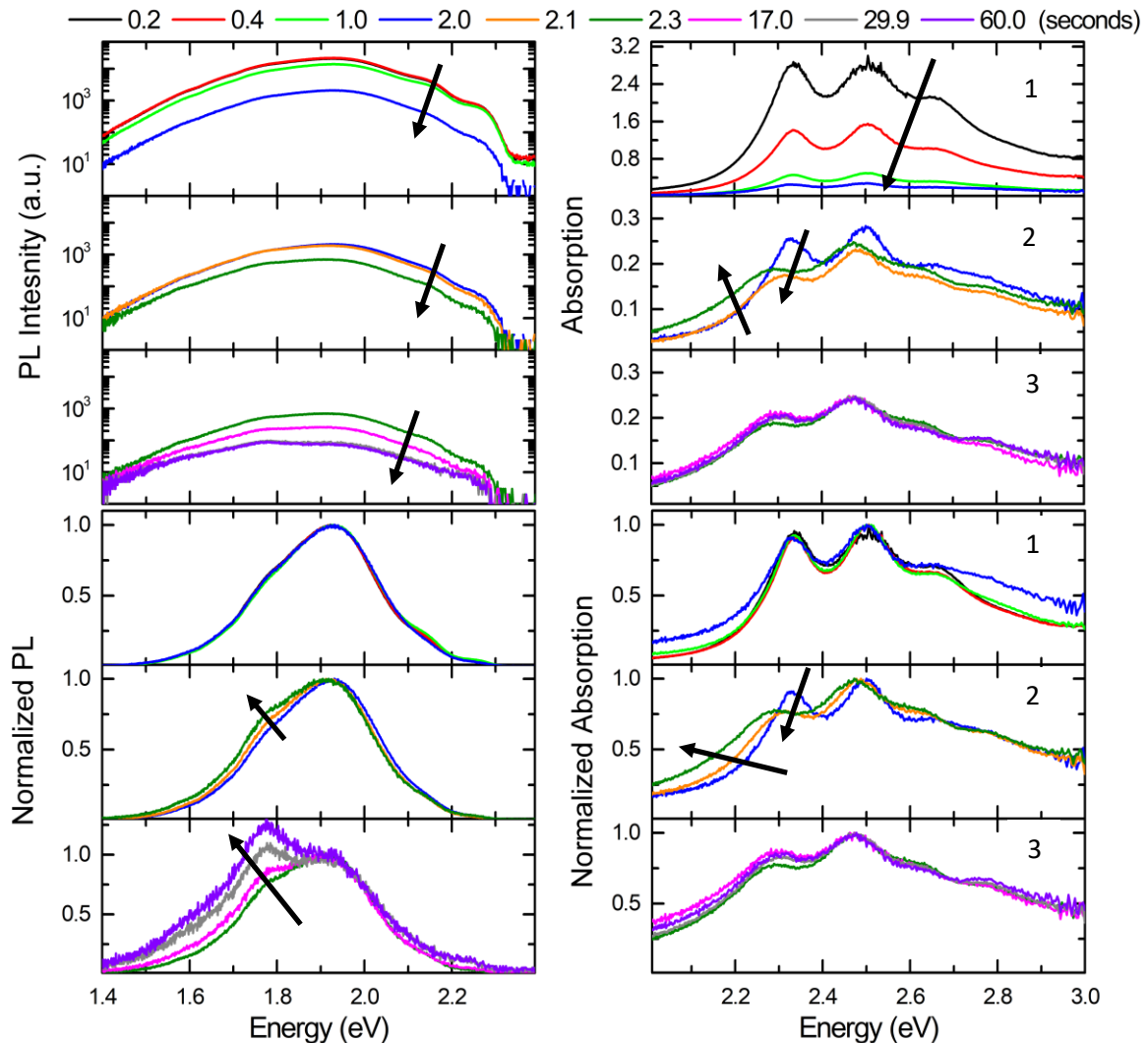


**Figure 11: Photoluminescence (left) and absorption (right) spectra during spin coating of PCBM:PPBI-alkyl (0.75:0.25) films from CF solutions at 10g/l at different times during spin coating. The top three panels show the as measured data while the bottom 3 panels show the normalized data. Photoluminescence was corrected for the absorption intensity at the excitation wavelength of 520nm.**

To get more insight about this observation which can be related to the intermixing between the PCBM and the PPBI-alkyl phases at the different ratios, I extracted the integrated PL from the measurements shown in figures 9, 10 and 11. Figure 12 shows the integrated PL quenching extracted during film formation of PCBM/PPBI-alkyl mixtures at different ratios with that of neat PPBI-alkyl as a reference. For the blends containing 25% and 50% PCBM, an abrupt decrease in the

PL intensity happens at the same time as the aggregation onset as evidenced from the spectral signatures in the absorption spectra shown in figure 9 and 10.

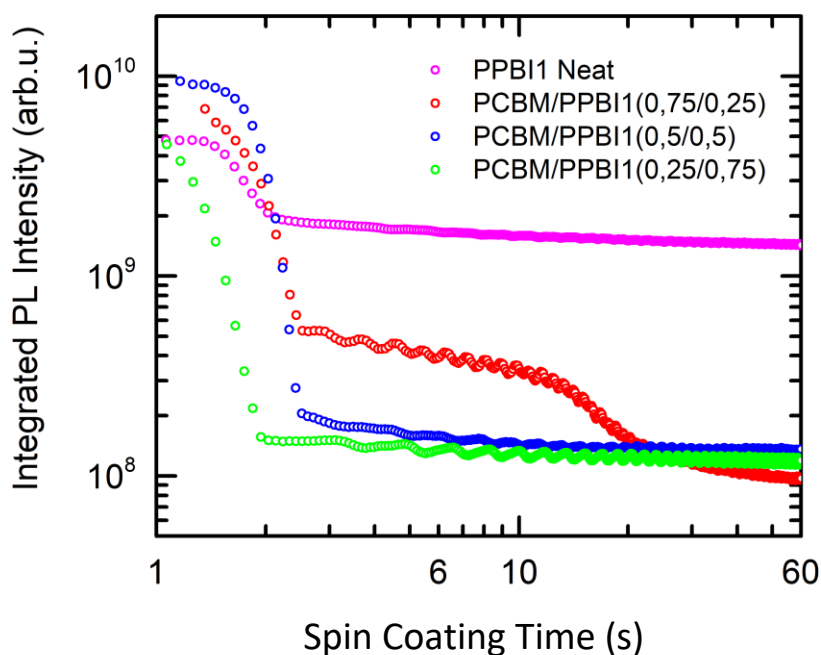


**Figure 12: Integrated PL intensity of the PCBM: PPBI-alkyl mixtures during spin coating at different ratios**

At the time where the films are finally formed (the start of stage 3) no significant decrease in the overall PL intensity is further observed. On the contrary, for 75% PCBM the PL quenching proceeds over an extended time where we observe a gradual decrease until the final PL intensity level is reached after the initial drop at the aggregation onset. The gradual decrease of PL over an extended time after the film is formed would indicate PCBM diffusion after formation of PPBI-alkyl domains which then leads to a more efficient PL quenching despite the lower PPBI-alkyl content. It is important to note that ideally microscopy measurements such as TEM measurements could have been used to further confirm these results. Unfortunately, this was not possible due to the lack of extra PPBI-alkyl material.

To then gain more insight about the correlation between the insitu spectra signatures I observed at the different mixing ratios and the solar cell characteristics related to the charge generation, I and *Mihirsinh Chauhan* further analyzed the J-V-curves of the corresponding solar cell devices. Figure 13 shows the fill factor as a function of illumination intensity. The dissociation probability as a function of internal field for the devices made using the different PCBM and PPBI-alkyl mixing ratios is also shown. It has been shown that the light intensity dependent fill factor can be used to distinguish the type of charge recombination mechanisms [7]. The decrease of the fill factor below

the maximum theoretical obtainable value at low light intensities can be related to geminate recombination [7] (blue area in figure 13.a). A decrease of the fill factor at higher light intensities in contrast can be attributed to non-geminate recombination [7] (yellow area in figure 13.a).

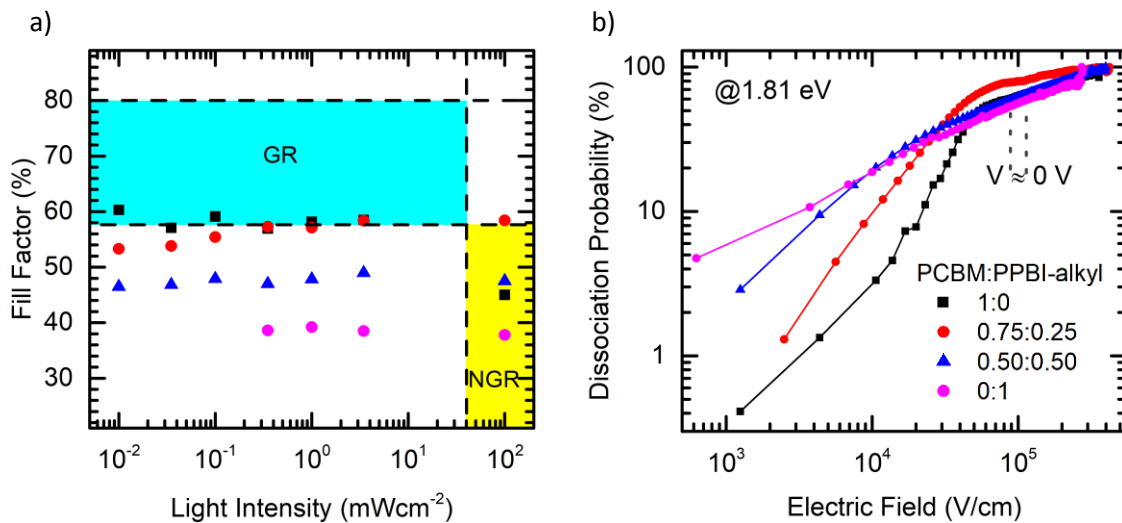


**Figure 13: a) Fill factor as a function of illumination intensity and b) the dissociation probability as a function of internal field for the devices made using the different PCBM and PPBI-alkyl mixing ratios.**

Taking this into account, it can be clearly seen that the addition of 25% PPBI-alkyl reduces the non-geminate recombination that is present when the bilayer solar cells are made from PCBM only. The addition of 25% PPBI-alkyl almost entirely suppresses the non-geminate recombination so that we observe no decrease in the fill factor at higher light intensities (AM1.5). This implies that upon charge dissociation at the interface with PCE11, the charges efficiently move into the donor and acceptor layers for extraction. Regarding the charge dissociation efficiency, it has been shown that it can be related to the ratio of  $J_{sc}$  and the saturation current [8]. This shows that in addition to the suppressed non-geminate recombination, the PCBM:PPBI-alkyl (0.75:0.25) provides the best charge dissociation efficiency of 80% compared to 66% for the PCBM only device. Overall, in the case of the PCBM:PPBI-alkyl (0.75:0.25) the improved device performance stems from an improved charge generation due to enhanced dissociation and reduced non-geminate recombination. These charge generation characteristics is related to the acceptor layer morphology and is in alignment with the blend insitu data. A better charge dissociation in the case of PCBM:PPBI-alkyl (0.75:0.25) would correspond to better diffusion of PCBM within the PPBI-alkyl domains and the formation of sufficient interfacial area between both components as mentioned earlier. In addition, the presence of PCBM provides a path of charge dissociation and transfer which corresponds to a reduced non-geminate recombination.

## 6.5 Discussion

Implementing PPBI-alkyl as an acceptor in organic solar cells combined with PCE11 as the donor showed comparable performance in both bilayer and BHJ configurations. This is opposite to PCBM which shows a massive improvement when implemented in a BHJ solar cell compared to bilayer solar cell (Figure 1). This different behavior hints towards an intrinsic problem related to charge generation when PDIs are used as the electron acceptor even when implemented in a side chain configuration. A possible reason for this might be the formation of large PPBI domains due to excessive aggregation and poor mixing with PCE11. Figure 14 shows the absorption measurements at the beginning of spin coating and at the end of spin coating after the film formation for the same PCE11:PPBI-alkyl blend used to fabricate the solar cells shown in figure 1.b.

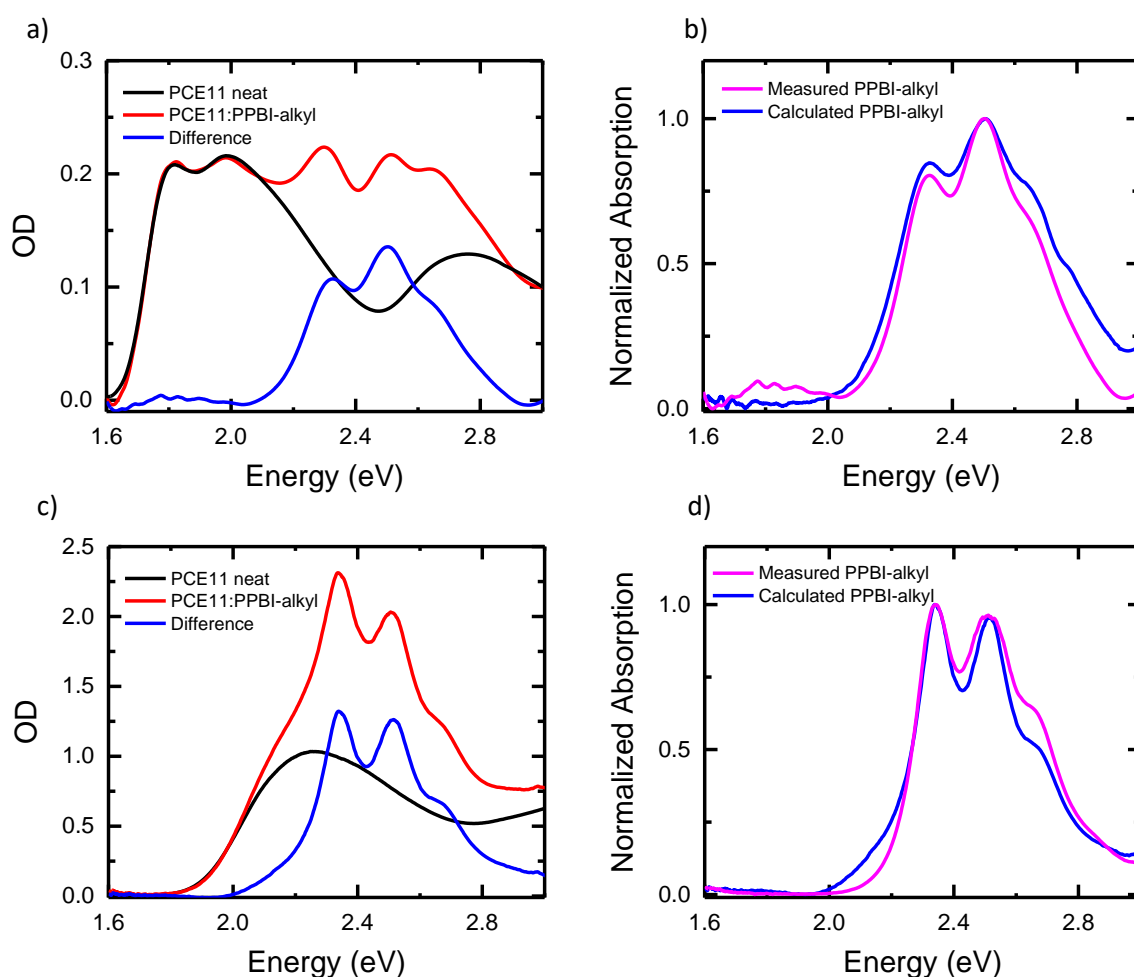


**Figure 14:** a) Absorption spectra at the beginning of spin coating for PCE11:PPBI-alkyl blend (1:1) (red line), PCE11 amorphous (black line) and the difference between them (blue line) that represents the calculated PPBI-alkyl spectrum. b) Normalized absorption spectra of PPBI-alkyl (black line) and the calculated PPBI-alkyl from a). c) Absorption spectra at the end of spin coating for PCE11:PPBI-alkyl blend (1:1) (black line), PCE11 (black line) and the difference between them (blue line) that represents the calculated PPBI-alkyl spectrum. b) Normalized absorption spectra of PPBI-alkyl (black line) and the calculated PPBI-alkyl from c).

Figures 14.a shows the absorption spectra at the beginning of spin coating for the PCE11:PPBI-alkyl blend with the PCE11 neat spectrum subtracted from it to extract a calculated PPBI-alkyl spectrum. This calculated spectrum is then compared to the measured PPBI-alkyl spectrum also at the beginning of spin coating as shown in Figures 14.b. It is apparent from this comparison that the difference between both the measured neat PPBI-alkyl spectrum and the extracted PPBI-alkyl spectrum from the blend with PCE11 is insignificant with an equal 0-0/0-1 peak ratio. The same is done for the spectra at the end of spin coating (i.e. the film spectra) which shows a similar result. This indicates that the PPBI-alkyl aggregation and film formation proceed in a similar manner regardless of blending with PCE11.

It has been already shown based on TEM measurements that the blends of PCE11 and PCBM show better intermixed morphology compared to blends of PCE11 and the PDI based acceptor di-PDI [9]. This was attributed to the similar surface energies of both PCE11 and PCBM [9]. Moreover, GIWAXS measurements showed that PCE11 tends to form larger domains when blended with di-PDI compared to its domain size when blended with PCBM [9]. The above measurement and literature data strengthen my aforementioned hypothesis of the poor mixing between PCE11 and PPBI-alkyl in a blend. It also explains the comparable performance of the PCE11:PPBI-alkyl bilayer and binary blend solar cells of PDIs as blending would not result in significant changes in the interface area between the donor and acceptor domains. However, among the two investigated PDI acceptors, PPBI-alkyl offers a slightly better solar cell performance compared to PPBI-OEG in both the bilayer and BHJ configurations. This might be attributed to the better ordering of the PPBI-alkyl in terms of a more extended backbone compared to the PPBI-OEG which would then facilitate charge transport along the PDI  $\pi$ -stacking direction which has been shown for other PDIs based polymers [10]. This more extended conformation might lead to better charge dissociation at the interface between PCE11 and PPBI-alkyl due to better overlap between their wave functions compared to PPBI-OEG. This is confirmed by the higher  $V_{oc}$  values in case of PPBI-alkyl which was shown to be directly correlated to the wave function overlap between the donor and acceptor materials at the interface [11, 12]. In contrast to the investigated PDIs, PCBM devices show a significant improvement when moving from bilayer to binary BHJ architectures. This has been attributed as previously mentioned to very good mixing between PCE11 and fullerene derivatives in organic blends leading to large interfacial area and better charge generation efficiency [9, 13-15].

Despite the drawbacks of PPBI-alkyl when used as an acceptor in a BHJ solar cell with PCE11, its advantages such as good light absorption and morphological stability can be utilized if used as a third component in a solar cell. In case of a bilayer structure, the addition of PPBI-alkyl and PCBM to form a mixed acceptor layer resulted in an improved solar cell performance (PCE almost as twice

as high as the PPBI-alkyl bilayer) mainly due to the improved  $V_{oc}$ . The increase in  $V_{oc}$  was directly proportional to the PPBI-alkyl content. Similar results were shown in various ternary solar cell blends and the observation was attributed to the formation of an alloy phase between the blend materials [16-18]. According to the alloy model, if a physical alloy is formed in a blend of two or more materials, the resulting  $V_{oc}$  would lie between that of the  $V_{oc}$  of either component in isolation and can then be tuned in this range via changing the composition of the blend [19, 20]. This implies proper mixing between PCBM and PPBI-alkyl and optimum phase separation on the nanoscale which in turn enhances the charge generation efficiency.

The underlying reasons of the improvement of the bilayer solar cell performance can be deduced by examining the spectral signatures of the mixtures. I examine three significant signatures in the PCBM/PPBI-alkyl insitu spectra compared to the neat PPBI-alkyl spectra:

- The behaviour of the PPBI-alkyl absorption peaks prior to the enhanced aggregation onset in the mixtures compared to their behaviour during spin coating of neat PPBI-alkyl.
- The delay of PPBI-alkyl aggregation onset in the mixtures compared to the neat state.
- The reduced rate of the PL intensity reduction as the PCBM content increases.

I examined the first two points by comparing the normalized absorption data of phase 1 during spin coating of the PCBM/PPBI-alkyl mixtures at different ratios (figures 9, 10 and 11) and stage 1 during spin coating of neat PPBI-alkyl (figure 5). One can clearly see that in the case of the mixtures there is no significant gradual reduction of the 0-0/0-1 peak ratio prior to the onset of film formation which is opposite to what happens in the case of the neat PPBI-alkyl. Based on my conclusions in chapter 5, this constant 0-0/0-1 peak ratio prior to the onset of aggregation might indicate no significant intermolecular aggregation occurring between the PDI chromophores located on the different backbones due to the presence of PCBM. Consequently, this means that as the PCBM content increases the extent of this intermolecular interaction decreases which is in alignment with the measured data. The almost constant 0-0/0-1 peak ratio during phase 1 of spin coating is most noticeable in the case of the PCBM/PPBI-alkyl (75/25) blend. This conclusion also explains the delayed onset of aggregation of PPBI-alkyl in the blend case compared to the neat case which is correlated with the PCBM content increase. These two signatures would mean that the excessive PPBI-alkyl aggregation is circumvented by the addition of PCBM, with 75% PCBM addition offering a balanced mixing ratio that provides the best solar cell performance.

The last point is examined through the insitu PL data in figure 12 that shows the most PL quenching in the PCBM:PPBI-alkyl (0.75:0.25) acceptor layer. At this mixing ratio, the PL reduction proceeds over an extended time after the film have been formed implying efficient PCBM diffusion within

the PPBI-alkyl aggregate phases. Electrical characterization of the solar cells further confirms this conclusion as shown in figure 13 where in addition to the suppressed non-geminate recombination better charge dissociation was obtained in the PCBM:PPBI-alkyl (0.75:0.25) acceptor layer.

Finally, the whole film formation process in the PCBM /PPBI-alkyl blends can be summarized based on the above observations. At the start of spin coating the addition of PCBM inhibits the excessive aggregation of PPBI-alkyl and the PPBI-alkyl aggregates start to form only upon sufficient solvent evaporation. Then a mixed phase between PCBM and PPBI-alkyl starts to form due to a continuous diffusion of PCBM through the PPBI-alkyl domains. This film formation process of the mixtures results in a film morphology that corresponds to a better solar cell performance compared to the performance in case of using the neat materials as the acceptor component separately. Based on the above proposed picture, figure 15 shows an illustration of the film forming process of the PCBM:PPBI-alkyl blends at the two different situations.

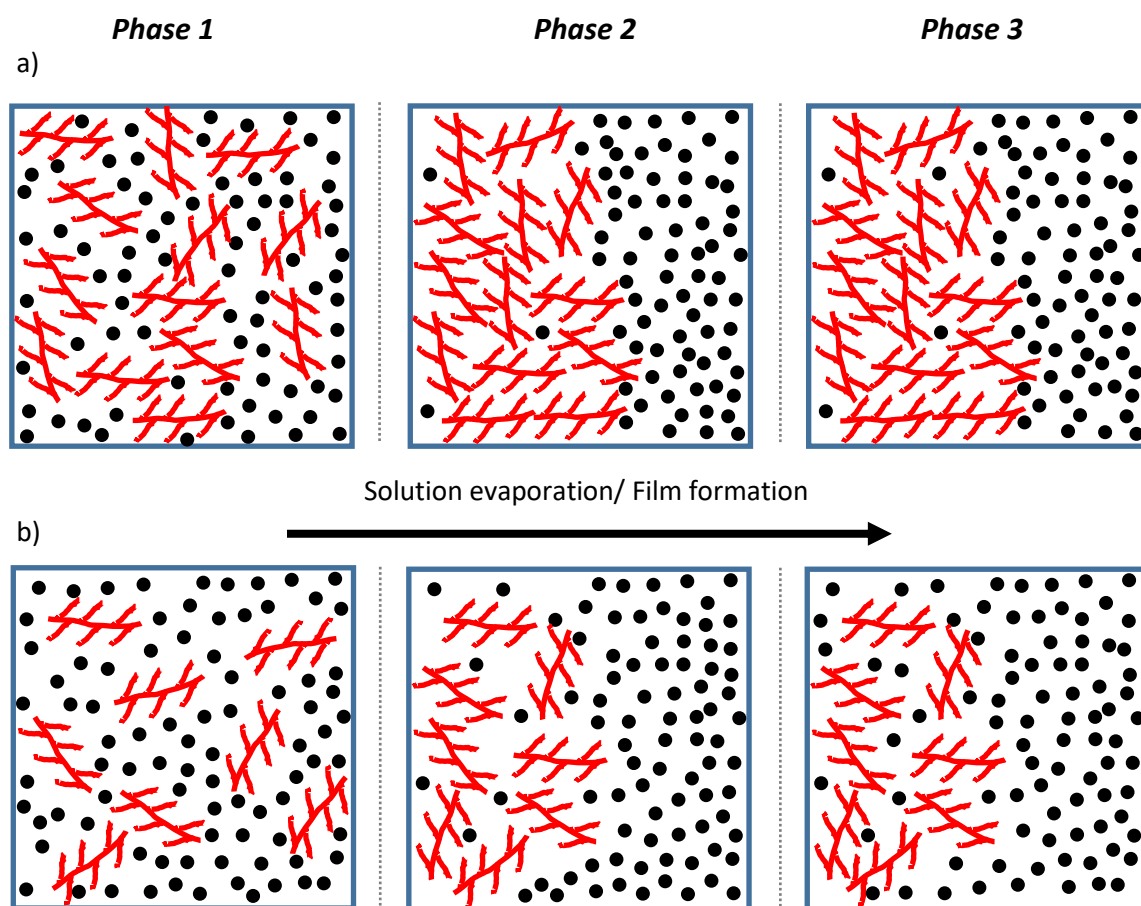


**Figure 15: Schematic presentation of a proposed film formation process for the PCBM:PPBI-alkyl mixtures at the case of a) (0.5:0.5) and b) (0.75:0.25). The black filled dots represent the PCBM molecules, and the red branched red lines represent the PPBI-alkyl polymer chains.**

The top two panels show the case for the film formation at the case of PCBM:PPBI-alkyl (0.5:0.5). In this case, upon solvent evaporation and film formation the formed PCBM and PPBI-alkyl phases are significantly separated with insignificant intermixed phases. After most solvent molecules evaporate no significant PCBM diffusion within the PPBI-alkyl phase occur.

The lower two panels show the case for the film formation at the case of PCBM:PPBI-alkyl (0.75:0.25). In this case upon solvent evaporation and film formation, the formed PCBM and PPBI-alkyl phases are more intermixed compared to the case with equal PCBM and PPBI-alkyl content. Even though the PPBI-alkyl is still expected to form large domains, the PCBM molecules are able to diffuse within the PPBI-alkyl domains due to its high content. Moreover, the PCBM diffusion within the PPBI-alkyl phase continue to proceed over an extended time after film formation.

## 6.6 Outlook

Based on the above, I concluded that there is an optimum mixing ratio between PCBM and PPBI-alkyl at which one can attain an optimum morphology for efficient devices. Nevertheless, I only investigated bilayer devices in which it is not possible to achieve high efficiency. So, the same idea (achieving the optimum mixing ratio of PCBM and PPBI-alkyl) was extended to fabricate ternary solar cells employing PCE11, PPBI-alkyl and PCBM. The aim was to evaluate if the above conclusions would transfer in the case of a donor/acceptor blend. The question was if this ternary blend combination at the same PCBM:PPBI-alkyl mixing ratio would lead to enhanced solar cell performance and if certain features in the insitu optical spectra would correspond to this enhancement. I hypothesized that due to the favorable mixing of PCBM with PCE11 and its diffusion within the PPBI-alkyl domain, we would achieve optimum morphology with good charge separation via PCBM and good percolation pathways through the PPBI-alkyl chains for favorable charge transport. This would result in efficient charge generation and transport and consequently improved solar cell performance.

Figure 16.a shows the solar cell performance of the ternary solar cell compared to the binary solar cells having either only PCBM or only PPBI-alkyl as the acceptor. All the devices were fabricated using donor:acceptor = 1:1. Similar to the mixed bilayer devices, the best ternary devices were achieved using a 0.75:0.25 PCBM to PPBI-alkyl acceptor ratio. The best devices showed up to 30% increase in  $J_{sc}$  which was the main origin of overall efficiency improvement (from 4.2% to 5.5%). I then compared these results to the PL quenching during the whole film deposition process of the same blends used to fabricate the solar cells. Similar to the trend for the mixed PCBM:PPBI-alkyl films, the ternary blend film using a 0.75:0.25 PCBM to PPBI-alkyl acceptor ratio corresponded to the most extended PL quenching behavior as shown in Figure 16.b.

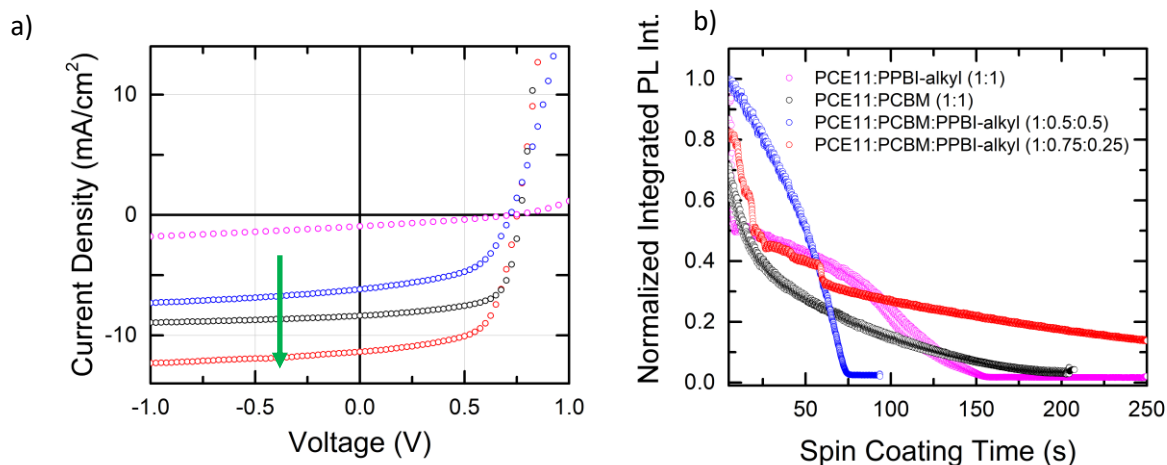


**Figure 16: a) J-V curves of the best BHJ solar cells consisting of PCE11:PCBM (1:1) (black), PCE11:PPBI-alkyl (1:1) (red) and PCE11:PCBM:PPBI-alkyl (1:0.75:0.25) (blue) b) Normalized Integrated PL intensity of the PCBM:PPBI-alkyl mixtures during spin coating at different ratios**

While this initially confirms that the PL quenching behavior in the blends might serve as an indication of a good device morphology that corresponds to an enhanced solar cell performance, investigating the film formation and aggregation dynamics for the binary and the ternary blends in more details is needed following the same methodology for the mixed acceptor layers. But in the case of the ternary blends, extracting useful insights from the insitu data is complicated due to the overlapping spectra of the different components. This means that a different approach is needed to decouple the evolution of the different components without impacting the results. Moreover, investigating different material systems (for example small molecule donor/polymer acceptor systems) would offer a generalized picture that enables one to rationally choose blend systems that offer good solar cell performance based on certain signatures appearing in the insitu optical spectra. In addition, although there was a 30% increase in the ternary solar cell PCE when adding 25% PPBI-alkyl was 30%, the best device PCE of 5.5% is very low. A possible improvement might be utilizing a less crystalline donor polymer instead of PCE11. A good candidate would be P3TEA which is a more amorphous TDA donor polymer. P3TEA showed good performance when combined with the small molecule PDI acceptor SF-PDI [21].

## 6.7 Conclusion

PDI side chain polymers were implemented as a polymer acceptor in organic solar cells but showed poor performance. This poor performance was attributed to excessive aggregation of PPBI-alkyl and poor mixing with the PCE11 polymer donor. The idea was then to use PDI side chain polymers

as a third component in a bilayer solar cell in combination with a fullerene acceptor. The idea was to benefit from the combined effect of both components in terms of better charge dissociation provided by the fullerene acceptor and a formation of percolation pathways for better charge transport provided by the polymer acceptors. In the bilayer devices, the overall efficiency increased by using a mixed PCBM and PPBI-alkyl acceptor layer compared to bilayers made with either component as the acceptor. This was attributed to the formation of an intermixed phase between both PCBM and PPBI-alkyl leading to better charge dissociation and less non geminate recombination at the interface with PCE11. PCBM inhibited the excessive aggregation of PPBI-alkyl and diffused within the PPBI-alkyl domains after solvent evaporation and film formation to form these intermixed domains between both components. This conclusion was consistent with the insitu spectroscopy data. Insitu data showed a long decay of the PL intensity even after the final films has been already formed signaling PCBM diffusion within the PPBI-alkyl domains that further enhanced the intermixing between both acceptors. In ternary BHJ devices, the addition of PPBI-alkyl as a third component to PCE11 and PCBM led to a 30% increase in solar cell performance. This was mainly due to increased  $J_{sc}$  which we attributed to the formation of an optimum morphology between the three components leading to better charge generation in a similar manner to the bilayer devices.

This work shows that as a first step, it is possible to predict the viability of an organic blend to be used to fabricate efficient solar cells. By investigating the PL quenching of different organic blends, one can gain information about the intermixing of domains between materials used in such blends. The reduction of the PL intensity over a long time after film formation indicates further formation of interfaces between the blend materials which offers a more favorable morphology for efficient organic solar cells.

## References

- [1] A.S. Lang, M.A. Muth, C.D. Heinrich, M. Carasco-Orozco, M. Thelakkat, Pendant perylene polymers with high electron mobility, *J Polym Sci Pol Phys*, 51 (2013) 1480-1486.
- [2] H. Lee, D. Lee, D.H. Sin, S.W. Kim, M.S. Jeong, K. Cho, Effect of donor-acceptor molecular orientation on charge photogeneration in organic solar cells, *Npg Asia Mater*, 10 (2018).
- [3] S. Wedler, C. Zhou, G.C. Bazan, F. Panzer, A. Köhler, Role of Torsional Flexibility in the Film Formation Process in Two pi-Conjugated Model Oligomers, *J Phys Chem Lett*, 11 (2020) 9379-9386.
- [4] H. Wang, Y.J. He, Y.F. Li, H.M. Su, Photophysical and Electronic Properties of Five PCBM-like C-60 Derivatives: Spectral and Quantum Chemical View, *J Phys Chem A*, 116 (2012) 255-262.
- [5] B. Ma, C.E. Bunker, R. Guduru, X.F. Zhang, Y.P. Sun, Quantitative spectroscopic studies of the photoexcited state properties of methano- and pyrrolidino-[60]fullerene derivatives, *J Phys Chem A*, 101 (1997) 5626-5632.
- [6] S. Nath, H. Pal, A.V. Sapre, Effect of solvent polarity on the aggregation of fullerenes: a comparison between C-60 and C-70, *Chem Phys Lett*, 360 (2002) 422-428.
- [7] T. Hahn, S. Tscheuschner, F.J. Kahle, M. Reichenberger, S. Athanasopoulos, C. Saller, G.C. Bazan, T.Q. Nguyen, P. Strohriegel, H. Bässler, A. Köhler, Monomolecular and Bimolecular Recombination of Electron-Hole Pairs at the Interface of a Bilayer Organic Solar Cell, *Adv Funct Mater*, 27 (2017).
- [8] M. Stephen, K. Genevicius, G. Juska, K. Arlauskas, R.C. Hiorns, Charge transport and its characterization using photo-CELIV in bulk heterojunction solar cells, *Polym Int*, 66 (2017) 13-25.
- [9] R. Singh, S.R. Suranagi, J. Lee, H. Lee, M. Kim, K. Cho, Unraveling the efficiency-limiting morphological issues of the perylene diimide-based non-fullerene organic solar cells, *Sci Rep-Uk*, 8 (2018).
- [10] P.E. Hartnett, A. Timalina, H.S.S.R. Matte, N.J. Zhou, X.G. Guo, W. Zhao, A. Facchetti, R.P.H. Chang, M.C. Hersam, M.R. Wasielewski, T.J. Marks, Slip-Stacked Perylenediimides as an Alternative Strategy for High Efficiency Nonfullerene Acceptors in Organic Photovoltaics, *J Am Chem Soc*, 136 (2014) 16345-16356.
- [11] N.A. Ran, S. Roland, J.A. Love, V. Savikhin, C.J. Takacs, Y.T. Fu, H. Li, V. Coropceanu, X.F. Liu, J.L. Bredas, G.C. Bazan, M.F. Toney, D. Neher, T.Q. Nguyen, Impact of interfacial molecular orientation on radiative recombination and charge generation efficiency, *Nat Commun*, 8 (2017).
- [12] A. Gusain, R.M. Faria, P.B. Miranda, Polymer Solar Cells-Interfacial Processes Related to Performance Issues, *Front Chem*, 7 (2019).
- [13] Y.H. Liu, J.B. Zhao, Z.K. Li, C. Mu, W. Ma, H.W. Hu, K. Jiang, H.R. Lin, H. Ade, H. Yan, Aggregation and morphology control enables multiple cases of high-efficiency polymer solar cells, *Nat Commun*, 5 (2014).
- [14] H. Cha, S. Wheeler, S. Holliday, S.D. Dimitrov, A. Wadsworth, H.H. Lee, D. Baran, I. McCulloch, J.R. Durrant, Influence of Blend Morphology and Energetics on Charge Separation and Recombination Dynamics in Organic Solar Cells Incorporating a Nonfullerene Acceptor, *Adv Funct Mater*, 28 (2018).
- [15] Y.W. Zhang, A.J. Parnell, O. Blaszczyk, A.J. Musser, I.D.W. Samuel, D.G. Lidzey, G. Bernardo, Effect of fullerene acceptor on the performance of solar cells based on PffBT4T-2OD, *Phys Chem Chem Phys*, 20 (2018) 19023-19029.

- [16] P.P. Khlyabich, B. Burkhardt, B.C. Thompson, Efficient Ternary Blend Bulk Heterojunction Solar Cells with Tunable Open-Circuit Voltage, *J Am Chem Soc*, 133 (2011) 14534-14537.
- [17] K. Jiang, G.Y. Zhang, G.F. Yang, J.Q. Zhang, Z.K. Li, T.X. Ma, H.W. Hu, W. Ma, H. Ade, H. Yan, Multiple Cases of Efficient Nonfullerene Ternary Organic Solar Cells Enabled by an Effective Morphology Control Method, *Adv Energy Mater*, 8 (2018).
- [18] P.P. Khlyabich, B. Burkhardt, B.C. Thompson, Compositional Dependence of the Open-Circuit Voltage in Ternary Blend Bulk Heterojunction Solar Cells Based on Two Donor Polymers, *J Am Chem Soc*, 134 (2012) 9074-9077.
- [19] R.A. Street, D. Davies, P.P. Khlyabich, B. Burkhardt, B.C. Thompson, Origin of the Tunable Open-Circuit Voltage in Ternary Blend Bulk Heterojunction Organic Solar Cells, *J Am Chem Soc*, 135 (2013) 986-989.
- [20] N. Gasparini, A. Salleo, I. McCulloch, D. Baran, The role of the third component in ternary organic solar cells, *Nat Rev Mater*, 4 (2019) 229-242.
- [21] J. Liu, S.S. Chen, D.P. Qian, B. Gautam, G.F. Yang, J.B. Zhao, J. Bergqvist, F.L. Zhang, W. Ma, H. Ade, O. Inganäs, K. Gundogdu, F. Gao, H. Yan, Fast charge separation in a non-fullerene organic solar cell with a small driving force, *Nat Energy*, 1 (2016).

## Chapter 7: Conclusion

One of the ultimate goals for solution processing of opto-electronic thin film devices based on organic materials is targeting the optimum active layer morphology that results in the best possible device efficiency. Similar to inorganic semiconductors, it would be better to achieve the desired film properties a priori by specifying certain parameters. This task can be made easier by better understanding the film formation process of organic materials during solution processing. Thanks to the advancement in insitu techniques, the investigation of the film formation became possible in recent years.

In my thesis I tried to answer 3 main questions related to this task:

- 1- What is the effect of blending on the polymer chain conformation within the polymer aggregates?
- 2- How does the aggregate formation occur during film deposition of organic thin films and how can this be manipulated to achieve the desired aggregate properties?
- 3- Can certain spectral signatures appearing during the film formation of blends used in organic solar cells be related to the resulting solar cell performance?

The combined answers of these three questions would give us a general guideline to construct a road map aiming to achieve targeted fabrication of organic optoelectronic devices with high efficiencies. Although in my thesis I focused solely on organic solar cells, my results are transferable to other devices based on organic semiconductor such as organic field effect transistors.

To answer the first question, I investigated the effect of blending PCE11 with an inert polymer on the conformational changes within the PCE11 aggregates. Upon blending, I observed changes in the PCE11 optical spectra which I quantified using Franck-Condon analysis. These results suggested that blending leads to a more planarized, longer conjugated PCE11 chains with a reduced degree of interchain molecular coupling. This was in agreement with the observed differences of the Raman spectra between the neat and the blend films.

In addition, two important conclusions could be drawn from this work although not directly related to the answer to question one. Firstly, this work shows experimentally how changes in the Raman mode characteristics of conjugated polymers are closely related to changes appearing in the optical spectra. Secondly, from a methodology point of view, this work presented a new approach towards a more reliable application of the Frank Condon analyses to donor-acceptor-type conjugated

polymers. Instead of relying on repeated fitting of the experimental spectra until a satisfactory result is approached, I followed a more statistical approach where the fitting results were presented as average values of individual fits with the accompanied error ranges. This represents a more objective approach -rather than a subjective one- to the Frank Condon analysis for organic materials with unstructured or broad optical spectra, while additionally delivering good accuracy of the extracted parameters.

Based on the results gained from the previous chapter, I then addressed the second question. In my opinion, this is a central question in the field of organic optoelectronic device fabrication. I tried to provide a detailed investigation of the aggregate formation dynamics for conjugated polymers which as far as literature goes, hasn't been done before in such detail. This investigation took into consideration the main processing conditions affecting the aggregate formation in conjugated polymer during solution processing of thin films. These conditions included the solvent quality, the solvent's boiling point, the film deposition temperature, the polymer's critical transition temperature in solution and the addition of an extra material.

I quantified the evolution of aggregate formation during blade coating P3HT films from solutions using Franck-Condon analysis. Based on the relationship between the solution processing conditions and the evolution of the aggregate properties during deposition, I concluded that the aggregate formation in solution processed conjugated polymer films follow one of two pathways. These were either a 2-step pathway where aggregates initially form in solution before solidification or via a 1-step pathway where aggregates only form at high polymer concentration upon sufficient solvent evaporation and film formation. The followed pathway determines the aggregate properties in the final film. Within the 2-step pathway, the initial aggregates start to form in a solvent rich atmosphere under reduced steric hindrance allowing more time for polymer chains to order before solvent evaporation. This pathway results in aggregates characterized by a more planar, more ordered structure. Within the 1-step pathway, the initial aggregates form at high polymer concentration during fast solvent evaporation and under more steric hindrance. These conditions do not allow the polymer chains to order and therefore keeping their initial quenched conformation in the aggregate domains within the final film. Consequently, this pathway results in aggregates characterized by a less planar, less ordered structure.

Following this aggregate formation picture, targeting the desired pathway can be achieved by manipulating the processing conditions and hence the aggregate formation dynamics to either allow or prohibit aggregates to form in solution. At deposition temperatures much higher or lower than the critical transition temperature, the main driver of the aggregation is the

solubility of the polymer while the other parameters offer little impact on the resulting aggregates. At deposition temperatures much higher than the critical transition temperature aggregates usually form following a 1-step pathway. On the contrary, at deposition temperatures much lower than the critical transition temperature aggregates usually form following a 2-step pathway. However, at deposition temperatures in the vicinity of the critical transition temperature, controlling the time allowed for aggregate to form in solution becomes crucial. Allowing a slight time window for aggregates to form in a solvent rich atmosphere, leads to the aggregate formation following the 2-step pathway even at temperatures slightly higher than the critical transition temperature.

To answer the final question, I compare the film formation dynamics and the solar cell performance of materials used in organic device fabrication. In a bilayer device based on a mixed fullerene acceptor:polymer acceptor (PCBM:PPBI-alkyl) layer, the overall device efficiency increased compared to bilayers made with either component as the acceptor. This enhanced device performance corresponded to a unique PL quenching signal appearing in the insitu data where reduction of the PL intensity proceeded over an extended time period even after the film has been already formed. This was attributed to the PCBM diffusing within the PPBI-alkyl domains for a long period after the film has been already formed, leading to the formation of intermixed domains between both components. This favourable intermixed morphology resulted in better charge dissociation and less non geminate recombination at the interface with PCE11. Similarly, in ternary BHJ devices, the addition of PPBI-alkyl as a third component to blends of PCE11 and PCBM led to an enhanced solar cell performance. This was mainly due to increased  $J_{sc}$ , which I attributed also to the formation of an optimum morphology between the three components leading to better charge generation. This enhanced device performance also corresponded to a delayed PL quenching signal appearing in the insitu data. Both of these results show that a delayed PL quenching signal appearing in blends of organic materials used in solar cells means that interfaces are formed between both materials for prolonged times even after the solid films have been already formed.

Overall, my work offers a general guideline about the relationship between the solution processing conditions, the resulting aggregate properties and the corresponding solar cell performance. It also shows that detailed analysis of the insitu optical spectroscopy of different organic blends can be used to predict efficiency of such blends in organic solar cell. This work lays the ground towards achieving targeted solution processing of organic blend films for efficient organic solar cells.



# Acknowledgements

I would like to express my pleasure of having spent the last 6 years in the EPII chair under the supervision of Anna Köhler. Although I went through a lot of ups and downs during my time here, being in such a professional, friendly and supportive environment really made a big difference.

First and foremost, I would like to thank Anna for having me in the group and supporting me through this long and tough journey. Without a doubt, I would not have been able to complete my thesis without her continuous support and encouragement both scientifically and personally. Of course a special thanks goes to Frank Schirmer and Irene Bauer. They are two cornerstones of the group and without their presence and help we would have faced a tough time. Whenever I had a problem they were always available with help and I don't remember a time where I needed help from them and it wasn't fixed within the same day. A special thanks goes to Fabian Panzer who was the first one to meet me from the group even before coming to Germany. I am really happy about the work we did together and all the long discussions that I really benefited from. I would also like to thank Konstantin Schötz for the collaboration and the work we did together. Probably he is the one that I worked the most with during my time here and I really learned a lot during this time. Another thanks to Julian Kahle. Although we didn't get to work a lot together, he always had answers and insights when I had any questions or problems regarding device fabrication and characterization. I would also like to thank Thomas Unger who helped me during my first weeks at the group and brought me up to speed with what to do and where to go if I need something. Another thanks to Denys Priadko. Despite not doing any work together, our long conversations about work and life were really unique and insightful.

Thanks to every single person I met here. Maybe we didn't work or talk a lot together but even a smile or a good morning in the corridor goes a long way. Overall, I am really happy for the time I spent with you all and the really friendly funny environment that was made possible by everyone here. Although I am not always the most outgoing person, I will remember any shared memory or time we spent together in a conference, in a BBQ or while having a nice meal together. I wish you all the best in your future.

The most important thanks but also an apology to my wife. I know that you endured a lot so that I would be able to finish this thesis, so I hope I can make it up to you one day. A very important thanks to my daughters. Although you would not understand this, but you were one of my main motivations for finishing this thesis. Finally, thanks to my family, my father, my brothers and especially my mother. You always supported me both emotionally and financially during the tough times I went through. I would not have been able to go this far without your support.



## Eidesstattliche Versicherung

Hiermit versichere ich an Eides statt, dass ich die vorliegende Arbeit selbstständig verfasst und keine anderen als die von mir angegebenen Quellen und Hilfsmittel verwendet habe.

Weiterhin erkläre ich, dass ich die Hilfe von gewerblichen Promotionsberatern bzw. -vermittlern oder ähnlichen Dienstleistern weder bisher in Anspruch genommen habe, noch künftig in Anspruch nehmen werde.

Zusätzlich erkläre ich hiermit, dass ich keinerlei frühere Promotionsversuche unternommen habe.

Bayreuth, den

Unterschrift

## Einverständniserklärung

gemäß § 9 (7) und (8) PromO BayNAT

Hiermit erkläre ich mich einverstanden, dass die elektronische Fassung meiner Dissertation unter Wahrung meiner Urheberrechte und des Datenschutzes einer gesonderten Überprüfung unterzogen werden kann.

Des Weiteren erkläre ich mich einverstanden, dass bei Verdacht wissenschaftlichen Fehlverhaltens Ermittlungen durch universitätsinterne Organe der wissenschaftlichen Selbstkontrolle stattfinden können.

Bayreuth, den

Unterschrift



